Characterising cosmic filaments and their surroundings in large-scale hydro-dynamical simulations

Daniela Galárraga-Espinosa

université
PARIS-SACLAY

Caractérisation des filaments cosmiques et de leur environnement dans des simulations hydrodynamiques cosmologiques

Characterising cosmic filaments and their surroundings in large-scale hydro-dynamical simulations

Thèse de doctorat de l'Université Paris-Saclay

École doctorale n° 127, Astronomie et Astrophysique d'Ile-de-France (AAIF)
Spécialité de doctorat: Astronomie et Astrophysique
Unité de recherche: Université Paris-Saclay, CNRS, Institut d'astrophysique spatiale, 91405, Orsay, France.
Référent: : Faculté des sciences d'Orsay

Thèse présentée et soutenue à Paris-Saclay, le 17/09/2021, par

Daniela Galárraga-Espinosa

Composition du jury:

David Elbaz Directeur de recherche, CEA	Président
Adrianne Slyz University lecturer, University of Oxford	Rapportrice & Examinatrice
Franco Vazza Associate Professor, University of Bologna	Rapporteur & Examinateur
Marius Cautun Assistant professor, Leiden Observatory	Examinateur
Françoise Combes Professeure, Collège de France et Observatoire de Paris	Examinatrice
Pekka Heinämäki Associate Professor, University of Turku	Examinateur

Direction de la thèse:

Nabila Aghanim Directrice de recherche, CNRS, Institut d'Astrophysique Spatiale	Directrice de thèse
Mathieu Langer Professeur, Université Paris-Saclay, Institut d'Astrophysique Spatiale	Co-directeur de thèse

Thèse de doctorat

NNT: 2021UPASP082

A mis papis Cristina y Gustavo,
A mis hermanos Camila y Martín,
A mis abuelos Glori y Mashi.

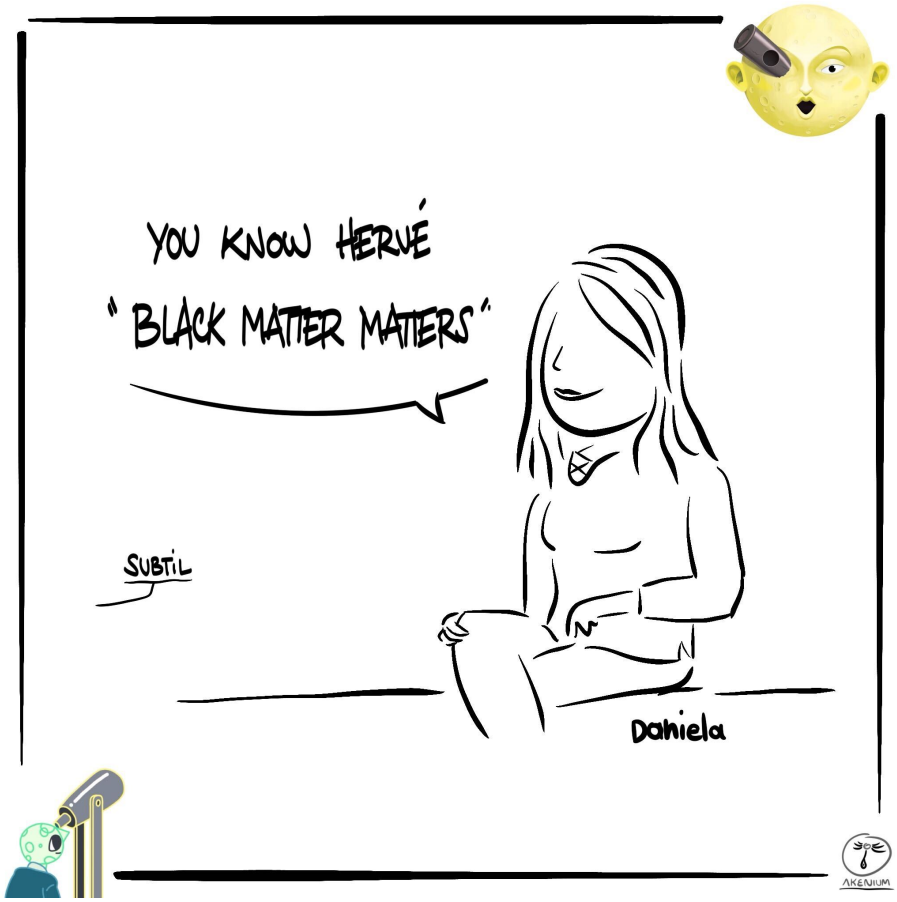

Sketch by Guillaume Monnain (AKENIUM), www.akenium.fr
'Du big bang aux big bands' festival, 2020.

Acknowledgments

This thesis is the result of three years of work at the Institut d'Astrophysique spatiale d'Orsay. It would not have been possible without all the people that accompanied me through this journey. I believe that, at a given moment in life, one is the reflection of our present environment, combined with our previous past experiences. Kind of like galaxies...

I would like to start by thanking my amazing supervisors, Nabila and Mathieu. Vous m'avez appris à aller toujours plus loin, à chercher toujours plus mieux et plus complet dans mes démarches et reflexions scientifiques. Je vous admire et apprécie énormément tous les deux.

Nabila, merci pour m'avoir 'choisie' et pour m'avoir donné l'opportunité de travailler avec toi et avec cette magnifique équipe que tu as crée au sein de ton projet ByoPiC. On ne se connaissait pas vraiment au début, et très rapidement tu as su me pousser en dehors de ma zone de confort pour dépasser ce que je pensais être mes limites. Je te remercie pour cela. Merci aussi pour toutes les discussions qu'on a eues dans ton bureau, pour celles qui portaient sur la science et aussi pour les autres. Les heures que tu as passées avec moi à discuter de la vie, ta sensibilité, ton empathie, et les précieux conseils que tu as su me donner, m'ont aidé à mieux vivre ma réalité de femme en science, dans un pays lointain, immergée dans une culture différente de la mienne.

Mathieu, contrairement à Nabila, on se connaissait depuis bien avant octobre 2018. Tu n'as pas seulement marqué mes années de Magistère, mais aussi les trois années qui ont suivi. J'ai énormément apprécié les discussions qu'on a pu avoir ensemble (sur tout plein de sujets très variés!) dans ton bureau, pendant un cours de Swedish fit, autour d'un verre, en faisant du kayak à bord du Yellow Pearl, dans les grottes du Quercy (and the list goes on!). Je suis heureuse d'avoir pu partager avec toi notre passion commune pour le sport, l'art, et la bonne bouffe. Merci aussi de n'avoir jamais laissé passer des fautes d'anglais dans mes papiers et dans mon manuscrit. La légende dirait qu'il nous est arrivé (quelques fois) de passer des après-midi entières à trouver la bonne formulation des phrases, à changer des mots et des virgules.

An enormous thank you to my family, in Ecuador. Papis, mis logros de hoy son obviamente gracias a ustedes y a todo lo que me han enseñado.

A mi mami Cristina, gracias por haberme empujado desde chiquita a salir de mis zonas de confort, siempre impulsándome a desarrollar mi capacidad de adaptación a cualquier situación. Gracias por los años enteros de tu vida en los que te dedicaste exclusivamente a educarnos a mi y a mi ñaño. Mami, me enseñaste la bondad, la serenidad, el positivismo y a siempre tener los pies sobre la tierra.

A mi papi Gustavo, gracias por haberme transmitido tu amor y pasión por la ciencia. Eres mi ejemplo de lucha inquebrantable, mi puerto seguro. Gracias por enseñarme a tener nervios de acero, y que nada es imposible si eres lo suficientemente loco para soñarlo. Si bien gracias a mi mami tengo los pies en la tierra, gracias a tí tengo la cabeza y mis ambiciones en el espacio.

Quiero agradecerles a mis abuelitos Glory y Mashi por llenarme de amor incondicional desde siempre, por su apoyo, y por todos los valores que me transmitieron. Mis logros de hoy son los suyos también.

Gracias a mi tío Marce por haberme lavado el cerebro hasta convencerme de ir a la prepa. Admito que te agradezco también por las infernales molestadas, que resultaron ser una lección de vida, fijando bien alto mi umbral de susceptibilidad.

Por sobretodo, gracias a mi ñaño Martín y a mi nueva hermana Célia, con quienes tuve el privilegio de compartir (casi) todos los días de esta aventura que empezó hace tres años.

Ñaño, vivir en coloc contigo ha sido una de las cosas más lindas que me ha pasado. Empezamos con un colchón inflable y un horno en la sala, y poco a poco fuimos creando nuestra casa con los muebles recogidos de la calle (y otros pocos comprados, o donados...). Pocas personas sabrán todas las configuraciones de tuvo nuestro departamento en Massy. Gracias por tu apoyo siempre, por haber estado ahí en absolutamente todos los momentos, por haberme escuchado, aconsejado, soportado, por haber calmado mis ideas y mis locuras (a veces no se si eres tú o yo el/la mayor de la familia). Gracias por haberme hecho la comida más rica del mundo. Gracias, ñaño, por ser tu.

Célia, la première fois que je t'ai vue tu étais blonde et tu venais d'arriver en France. Tu es très vite devenue ma soeur, ma confidente, ma complice. Merci d'avoir été présente pendant ces trois années, merci pour ton soutien, tes mots, et ton empathie. Merci de toujours rayonner cette énergie très belle qui te caracterise.

Céline, ma go, ma besta. Je ne trouve toujours pas les mots pour te remercier pour tout ce que tu m'as apporté pendant cette période. Tu es de ces personnes qu'on ne trouve qu'une seule fois dans la vie, le coup de foudre amical. Je suis si heureuse d'avoir eu l'opportunité de te rencontrer, de partir en voyage avec toi, de se *'sapper comme jamais'*, d'avoir passé des heures à regarder Koh-lanta et encore plus d'heures à discuter (ou plus communément, à *'bitcher'*). Merci pour ton soutien inconditionnel et pour avoir été ma copine d'aventures de tout genre. J'attends avec impatience de vivre ensemble les nouvelles saisons de la série qui raconte notre vie, et qui est digne des plus grandes plateformes de streaming.

Quentin, Alex, Walt, Aymeric: sans vous je ne serais certainement pas la même personne aujourd'hui. Merci pour votre soutien émotionnel, pour votre écoute, pour les bières et/ou chocolats chauds, et pour votre présence rassurante et apaisante pendant toutes ces années.

Un grand merci aux colocs du L.A.B.O. Cette thèse ne serait pas la même sans vous. Six mois avant la fin de ma thèse je suis arrivée dans cette maison mythique dans la campagne d'Orsay, pleine d'êtres vivants bienveillants (les trois poules inclues). J'ai appris à vous connaître et à vous aimer comme des frères. Merci Antouane, Arthur, tonton Baptiste, Fabiche, et Tibo pour tous les moments qu'on a partagé ensemble, pour les discussions, les soirées films, le foot, les calzones du chef (avec sauce tomate), le pèlerinage en Chartreuse, la Chartreuse, pour avoir été mon support moral (et pour m'avoir nourri) pendant les pires moments de la redaction de ma thèse. Merci Fab et Arthur pour les pâtes aux olives.

This thesis could not have been possible without the support of my friends and colleagues of IAS. A mes copains de galère, Tony, Marion et Tibo: merci d'avoir été là. En ouvrant la porte du bureau des princesses on trouvait toujours: *(i)* le sourire accueillant de Tony, *(ii)* Tibo,

l'intrus, avec ses t-shirts innapropriés, *(iii)* la petite tortue rassurante de Marion, et *(iv)* notre maman Céline qui essayait par tous ses moyens (un lexo?) d'éviter qu'on pète les plombs. Je n'ose meême pas imaginer comment ces trois ans auraient été sans vous!

Adelie, merci pour ton aide, ton écoute, ton empathie, ton enthousiasme contagieux et pour tes très bons gouts musicaux. Best office mate ever.

Edouard, merci pour cette conversation qu'on a eue dans ce bar à la fin de mon M2 et qui, de toute évidence, a été une bifurcation dans ma vie puisque tu m'as parlé de ByoPiC pour la première fois. Merci de me faire rire à chaque fois, et pour tes conseils dignes de psychologue/coach personnel.

Pierre, Louise, Natalia, Aurélien et Florian, merci pour votre soutien et pour votre amitié depuis mon arrivée à Orsay. Vous m'avais transmis votre passion pour l'astro, et c'est grâce à vous que je me suis retrouvée à l'IAS! Au début je me sentais un peu comme une intruse qui ne savait pas trop ce que c'était une galaxie dans ce labo dont je vous avais tant entendu parler et parler et parler, mais j'ai très vite compris pourquoi vous étiez si fous d'astro et, plus que tout, heureuse d'avoir la chance d'être entouré au quotidien par vous, mes amis. Louise, merci pour la complicité depuis 2015. Nat, gracias por las refrescantes pausas en español.

A ceux qui sont partis, Victor et Loulou, merci pour les bons moments qu'on à partagé pendant une partie de ces trois ans. Loulou, merci d'avoir enflamé le bureau et le dancefloor avec ton groove.

Thanks Joseph, my office mate, for your good vibes, for all the laughs and advices, and for always keeping the office freaking cold (!).

A big thank you to all the members of the ByoPiC team and the cosmology group. Most particularly thanks Hideki, Nicola, Marian and Julien for the enlightening discussions and for the time you took to answer my many questions during these three years. Merci Hervé pour toutes les opportunités de médiation scientifique. Laura, thanks for all your support and your friendship.

Merci à mes copines de la Troupe de danse de Paris-Saclay. Danser avec vous m'a permis de maintenir mon équilibre physique et moral pendant ces trois années de thèse (et même depuis bien avant!). Merci Claudie de m'avoir offert un lieu sûr et une place pour m'exprimer à travers tes magnifiques oeuvres que j'ai dansé pendant un peu plus de 6 ans. Elise, ma soeur de coeur, merci pour tous les duos, les scènes partagées, et pour m'avoir offert des petites pauses d'air frais dans les montagnes de Savoie.

I would also like to thank the members of the jury for taking the time to read and understand my work and my manuscript. Thank you for all your relevant comments and advice, that will help me in my future research.

Por ultimo quiero dedicarle este trabajo a mi hermanita (ya no tan chiquita) Camila, la cual me cambió la vida hace 13 años. Cami, gracias por ser mi luz y brindarme tanta alegría con tu existencia. Atrévete a soñar y a luchar con fuerza por lo que tú quieres. Tus límites son los que tu misma te impones, y yo siempre voy a estar ahí cuando me necesites para enfrentar juntas cualquier obstáculo en tu camino.

List of main musical inspirations

Chapter 2

- Yann Tiersen (all)
- Sons of the East (all)
- Cat Stevens, Neil Young

Chapter 3

- Nekfeu - Ciel Noir, Ecrire
- French rap (e.g. Jul - Bande organisee)
- Disney instrumental songs (mainly the Little Mermaid)
- Pyotr Illych Tchaïkovski - The Nutcracker

Chapter 4

- Billie Eilish (all)
- AC/DC - Highway to hell
- ABBA (all)

Chapter 5

- Mumford and Sons (all their albums, but mainly Delta)
- Top 100 Disney songs
- Orelsan - Simple, Basique
- Lomepal - Amina (full album)

Chapter 6

- Pyotr Illych Tchaïkovski - Swan Lake, No. 5 Pas de Deux
- Ludovico Einaudi
- Nekfeu - Les etoiles vagabondes (full album)
- Coldplay - Ghost stories (full album)

Résumé (en français)

La matière dans l'Univers s'assemble sous l'action de la gravité pour former un gigantesque réseau composé de noeuds, de filaments, de murs et de vides, appelé la toile cosmique. Cette structure est principalement définie par la dynamique de la matière noire, qui forme le squelette sur lequel la matière baryonique (ou ordinaire) est accrétée. Alors que les structures cosmiques les plus denses, tracées par les amas de galaxies les plus massifs, ont été minutieusement étudiées, en raison de leurs densités plus faibles et de leurs morphologies complexes, les filaments cosmiques et les propriétés de la matière qui les entoure sont encore mal connus. Cependant, selon les études basés sur des simulations numériques, les filaments cosmiques sont censés contenir près de la moitié de la matière de l'Univers. L'étude de la matière aux plus grandes échelles est donc inévitablement liée à celle des filaments.

Cette thèse propose la première étude complète des filaments cosmiques au décalage spectral $z = 0$. Les filaments analysés sont détectés dans la distribution des galaxies de simulations hydrodynamiques cosmologiques. Ces structures cosmiques sont tout d'abord caractérisées par leurs profils radiaux de densité de galaxies, révélant que la distribution des galaxies autour des filaments varie avec la longueur de ceux-ci. Deux populations différentes sont ainsi identifiées: les filaments courts ($L_f < 9$ Mpc) et les longs ($L_f \geq 20$ Mpc). Je montre que ces deux populations tracent des environnements différents de la toile cosmique. Les filaments courts sont plus denses, plus épais, et plus chauds que les longs. Ils correspondent aux ponts de matière entre des structures sur-denses, alors que les filaments longs sont à la base du squelette cosmique, souvent enchâssés dans des régions sous-denses.

Les propriétés du gaz autour des filaments cosmiques sont ensuite caractérisées en distinguant différentes phases en fonction de la température et de la densité de gaz. Je montre que les filaments cosmiques sont essentiellement constitués de gaz associé au milieu intergalactique chaud (WHIM), et que leurs parties centrales hébergent également d'importantes contributions de phases gazeuses plus chaudes et plus denses, dont les fractions dépendent du type de filament. En construisant des profils radiaux de température et de pression, je trouve que les filaments cosmiques possèdent des coeurs isothermes et des valeurs de pression environ mille fois inférieures à celles des amas. De plus, la population de filaments courts est caractérisée par des valeurs de densité, de température, et de pression du gaz qui sont trois fois supérieures à celles des filaments longs. Étant donné que certaines propriétés des galaxies sont intimement liées aux propriétés de leur environnement à grande échelle, j'étudie également l'influence des différents environnements tracés par les populations de filaments sur la masse et l'activité de formation d'étoiles des galaxies, en trouvant différentes tendances pour les filaments courts et longs.

Contrairement aux propriétés physiques du gaz et des galaxies, la distribution relative de la matière noire, du gaz et des étoiles autour des filaments s'avère universelle, indépendante de la population de filaments. En obtenant des profils de fraction de baryons, je montre que la distribution de la matière baryonique s'écarte de celle de la matière noire à des distances inférieures à ~ 7 Mpc aux axes des filaments, indiquant un rayon caractéristique du profil des baryons dans

ces structures. Enfin, les coeurs des filaments sont fortement appauvris en baryons, tandis que leurs périphéries présentent un excès par rapport à la fraction cosmique, correspondant au gaz dans le WHIM.

La majeure partie du travail réalisé pendant ces trois années de thèse a donné lieu à l'écriture de trois articles en premier auteur: *Galárraga-Espinosa et al. (2020)*, *Galárraga-Espinosa et al. (2021)*, et *Galárraga-Espinosa et al. (2021b)*. Les deux premiers ont été publiés dans le journal Astronomy & Astrophysics, respectivement en septembre 2020 et en mai 2021. Le troisième article, *Galárraga-Espinosa et al. (2021b)*, est actuellement en cours de révision dans ce même journal. Pendant ma thèse j'ai aussi pu travailler en collaboration avec d'autres membres de mon équipe de recherche. J'ai notamment participé a la production de l'article *Malavasi et al. (2021)*, qui est actuellement en cours de révision.

Abstract

Matter in the Universe is assembled under the action of gravity to form a gigantic network of nodes, filaments, walls, and voids, called the cosmic web. This structure is mainly set by the dynamics of dark matter (DM), which forms the skeleton onto which baryonic (or ordinary) matter is accreted. While the denser cosmic structures, traced by the most massive clusters of galaxies, have been thoroughly studied, because of their lower densities and complex morphologies, cosmic filaments and the properties of matter around them are still poorly known. However, these structures are believed to contain almost half of the matter in the Universe. The study of matter at the largest scales is therefore inevitably linked to that of filaments.

This thesis offers the first comprehensive study of cosmic filaments at redshift $z = 0$. The analysed filaments are detected in the distribution of galaxies of large-scale hydro-dynamical simulations. These cosmic structures are firstly characterised by their radial profiles of galaxy density, revealing that the distribution of galaxies around filaments varies with filament length. Two different filament populations are thus identified, the short ($L_f < 9$ Mpc) and the long ($L_f \geq 20$ Mpc). I show that these two populations are tracers of different environments of the cosmic web. Short filaments are denser, puffier, and hotter than long filaments. The former correspond to the bridges of matter between over-dense structures, whereas the latter are at the basis of the cosmic skeleton, often embedded in under-dense regions.

The properties of gas around cosmic filaments are then characterised by distinguishing different phases according to temperature and density. I show that cosmic filaments are essentially made of gas in the warm-hot intergalactic medium (WHIM) phase, and that their cores also host large contributions of hotter and denser gas phases whose fractions depend on the filament population. By building radial temperature and pressure profiles, I find that cosmic filaments possess isothermal cores and pressure values that are ~ 1000 times lower than those of clusters. Moreover, the population of short filaments is characterised by values of gas density, temperature, and pressure that are a factor of three larger than these of long filaments. Since many properties of galaxies are intimately linked to the properties of their large scale environment, I also investigate the influence of the different environments traced by the filament populations on the mass and star-formation activity of galaxies, finding different trends in short and long filaments.

Contrary to the properties of gas and galaxies, the relative distribution of DM, gas, and stars around filaments is found to be universal, independent from the filament population. By deriving baryon fraction profiles, I show that baryonic matter deviates from the DM density field at distances closer than ~ 7 Mpc to the filament spines, indicating a characteristic radius of baryons in filaments. Finally, cores of filaments are strongly baryon depleted, and their outskirts present an excess of baryons with respect to the cosmic fraction, made essentially of WHIM gas.

Contents

Chapter 1

Introduction

Contents

1.1 The Universe on its largest scales

After the first observation of the galaxy distribution around the Perseus cluster (Jõeveer et al., 1978) and in the Center for Astrophysics (CfA) galaxy survey (de Lapparent et al., 1986), it appeared that on the largest scales, matter in the Universe is organised in clusters, filaments, walls, and voids. These structures form the cosmic web (Bond et al., 1996), a gigantic network of dark matter (DM) and gas, which formed under the effect of gravity from the anisotropic collapse of initial fluctuations of the density field (Zel'dovich, 1970).

Within the cosmic web, DM assembles from voids to walls, flows to filaments, and departs from filaments to reach the highest density regions, the nodes. This flow of matter forms the basis of the cosmic skeleton (as shown by the top panel of Fig. 1.1), onto which baryonic (or ordinary) matter falls, pulled by gravity (bottom panel of Fig. 1.1). Nevertheless, unlike DM which is purely non-collisional, baryonic matter is also subject to other physical processes (such as fluid pressure, heating by AGN feedback, cooling, galactic winds, or radiation) that prevent its indefinite collapse into singular objects. The physics of baryons thus alters their spatial distribution, which is usually broader (or more extended) with respect to the underlying DM density field as is clearly illustrated by Fig. 1.1.

In the last few decades, the cosmic web as traced by galaxies has been observed and studied in many galaxy surveys with increasing resolution and statistics. For example, the filamentary web-like pattern has been detected in the Sloan Digital Sky Survey (SDSS, York et al., 2000), the two degree Field Galaxy Redshift Survey (2dFGRS, Colless et al., 2003), the Cosmic Evolution and COSMOS2015 surveys (Scoville et al., 2007; Laigle et al., 2016), the 6dF Galaxy Survey (6dFGS, Jones et al., 2009), the Galaxy and Mass Assembly survey (GAMA, Driver et al., 2009, 2011), the VIMOS VLT deep survey (VVDS, Le Fèvre et al., 2005), VIPERS (Guzzo et al., 2014), WISExSuperCOSMOS (WISExSCOS, Bilicki et al., 2016), and SAMI (Bryant et al., 2015) surveys, among others.

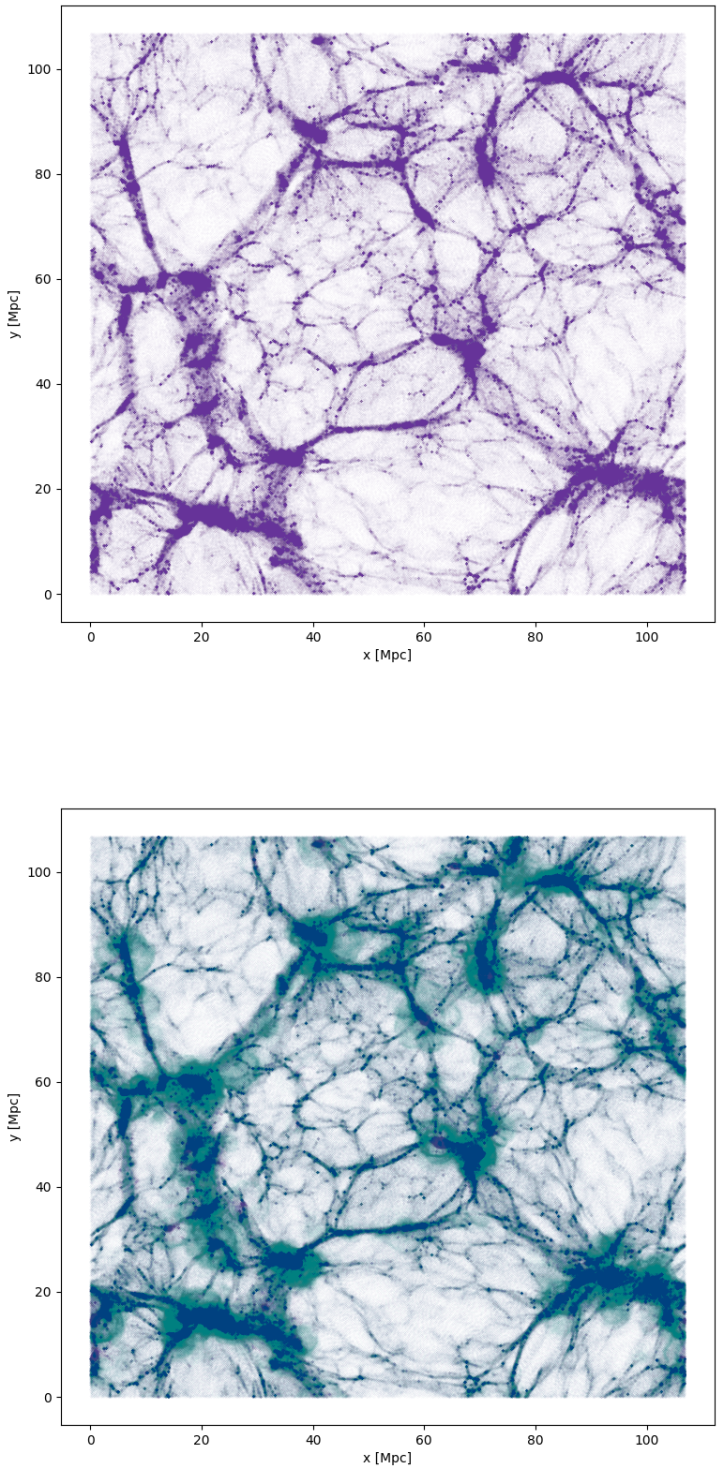

Figure 1.1: Illustration of the DM cosmic skeleton (top panel) as seen in a slice of the Illustris-1 simulation (Nelson et al., 2015). The bottom panel shows the distribution of baryons (green) around the corresponding DM density field (blue). It is worth mentioning that the distribution of baryons with respect to DM is particularly wider due to the strong feedback prescriptions used in this simulation (see Sect. 2.1.1).

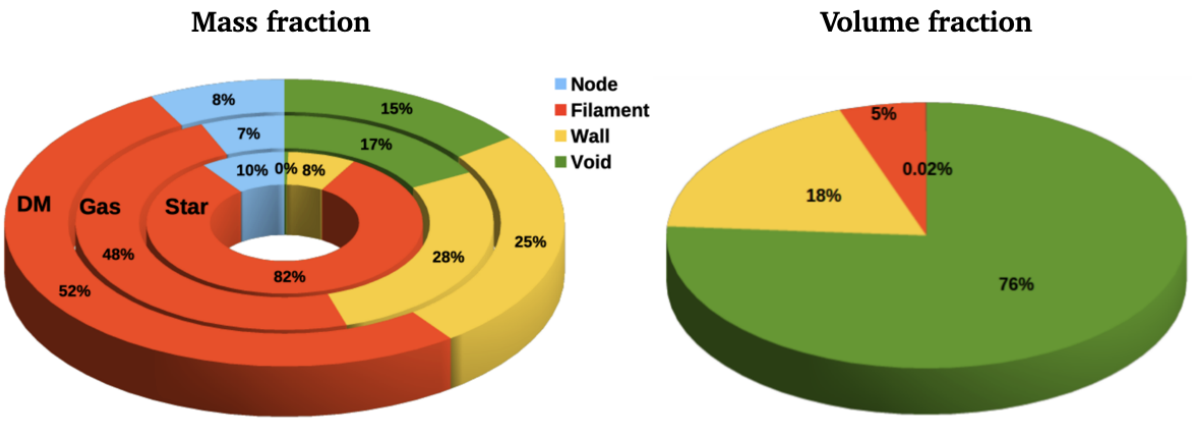

Figure 1.2: Volume and mass fractions of the nodes, filaments, walls and voids of the cosmic web (identified by the NEXUS code of Cautun et al. 2013 in the EAGLE simulation, Schaye et al. 2015). These results are reproduced from Ganeshaiah Veena et al. (2019).

However, despite these observations, mostly studies in large-scale hydro-dynamical simulations have been able to really asses the content and main properties of the different cosmic structures. Indeed, these virtual laboratories, introduced in Sect. 2.1, represent ideal tools to explore the cosmic web without the difficulties specific to observational data analysis (e.g. foreground contamination, low signal to noise ratio, redshift uncertainties, etc.).

The milestone analysis of Cautun et al. (2014) and, most recently, of Ganeshaiah Veena et al. (2019) have shown that most of the volume of the Universe is occupied by voids ($\sim 76\%$), followed by walls and filaments, and that nodes only occupy a tiny fraction ($\sim 0.02\%$) of the volume. Concerning mass, most of it is contained in filaments: these structures host $\sim 50\%$ of the DM and gas, and 82% of the stellar mass of the Universe! These fractions, presented in the diagrams of Fig. 1.2, show that the study of matter at the largest scales is inevitably tied to that of filaments.

1.2 Cosmic filaments

While a lot of attention has been drawn to the study of the densest cosmic structures traced by the most luminous clusters of galaxies (by characterising e.g. their galaxy content, galaxy properties, gas composition, and density profiles Nagai et al., 2007; Arnaud et al., 2010; Baxter et al., 2017a; Bartalucci et al., 2017; Pintos-Castro et al., 2019; Ghirardini et al., 2019), filaments have been only poorly characterised. This is principally due to their low matter densities, which result in a fainter signal with respect to that of the nodes. For example, Fig. 1.3 shows that the probability distribution function (PDF) of the DM over-density field in filaments (blue) is roughly two orders of magnitude lower than that in nodes (yellow). The observation of cosmic filaments is thus extremely challenging.

In Fig. 1.3 one can also see that the density distribution in filaments partially overlaps with that in nodes towards the higher density values, and with that in voids towards the lower ones, encompassing a broad range of almost five orders of magnitude. This clearly hints at the diversity of the filamentary structures, since filaments with over-densities similar to those of voids (i.e. $1 + \delta \sim 0.1 - 1$) most probably differ from the most over-dense filaments (i.e. $1 + \delta \sim 100$) by more than just their density.

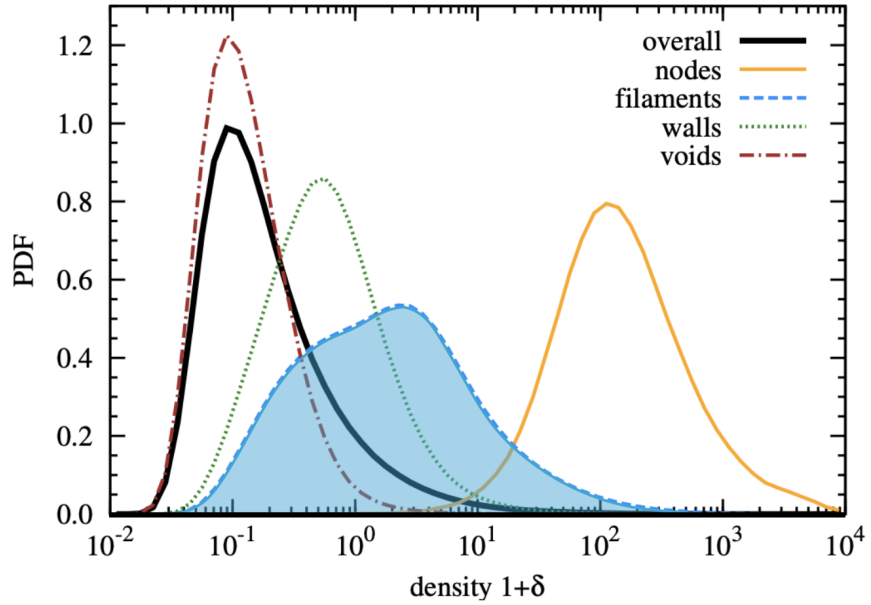

Figure 1.3: DM over-density PDF of the nodes, filaments, walls and voids of the cosmic web (identified by the NEXUS code of Cautun et al. 2013 in the Millenium simulation, Springel 2005, Boylan-Kolchin et al. 2009). This plot is reproduced from Cautun et al. (2014).

The diversity of the filamentary structures has also been detected in observational data. For example, filaments were detected in the cluster outskirts at small scales (e.g. Eckert et al., 2015, in the X-ray domain), but also in larger scales (e.g. Malavasi et al., 2020b). Bridges of matter (of scales of few megaparsecs) were observed between individual pairs of clusters (e.g A399-A401 Akamatsu et al., 2017; Bonjean et al., 2018; Govoni et al., 2019; Biffi et al., 2021) and stacked pairs of clusters (Tanimura et al., 2019; de Graaff et al., 2019; Vernstrom et al., 2021). Larger filaments (of scales of tens of megaparsecs) were detected in galaxy surveys (e.g. Alpaslan et al., 2016; Malavasi et al., 2017; Chen et al., 2017; Malavasi et al., 2020a; Rost et al., 2020; Bonjean et al., 2020). These studies revealed different properties (densities, temperatures, magnetic field strength, etc.) that need to be further characterised in order to better understand the multifaceted aspect of cosmic filaments.

1.3 Open questions addressed in this Thesis

The main goal of my Thesis is to build a more comprehensive picture of cosmic filaments and of the properties of matter around them in the present Universe, i.e. at redshift $z = 0$.

The study is performed using the outputs of large-scale hydro-dynamical simulations and the `DisPerSE` filament finder, all of them presented in Chapter 2. After the extraction of the different cosmic skeletons from the simulated galaxy catalogues (Chapter 3), they are extensively studied with the aim of addressing the following questions:

1. ***How is matter distributed around cosmic filaments?***
   Given the established diversity of filaments, one can wonder whether all components of matter (dark and baryonic) are distributed in a similar manner regardless of the filament characteristics, such as length. One could furthermore investigate whether the so-called 'universality' of the baryon fraction in galaxy clusters is observed in the lower-density

and larger-scales cosmic filaments. Also, a universal profile describing the matter distribution has been proposed for the nodes of the cosmic web. Therefore, an open question is whether such a profile could be built for the non-univocally defined cosmic filaments. These topics will be addressed in Chapter 4.

2. ***What are the physical properties of gas in cosmic filaments?***
   Dark and baryonic matter co-exist in the cosmic web structures. Their interplay defines the physical properties of the gaseous state of baryons. In filaments, the detailed properties (density, temperature, pressure) of gas are poorly known. Their study and characterisation is thus a necessary step to understand the physical environment in which galaxies will form and evolve. Such a comprehensive study will be presented in Chapter 5.

3. ***How do cosmic filaments contribute to shaping the properties of galaxies?***
   Gravity is the main driver of galaxy formation. However, the properties of galaxies in filaments are also shaped by the full physical environment defined by the gas distribution and its properties. A blooming research avenue is thus the study of star-formation activity and its variations as a function of the observed diversity of filaments. Chapter 6 offers a first attempt at uncovering this relationship.

A summary of the main results and of prospects for the future, presented in Chapter 7, concludes the thesis.

The results presented in this manuscript have also led to the following articles that are published or in preparation:

- *Populations of filaments from the distribution of galaxies in numerical simulations*, **D. Galárraga-Espinosa**, N. Aghanim, M. Langer, C. Gouin and N. Malavasi, 2020, A&A, 641, A173
- *Properties of gas phases around cosmic filaments at $z = 0$ in the IllustrisTNG simulation*, **D. Galárraga-Espinosa**, N. Aghanim, M. Langer and H. Tanimura, 2021, A&A, 649, A117
- *Relative distribution of DM, gas and stars around cosmic filaments in the IllustrisTNG simulation*
  D. Galárraga-Espinosa, M. Langer and N. Aghanim, 2021,
  submitted to A&A (arXiv:2109.06198)
- *On the relative effect of nodes and filaments of the cosmic web on the quenching of galaxies and the orientation of their spin*,
  N. Malavasi, M. Langer, N. Aghanim, **D. Galárraga-Espinosa**, and C. Gouin, 2021, submitted to A&A (arXiv:2109.14623)

Chapter 2

Data and Methods

Contents

This Chapter is divided in two main sections. The first, Sect. 2.1, introduces the main datasets used this Thesis, the large-scale hydro-dynamical simulations. The second, Sect. 2.2, focuses on the method used for detecting the cosmic filaments in those simulations, and thus introduces the key features of the `DisPerSE` skeleton finder.

2.1 Large-scale hydro-dynamical simulations in a nutshell

The last decade has witnessed a remarkable progress in the modelling of the formation and evolution of the large-scale structure as a whole. The community has gone from simulating, at various levels of sophistication, the collisionless interactions of DM (i.e. N-body simulations, see e.g. Bond et al. 1996; Springel 2005; Boylan-Kolchin et al. 2009; Klypin et al. 2011; Prada et al. 2012; Potter et al. 2017), to simulating not only DM, but also the more complex physics of gas and the astrophysical processes required for the production of a realistic galaxy population (i.e. compatible with actual observations). Such simulations are called hydro-dynamical simulations, and have been achieved by several projects such as the Illustris (Vogelsberger et al., 2014; Nelson et al., 2015) and IllustrisTNG (Nelson et al., 2019b) simulations, Magneticum (Hirschmann et al., 2014; Dolag, 2015; Ragagnin et al., 2017), EAGLE (Schaye et al., 2015), Horizon-AGN (Dubois et al., 2014), or Simba (Davé et al., 2019) simulations, illustrated in Fig. 2.1.

In both N-body and hydro-dynamical simulations, large simulated volumes with good enough resolutions are needed in order to probe the spatial scales and mass ranges required for the study of galactic (and larger-scale) physics, but also to produce a large enough number of structures (in particular galaxy clusters) to allow for statistical analyses. This yields an inevitable competition between resolution and volume. Due to computational limitations

(most notably memory and time), hydro-dynamical simulations usually favour one of these two aspects. For example, as shown by the diagram of Fig. 2.2, high-resolution ($m_{\rm b} \sim 10^4$ $M_\odot$) simulations usually possess small volumes ($\sim (100\,{\rm cMpc})^3$, see the points at the upper left part of the plot), while simulations with a statistically significant number of resolved galaxies ($\sim 10^5$) tend to have lower resolutions. Sophisticated techniques, such as the adaptive mesh refinement (AMR), have been developed in order to alleviate these limitations. This enables the local increase of resolution in the zones with the highest densities, see e.g. the RAMSES (Teyssier, 2002), AREPO (Springel, 2010), or ENZO (Bryan et al., 2014) codes. The state-of-the-art hydro-dynamical simulations, such as the TNG50 (Nelson et al., 2019a) or the NewHorizon simulation (Dubois et al., 2020), aim at pushing towards the upper right part of the plot by performing substantial improvements to the numerical framework (e.g. new time integration schemes, improved spatial gradient estimators) and by intensively exploiting some of the largest computational resources currently available.

Starting from Gaussian initial conditions describing the primordial density field (e.g. Peebles, 1982; Davis et al., 1985a), hydro-dynamical simulations simultaneously solve the coupled equations of gravity (i.e. the Poisson−Vlasov system) and hydro-dynamics (i.e. Navier−Stokes) in an expanding Universe, defined by a cosmological volume evolving in time. Together with these coupled equations, hydro-dynamical simulations also include additional processes that are of outmost importance for reproducing the formation and evolution of galaxies. These are, for example, the heating of gas by astrophysical processes (e.g. Haardt, Madau, 1996), star-formation (e.g. Kennicutt, 1998), the feedback from supernovae and massive black holes (e.g Leitherer et al., 1999; Dubois et al., 2012). These baryonic processes typically take place at scales ranging from the sub pc to the Mpc, which are significantly smaller with respect to the large cosmological volumes covered by the different simulations (i.e. hundreds of Mpc).

Because of the intrinsically limited numerical resolution, these processes need to be implemented through sub-resolution (or sub-grid) models, or prescriptions, aiming at giving an effective description of the relevant physics. For illustration, some of the physical processes that are implemented in a sub-resolution manner in most of the current hydro-dynamical simulations are presented in Fig. 2.3. These physical prescriptions absolutely need to be developed and calibrated to match the observed properties of galaxies (e.g. the cosmic star formation rate density, or the stellar mass function). This is non-trivial to achieve, and accurate and precise enough sub-resolution models (such as those of the simulations described above, see e.g. Pillepich et al., 2018) have only recently emerged.

Thanks to these substantial advances, hydro-dynamical simulations have now reached a maturity that allows the study of galaxies together with their large-scale environment, i.e. the cosmic web. For reference, the hydro-dynamical simulations analysed in this Thesis, namely the TNG300, TNG100, Illustris, and Magneticum simulations, are highlighted by the three black circles in Fig. 2.2. An overview of the main characteristics is presented in Table 2.1, and further details are given in the next sections.

2.1.1 The IllustrisTNG simulations

The IllustrisTNG project[1], hereafter TNG, (Nelson et al., 2019b) is a hydro-dynamical simulation that follows the coupled evolution of DM, gas, stars, and black-holes from $z = 127$ to the present day $z = 0$ by adopting the cosmological parameters from Planck Collaboration et al.

[1] https://www.tng-project.org

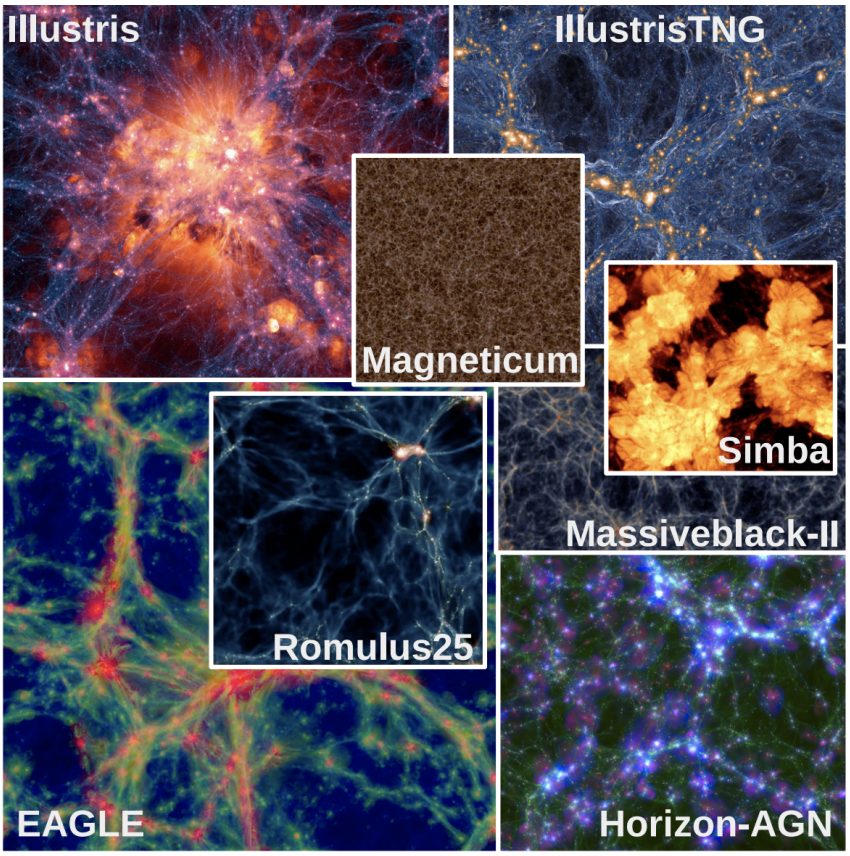

Figure 2.1: Visual impression of some of the current hydro-dynamical simulations. This figure is extracted from Vogelsberger et al. (2020).

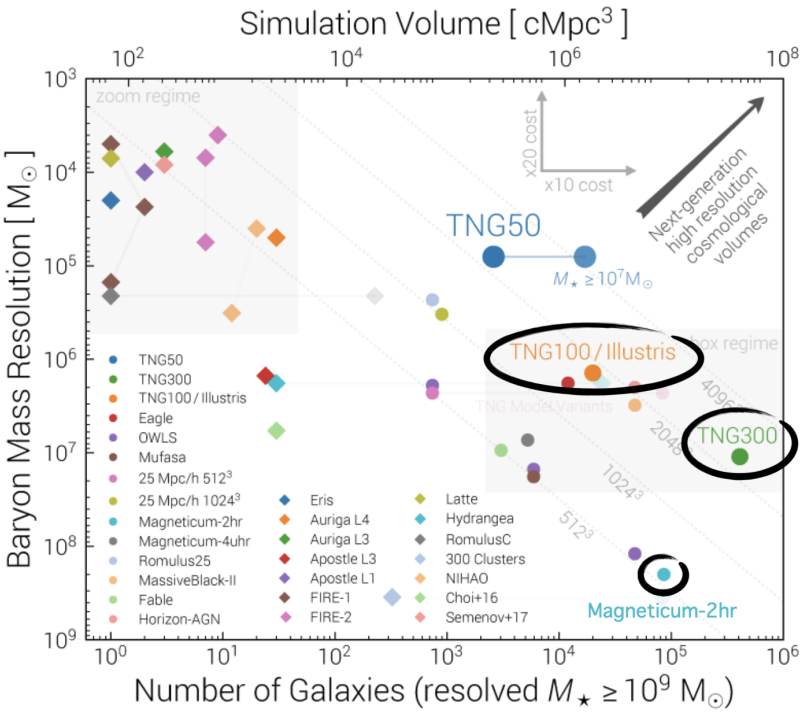

Figure 2.2: Comparison between current hydro-dynamical simulations. This diagram presents the place of a given simulation in the resolution vs volume (or number of galaxies) plane. This figure is extracted from Nelson et al. (2019a).

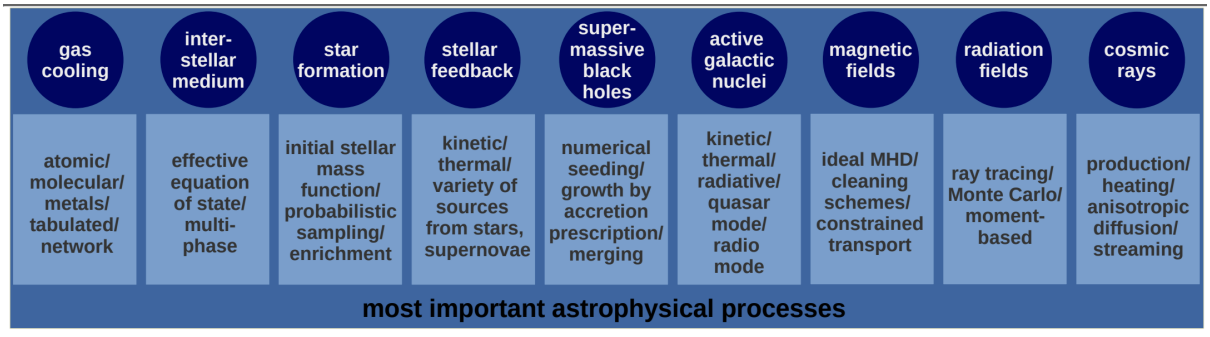

Figure 2.3: Overview of the main astrophysical processes implemented in current hydro-dynamical simulations. This figure is extracted from Vogelsberger et al. (2020).

Table 2.1: Overview of the five simulations used in this Thesis.

	TNG300-1	Magneticum	TNG300-2	TNG100-2	Illustris-2
Box size [Mpc^3]	302.6^3	500^3	302.6^3	110.7^3	106.5^3
Cosmology	*Planck* 2015	WMAP7	*Planck* 2015	*Planck* 2015	WMAP7
DM resolution [$M_\odot/h$]	4.0×10^7	6.9×10^8	3.2×10^8	4.0×10^7	3.5×10^7

(2016a), namely $\Omega_{\Lambda,0} = 0.6911$, $\Omega_{m,0} = 0.3089$, $\Omega_{b,0} = 0.0486$, $\sigma_8 = 0.8159$, $n_s = 0.9667$ and $h = 0.6774$.

Three different volumes are available in the TNG project: TNG50, TNG100, and TNG300. In this Thesis, most of the analysis is performed on the TNG300-1 simulation, which corresponds to the largest box (of volume $(302.6\,\mathrm{Mpc})^3$) with the highest mass resolution ($m_{\rm DM} = 4.0 \times 10^7 M_\odot/h$) available. This box is taken as the reference in the following studies, given that it allows to accurately describe large cosmic filaments and their content down to small scales.

Other runs of the TNG suite are also analysed in this Thesis for specific purposes. The TNG300-2 simulation box is systematically used to test for the effects of resolution. This box is the medium resolution run of the TNG300 suite, meaning that it has the same characteristics as the TNG300-1 simulation except for a mass resolution of $m_{\rm DM} = 3.2 \times 10^8 M_\odot/h$, that is eight times lower than the reference. The outputs of two other boxes, namely TNG100-2 and Illustris-2, are also studied in Sect. 4.1 in order to asses the impact of the sub-resolution models of the simulations on the results. Indeed, these two boxes have the same initial conditions, similar box sizes and mass resolutions (which enables direct comparison, see Table 2.1 for details), but they involve significantly different physical models. The TNG project is the successor of the original Illustris simulation[2] (Nelson et al., 2015; Genel et al., 2014; Vogelsberger et al., 2014; Sijacki et al., 2015), and was specifically calibrated on the observed galaxy properties and statistics (Nelson et al., 2019b). The main differences between the TNG and the Illustris physical models thus reside in the formation, growth and feedback of supermassive black holes, as well as in the galactic winds, stellar evolution and gas chemical enrichment models. A full and detailed comparison of the two can be found in Pillepich et al. (2018).

The gaseous component in the Illustris and TNG simulations is spatially discretised following the Adaptive Mesh Refinement (AMR) code AREPO (Springel, 2010). Within this description of the gas fluid, the Voronoi cells evolve in time using Godunov's method (Nelson et al., 2019b), they track the conserved quantities of the gas fluid (e.g. mass, momentum, energy) thanks to Riemann solvers at the cell interfaces, and are refined and de-refined according to a mass target of $7.6 \times 10^6\,M_\odot/h$ (Springel, 2010; Nelson et al., 2019b; Weinberger et al., 2020; Pillepich et al., 2018).

Finally, the baryonic processes, implemented in a sub-resolution manner and required for the study of the formation and evolution of galaxies, are described by the 'TNG model' (Pillepich et al., 2018). This model was specifically calibrated on observational data to match to the observed galaxy properties and statistics (Nelson et al., 2019b), and includes the following:

- Primordial and metal-line radiative cooling in the presence of an ionizing background radiation field which is redshift-dependent and spatially uniform, including self-shielding corrections
- Stochastic star formation in dense gas of the inter-stellar medium (ISM), determined by a threshold in density

[2] https://www.illustris-project.org/

- Evolution of stellar populations, with the associated chemical enrichment and mass loss (gas recycling)
- Galactic winds (stellar feedback) with an energy-driven, kinetic wind scheme.
- Formation, growth and feedback of (supermassive) black-holes
- AGN feedback with two modes of energy release: a thermal 'quasar' mode at high accretion rates and, a kinetic 'wind' mode at low accretion rates
- Magnetic fields under the assumption of ideal MHD: amplification of a small (primordial) seeds and dynamical impact

The complete description of this model and of its calibration can be found in Pillepich et al. (2018). Table 2.2 concisely summarises the references and compares them to the other simulations used in this Thesis.

Computation of the temperature and pressure of gas in TNG

The TNG simulation offers detailed information about various properties and characteristics of the different matter components of the Universe. While some of them can be directly read from the outputs of the simulation (e.g. the coordinates, masses, velocities), a few important characteristics used in this Thesis, namely gas temperature and pressure (see Chapter 5), require some post-processing.

To derive the temperature and pressure of gas, I used the `InternalEnergy`, `Density` and `ElectronAbundance` fields (respectively u, $\rho_{\rm cell}$ and x_e) of the TNG gas cells (`PartType0`). Gas cell temperature was computed under the assumption of perfect monoatomic gas:

$$T_{\rm cell} = (\gamma - 1) \times \frac{u}{k_{\rm B}} \times \mu. \tag{2.1}$$

In this equation, γ corresponds to the adiabatic index of perfect monoatomic gas ($\gamma = 5/3$), $k_{\rm B}$ is the Boltzmann constant, and μ denotes the mean molecular weight. The latter is estimated as follows:

$$\mu = \frac{4}{1 + 3X_{\rm H} + 4X_{\rm H}x_e} \times m_{\rm p}, \tag{2.2}$$

where $X_{\rm H}$ is the hydrogen mass fraction ($X_{\rm H} = 0.76$) and $m_{\rm p}$ denotes the mass of the proton. In these equations, all the quantities are expressed in the International System of Units.

The thermodynamic pressure was estimated from the temperature and electron density as:

$$P_{\rm cell} = n_e \, k_{\rm B} \, T_{\rm cell}. \tag{2.3}$$

The electron density n_e, in m^{-3}, was computed as the electron abundance times the hydrogen density, $n_e = x_e \times n_{\rm H}$, where $n_{\rm H} = X_{\rm H} \, \rho_{\rm cell}/m_{\rm p}$. The resulting pressure was then converted from pascals to the more usual unit in astrophysics of $\mathrm{keV.cm}^{-3}$.

2.1.2 The Magneticum simulation

This Thesis also uses the outputs of the Magneticum Pathfinder[3] simulation (Hirschmann et al., 2014; Dolag, 2015; Ragagnin et al., 2017) at the smallest redshift available, $z = 0.066$. This simulation consists of a cube of 500 Mpc side length with a DM resolution of $m_{\rm DM} = 6.9 \times$

[3] http://www.magneticum.org

Table 2.2: Brief overview of the sub-resolution models of the different sets of simulations analysed in this Thesis.

	TNG	Illustris	Magneticum
Radiative cooling	Wiersma et al. (2009a)	Wiersma et al. (2009a)	Wiersma et al. (2009a)
Star-formation and multiphase structure of the ISM	Springel, Hernquist (2003)	Springel, Hernquist (2003)	Springel, Hernquist (2003)
Metals and chemical enrichment	Naiman et al. (2018), Pillepich et al. (2018)	Wiersma et al. (2009b)	Tornatore et al. (2003), Tornatore et al. (2007) Wiersma et al. (2009b)
Stellar feedback	Vogelsberger et al. (2013), Pillepich et al. (2018)	less sophisticated than TNG	Springel, Hernquist (2003)
Black holes and AGN feedback	Vogelsberger et al. (2013),Weinberger et al. (2017)	Same as TNG	Springel et al. (2005), Di Matteo et al. (2005), Fabjan et al. (2010), Hirschmann et al. (2014)
Magnetic Fields	Pakmor et al. (2011), Pakmor, Springel (2013)	Not included	Dolag, Stasyszyn (2009)

$10^8 M_\odot/h$. The cosmological parameters of this simulation are different from TNG, as the cosmology is described according to results of the seven-year Wilkinson Microwave Anisotropy Probe (WMAP7) data (Komatsu et al., 2011): $\Omega_{\Lambda,0} = 0.728$, $\Omega_{m,0} = 0.272$, $\Omega_{b,0} = 0.0456$, $\sigma_8 = 0.809$, $n_s = 0.963$ and $h = 0.704$.

Contrary to the AMR technique employed in TNG (see above), the gas fluid in the Magneticum simulation is discretised in mass, based on the Smooth Particle Hydrodynamics (SPH) code P-GADGET3 (Springel, 2005). For reference, the physical models implemented in this simulation are listed in Table 2.2.

2.1.3 Halo finders

Hydro-dynamical simulations output a 'raw' distribution of DM, gas, and stellar particles or cells. Further steps are needed to identify the haloes and galaxies, and these are achieved in post-processing by algorithms such as the Friends-of-friends (FoF, Huchra, Geller, 1982; Press, Davis, 1982; Davis et al., 1985b), that allow to identify the haloes, and the SUBFIND algorithm (Springel et al., 2001; Dolag et al., 2009), used to find the gravitationally bound substructures (i.e. the galaxies) within the FoF haloes.

The main idea behind the FoF algorithm is to link particles together (and form groups) if their distance lies below a certain threshold, called the linking length. This length is usually chosen to be 0.2 times the mean DM particle separation, given that it yields groups having an average enclosed density contrast of roughly $\Delta \sim 180$. This is appealing for structures such as haloes because such a Δ value is close enough to the predicted enclosed density of virialised objects by the spherical collapse model. The small groups having less than 20 particles are

usually discarded, since they are likely to be only spurious clumps. In practice, the FoF algorithm is applied only to the DM particles of the simulation, and gas and stars are included into the FoF group of their nearest DM particle. In this way, the final FoF halo is composed by the initially identified DM particles plus the associated baryonic particles. In this Thesis, the most massive FoF haloes ($> 10^{13}\,M_{\odot}/h$) of the TNG300-1 simulation will be assimilated to clusters of galaxies, and used in e.g. Sect. 3.3 and Sect. 5.2.4.

The SUBFIND algorithm was first introduced in Springel et al. (2001) for DM simulations, and adapted by Dolag et al. (2009) to treat gas and star particles of hydrodynamical simulations. The aim of this algorithm is to identify the subhaloes, i.e. the substructures within FoF haloes, by detecting locally over-dense, gravitationally bound groups of particles. These are identified by first estimating the local density at the position of each particle using adaptive kernels. Then, the locally over-dense regions inside the input FoF haloes, i.e. the subhalo candidates, are found by using an excursion set approach (i.e. the density threshold is progressively lowered to find the peaks). A crucial requirement is that the subhalo candidates need to be self-bound gravitationally. The unbound particles (those having positive total energies) are thus removed and become part of the background, the 'fuzz'. After this procedure, the subhalo candidate is kept only if it is formed by more than $N = 20$ dark-matter and star particles. The structures satisfying these criteria can thus be considered as galaxies or groups, and their integrated properties (such as stellar mass or star-formation rate) can then be computed. All the simulated galaxy catalogues used in this Thesis (see e.g. Sect. 3.1.1) were found using the SUBFIND algorithm.

2.2 The DisPerSE algorithm

While it is fairly straightforward to define haloes as gravitationally bound structures and to thus identify them in simulated and observed data, the diversity and the lack of an unequivocal definition of filaments makes their study more difficult. For example, the simple detection of these structures in observational or simulated data sets (which is commonly the first step in any study) poses already a challenge. A variety of algorithms have been developed to detect and identify the filamentary structures from the distribution of galaxies or from the DM particles in simulations. As shown by the detailed review of Libeskind et al. (2018), each of these methods adopts a different, and thus complementary, approach. For example, some algorithms define filaments based on the topology of the matter density field (e.g. Sousbie et al., 2011), on statistical representations of stochastic processes (e.g. Stoica et al., 2007; Tempel et al., 2016), through the relative strength between eigenvalues of the Hessian matrix of the density field (e.g. Aragón-Calvo et al., 2007a, 2010a; Cautun et al., 2013), using machine learning classification tools (e.g. Buncher, Carrasco Kind, 2019), graph theory (e.g. Pereyra et al., 2020), and regularised minimum spanning trees (e.g. Bonnaire et al., 2020).

This Thesis studies the filamentary structures detected by the Discrete Persistent Structure Extractor (`DisPerSE`) of Sousbie (2011). As it will be explained in the next sections, this algorithm identifies the cosmic skeleton from the topology of the density field, using the Discrete Morse Theory and the theory of persistence, introduced respectively in Sects. 2.2.1 and 2.2.2. Note that all the details of the `DisPerSE` algorithm can be found in Sousbie (2011) and Sousbie et al. (2011). Here, I summarise the main theoretical aspects of this method by introducing and defining only the concepts that are required in the context of this Thesis, i.e. of the detection of cosmic filaments.

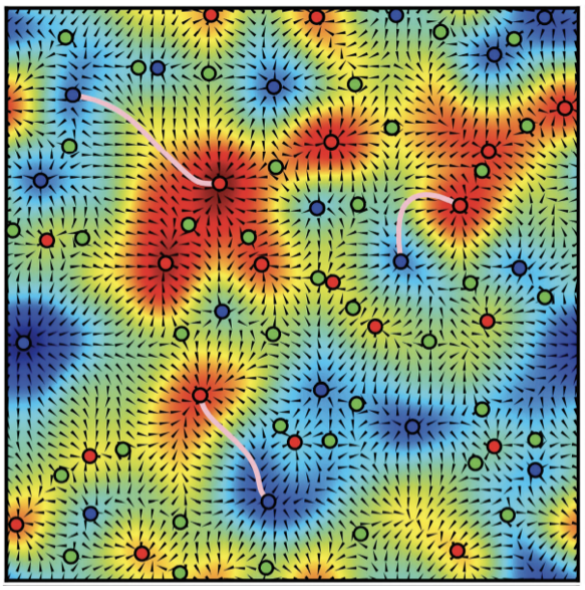

Figure 2.4: Example of a 2D density field, ρ, and its gradient. The red, green, and blue points correspond respectively to the CPmax, saddles, and minima critical points. This figure is extracted from Sousbie (2011).

2.2.1 Discrete Morse theory

This Section first presents the main characteristics of Morse theory, one of the pillars of the `DisPerSE` algorithm. Note that Morse theory is developed within the framework of smooth and continuous functions, so the *discrete* Morse theory, which applies to a discrete set of points (such as the distribution of galaxies or DM particules) is presented in the second part of this Section.

Morse Theory in a nutshell

For simplicity and illustrative purposes, the method is firstly introduced in the two dimensional (2D) case. Its extension to the 3D space is presented only in the last paragraph.

Let us consider a 2D smooth density field, ρ, such as the one shown in Fig. 2.4, where blue to red colours correspond respectively to the regions ranging from lower to higher densities. The gradient of this field $\vec{\nabla}\rho$, defines a preferential direction at every point of space, which corresponds to that of the steepest ascent (shown by the small arrows in Fig. 2.4). The points where the gradient vanishes, $\vec{\nabla}\rho = \vec{0}$, are called the *critical points* of the density field. These can be classified into different classes according to the sign of the eigenvalues of the Hessian matrix (i.e. the $d\times d$ matrix of the second derivatives of the field, where d is the space dimension) at the position of a critical point. The number of negative eigenvalues thus determines the *order* of the critical point. More precisely, let us consider a critical point P of position $\vec{p}$, and call λ_i ($i = 1, 2$ in 2D) the eigenvalues of the Hessian matrix at this position. The critical point P can thus correspond to one of the following types:

- a maximum of the density field if all the eigenvalues are negative ($\lambda_1, \lambda_2 < 0$). In this case, P is a critical point of order 2. For example, all the maximum density critical points (CPmax, in the rest of this Thesis) of the density field ρ are depicted by the red points in

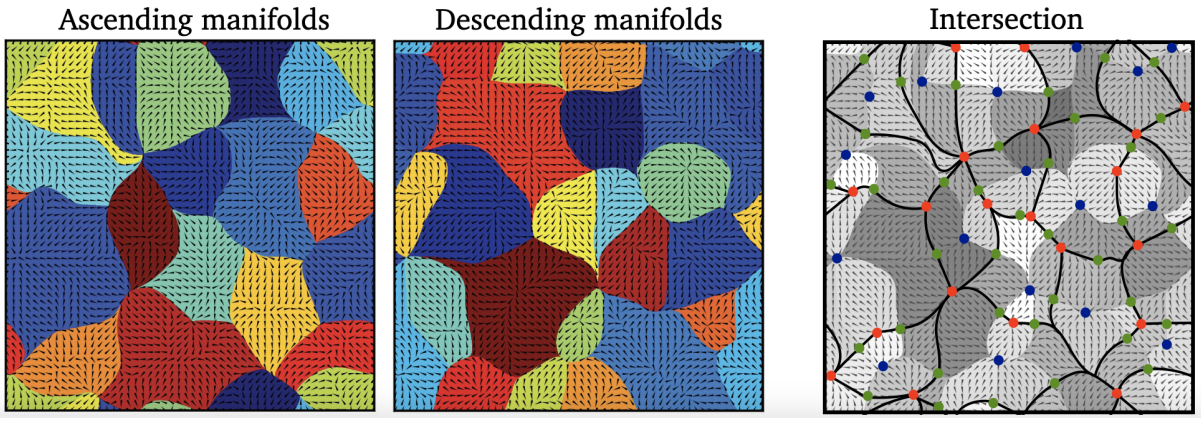

Figure 2.5: *Left:* Ascending and descending manifolds of the density field of Fig.2.4, reproduced from Sousbie (2011). *Right:* Intersection between the ascending and descending manifolds presented in the left panels. The intersection lines that connect CPmaxs (red) to saddles (green) correspond to the filaments (black lines). The minima of the density field are marked by the blue points.

Fig. 2.4.

- a saddle of the density field, which is a critical point of order 1, if $\lambda_1 < 0$ and $\lambda_2 > 0$. Saddles are shown by the green points in Fig. 2.4.

- a minimum of the density field (order 0), if all the eigenvalues are positive ($\lambda_1, \lambda_2 > 0$). These points are shown in blue in Fig. 2.4.

It is important to specify that, within the Morse theory, the eigenvalues of the Hessian must necessarily be non-zero, so that the critical points are non-degenerate. This (strong) requirement is essential to this theory, and the functions satisfying the latter condition are called *Morse* functions.

The critical points of the density field are connected to each other by *integral lines*. These are lines that flow parallel to the gradient without intersecting. They depart from one critical point (of lower order), follow the gradient, and arrive to another critical point of higher order. For example, three integral lines are illustrated by the pink curves in Fig. 2.4.

The set of all integral lines covers the full space, and naturally partitions the space into *ascending* and *descending manifolds*. Indeed, ascending (resp. descending) manifolds are defined as the set of points that are reached by an integral line with origin (resp. destination) the critical point P. These concepts are clearly illustrated in the left panels of Fig. 2.5. Note that the set of ascending and descending manifolds is usually referred to as the *Morse complex*, which establishes the link between the geometrical (where are the critical points?) and topological (how are critical points connected?) properties of the density field. This is the main essence of Morse theory.

Finally, filaments are defined as the lines where the ascending and descending manifolds intersect, and that specifically connect the CPmax to the saddles of the density field. The filaments corresponding to the density field ρ of Fig. 2.4 are presented by the black lines in the right panel of Fig. 2.5.

Let us now consider a 3D density field, such as presented in the first panel of Fig. 2.6. In the 3D space, the Hessian matrix at the position of a critical point P possesses three eigenvalues,

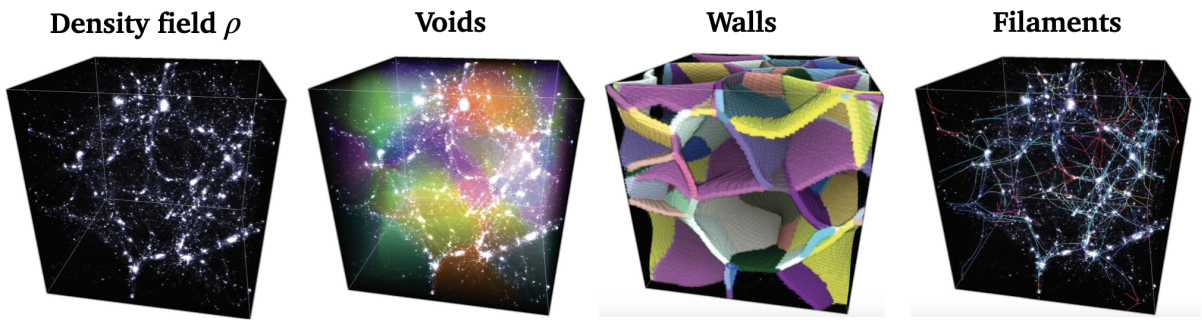

Figure 2.6: Application of Morse theory to a 3D density field. The different panels are extracted from Sousbie (2011).

so the different possible sign combinations result in four types of critical points: the maxima (order 3), two types of saddles (orders 2 and 1), and the minima (order 0). The corresponding $3-k$-ascending manifolds, and k-descending manifolds (here $k \in [0,3]$) thus define regions of space with different dimensions. For example, a 0-manifold corresponds to a critical point, a 1-manifold is a line, a 2-manifold a surface, and a 3-manifold a volume. As in the 2D case, the intersection between ascending and descending manifolds gives birth to the different features of the density field which are, in the cosmological context, identified with voids, walls, and filaments, as shown in the example of Fig. 2.6 (note that the nodes are defined by the CPmax). It is important to state that the application of Morse theory (and thus of the `DisPerSE` algorithm) to the cosmic web, relies on the fundamental assumption that the ascending and descending manifolds of the density field are representative of the cosmic structures.

From continuous to discrete

What is presented so far works for continuous and at least twice differentiable functions, i.e. for Morse functions (see above). In nature, Morse functions can describe, for example, the height of a mountain, or the temperature in a room. However, the spatial distribution of galaxies, i.e. the data to which `DisPerSE` aims to applied in cosmology, cannot be described by a Morse function because of its discrete nature. Indeed, galaxies are only biased tracers of the underlying DM density field, meaning that they correspond to a discrete realisation of the continuous DM field. In order to find the cosmic skeleton, one could thus think of applying Morse theory directly to the DM density field but this faces other problems: the DM density cannot be directly measured in observations, and numerical simulations present only a sample of it (via the DM 'particles') thus coming back to a discrete representation.

In order to deal with the type of data sets available in astrophysics, `DisPerSE` thus adopts the *discrete* Morse theory, introduced by Forman (1998, 2002). In this theory, the *discrete* Morse Complex is computed for intrinsically discrete functions by defining them over *simplicial complexes*. Basically, for a distribution of n points, a simplicial complex is a set of geometrical entities (points, segments, triangles, tetrahedrons) defined by $n+1$ points such that they cover the full space by encompassing the smallest possible volume.

Within the `DisPerSE` framework, the adopted simplicial complex is the *Delaunay tessellation*, usually used in astrophysics. Applied to e.g. the galaxy distribution, this tessellation reconstructs the topological cosmic web while also giving an estimation of the density at each point (i.e. each galaxy), thanks to the Delaunay tessellation field estimator (DTFE). The latter is introduced by Schaap, van de Weygaert (2000) and van de Weygaert, Schaap (2009), and the main steps of this reconstruction algorithm are illustrated in the 2D example of Fig. 2.7.

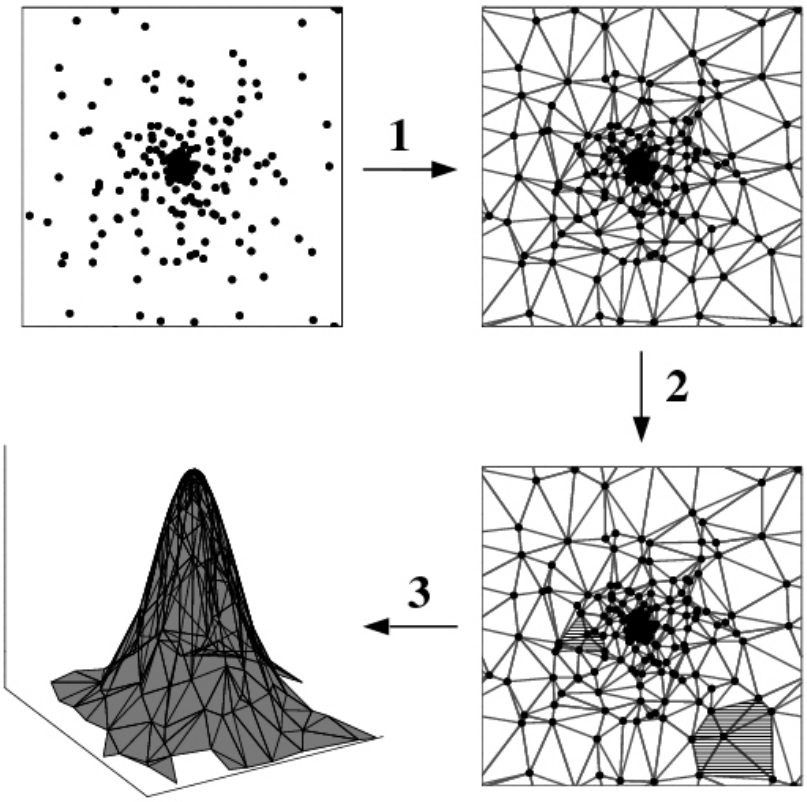

Figure 2.7: Main steps of the Delaunay tessellation field estimator (DTFE). This figure is extracted from van de Weygaert, Schaap (2009).

These are: (1) from the initial set of points, the Delaunay tessellation is computed, (2) the local density ρ_{DTFE}, defined as the inverse of the area of the surrounding Delaunay triangles, is estimated at the position of each point, and (3) the density estimates are interpolated to any point of space by assuming that the density varies linearly inside each triangle. The DTFE thus gives a multi-scale and parameter-free reconstruction of the density field, that only depends on the initial set of points. It is important to keep this dependence in mind, since it results in an intrinsic sensitivity of the `DisPerSE` algorithm to the number of points residing in the analysed spaces or volumes. The latter is also called the density of tracers, and in the context of this Thesis it corresponds to the number of galaxies per megaparsec cube of the input galaxy catalogue ($n_{\mathrm{gal}}^{\mathrm{box}}$). The dependence of the output skeleton on the density of tracers will be clearly illustrated in Chapter 3, where simulations characterised by different $n_{\mathrm{gal}}^{\mathrm{box}}$ are used.

Because of the finite sampling, Poisson noise is intrinsically present in discrete data sets such as galaxy catalogues. Shot noise thus naturally biases the topology of the reconstructed DTFE field (by contaminating the density estimates), thus affecting the resulting `DisPerSE` skeleton. As shown by Sousbie (2011); Sousbie et al. (2011) and e.g. Malavasi et al. (2020a), the contamination by shot noise can be partially mitigated by performing a smoothing of the Delaunay density field prior to the application of the discrete Morse theory (this will be also illustrated in Sect. 3.1.2). This smoothing of the density field can also prevent the extraction of very small-scale features that would not correspond to those of the cosmic web (e.g. a local filament between two galaxies), but that are likely to be identified as structures due to the multi-scale nature of the Delaunay tessellation (see also the study presented in Sect. 3.1.2.

Nevertheless, the identification of the actual skeleton needs to be addressed with a more

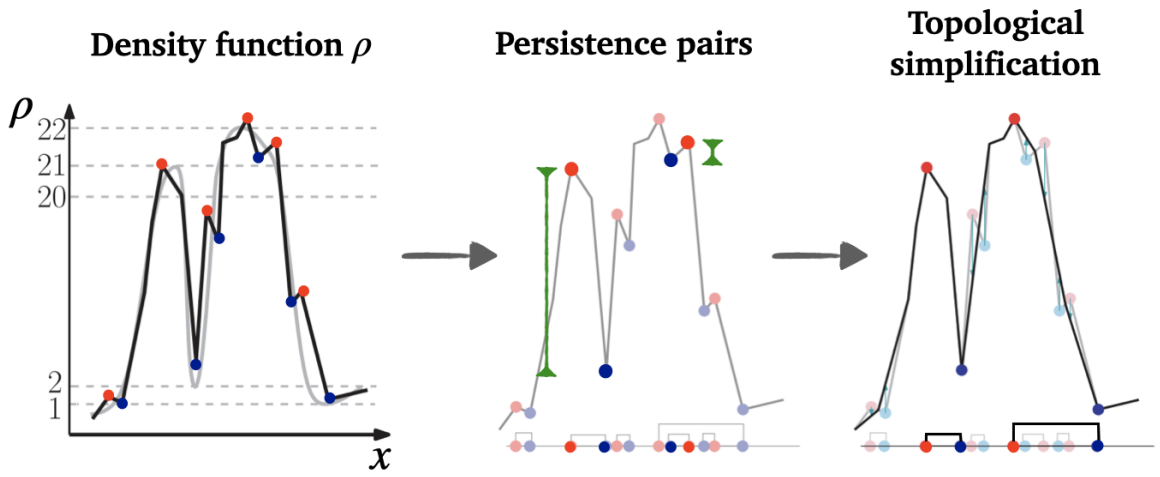

Figure 2.8: Illustration of the application of persistence theory to a function in 1D. The different panels are based on the figures of Sousbie (2011).

quantitative and secure approach. The one adopted by the `DisPerSE` algorithm is the systematic filtering of the different features of the skeleton thanks to the use of persistence theory, which is presented in the following Section.

2.2.2 Persistence theory

As explained above, the cosmic skeleton can be detected in a discrete sample like the distribution of galaxies (or the distribution of DM particles in numerical simulations) thanks to the application of Discrete Morse theory. Nevertheless, a main issue is left to solve: how to deal with the intrinsic Poisson noise of the discrete data set? Or, in other words, how can we distinguish 'true' cosmic filaments from the spurious filaments arising from Poisson noise? The answer to these questions comes from the persistence theory, whose main characteristics are explained in the following.

Let us consider the 1D density function presented by the black line in the first panel of Fig. 2.8. This density function resembles the one in gray, except for the added noise (as shown by the small peaks). Let us thus assimilate the black function to a result of the DTFE method introduced above. By looking at the corresponding critical points (marked by the blue and red points), it is clear that some of them are generated by noise (i.e. they are spurious) and they do not describe the trends of the underlying density. The main goal of persistence theory is thus to remove them from the topology, and to adapt the discrete Morse complex (see Sect. 2.2.1) to keep only the features truly arising from the density field, i.e. the persistent features.

First, the excursion sets of the function are computed. These are defined as the sets of points with values higher than a given density threshold, which are here chosen to correspond to the different values of the critical points. The scanning of the density field at these different thresholds groups different types of critical points in pairs. For example, the pairing of the critical points resulting from the excursion sets of our 1D function is presented in the second panel of Fig. 2.8. A *persistence* value is associated with each pair, and corresponds to the difference of density between the two critical points (represented by the length of the green arrows in the example of Fig. 2.8). Basically, the persistence value measures how much the density field has to change for a given topological feature to disappear. This can be seen as the 'lifetime' of the

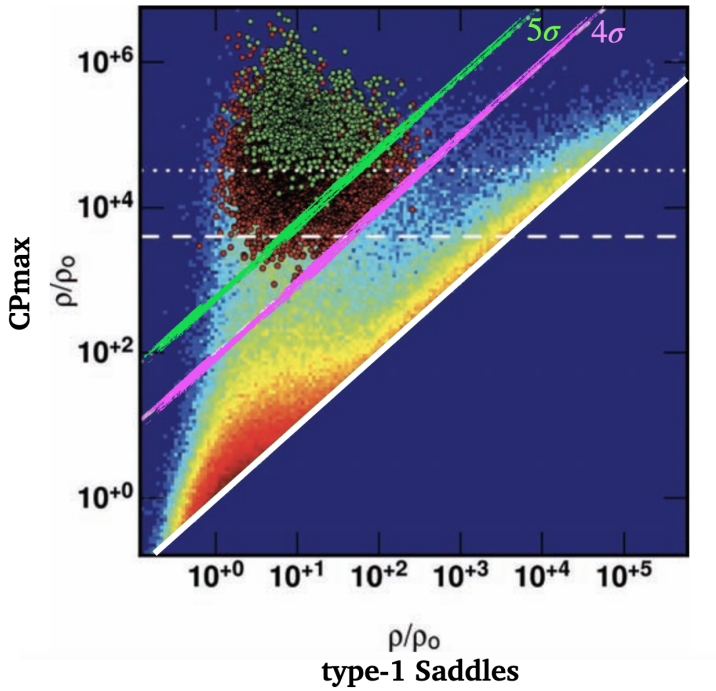

Figure 2.9: Persistence diagram of pairs of critical points. This figure is extracted from Sousbie et al. (2011).

pair in the excursion set or, equivalently, as the robustness of the pair with respect to changes in the density function. In this sense, low-persistence pairs such as the one with the smallest green arrow in Fig. 2.8 can be simplified (i.e. eliminated) without significant changes in the topology of the density field. This topological simplification is illustrated in the last panel of Fig. 2.8, where the least persistence pairs of critical points have been eliminated, thus keeping only the robust features which arise from the density function.

In practice, the `DisPerSE` user can choose the level of persistence of the resulting skeleton by fixing the value of the persistence ratio, i.e. the ratio of the density of the two critical points in a pair, (expressed in numbers of σ). This threshold thus separates the features that are considered as characteristic of the underlying density field, from the spurious ones that are thought to be generated by noise (and which are thus simplified from the topology). Sousbie et al. (2011) show an example of how persistence thresholds simplify (or clean) the set of critical points. They apply `DisPerSE` to an N-body simulation and then plot the persistence diagram of a given type of pairs (e.g. CPmax and type-1 saddle pairs). This diagram, shown in Fig. 2.9, simply represents the 2D probability distribution function of the density values of the corresponding persistence pairs (see continuous colour-map, from blue to red). The white diagonal line marks the persistence limit of '0σ', and all the values are distributed towards the left-hand side of this line, as expected, since by definition the CPmax are denser than any other type of critical point. The pink and green lines show respectively the 4 and 5σ thresholds. Therefore, if the user fixes the persistence ratio to 4σ (resp. 5σ), all the critical points located at the right-hand side of the pink (resp. green) line will be eliminated, and the topology of the density field will be simplified from these points. Note that the green and red points correspond to the FoF haloes of the simulation, and the discussion of their relative location in this plot is not relevant in the context of the present Section.

As it can already be guessed at this stage, the choice of a persistence threshold can have strong repercussions on the resulting filaments, which are defined as the ridges of the Delaunay tessellation connecting two critical points. The effects of the persistence parameter on the detected skeletons will be illustrated in Chapter 3, by the direct application of the `DisPerSE` algorithm to the different simulations analysed in this Thesis.

2.2.3 Filaments with DisPerSE: at a glance

Let us finish this Section by recalling the main steps of this skeleton finder. The `DisPerSE` algorithm extracts the cosmic skeleton from a discrete distribution (a galaxy catalogue, an N-body simulation, etc.) by :

1. First computing the Delaunay tessellation of the distribution of points (galaxies, particles, etc.).

2. Assigning a density value, $\rho_{\rm DTFE}$, to each vertex of the tessellation (e.g. each galaxy) by using the DTFE (Schaap, van de Weygaert, 2000; van de Weygaert, Schaap, 2009). An optional smoothing of the resulting Delaunay density field can be performed at this step.

3. Computing of the discrete Morse complex (Forman, 1998, 2002) that determines the critical points and the ascending/descending manifolds of the density field, thus yielding the nodes, filaments, walls and voids.

4. Applying persistence theory in order to filter the features that are likely to have been generated by noise.

This algorithm mainly depends on three quantities: the density of tracers $n_{\rm gal}^{\rm box}$, that determines the topology of the Delaunay density field, the number of smoothing cycles (if any) of the Delaunay density field prior to the application of the discrete Morse theory, and the value of the persistence threshold. The impact of these parameters on the resulting skeleton will be explicitly studied in the next Chapter, where the `DisPerSE` algorithm is applied to the simulations introduced above in order to extract the cosmic filaments studied throughout this Thesis.

Chapter 3

Detecting the filaments

Contents

The main goal of this thesis is to provide a characterisation of cosmic filaments and of matter around them. But before any physical analysis, it is fundamental to properly define these cosmic structures and to introduce the filament catalogues used throughout this work. Thus, this Chapter presents the detection of cosmic filaments in the numerical simulations of Sect. 2.1, and it is organised as follows. The details of the extraction of the cosmic skeleton using the DisPerSE algorithm are presented in Sect. 3.1, the important features of the resulting filaments are shown in Sect. 3.2, and robustness checks of the skeleton are performed in Sect. 3.3. A special focus is given on the filaments of the TNG300-1 simulation, which is the reference skeleton in all the following chapters of this thesis.

3.1 Extraction of the skeleton

In the following, the skeleton is defined as the set of features characterising the density of the cosmic web, and is thus composed by the collection of filaments and critical points, as identified by DisPerSE. In this thesis, the skeleton is detected from the galaxy distributions of the considered simulations. This choice was motivated by the fact that galaxies are biased tracers of the matter density field, so most analyses in observations detect the cosmic skeleton from the distribution of galaxies in different surveys, like for example VIPERS, COSMOS2015, SDSS, and SAMI (respectively in Malavasi et al., 2017; Laigle et al., 2018; Bonjean et al., 2020; Welker et al., 2020).

3.1.1 Galaxy catalogues in simulations

The building of the galaxy catalogues of the Illustris, TNG and Magneticum simulations are presented in the next paragraphs. These catalogues are at the basis of the different skeletons used in this thesis. Before presenting the details, it is important to mention that this thesis is not

meant to reproduce actual observations (for example by mimicking selection effects and magnitude cuts of a given survey), so the galaxies in the different simulations are selected based on a simple cut in stellar mass. A study in simulations that aims at actually reproducing observations can be found in, e.g. Tuominen et al. (2021). The authors replicate the observational constrains of the SDSS survey to detect cosmic filaments in the EAGLE simulation Schaye et al. (2015).

For the Illustris and TNG series (i.e. Illustris2, TNG100-2, TNG300-2, and TNG300-1) the galaxies were selected from the corresponding `SUBFIND` subhalo catalogues, which are lists of gravitationally bound over-densities (see Sect. 2.1.3). For the sake of conciseness, only the details for the TNG300-1 box are given, since the galaxy catalogues of the other boxes were built in the exact same way.

From the original subhalo catalogue, and following Nelson et al. (2019b), I discarded all the objects that have been flagged as not following the usual processes of galaxy formation (using the field `SubhaloFlag` of the `SUBFIND` catalogue). This avoids contamination by fragments or clumps, originated from non-gravitational (baryonic) processes. The discarded subhalos account for 50,098, and represent only a very small fraction ($\sim 0.03\%$) of the initial subhalo catalogue.

A cut in stellar mass (field `SubhaloMassType`) was then applied to the remaining subhalos. Indeed, following the observational limits of Brinchmann et al. (2004) and Taylor et al. (2011), the stellar mass of the subhalos was required to be in the range $10^9 \leq M_*[M_\odot] \leq 10^{12}$. After this selection in stellar mass, 275,818 subhalos remained. These objects are referred to as galaxies, and they constitute the catalogue on which the `DisPerSE` algorithm is applied. Some slices of the resulting galaxy catalogues of the TNG300-1, TNG300-2, TNG100-2 and Illustris-2 simulations are presented in the left panels of Figures 3.1 and 3.2. The filamentary structure of the cosmic web is already discernible in the presented slices.

In the case of the Magneticum simulation, the cut in stellar mass was applied to the large `Box2/hr` galaxy catalogue, resulting in 1,266,306 galaxies in the mass range $10^9 \leq M_*[M_\odot] \leq 10^{12}$. The Magneticum galaxy catalogue is ~ 4.6 times larger than the TNG300-1 one, which is not surprising considering that the simulation box is 2.5 times bigger. A slice of this catalogue is presented in Fig. 3.3. Table 3.1 reports the number of galaxies in the five resulting catalogues. It is important to mention that the resulting `DisPerSE` filaments strongly depend on the density of tracers of the input galaxy catalogue. This quantity, denoted $n_{\rm gal}^{\rm box}$, corresponds to the number of galaxies per Mpc^3, and Table 3.1 already shows that the five simulations possess different densities of tracers, that go from 5.4×10^{-3} to 16.9×10^{-3} galaxies per megaparsec cube.

3.1.2 Application of `DisPerSE` to the galaxy catalogues

The detection and extraction of the skeleton was performed by applying the `DisPerSE` code to the previously extracted galaxy catalogues. This publicly available code was introduced in 2.2, and this section shows the details of its application to the studied set of simulations. It is important to mention that, in order to be able to compare one skeleton to another, the same procedure (with the same parameter values) was applied to all the simulations. For illustration, the resulting filaments in a given slice of the simulated boxes can be found in the left panels of Figs. 3.1, 3.2, and 3.3.

The extraction of the `DisPerSE` skeletons was performed as follows:

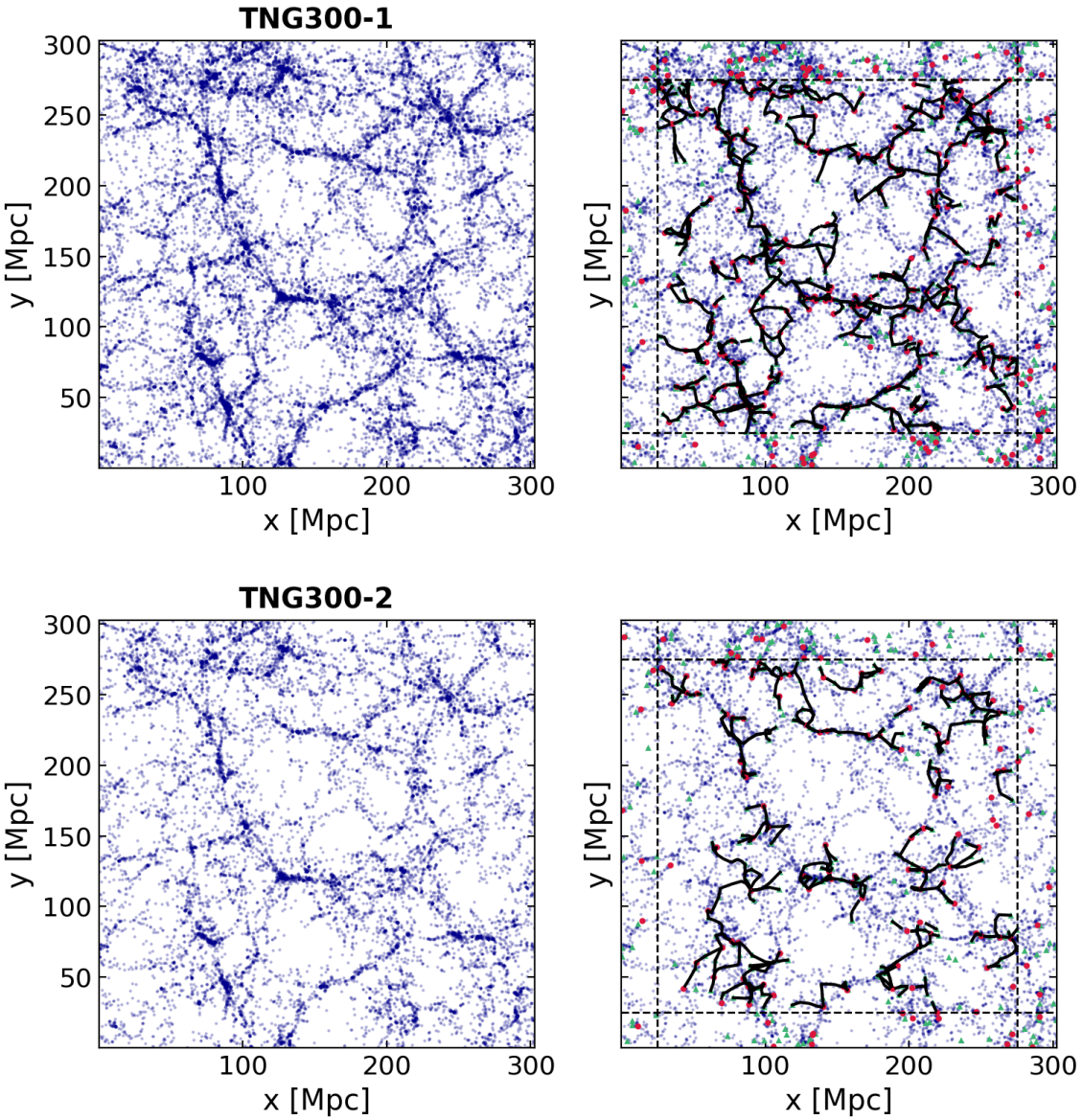

Figure 3.1: Galaxy distribution and associated `DisPerSE` filaments of the TNG300-1, TNG300-2 and simulation boxes. *Left: xy* projection of the galaxy distribution in the same slice of thickness 25 Mpc. *Right:* Filaments (black solid lines), CPmax (red points), and saddles (green triangles) in the slice. The dashed lines show the limit of the analysed volume of of 250^3 Mpc.

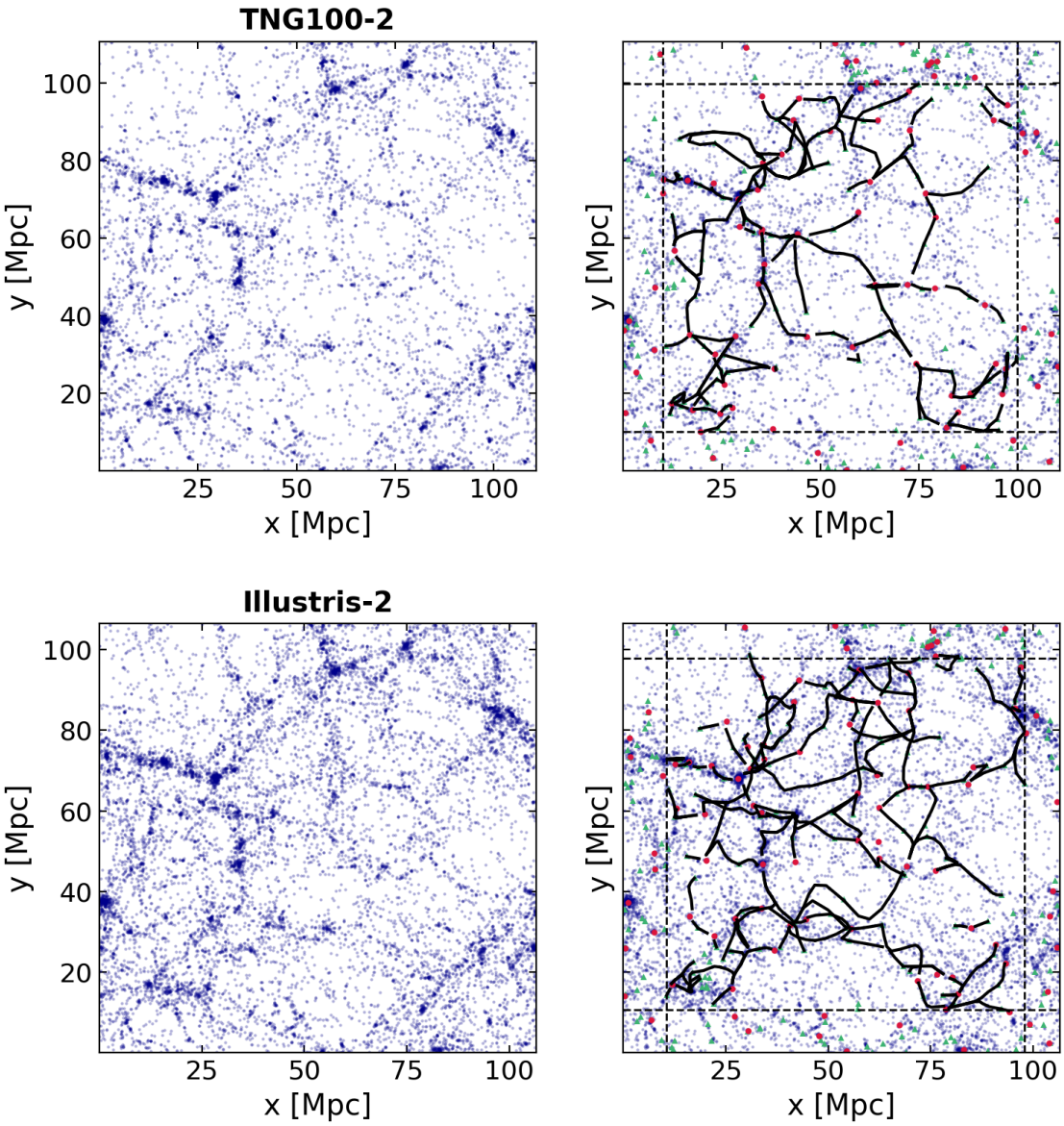

Figure 3.2: Galaxy distribution and associated `DisPerSE` filaments of the TNG100-2 and Illustris-2 simulations. *Left: xy* projection of the galaxy distribution in a slice of thickness 60 Mpc. *Right:* Filaments (black solid lines), CPmax (red points), and saddles (green triangles) in the slice. The dashed lines show the limit of the analysed volume of 90^3 Mpc.

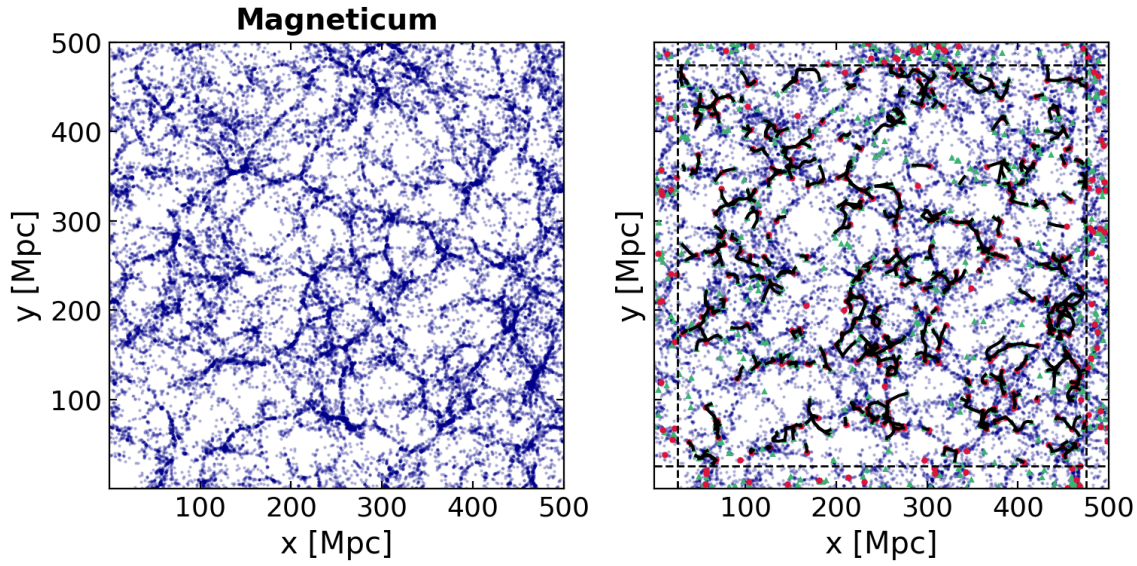

Figure 3.3: Galaxy distribution and associated `DisPerSE` filaments of the Magneticum `Box2/hr` box. *Left: xy* projection of the galaxy distribution in a slice of thickness 15 Mpc. *Right:* Filaments (black solid lines), CPmax (red points), and saddles (green triangles) in the slice. The dashed lines show the limit of the analysed volume of 450^3 Mpc.

Table 3.1: Overview of the five different galaxy catalogues and of the derived `DisPerSE` skeletons for the five simulations. All these skeletons were extracted with one smoothing cycle of the density field, and a persistence threshold of 3σ. The numbers for filaments and critical points correspond to the values inside the analysed volume (i.e. inside the central sub-boxes after removing the borders).

	TNG300-1	Magneticum	TNG300-2	TNG100-2	Illustris-2
Galaxies					
$N_{\rm gal}^{\rm box}$	275,818	1,266,306	148,369	13,680	20,426
$n_{\rm gal}^{\rm box}$ [Mpc^{-3}]	10.0×10^{-3}	10.1×10^{-3}	5.4×10^{-3}	10.1×10^{-3}	16.9×10^{-3}
Analysed volume [Mpc^3]	250^3	450^3	250^3	90^3	90^3
$N_{\rm gal}$	161,357	928,034	86,856	6,918	10,900
Filaments					
N_f	5,550	38,278	2,885	213	223
$L_f^{\rm min}$ [Mpc]	0.4	0.1	0.6	1.5	1.4
$L_f^{\rm max}$ [Mpc]	65.6	93.6	85.2	54.0	52.1
$L_f^{\rm mean}$ [Mpc]	10.9	12.2	14.3	10.7	11.2
$L_f^{\rm median}$ [Mpc]	8.8	9.8	11.4	8.3	9.2
Critical points					
$N_{\rm CPmax}$	1,731	9,610	882	73	78
$N_{\rm Saddles}$	3,133	21,998	1,627	136	151
$N_{\rm Bifurcations}$	1,651	14,432	911	71	100

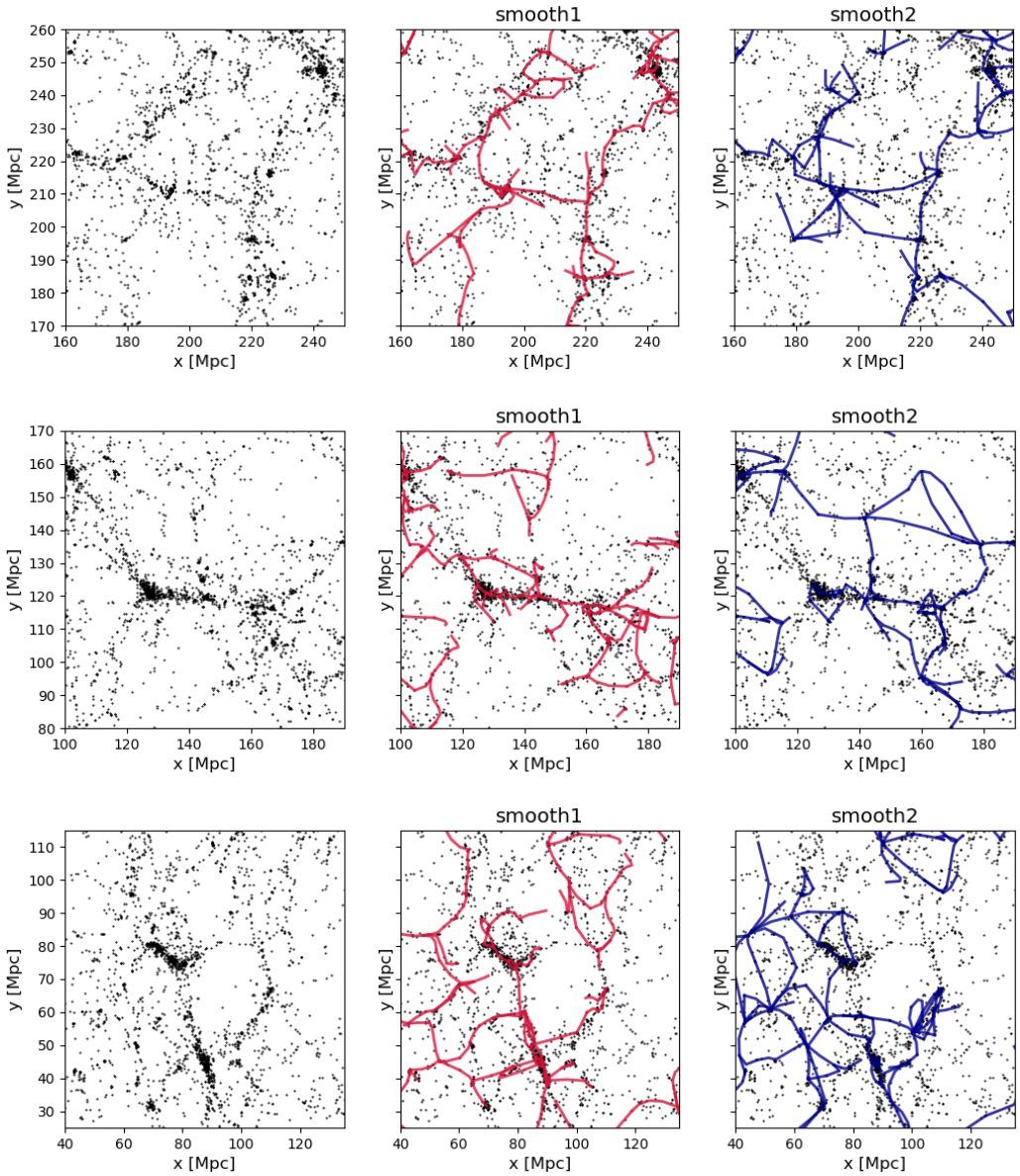

Figure 3.4: *From top to bottom*: visualisation of three different (arbitrarily selected) regions of the TNG300-1 box showing the distribution of galaxies (black points), and the filaments extracted with one or two smoothing cycles of the density field (respectively in red and blue). The persistence threshold of these plots is fixed to 3σ.

1. *Smoothing the density field*

   As a first step, `DisPerSE` computed the Delaunay density field based on the input galaxy distribution. I chose to perform a single smoothing of the resulting Delaunay field in order to minimise the contamination by shot noise and to prevent the identification of spurious features (Malavasi et al., 2020a,b). This smoothing is achieved by averaging the value of the density at each vertex (which corresponds to the position of a galaxy) with the surrounding vertices of the Delaunay tessellation. Note that increasing the number of smoothing cycles (e.g. smoothing the density field twice) reduces the capability of `DisPerSE` to recover low-density features. This harms the precision of the skeleton in finding actual filaments close to regions with low galaxy densities (e.g. near the voids). This can be seen, for example, in the zoomed visualisations of three different zones of the TNG300-1 box, presented in Fig. 3.4. In this figure, some of the filaments arising from a field with two smoothing cycles (blue) appear to be off with respect to the initial distribution of galaxies (black points), especially in the regions with few galaxies. Moreover, given that increasing the value of the smoothing parameter naturally narrows down the range of explored densities, the number of detected features arising from highly smoothed fields is reduced, leading to longer filaments on average. This is shown by the values of Table 3.2, and by the length distributions of Fig. 3.5, where it is evident that, for a fixed value of persistence threshold, the distributions of filament portions extracted from a density field smoothed twice ("smooth2") are shifted towards higher values with respect to an extraction with a single smoothing.

2. *Persistence threshold*

   The extraction of the (3D) skeleton by the discrete Morse theory was executed using a persistence threshold fixed to 3σ, for all the simulations. The choice of this value was determined by the study of the TNG300-1 box (which is the reference simulation). In that case, a lower persistence value resulted in a larger number of small scale features likely to emerge from the noise, whereas a higher value provoked a significant drop in the number of filaments, as only the most reliably identified structures were kept. Indeed, Table 3.2 and Fig. 3.5 (right panel) demonstrate that the number of filament portions decreases by a factor $\sim$ 16 between the 3σ and 7σ skeletons (with one smoothing cycle) of the TNG300-1 box. Notice that, for the lower values of persistence thresholds (from 3σ to 5σ) the length distributions of Fig. 3.5 exhibit a peak close to zero. This peak corresponds to extremely short filament portions arising from the noise, which are naturally cleaned from the skeleton in post-processing (see next Section). Another decisive argument for choosing a fiducial value of 3σ persistence threshold was that the resulting TNG300-1 skeleton accurately identified 91% of the most massive structures (clusters of galaxies) as CPmax, whereas this fraction was only 75% and 42% in skeletons with 4σ and 5σ persistence, respectively. A dedicated analysis on the link between CPmax and galaxy clusters is shown in the robustness tests of Sect. 3.3.

   For reference, Fig. 3.6 shows the filaments arising from different combinations of smoothing and persistence thresholds in a slice of the TNG300-1 box (the same as in Fig. 3.1). It is worth mentioning that the effect of these `DisPerSE` parameters has also been assessed in skeletons extracted from observational data, like e.g. Malavasi et al. (2020a), who builds a filament catalogue by applying `DisPerSE` to the SDSS survey.

3. *Smoothing the skeleton*

Table 3.2: Variation of the TNG300-1 skeleton with different `DisPerSE` parameters (smoothing of the density field and persistence thresholds). This Table focuses on the number of portions of filaments, their minimum, maximum and mean lengths. Note that portions of filaments are the raw output of `DisPerSE`, and since they consist in sets of segments connecting any type of critical point, they are different from the actual cosmic filaments defined in Sect. 3.1.3.

`DisPerSE` parameters	Number	Min length [Mpc]	Max length [Mpc]	Mean length [Mpc]
3σ - smooth1	14266	0.007	59.2	7.8
3σ - smooth2	12744	0.007	68.4	10.1
4σ - smooth1	10592	0.01	60.3	8.9
4σ - smooth2	10029	0.02	68.4	11.2
5σ - smooth1	5453	0.02	99.9	11.9
5σ - smooth2	5708	0.02	85.7	13.8
6σ - smooth1	2109	0.02	162.7	19.5
6σ - smooth2	2724	0.06	114.6	19.0
7σ - smooth1	863	0.05	428.9	31.2
7σ - smooth2	1127	0.08	151.9	27.8

A smoothing was then performed on the resulting skeleton. This aimed at alleviating the effect of shot noise on the geometry of the filaments, which would otherwise generate sharp and possibly nonphysical edges between the segments composing the filaments. This smoothing of the skeleton was done by shifting each segment extremity to the middle position of the contiguous extremities.

4. *"Breaking" the filaments*

   Finally, I applied the `DisPerSE` 'breakdown' procedure to break filaments sharing one or more segments into separate portions of filaments. Indeed, as it is clearly illustrated by, for example, the Illustris-2 skeleton (Fig. 3.2), some of the detected filaments have segments that belong to more than just one structure (i.e. they share common 'paths'). These segments should not be counted twice in the statistical analysis, since their repetition would bias the results. Therefore, the 'breakdown' procedure introduces bifurcation points at the positions where filaments merge. In this way, portions of filaments are delimited either by a CPmax, a saddle or a bifurcation point.

3.1.3 Post-processing the skeleton

After the different steps described above, the ouput of the `DisPerSE` code is a set of filament segments organised in portions and delimited by either a CPmax, a saddle or a bifurcation. In this section I explain how this 'raw' output was post-processed in order to retrieve the final filament catalogues that will be used in the analyses of the next Chapters.

Dealing with border effects

After visual inspection of the extracted skeletons, a salient feature was the (artificial) excess of critical points near the borders of the simulation boxes (see e.g. the case of TNG300-1 in Fig. 3.1). These could have been removed using dedicated flags in `DisPerSE` (Sousbie, 2011), but in a more conservative way, the borders of the box affected by this excess were

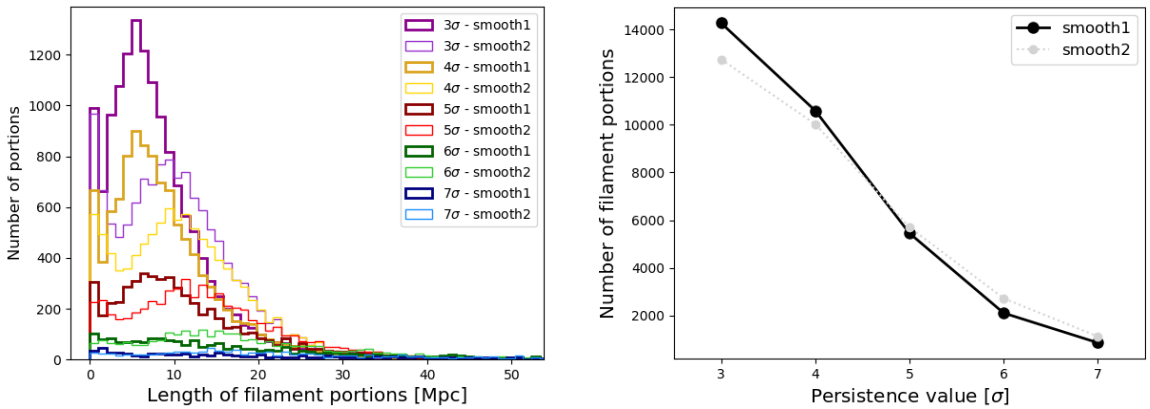

Figure 3.5: Tests of different `DisPerSE` parameters (smoothing of the density field and persistence threshold) in the TNG300-1 simulation. *Left:* Length distribution of the filament portions of skeletons with different sets of parameters. *Right:* Variation of the number of filament portions as a function of the value of the persistence threshold and the smoothing.

completely disregarded instead. The filament analyses are thus focused exclusively on the central volumes of the simulations, which excluded the regions of 25 Mpc thickness at the borders of the largest boxes (i.e. TNG300-1, TNG300-2, and Magneticum). This value was chosen because it corresponds to twice the width of the zones presenting the excess of critical points. For the sake of statistics, the discarded regions were limited to 10 Mpc in the smallest boxes (i.e. TNG100-2 and Illustris-2). Removing these regions naturally cleaned the filament skeleton from the very short and spurious portions. This is shown by Fig. 3.7, where the first peak of the length distributions of portions in the new volume (without the borders) is significantly lower ($\sim 26\%$ in the 3σ case) with respect to the results in the full box.

In the following, all the studies of the TNG300-1, TNG300-2, TNG100-2, Illustris-2, and Magneticum simulations are performed in the sub-boxes of respective volumes $[250\,\mathrm{Mpc}]^3$, $[250\,\mathrm{Mpc}]^3$, $[90\,\mathrm{Mpc}]^3$, $[90\,\mathrm{Mpc}]^3$, and $[450\,\mathrm{Mpc}]^3$. These analysed volumes are shown by the black dashed lines in Figs. 3.1, 3.2, and 3.3.

Reconnecting the portions to retrieve 'complete' filaments

The final filament catalogues were built by reconnecting the portions resulting from the 'breakdown' procedure in order to retrieve full filaments, i.e. filaments linking CPmaxs to saddle points. This topological definition is physically motivated by the fact that matter within a filament is presumed to flow from the saddle (a local minimum in the axis of a filament but a maximum in the transverse axis) to the point of maximum density, that is the CPmax (Kraljic et al., 2019). This final step of reconstruction of filaments that have been broken by the introduction of bifurcation points is crucial. Indeed, while the statistical analysis needs to be performed on the individual portions of 'broken' filaments (to avoid counting twice the shared filament segments), the general filament properties, such as their length, have to be determined from the full, maxima-to-saddle, filaments.

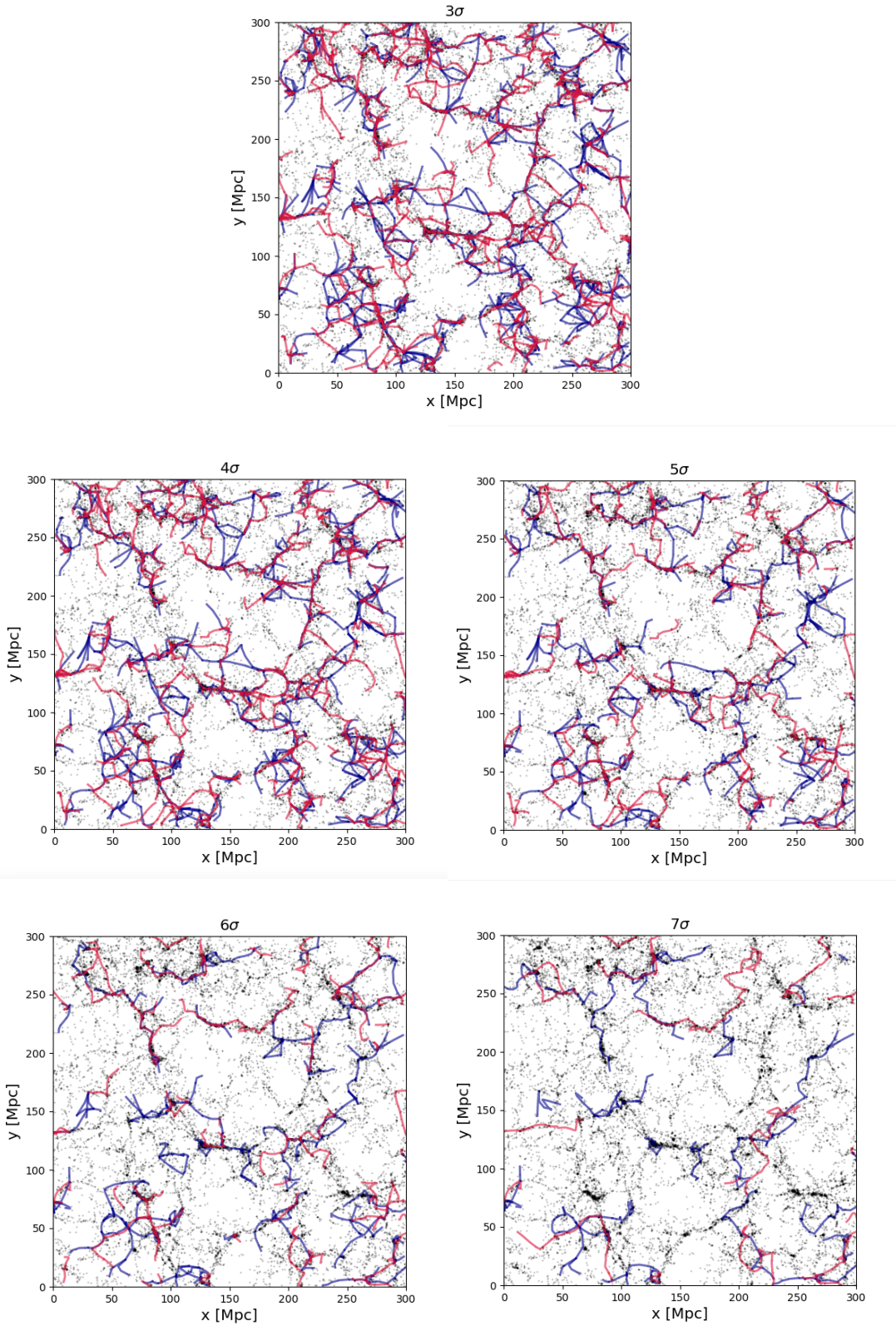

Figure 3.6: Filaments resulting from different combinations of `DisPerSE` parameters. Red and blue filaments correspond respectively to structures arising from one and two smoothing cycles of the density field, and the value of the persistence threshold (from 3 to 7σ) is indicated in the title of each panel.

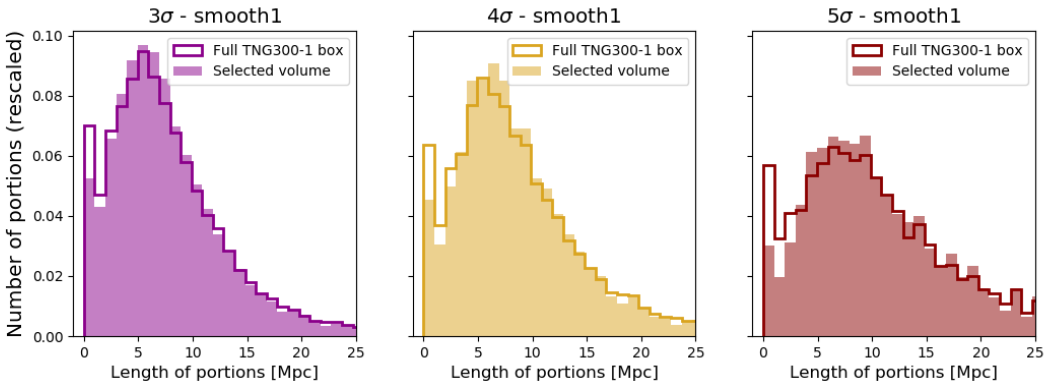

Figure 3.7: Length distribution of the filament portions of the 3σ, 4σ and 5σ skeletons before (plain lines) and after removing the excess of critical points (filled histograms) located at the borders of the simulation box. In this simulation (the reference TNG300-1), the selected volume is the $[250\,\mathrm{Mpc}]^3$ central sub-box, shown by the black dashed lines in Fig. 3.1.

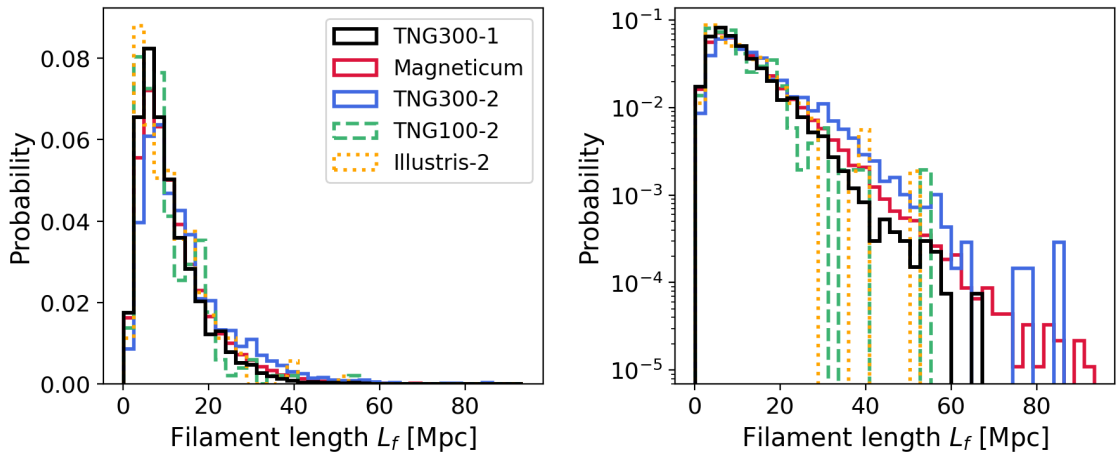

Figure 3.8: Filament length distributions of the five simulations analysed in this work, respectively in linear (left) and log space (right panel). Filaments are defined as the sets of segments connecting a CPmax with a saddle point of the density field. This figure is extracted from Galárraga-Espinosa et al. (2020).

3.2 The filament catalogues

This Section presents some general characteristics of the derived `DisPerSE` skeletons, such as the total number of filaments, critical points, and the filament length distributions. All the relevant values can be found in Table 3.1. Note that these numbers correspond to the values inside the central sub-boxes after discarding the borders (i.e. inside the analysed volumes).

Let us first focus on the number of filaments in the final catalogues. This number depends on: *(i)* the size of the simulation box, and *(ii)* the density of tracers, $n_{\rm gal}^{\rm box}$, corresponding to the number of galaxies per Mpc^3. The first dependency translates the fact that, at fixed density of tracers, smaller simulation boxes contain less filaments than bigger volumes, as expected by statistical considerations (see e.g. TNG300-1 v.s. Magneticum). The second dependency justifies the differences between boxes of the same volume (e.g. the reduced number of filaments in TNG300-2 with respect to the reference TNG300-1). Indeed, as explained in Sect. 2.2, the output skeleton of the `DisPerSE` code is sensitive to the input density of tracers, $n_{\rm gal}^{\rm box}$. Due to its lower resolution, TNG300-2 has a value of $n_{\rm gal}^{\rm box}$ that is almost twice as low as the reference TNG300-1, leading to less refined features in the density field, and thus to a reduced number of detected filaments ($2,885$ v.s. $5,550$). This is also clearly reflected in the visualisations of Fig. 3.1, where some of the features apparent in the TNG300-1 skeleton are clearly missing from the TNG300-2 one.

The length of each filament is computed as the sum of the lengths of all the segments that it is made of, from CPmax to saddle. The length distributions of the TNG300-1, Magneticum, TNG300-2, TNG100-2 and Illustris-2 filaments are presented in Fig. 3.8. A striking property of these distributions is their exponential tail, which is in agreement with previous findings (Bond et al., 2010; Choi et al., 2010; Malavasi et al., 2020a) and reflects the hierarchical and multi-scale character of the filamentary network, with significantly more short (peak at $\sim 5-6$ Mpc for TNG300-1) than long filaments (e.g. Aragón-Calvo et al., 2010b; Cautun et al., 2014). Note that the peak of the TNG300-2 distribution (blue histogram) is slightly shifted towards higher values, and this can once again be explained by the lower density of tracers of this simulation, resulting in a skeleton with fewer short filaments and to filaments that are longer on average. The length of filaments also depends on the size of the simulation box (as expected), and this figure clearly shows that filaments from small boxes do not reach the same lengths as these of the larger boxes (e.g. TNG100-2 v.s. Magneticum). It is worth noticing that none of these distributions show a peak at length ~ 0 Mpc (which was first seen in Fig. 3.5, reduced by the volume selection, but still present in Fig. 3.7). This is a natural consequence of the concatenation of small portions into filaments. For reference, the maximum, minimum, mean and median lengths of these filaments are also presented in Table 3.1.

Finally, the average number of filaments per CPmax is 3.25, meaning that on average each topological node is connected to three filaments. This in agreement with the studies of the connectivity of galaxy clusters of Gouin et al. (2020, 2021).

3.3 Robustness tests

In order to ensure that most of the features of the cosmic web are indeed detected (and well traced), the accuracy of the extracted `DisPerSE` skeleton (i.e. the filamentary network and

critical points) needs to be tested. With respect to the filamentary network, testing the robustness of the positions of the spines recovered by `DisPerSE` is far from being trivial, since a 'true' physical reference can not be easily determined in the simulations. To bypass this problem one could think of extracting the skeleton with another detection technique (e.g. Bonnaire et al., 2020; Cautun et al., 2013; Tempel et al., 2014) and comparing the corresponding outputs. However, this would rather be a characterisation of the similarities and differences of the different methods (Libeskind et al., 2018), and would not yield results on the accuracy of the skeletons in detecting the actual filaments.

On the other side, most simulations present a catalogue of haloes, usually identified from the DM particle distribution thanks to specific (`DisPerSE` independent) algorithms (e.g. the FoF or Subfind algorithms, see Sect. 2.1). It is thus straightforward to draw a comparison between these haloes and the denser ending points of the filamentary structures, the `DisPerSE` CPmax, which by construction correspond to the topological nodes of the skeleton. Therefore, this Section presents a comparative study of the positions, the masses, and the DM distributions between the `DisPerSE` CPmaxs and the haloes of the reference TNG300-1 simulation.

Matching the positions of CPmax with the FoF haloes

For this comparison, the publicly available catalogue of friend-of-friend (FoF) haloes of the TNG300-1 simulation was divided into the following mass bins, which I chose in order to encompass the main classes of objects:

- $M_{200} < 10^{11}\,\mathrm{M}_\odot/\mathrm{h}$ (small haloes),
- $M_{200} \in [10^{11}, 5\times10^{12}]\,\mathrm{M}_\odot/\mathrm{h}$ (galactic haloes),
- $M_{200} \in [5\times10^{12}, 5\times10^{13}]\,\mathrm{M}_\odot/\mathrm{h}$ (groups),
- $M_{200} \geq 5\times10^{13}\mathrm{M}_\odot/\mathrm{h}$ (clusters).

The total number of these structures in the TNG300-1 simulation box is respectively 4089, 154098, 4642, and 430. Note that, prior to this binning in mass, the FoF haloes were selected in order to contain at least one galaxy of stellar mass $10^9 \leq \mathrm{M}_*[\mathrm{M}_\odot] \leq 10^{12}$.

A slice of the simulation showing the positions of these structures and that of the `DisPerSE` CPmax is presented in Fig. 3.9. Note that this is the same slice as in Fig. 3.1. Overall, there is a good match between the positions of the CPmax and these of the most massive FoF haloes. Indeed the fraction of clusters hosting a CPmax within their R_{200} radii is 91%, showing that the most massive structures ($M_{200} \geq 5\times10^{13}$ $\mathrm{M}_\odot/\mathrm{h}$) are generally well traced by the `DisPerSE` skeleton. The fractions are much smaller in lower mass haloes, as expected for less massive objects. Conversely, 93% of CPmax lie within R_{200} of a FoF halo of any type, the other 7% probably being located in less dense environments of the cosmic web. All the previous values (and more) are reported in Table 3.3.

The absence of a one-to-one match between CPmax and FoF clusters is not surprising, given that the `DisPerSE` code identifies the critical points from the local density (see Sect. 2.2), which naturally leads to multi-scale features spanning broad density ranges. Of course, the fraction of CPmax in these low dense environments can be lowered by increasing the persistence threshold of the extracted skeleton (that corresponds to 3σ in this case). However this would lead to a skeleton that misses some of the most salient features of the density field, like clusters of

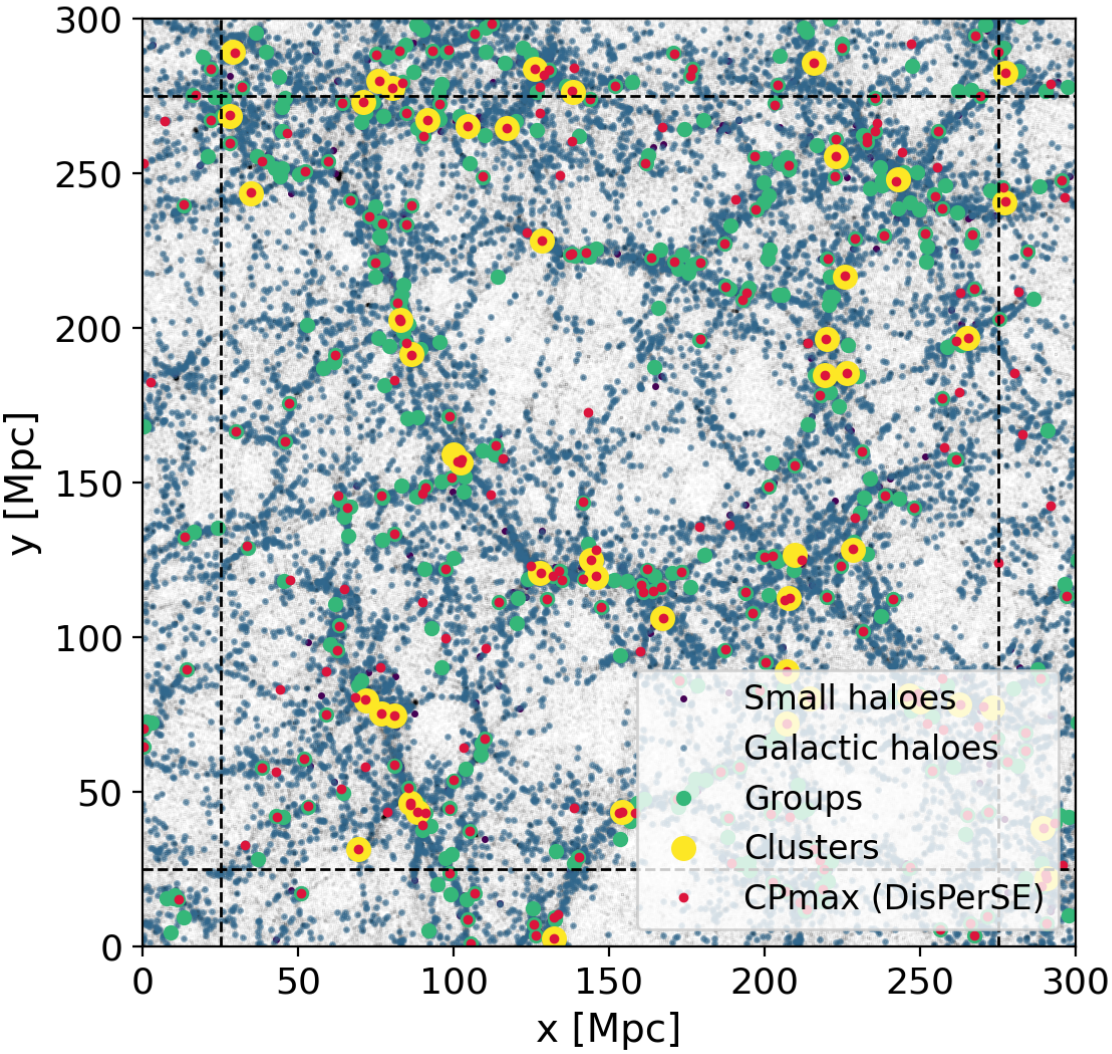

Figure 3.9: *xy* slice of the TNG300-1 simulation showing the positions of the `DisPerSE` CP-max (red points) in comparison with the location of the FoF haloes (coloured disks, from purple to yellow). The grey points represent the underlying DM distribution. This slice is the same as that of Fig. 3.1.

Table 3.3: Matching the `DisPerSE` CPmaxs with the FoF haloes of the TNG300-1 simulation. This table presents the fraction of FoF haloes hosting a CPmax within their R_{200}, and the fraction of CPmax coinciding with the positions of haloes (also within the clusters' R_{200}). The mass ranges of small haloes, galactic haloes, groups, and clusters are defined in the text, and their numbers are respectively 4089, 154098 and 4642, and 430. Each column corresponds to a different extraction of the skeleton, where only the persistence threshold is modified, going from 3 to and 5σ. All the other parameters correspond to these described in Sect. 3.1.2.

	3σ skeleton	4σ skeleton	5σ skeleton
Small haloes hosting CPmax	0.0%	0.0%	0.0%
Galactic haloes hosting CPmax	0.3%	0.1%	0.1%
Groups hosting CPmax	40%	26%	12%
Clusters hosting CPmax	91%	75%	42%
CPmax in Small haloes	0.0%	0.0%	0.0%
CPmax in Galactic haloes	17%	12%	10%
CPmax in Groups	62%	64%	63%
CPmax in Clusters	14%	18%	22%
Total fraction of matched CPmax	93%	94%	94%

galaxies. Indeed, the second and third columns of Table 3.3 show the resulting CPmax-FoF halo matching of other `DisPerSE` skeletons derived with higher values of the persistence threshold, namely 4σ and 5σ. While the improvement on the total number of CPmax lying within massive FoF haloes (i.e. clusters) is only mild (it increases from 14% in the 3σ fiducial skeleton to 22% in the extreme case of 5σ), the number of these structures that are actually traced by the skeleton drops dramatically. For example, in the 4σ case only 75% of clusters host a CPmax, and in the 5σ skeleton this fraction is 42%, meaning that more than half of the clusters are not identified as CPmaxs. These studies comfort the choice of using a 3σ persistence threshold as the fiducial value for the extraction of the `DisPerSE` skeletons in Sect. 3.1.

Mass distributions of nodes and haloes

Figure 3.10 shows the M_{200} mass distribution of the `DisPerSE` CPmax and of the FoF clusters for the 3σ skeleton of the TNG300-1 simulation. The mean and median values of the distributions are marked respectively by the long thin and short thick bars.

For each CPmax, I computed the M_{200} mass by summing the masses of all the DM particles in a sphere centered at the position of the CPmax and of radius R_{200}, the critical radius. The latter is defined as the radius of the sphere (centred on the CPmax position) whose mean enclosed density is 200 times ρ_c (the critical density of the Universe). For each CPmax, the R_{200} radii were determined by following the iterative scheme explained in Sect. 4.1.1.

In the case of the FoF haloes, the masses were directly obtained from the simulation output (field `Group_M_Crit200`), and correspond to the total mass of the halo, enclosed in a sphere whose mean density is 200 times the critical value of the Universe.

The CPmax mass distribution shows a symmetrical shape that peaks at $\sim 10^{12.8}$ $M_\odot$/h, corresponding to the median value of the distribution. In the high mass regime (higher than $\sim 10^{12.8}$ $M_\odot$/h), the distribution follows the same trend as that of massive FoF haloes (groups and clusters), with a decreasing number of objects with increasing mass. Precisely, 4% and 51% of CPmax lie in the mass bins corresponding to groups and clusters. On the other side,

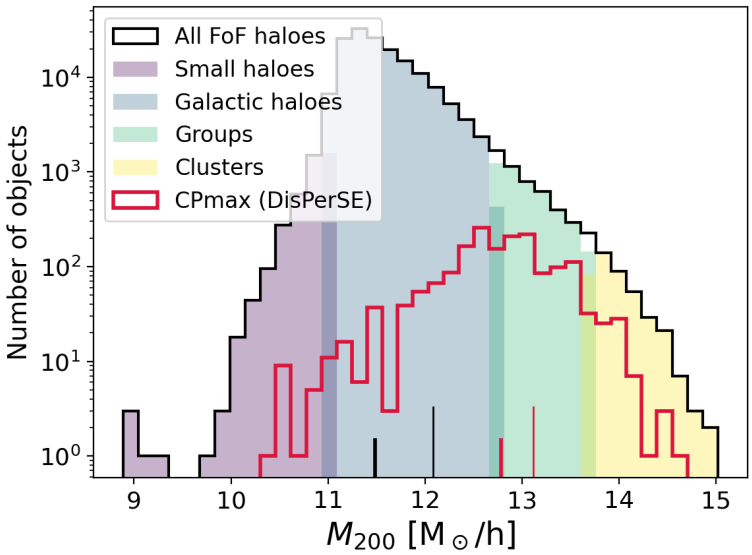

Figure 3.10: Mass M_{200} distribution of CPmaxs and FoF haloes of the TNG300-1 simulation. The means and medians of the distributions are shown respectively by the long-thin and short-thick vertical lines. Their corresponding values for CPmaxs and FoF haloes are respectively $10^{13.1}$ and $10^{13.6}$ (means), and $10^{12.8}$ and $10^{13.2}$ $M_\odot$/h (medians). The histogram in very thin grey lines represents the mass distribution of all the FOF haloes hosting at least one galaxy of mass $10^9 < M_* \leq 10^{12}$ $M_\odot$/h.

in the lower mass regime, these two distributions are very different, since the CPmax masses steadily decrease (down to the minimum mass $10^{10.4}$ $M_\odot$/h), while the distribution of FoF haloes peaks only at $10^{11.3}$ $M_\odot$/h (which is the typical mass of haloes hosting galaxies of stellar mass $\sim 10^9$ $M_\odot$/h) and rapidly drops at lower masses. The fraction of CPmax in the mass bins corresponding to small haloes and to galactic haloes is respectively 1% and 44%.

This Figure also shows that massive CPmax points have on average lower masses than massive FoF haloes. This does not come from the fact that baryons were not taken into account in the computation of the M_{200} masses of these `DisPerSE` objects, since by computing the mass contribution specific to baryons for the FoF haloes, I estimated that on average baryons account for only $\sim$ 11% of the total mass in these objects. Therefore, by assuming the same baryon contribution in CPmaxs, it is straightforward to conclude that the mass distribution is almost unchanged when baryons are taken into account. This mass difference can rather explained by the fact that, by construction, CPmax points coincide with the positions of galaxies of mass $10^9 < M_* \leq 10^{12}$ $M_\odot$. Galaxies in this mass range might not always represent the brightest cluster galaxies (BCG) of the parent halo, and thus CPmax points might be miscentred from the position of the center of the halo (defined as the position of the most bound particle), leading to lower M_{200} masses of CPmax nodes with respect to FoF haloes.

DM density profiles of nodes and haloes

With the aim of characterising the distribution of matter around the CPmaxs, the DM density profiles of these structures were compared to these of clusters of galaxies. The resulting average profiles are shown in Figure 3.11. These were computed by summing the DM masses in concentric shells around the centres of the structures, and then dividing the resulting mass by

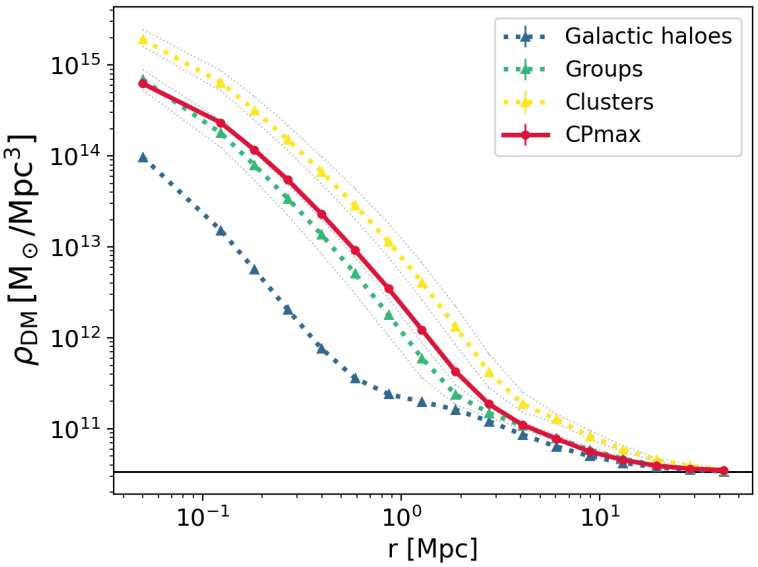

Figure 3.11: DM density profiles of CPmaxs and FoF haloes in the TNG300-1 simulation. The radial distance r is taken from the centre of the structure outwards. The thin grey lines correspond to the average density profiles in thinner mass bins, which are, from bottom to top, $[5 \times 10^{12}, 10^{13}]$, $[10^{13}, 5 \times 10^{13}]$, $[5 \times 10^{13}, 10^{14}]$, and $[10^{14}, 10^{15}]$ $M_\odot$/h. The black horizontal line shows the mean DM density of the simulation, computed as the total DM mass divided by the volume of the box.

the volume of the corresponding shell.

This figure clearly shows that the CPmax density profile is bracketed between these of groups and clusters. By performing a finer binning in mass, one can see that the CPmax profile is very similar to that of FoF haloes in the mass range $M_{200} \in [10^{13}, 5 \times 10^{13}]$ $M_\odot$/h, which is compatible with the previous analysis of the mass distributions. The resemblance in shape and amplitudes between the CPmax and massive FoF haloes profiles shows that the spatial distribution of DM around the `DisPerSE` CPmaxs is compatible with that of the more 'physically'-defined objects that are groups and clusters of galaxies.

3.4 Conclusion

This Chapter presented the filament catalogues used in this work. These were extracted by applying the `DisPerSE` algorithm to the galaxy distributions of the different simulations, using a 3σ persistence threshold and one smoothing cycle of the density field (see Sect. 3.1). These parameters were chosen by the study of the TNG300-1 box, which is the reference simulation in all the analyses presented in the next Chapters. The impact of the `DisPerSE` parameters on the resulting skeleton was assessed by studying the number and length of the detected portions of filaments, and the main general properties of the detected filaments were presented in Sect. 3.2.

However, given the difficulty in testing the accuracy of the positions of the filament spines, the robustness of the skeleton was assessed by comparing the positions, mass distributions, and DM density profiles of the CPmax (i.e. the denser ends of filaments) to the equivalent properties of the FoF haloes of the simulation. These tests showed that, when tracing filaments using galaxies in the stellar mass range of $10^9 - 10^{12}$ $M_\odot$, the 3σ skeleton is the best that can

possibly be extracted within the DisPerSE framework.

In conclusion, the reference DisPerSE skeleton is robust enough to trace the most massive structures of the cosmic web, which is a crucial requirement for the study of matter around filaments which I will present in the next Chapters.

Chapter 4

Distribution of matter around cosmic filaments

Contents

This Chapter aims at giving a comprehensive characterisation of the distribution of matter around cosmic filaments, whose detection was described in Chapter 3. The first section, Sect. 4.1, presents the study of the distribution of galaxies around the cosmic filaments of the TNG, Illustris, and Magneticum skeletons previously introduced. The distribution of the matter components, namely DM, gas and stars, is then studied for the TNG300-1 filaments in Sect. 4.2. Finally, a discussion on the large-scale environment of the different populations of filaments is performed in Sect. 4.3.

4.1 Galaxies around filaments

Since its first detection around the Perseus cluster (Jõeveer et al., 1978) and in the Center for Astrophysics (CfA) galaxy survey (de Lapparent et al., 1986), the cosmic web, as traced by galaxies, has been observed in many galaxy surveys with increasing resolution and statistics. For example, over the last two decades, the distribution of galaxies in this web-like filamentary pattern has been detected in the Sloan Digital Sky Survey (SDSS, York et al., 2000), the two degree Field Galaxy Redshift Survey (2dFGRS, Colless et al., 2003), the Cosmic Evolution Survey (COSMOS, Scoville et al., 2007), the 6dF Galaxy Survey (6dFGS Jones et al., 2009), the Galaxy and Mass Assembly (GAMA, Driver et al., 2011), the VIMOS VLT deep survey (Le Fèvre et al., 2005, VVDS), VIPERS (Guzzo et al., 2014) and SAMI (Bryant et al., 2015) surveys. A study of cosmic filaments in observations can thus be achieved by using the posi-

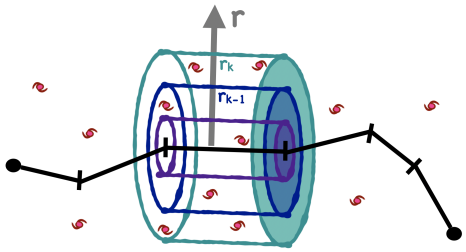

Figure 4.1: Illustration of the method to compute radial density profiles of filaments. The concentric cylinders are shown only for one segment of the filament (black straight lines). The radial distance to the axis of the filament is called r. This figure is extracted from Galárraga-Espinosa et al. (2020).

tions of galaxies as proxies. However, this has intrinsic limitations (due to e.g. galaxy selection effects and Fingers of God effects Malavasi et al., 2020a), so a study in numerical simulations is necessary in order to guide observational analyses.

This section presents a study of the distribution of galaxies in filaments from simulations (see Chapter 3). This distribution is characterised via the building of galaxy density radial profiles, and identifying dependencies with filament properties, such as their length and large-scale environment. Inspired by the galaxy cluster literature and following an empirical approach, this section also investigates whether some analytical models can be adapted to describe the radial profiles of cosmic filaments.

4.1.1 Galaxy density profiles of filaments

The distribution of galaxies around filaments can be studied by computing the radial profile of galaxy density around these cosmic structures. This quantity is defined as the number density of galaxies along the perpendicular direction to the filament spine (hereafter called r). This Section presents the method and the first results of galaxy density profiles around the filaments of the TNG300-1, TNG300-2, TNG100-2, Illustris-2, and Magneticum skeletons.

Method

The profiles of galaxy density around filaments are computed in the following way. I start by estimating the radial profile around a segment i of a filament by counting the number of galaxies in concentric cylindrical shells around the axis of the segment, as illustrated in Fig. 4.1, according to the equation:

$$n^i(r_k) = \frac{N_k}{\pi(r_k^2 - r_{k-1}^2)\, l_i}. \tag{4.1}$$

Here, l_i is the length of segment i, the index k stands for the cylindrical shell of thickness $r_k - r_{k-1}$ and N_k is the number of galaxies in the k-th shell. The radial distance r is binned in 20 equally spaced logarithmic bins, starting from the axis of the segment and up to $r = 100$ Mpc.

The (total) radial profile of galaxy density around filaments is then computed by averaging the profiles of all the set of segments. In this average, each segment is counted only once, regardless of the number of reconstructed filaments to which it belongs. Indeed, let us recall that, as presented in Sect. 3.1.2, different filaments can share one or more segments, so in order to avoid counting twice the same segment in the statistical analysis, the `DisPerSE` 'breakdown' procedure (which breaks these common paths into separate portions) was applied during the

extraction of the skeleton.

The errors on the filament profiles are computed by bootstrapping over the set of individual segment profiles, i.e. for a set of N segments, N profiles are randomly selected (with replacement), and then averaged together. This procedure is repeated N times in order to obtain N averages, and the errors of the filament profile are thus the dispersion of these N averages.

In order to retrieve the properties that are solely specific to cosmic filaments, I removed from the analysis the filament segments that are connected to the nodes. Indeed, including these segments would add contributions from cluster outskirts, and this would bias the analysis of the main filament stems, which are the regions of interest in this work. Within the `DisPerSE` framework, the topological nodes of the skeleton are determined by the position of the CPmaxs, and for simplicity they were considered as spherically symmetric objects. By assuming that the CPmax lie at their centre, for each node I computed the radius R_{200} using the DM particles of the simulations[1]. More precisely, the R_{200} radius of a given CPmax, defined as the radius of the sphere whose mean density is 200 times ρ_c (the critical density of the Universe), was determined by following the iterative scheme of computing the DM density in spheres of increasing radii, until finding the radius for which the enclosed density equals the expected value of $200\,\rho_c$.

The filament segments and galaxies inside the spheres of radius $3\times R_{200}$ were then removed from the analysis. The choice of this rather conservative factor was determined by testing the effect of different radii on the galaxy density profiles around the filaments. This is shown in Fig. 4.2 for the TNG300-1 simulation, where a comparison between the profile without any mask and those using a mask of 1, 2 and $3\times R_{200}$ is presented. At the core of the filaments, the unmasked curve (gray) and the $1\times R_{200}$ masked profile (green) are 39 σ apart. However, the differences between the 1, 2 or $3\times R_{200}$ masked profiles are not significant as the signal is stable, proving that a mask of 1, 2 or $3\times R_{200}$ is equivalently good enough to remove the contribution from the nodes. Nevertheless, for the filament analyses, a preference is given for the use of a $3\times R_{200}$ mask (the higher value), in order to avoid the contamination by other effects at the outskirts of clusters, like splash-back features (More et al., 2015, 2016; Baxter et al., 2017b; Diemer et al., 2017; Chang et al., 2018; Shin et al., 2019), for example. The remaining filament segments after this masking procedure are shown in the schematic illustration of Fig. 4.3a

The final step for computing galaxy density profiles around filaments consists in dealing with the effects arising from the simulation volume limitations. With the aim of reducing them in the density profiles, I concatenated the galaxy distributions at the borders of the TNG300-1 simulation box in order to construct a $[3\times250\,\mathrm{Mpc}]^3$ volume. The filaments, defined in the central volume of $[250\,\mathrm{Mpc}]^3$, are not replicated, as is shown in the 2D illustration of Fig. 4.3b. As the study focuses only on statistical trends of the galaxy density field, this concatenation (which only affects the continuity of the field at the borders) does not undermine the results. The same replication procedure was applied to the Magneticum, TNG300-2, TNG100-2 and Illustris-2 simulations to construct $[3\times450\,\mathrm{Mpc}]^3$, $[3\times250\,\mathrm{Mpc}]^3$, $[3\times90\,\mathrm{Mpc}]^3$ and $[3\times90\,\mathrm{Mpc}]^3$ volumes, respectively.

[1]DM particles were used instead of galaxies in order to have an unbiased description of the density field around the nodes of the skeleton. Notice that for the Magneticum simulation the R_{200} radii were computed from the galaxy distribution instead, because the DM distribution is not publicly available.

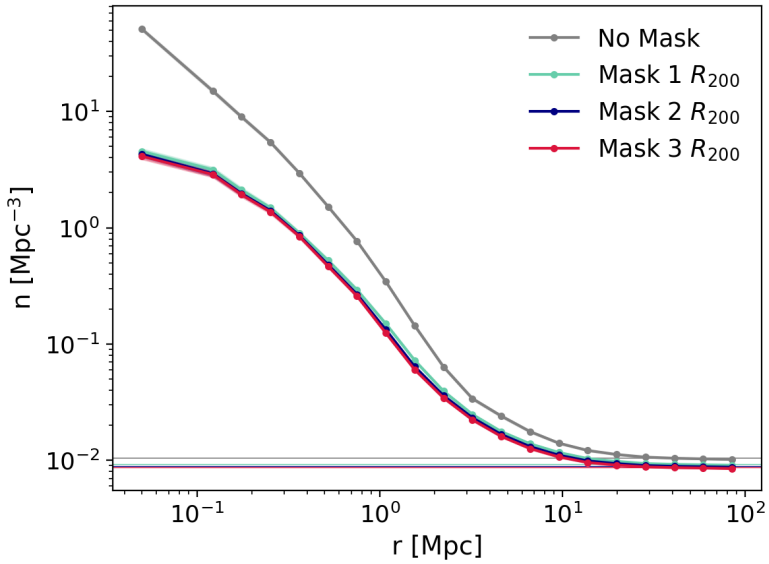

Figure 4.2: Density profiles of galaxies around filaments with different masks of the CPmax: $1\times R_{200}$ (green), $2\times R_{200}$ (blue) and $3\times R_{200}$ (pink). The gray curve represents the density profile without applying any mask. The horizontal thin lines represent the corresponding background galaxy densities after removing the masked galaxies. This figure is extracted from Galárraga-Espinosa et al. (2020).

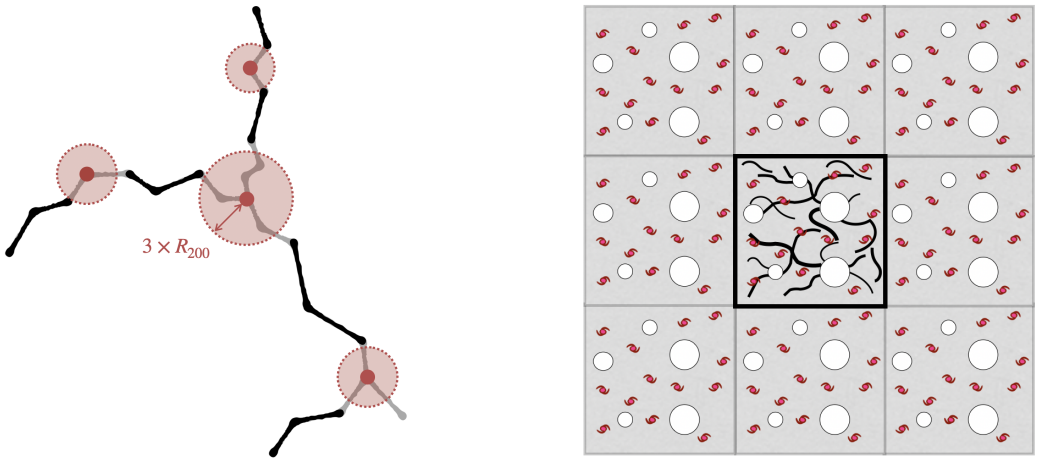

(a) Masking the nodes

(b) Concatenating the boxes

Figure 4.3: **(a)**: Illustration in 2D of the remaining filament segments (black lines) after masking the segments located within the spheres of radius $3\times R_{200}$ centred on the CPmax (red points). The masked segments are shown by the gray lines. **(b)**: Illustration in 2D of the concatenation procedure aiming at reducing the effects of a volume-limited box in the density profiles. The galaxy distribution is replicated at the borders of the central simulated volume, where the filaments are defined. The white circles correspond to the masked regions of the CPmax.

Results

The galaxy density profile of filaments is computed by averaging all the segment profiles in the catalogue. The result for the TNG300-1 filaments is shown in the upper panel of Fig. 4.4 (black curve). This figure also shows the corresponding null-test (light blue curve), which is obtained by shifting the positions of all the filaments of the catalogue by random offsets, and computing the galaxy density profile of these shifted filaments. This procedure is repeated 100 times to create 100 different realisations of the original catalogue of 5550 filaments. The values of the null-test are then given by the average profiles of these 5550×100 randomly shifted filaments.

The average galaxy density profile of filaments exhibits a clear excess with respect to the background density. The significance at the core of the filaments with respect to the null-test is found to be $\sim 20\,\sigma$. This is compatible with the significance range $[\sim 5\sigma, 32\sigma]$ of the over-density profiles of Bonjean et al. (2020), who performed a similar study using $0.1 < z < 0.3$ galaxies from the WISExSCOS catalogue around `DisPerSE` detected filaments (with a mask of $3 \times R_{500}$ for the clusters). Also, note that the significance of the detection in Fig. 4.4 is above 5σ up to radial distances of $r = 27$ Mpc. The galaxy density decreases with increasing distance r, until it reaches the average density of the simulation box (gray horizontal line). The null-test of Fig. 4.4 yields the average galaxy density of the simulation box, demonstrating that the method used to compute the profiles is not biased.

Similarly, I computed the average galaxy density radial profile of filaments in the Magneticum, TNG300-2, TNG100-2 and Illustris-2 simulations. The results are shown in the lower panel of Fig. 4.4, respectively in red, blue, green and yellow, along with the reference (TNG300-1) profile that is shown in black. For the sake of comparison with the profile obtained from the TNG300-1 simulation, all the profiles are rescaled by their respective background densities.

The TNG300-1, Magneticum, TNG300-2 and TNG100-2 profiles are essentially the same, despite some differences that will be discussed in the next paragraph. Let us here focus on the Illustris-2 profile, which is significantly different from the others particularly near the core of the filament. The shallow core of this profile might be caused by AGN and possible other feedback effects that are known to be more important in this simulation. For example, these effects have already been identified as responsible of the excessively high depletion rate of gas in massive haloes at low redshift, leading to tensions with observations (Genel et al., 2014; Haider et al., 2016). To confirm this hypothesis, I computed galaxy density profiles in nodes in the Illustris-2 and TNG100-2 simulations, presented in Fig. 4.5, assuming spherical symmetry. Recall that nodes are identified by the CPmax, and these objects are masked in the analysis of filaments (see previous Section). The resulting profiles in nodes exhibit the same trend as the profiles of filaments, i.e. the Illustris-2 slope is shallower and the densities at the centre of the nodes are smaller in this simulation than in the TNG100-2 one. These results already support the fact that the densest regions of the cosmic web, like massive haloes and cores of filaments, are particularly sensitive to feedback effects. Nevertheless, while baryonic physics plays a role in the distribution of matter around filaments, the essential and dominant driver remains gravity (as expected), as is shown by the strong similarity of the density profiles of the other simulations (cf. Fig. 4.4), even though their feedback models (TNG and Magneticum models) are not identical[2]. Note that a more extensive study on the effects of AGN feedback on the distribution of matter around filaments is presented in Sect. 4.2.2.

[2]Indeed, the TNG feedback model follows Weinberger et al. (2017), whereas the Magneticum model is described by Springel et al. (2005) and Fabjan et al. (2010). See also Sect. 2.1 for details.

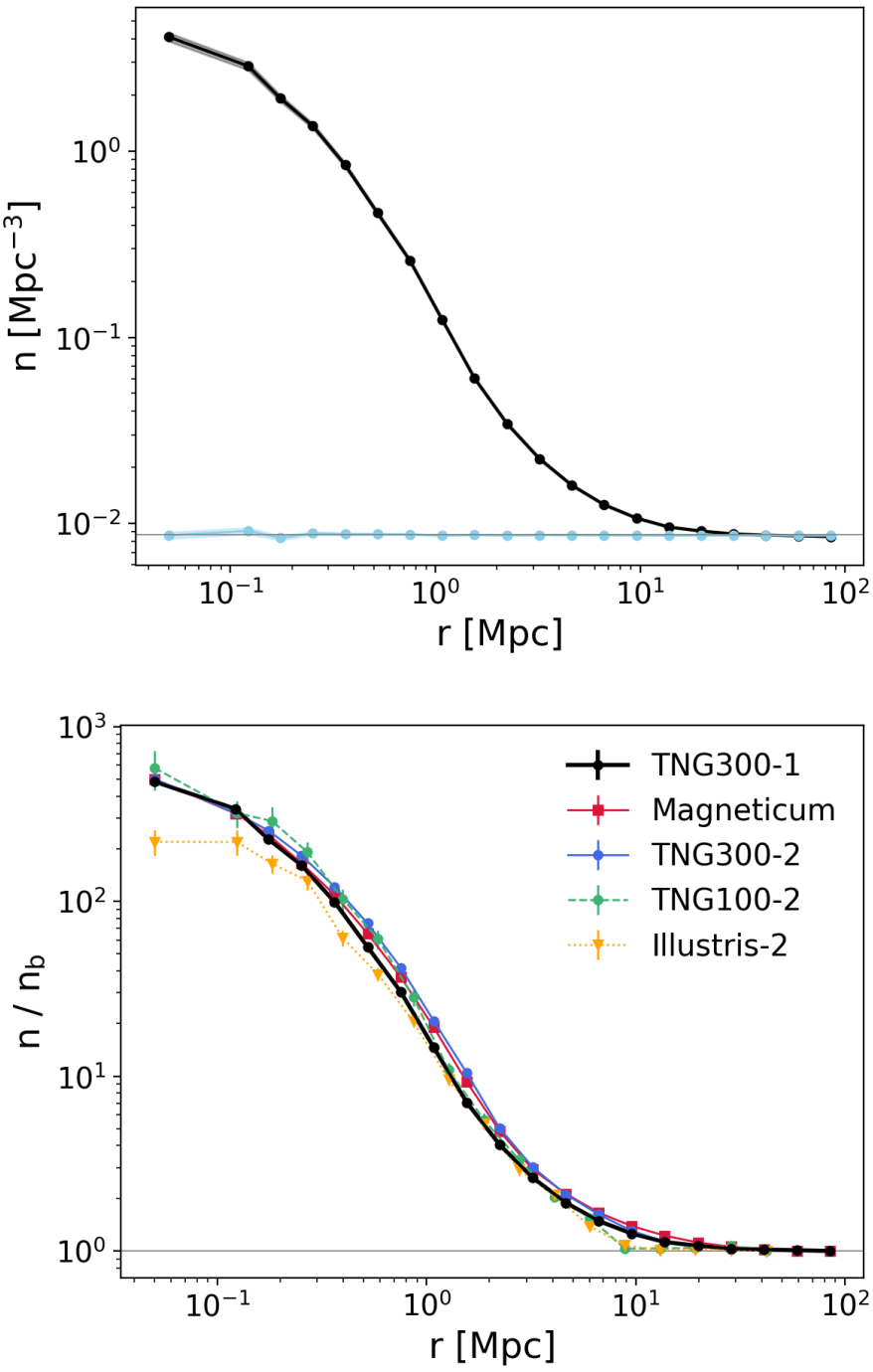

Figure 4.4: *Top:* Radial density profile of galaxies around filaments of the reference catalogue (TNG300-1). The black curve shows the average galaxy density of all filaments. The blue curve presents the null-test, which is obtained by computing the density of galaxies around randomly shifted filament positions. The gray horizontal line represents the mean galaxy density of the simulation box. *Bottom:* Radial density profile of filaments of the TNG300-1 (black curve), Magneticum (red), TNG300-2 (blue), TNG100-2 (green) and Illustris-2 catalogues (yellow curve). For the sake of comparison, each profile n has been rescaled by its background density, n_b. This figure is extracted from Galárraga-Espinosa et al. (2020).

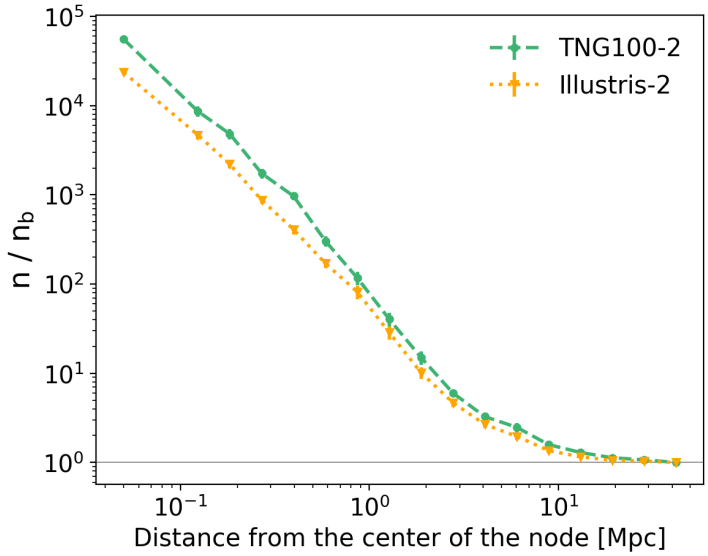

Figure 4.5: Galaxy density profiles in nodes (i.e. CPmax), for the Illustris-2 and the TNG300-2 simulation. This figure is extracted from Galárraga-Espinosa et al. (2020).

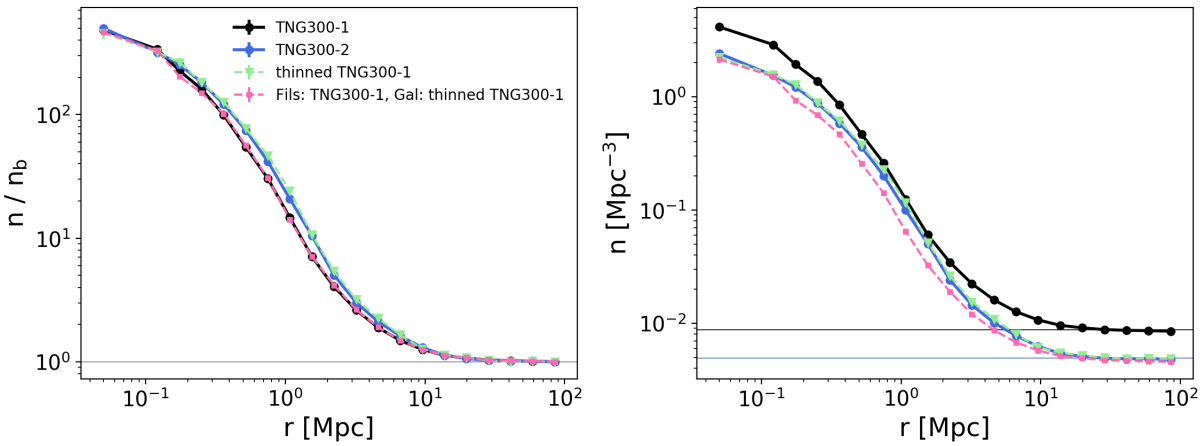

Figure 4.6: Study of resolution effects in the density profiles. The black and blue curves present the galaxy density profiles of the TNG300-1 and TNG300-2 simulations, as shown in Fig. 4.4. The green dashed curve with triangles corresponds to the density profiles of the thinned TNG300-1 galaxy catalogue around and the corresponding `DisPerSE` filaments. The pink dashed profile with squares represents the density of the thinned TNG300-1 galaxy catalogue around the reference TNG300-1 original skeleton. *Left:* Rescaled density profiles. *Right:* Density profiles at their respective galaxy backgrounds. This figure is extracted from Galárraga-Espinosa et al. (2020).

Despite the good visual agreement in the other profiles of Fig. 4.4 (i.e. the TNG300-1, Magneticum, TNG300-2, and TNG100-2 profiles), let us now discuss the slight deviations spotted at distances of $r \sim 1$ Mpc. Indeed, from the core to the outskirts of the filament, the TNG300-2 profile (blue) exhibits a softer decrease of galaxy density with respect to the TNG300-1 reference profile (black), yielding a more extended and fatter core in this lower resolution run. This effect could be explained by a reduced precision in the detection of filaments by the DisPerSE algorithm, coming from the smaller number of tracers (i.e. galaxies) in lower resolution simulations. In order to verify this hypothesis, the TNG300-1 galaxy catalogue was thinned by randomly removing every other galaxy so that the density of tracers, $n_{\rm gal}^{\rm box}$, matches that of TNG300-2 (see Table 3.1). The skeleton of this thinned catalogue was then extracted using the same `DisPerSE` parameters as presented in Sect. 3.1.2, and the galaxy density profiles of the thinned catalogue around these newly extracted filaments were then computed. The resulting average profile is displayed in Fig. 4.6 (green dashed curve with triangles) and shows a perfect agreement with the TNG300-2 profile (in blue). Notice that the left panel of this figure displays the rescaled density profiles, while the right panel shows the profiles at their respective galaxy backgrounds (denoted by the horizontal lines). In addition, I also analysed the distribution of galaxies of the thinned TNG300-1 catalogue around the original TNG300-1 reference filaments. This resulted in the pink dashed profile with squares, which has exactly the same shape as the TNG300-1 reference. Indeed, this curve perfectly overlaps with the reference in the left panel of rescaled profiles, proving that the distribution of galaxies around filaments is not changed with resolution. Hence, these tests show that the fatter core of the TNG300-2 profile is purely due to `DisPerSE` precision effects, that increase the uncertainty in the position of filaments in simulations with lower densities of tracers.

Finally, the Magneticum profile (red curve) of Fig. 4.4 seems to be in good agreement with that of TNG300-2. While the Magneticum simulation has a DM resolution similar to that of TNG300-2 (see Table 2.1), its density of tracers $n_{\rm gal}^{\rm box}$ is rather compatible with that of the reference TNG300-1 (Table 3.1). Therefore, the aforementioned `DisPerSE` precision effects are not likely to explain the fatter core of Magneticum with respect to the reference profile. The Magneticum simulation has a different cosmology, slightly different redshift ($z = 0.066$), and different physical models than the TNG series (see Table 2.2), but these effects can not be disentangled in the density profiles of this work. Still, despite these differences, the profiles of TNG300-1 and Magneticum are remarkably similar from a statistical point of view, as confirmed by the p-value of 0.22 obtained from the two-sample Kolomogorov-Smirnov test.

4.1.2 Identifying two different populations of filaments

Galaxy density v.s. filament length

The average galaxy density profiles obtained in Sect. 4.1.1 characterise the entire population of filaments, regardless of specific filament properties. In order to explore possible dependencies with the filament lengths, the TNG300-1 filament catalogue is split in eight different bins of length chosen so that each contains the same number of segments, $\sim$ 2200. Following the method introduced in Sect. 4.1.1, the profile of filaments in a given bin of length is computed as the average of the profiles of the segments forming the filaments in this bin. The eight resulting profiles are presented in the top panel of Fig. 4.7 (from yellow to blue curves), where the average profile of all the filaments is also displayed (black dotted curve). This figure clearly shows that filaments of different lengths have significantly different radial galaxy densities.

The profiles of the shortest filaments lie above the average at all radial distances, whereas the longest filaments are found below the average. The bottom panel shows the deviation from the average profile for each bin of length, is defined as

$$D_{\text{subset-tot}} = \frac{n_{\text{subset}} - n_{\text{tot}}}{\sqrt{\sigma^2_{\text{subset}} + \sigma^2_{\text{tot}}}}, \tag{4.2}$$

where n_{subset} is the profile of the filaments in a given bin, n_{tot} is the average profile (as in Fig. 4.4), σ_{subset}, and σ_{tot} are the bootstrap errors of the corresponding profiles.

While the filaments of lengths in the range $9 \leq L_{\text{f}} < 20$ Mpc do not present significant deviations from the average profile ($|D_{\text{subset-tot}}| < 2$), the shortest and longest bins of length deviate by more than 2σ, and the differences are the most significant ($|D_{\text{subset-tot}}| \sim 8$) for distances between 1 to 10 Mpc from the filament spine. Therefore the filament catalogue is split into two populations: short filaments with lengths shorter than 9 Mpc, and long filaments with lengths longer than 20 Mpc.

Short and long filaments

I computed the average profiles of all the short ($L_{\text{f}} < 9$ Mpc) and long filaments ($L_{\text{f}} \geq 20$ Mpc), respectively $\mathcal{S}$ and $\mathcal{L}$ profiles hereafter. Despite a larger number of short filaments (2846 vs 611), the average $\mathcal{S}$ and $\mathcal{L}$ profiles are computed from approximately the same number of segments (respectively 4733 and 4129). Consequently, short filaments are statistically made of less segments than long filaments: the mean number of segments per filament are $\bar{N}^{\mathcal{S}}_{\text{seg}} = 1.7$ for short and $\bar{N}^{\mathcal{L}}_{\text{seg}} = 6.5$ for long.

The following paragraphs present a study of short and long filaments by using Kolmogorov-Smirnov (KS) statistical tests. First, the measured $\mathcal{S}$ (resp. $\mathcal{L}$) profile is compared with an average bootstrap profile computed from the complementary set of segments, i.e. the subset of profiles whose segments do not belong to the $\mathcal{S}$ (resp. the $\mathcal{L}$) population. The KS is used to test the null hypothesis which assumes that the $\mathcal{S}$ and the related bootstrap profiles (resp. the $\mathcal{L}$ and the related bootstrap profiles) are drawn from the same parent distribution. This procedure is repeated 1000 times in order to have a distribution of p-values that takes into account the statistical properties of the complementary population. The resulting p-value distributions are presented in Fig. 4.8, for the short and long populations respectively in the left and right panels. These are found to be always smaller than 6×10^{-3} and 4×10^{-6}, respectively for each population, indicating that the density profiles of short and long filaments can not be randomly reproduced. Therefore, these results are a strong indication that there are at least two populations in the total set of filaments.

Finally, a unique two-sample KS test is performed to directly compare the $\mathcal{S}$ and $\mathcal{L}$ profiles. The resulting p-value of 5.9×10^{-11} is a statistical confirmation that the two populations of filaments have different average profiles.

The average short and long profiles of the Magneticum, TNG300-2 and TNG100-2 filaments were also computed. To do so, I followed the same procedure as for the reference TNG300-1, i.e. for each simulation the filament catalogue was split in thin bins of length having the same number of segments, and the $\mathcal{S}$ and $\mathcal{L}$ populations were defined from the subset profiles that deviated by more than 2σ from the total average profile. Note that the significance of the deviations $D_{\text{subset-tot}}$ (defined in Eq. 4.2) strongly depends on the statistics of the corresponding filament catalogue, as the errors on the average profiles are sensitive to the number of

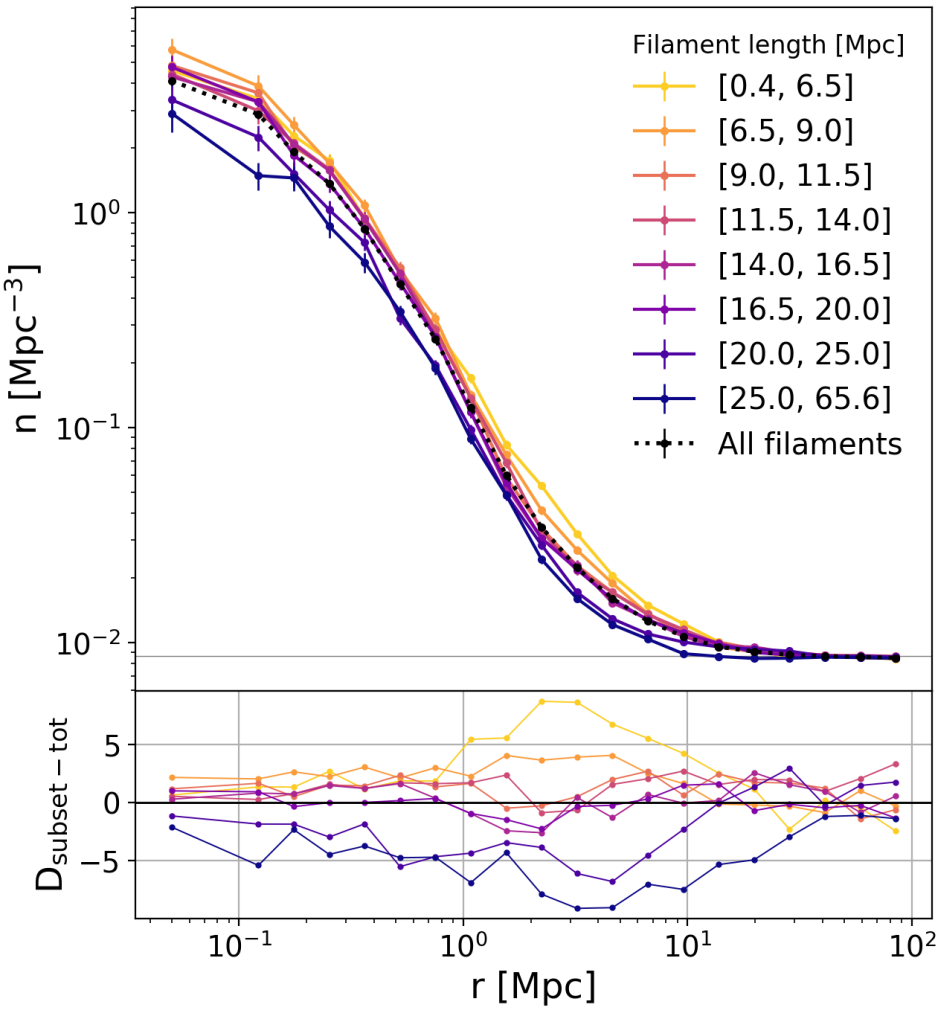

Figure 4.7: *Top:* Radial galaxy density profiles of filaments by bins of filament length for the reference catalogue (TNG300-1). The black curve corresponds to the average of all the filaments, regardless of their length, as presented in Sect. 4.1.1. The coloured curves correspond to the average of length-selected filaments. The gray horizontal line represents the background galaxy density of the simulation box. *Bottom:* Deviation from the mean $D_{\mathrm{subset-tot}}$ of the length-selected profiles (see definition in Eq. 4.2). This figure is extracted from Galárraga-Espinosa et al. (2020).

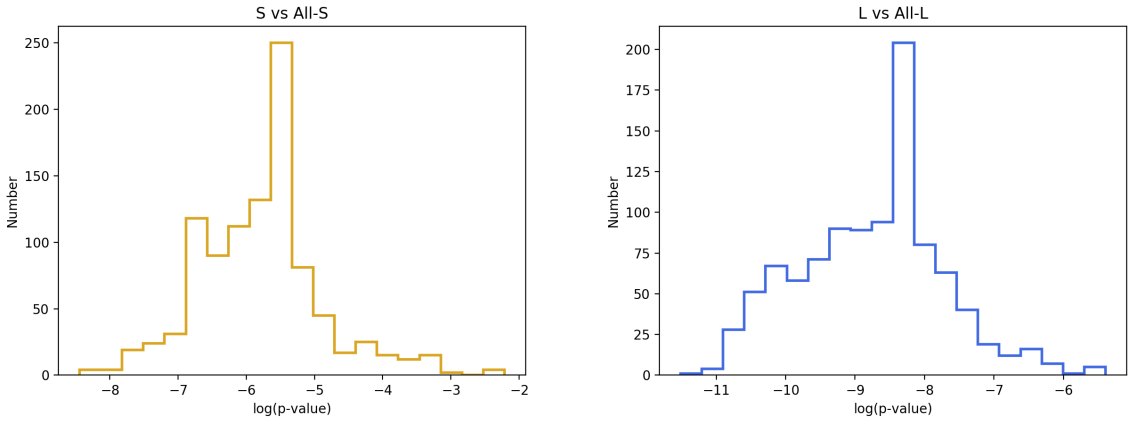

Figure 4.8: Distribution of p-values of the 1000 "bootstrap"-KS tests performed for the $\mathcal{S}$ and the $\mathcal{L}$ profiles (respectively in the left and right panels) of the TNG300-1 simulation. The bootstrap profile is computed by averaging randomly selected profiles (with replacement) among the complementary set of filaments (that is All-S and All-L, respectively for the two populations).

filament segments in each simulation ($\sigma \propto \sqrt{N}$). In order to take into account these effects and to be able to compare the deviations of catalogues with different statistics, the errors of the simulations were thus rescaled to those of TNG300-1 by replacing σ with $\sigma \times \sqrt{N/N^{\rm ref}}$ in Eq. 4.2. Here, N denotes the number of segments either in the subset bin or in the total catalogue of the corresponding simulation, and $N^{\rm ref}$ corresponds to the same quantities in TNG300-1, the reference simulation. The resulting galaxy density profiles with rescaled errors are presented in Fig. 4.9, and the derived lengths defining the $\mathcal{S}$ and $\mathcal{L}$ populations for each simulation are shown in Table 4.1. As expected, the length boundaries for the TNG300-2 profiles (14.4 and 27.2 Mpc) differ the most from the reference values (9 and 20 Mpc), and this is due to the significantly different filament length distributions of these simulations (as discussed in Sect. 3.2.)

A surprising result was found in the case of the Illustris-2 filaments, that is that their galaxy densities showed no dependency whatsoever with filament length. Indeed, the splitting of this catalogue in thin bins of length resulted in profiles that closely followed the total average (see lower right panel of Fig. 4.9). The shortest and longest bins did not show the expected trend (clearly exhibited by all the other simulations) and all the corresponding deviations displayed an oscillation around zero. This result is not due to the lower statistics of the Illustris-2 box, as the populations of filaments were clearly detected in the TNG100-2 simulation, whose box contains almost the same number of filaments as Illustris-2. Most likely, this surprising finding might be related with the specific model of baryonic physics of this simulation (Genel et al., 2014; Haider et al., 2016), which was already discussed in Sect. 4.1.1. This may be a hint that different populations of filaments are not only a natural result of cosmological accretion, but they also rely on the physics of baryons, which shapes the distribution of matter around filaments to a certain extent. Note that the interplay between DM and baryons in filaments will be discussed in details in Sect. 4.2.

That being said, Fig. 4.10 presents the derived $\mathcal{S}$ and $\mathcal{L}$ profiles of filaments in the TNG300-1, TNG300-2, Magneticum and TNG100-2 simulations. Orange and blue colours denote respectively short and long filaments. The $\mathcal{S}$ and $\mathcal{L}$ profiles of these four simulations are remarkably compatible, modulo the broader cores of the Magneticum profiles, and some resolution

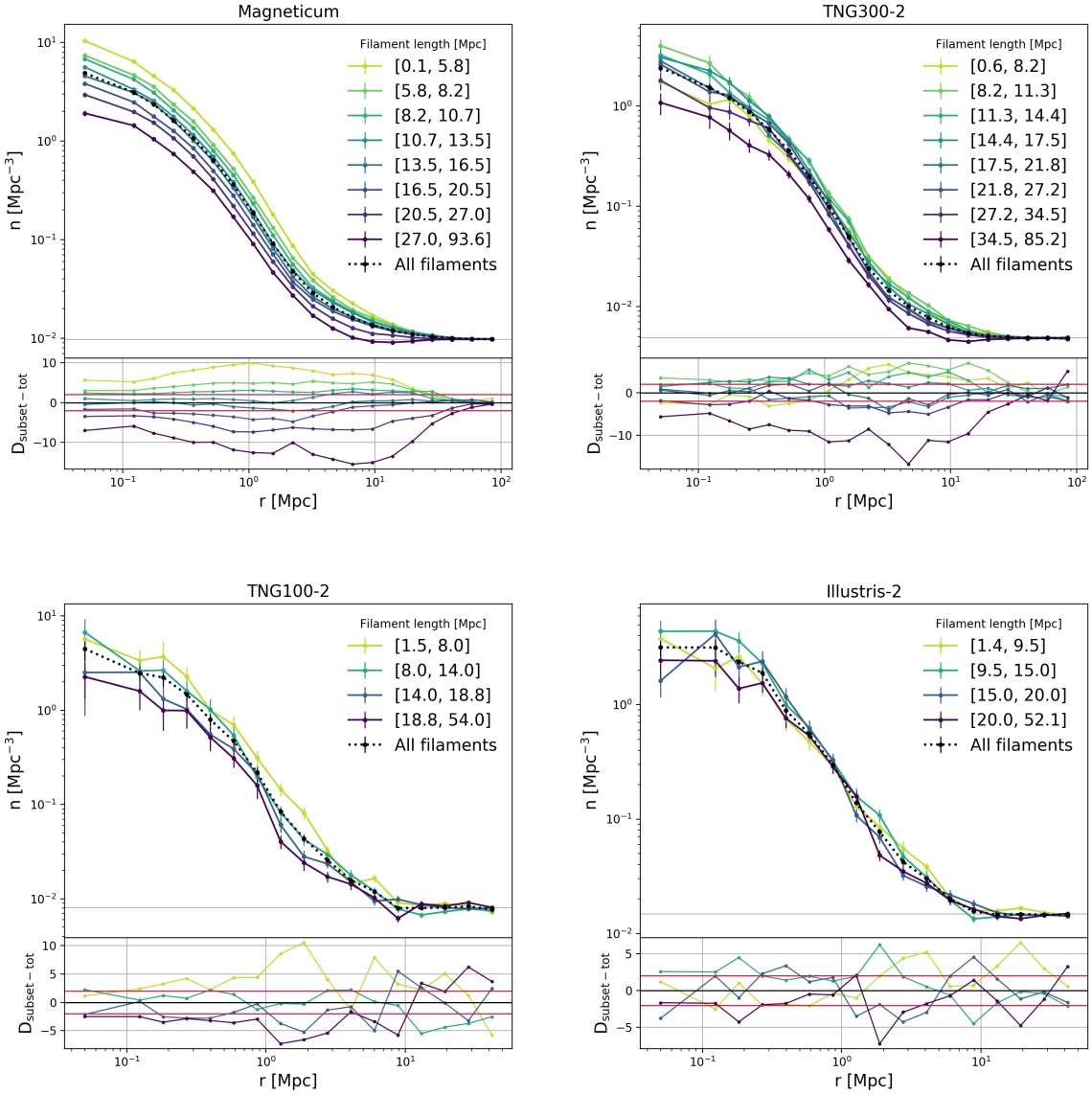

Figure 4.9: Same as Fig. 4.7 but for the Magneticum (upper left), TNG300-2 (upper right), TNG100-2 (lower left), and Illustris-2 (lower right panel) simulations.

Table 4.1: Definition of short and long filaments for the different simulations analysed in this work. The details concerning the simulations are shown in Table 2.1, and these related with the filament catalogues can be found in Table 3.1.

Simulation	Short [Mpc]	Long [Mpc]
TNG300-1	$L_{\rm f} < 9.0$	$L_{\rm f} \geq 20.0$
Magneticum	$L_{\rm f} < 10.7$	$L_{\rm f} \geq 16.5$
TNG300-2	$L_{\rm f} < 14.4$	$L_{\rm f} \geq 27.2$
TNG100-2	$L_{\rm f} < 8.0$	$L_{\rm f} \geq 18.8$

effects in the TNG300-2 filaments (as previously discussed in Sect. 4.1.1). In addition, the Magneticum profile also shows slightly higher density values at the core of the short filaments, which might be due to the different (but compatible) physical models of Magneticum with respect to the TNG suite (see Sect. 2.1 and particularly Table 2.2). Finally, the small deviations of the TNG100-2 filaments with respect to the other profiles may be caused by the very reduced statistics in this simulation box. Indeed, the short and long profiles in TNG100-2 result from the average of only $\sim$ 200 segments (vs 2200 in the reference TNG300-1), so the mean values may not be representative of the underlying density distribution.

Finally, let us present some characteristic radial scales for the TNG300-1 profiles. First, the radial extent of the $\mathcal{L}$ profile, $r_{\rm e}^{\mathcal{L}} \sim 19$ Mpc, computed with respect to the corresponding null-test, is found to be almost twice as small as that of the $\mathcal{S}$ profile, $r_{\rm e}^{\mathcal{S}} \sim 35$ Mpc. Likewise, the radius r_2, defined as the radius for which the galaxy density is twice the value of the background density $n_{\rm b}$, is smaller for long ($r_2^{\mathcal{L}} \sim 3$ Mpc) than for short filaments ($r_2^{\mathcal{S}} \sim 5$ Mpc). Qualitatively, similar results were found in the other simulations, namely that long filaments are radially less extended than short filaments, and thinner at all radial scales.

4.1.3 Analytical models

As mentioned previously, galaxies are the most direct (and accessible) tracers of the density field in observations. With the aim of having an analytical expression of the radial distribution of galaxies around cosmic filaments that can be useful in observational studies, this section presents the results of the fitting of the density profiles of the previous subsection to different analytical models. The following results focus on the TNG300-1 profiles, the reference.

Several analytic models can be proposed for the radial profiles of galaxy densities. Some of these are borrowed from the cluster literature, like the generalised Navarro, Frenk and White model (GNFW, Hernquist, 1990; Navarro et al., 1997; Nagai et al., 2007; Arnaud et al., 2010), presented in Eq. 4.3 ,

$$n^{\rm GNFW}(r) = \frac{n_0}{\left(\frac{r}{r_{\rm f}}\right)^{\alpha}\left[1+\left(\frac{r}{r_{\rm f}}\right)^{\gamma}\right]^{\frac{\beta-\alpha}{\gamma}}} + n_{\rm b}, \tag{4.3}$$

the Einasto model (Einasto, 1965; Ludlow, Angulo, 2017) of Eq. 4.4,

$$n^{\rm Einasto}(r) = n_0 \exp\left[-\left(\frac{r}{r_{\rm f}}\right)^{a}\right] + n_{\rm b} \tag{4.4}$$

and β models of Eq. 4.5 (Cavaliere, Fusco-Femiano, 1976; Arnaud, 2009; Ettori et al., 2013).

$$n^{\beta}(r) = \frac{n_0}{\left[1+\left(\frac{r}{r_{\rm f}}\right)^{\alpha}\right]^{\beta}} + n_{\rm b}. \tag{4.5}$$

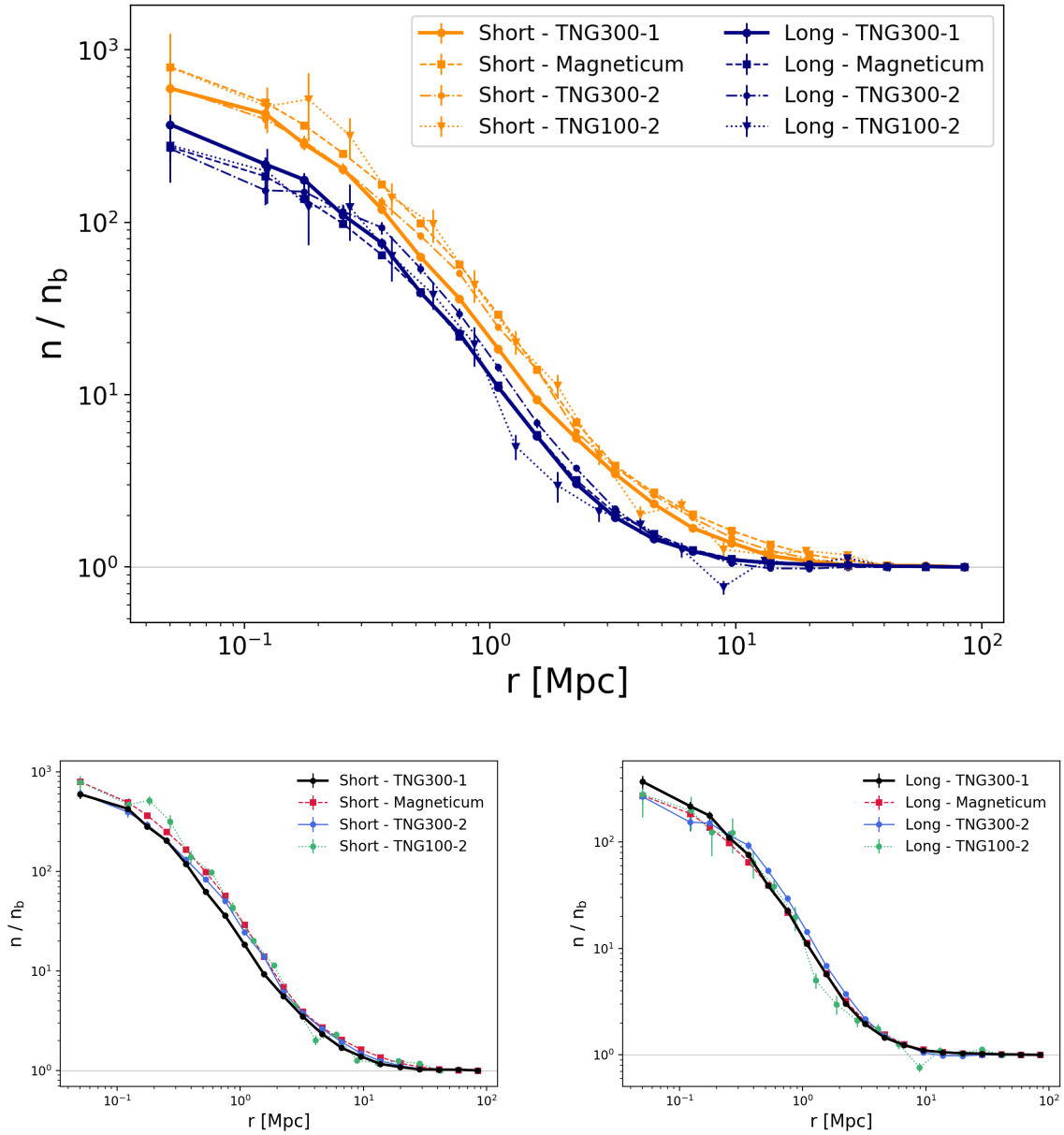

Figure 4.10: *Top*: Average galaxy density profiles around short (orange curves) and long filaments (in blue) for the reference TNG300-1 simulation, and the Magneticum, TNG300-2, and TNG100-2 simulations. The length limits defining short and long filaments in each simulation are presented in Table 4.1. For the sake of comparison, all the profiles have been rescaled by their respective background. This figure is extracted from Galárraga-Espinosa et al. (2020). *Bottom*: Same as top, but for clarity short and long filaments are presented separately, respectively in the left and right panels.

Table 4.2: Results of the MCMC fits on short filaments ($L_f < 9$ Mpc). The $\mathcal{S}$ galaxy density profile is adjusted using the models described in Eq. 4.3, 4.5, 4.6 and 4.7.

	n_0 [Mpc^{-3}]	r_f [Mpc]	α	β	γ	χ^2_ν
GNFW	$2.80^{+1.36}_{-0.726}$	$0.21^{+0.04}_{-0.04}$	$0.41^{+0.18}_{-0.25}$	$1.80^{+0.02}_{-0.02}$	$3.54^{+2.64}_{-1.03}$	**1.96**
β-profile	$5.36^{0.75}_{-0.65}$	$0.15^{+0.01}_{-0.01}$	$2.18^{+0.38}_{-0.28}$	$0.84^{+0.13}_{-0.13}$	-	**1.87**
PL2	$6.69^{+0.76}_{-0.71}$	$0.13^{+0.01}_{-0.01}$	$-0.18^{+0.15}_{-0.16}$	$1.82^{+0.02}_{-0.02}$	-	**1.88**
PL1	$6.07^{+0.52}_{-0.48}$	$0.14^{+0.01}_{-0.01}$	-	$1.82^{+0.01}_{-0.01}$	-	**1.85**

Table 4.3: Results of the MCMC fits on long filaments ($L_f \geq 20$ Mpc). The $\mathcal{L}$ galaxy density profile is adjusted using the models described in Eq. 4.3, 4.5, 4.6 and 4.7.

	n_0 [Mpc^{-3}]	r_f [Mpc]	α	β	γ	χ^2_ν
GNFW	$1.15^{+0.91}_{-0.35}$	$0.31^{+0.06}_{-0.06}$	$0.54^{+0.19}_{-0.31}$	$2.10^{+0.06}_{-0.04}$	$2.63^{+1.42}_{-0.79}$	**1.11**
β-profile	$3.15^{+0.72}_{-0.54}$	$0.21^{+0.02}_{-0.02}$	$1.60^{+0.31}_{-0.25}$	$1.35^{+0.29}_{-0.24}$	-	**1.27**
PL2	$1.96^{+0.37}_{-0.35}$	$0.25^{+0.04}_{-0.03}$	$0.28^{+0.13}_{-0.14}$	$2.14^{+0.04}_{-0.04}$	-	**1.12**
PL1	$2.50^{+0.26}_{-0.24}$	$0.21^{+0.02}_{-0.01}$	-	$2.09^{+0.03}_{-0.03}$	-	**1.26**

Other models are empirical expressions proposed to describe filaments, like the double power law (Aragón-Calvo et al., 2010b) of Eq. 4.6, hereafter called PL2,

$$n^{\mathrm{PL2}}(r) = \frac{n_0}{\left(\frac{r}{r_\mathrm{f}}\right)^{\alpha} + \left(\frac{r}{r_\mathrm{f}}\right)^{\beta}} + n_\mathrm{b} \tag{4.6}$$

or simply a single power law (PL1) of Eq. 4.7 (Colberg et al., 2005),

$$n^{\mathrm{PL1}}(r) = \frac{n_0}{1 + \left(\frac{r}{r_\mathrm{f}}\right)^{\beta}} + n_\mathrm{b}. \tag{4.7}$$

These models usually describe two regimes: small ($r \ll r_\mathrm{f}$) and large ($r \gg r_\mathrm{f}$) radii (where r_f is a characteristic radius), with a possibility of a transitional region between them in the GNFW case determined by the parameter γ. Each model listed above is characterised by slopes describing the small and large radii regimes. Notice that the names of the exponents in the formulae above have been chosen with the aim of easing the comparison of the models, and may not correspond to the usual labelling.

The average galaxy density profiles obtained for the total filament population, as well as those for the short and long filaments were fitted to these analytic models using Monte Carlo Markov Chains (MCMC). Figure 4.11 displays the reduced chi-squared values, χ^2_ν, resulting from the fit. First, one can observe that the fit to the Einasto profile (purple dashed line) always yields the highest χ^2_ν values indicating that it is not an adequate model to describe the galaxy density profiles of filaments. Also, note that the fits perform always worse ($\chi^2_\nu \sim 9$) for the entire filament set than for the short or the long filament populations considered separately (with respectively $\chi^2_\nu \sim 1.9$ and ~ 1.2), as expected for the two different filament populations. We point out that all the tested models perform equally well, in terms of their χ^2_ν values in Fig. 4.11, for the short or the long filaments populations.

Let us now focus on the parameters of the fits for the short, long and total populations. In the following, the Einsato model is discarded and the n_b parameter is fixed to the background galaxy density of the simulation box. The results of the MCMC exploration are presented in the

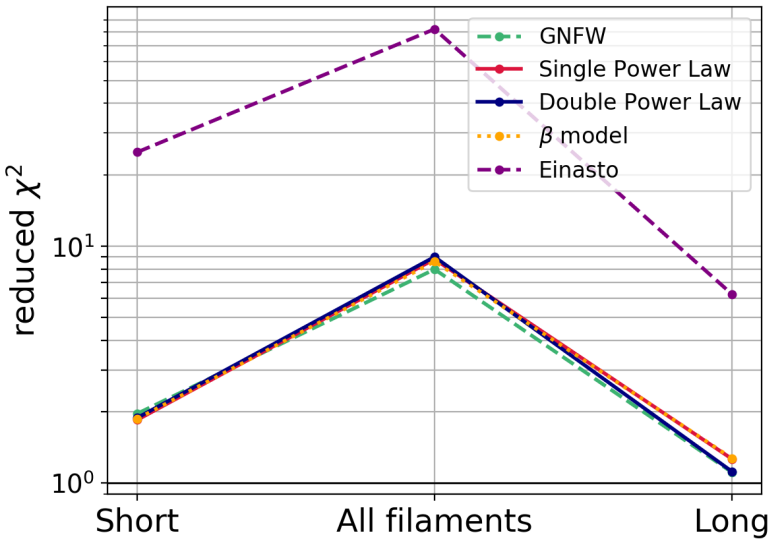

Figure 4.11: χ^2_ν results of the fitting of different models to short, all and long filaments in the TNG300-1 simulation. Each colour represents a different model. A segregation between the short and long populations is clearly seen: when mixed together, these populations are less well fitted than when taken separately. This figure is extracted from Galárraga-Espinosa et al. (2020).

Table 4.4: Results of the MCMC fits on the total population of filaments. The total galaxy density profile is adjusted using the models described in Eq. 4.3, 4.5, 4.6 and 4.7.

	n_0 [Mpc^{-3}]	r_f [Mpc]	α	β	γ	χ^2_ν
GNFW	$1.67^{+0.26}_{-0.19}$	$0.25^{+0.02}_{-0.02}$	$0.57^{+0.07}_{-0.08}$	$1.87^{+0.01}_{-0.01}$	$4.94^{+1.59}_{-0.98}$	**7.97**
β-profile	$3.93^{+0.27}_{-0.25}$	$0.16^{+0.01}_{-0.01}$	$2.43^{+0.19}_{-0.17}$	$0.77^{+0.06}_{-0.06}$	-	**8.60**
PL2	$5.18^{+0.30}_{-0.29}$	$0.14^{+0.01}_{-0.01}$	$-0.17^{+0.07}_{-0.08}$	$1.89^{+0.01}_{-0.01}$	-	**9.00**
PL1	$4.69^{+0.20}_{-0.20}$	$0.16^{+0.01}_{-0.01}$	-	$1.90^{+0.01}_{-0.01}$	-	**8.80**

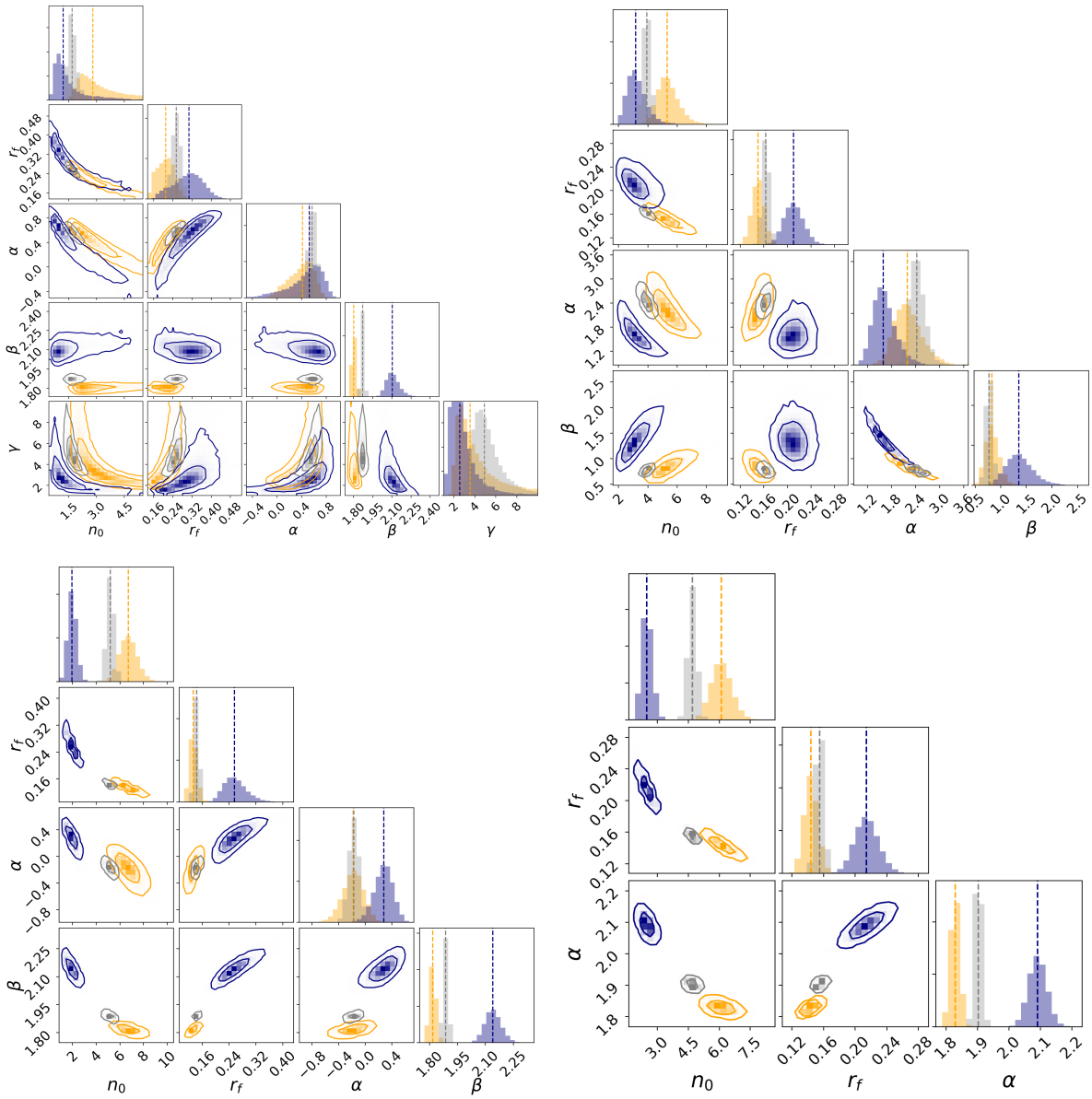

Figure 4.12: MCMC exploration of the distribution of parameters of four different models fitting the short (orange) and long (blue) filament populations. The total population (black) is displayed for comparison. *Top left*: the GNFW model presented in Eq. 4.3, *Top right*: the β-model of Eq. 4.5, *Bottom left*: the double power law of Eq. 4.6, and *Bottom right*: the single power law model (Eq. 4.7). These corner plots are extracted from Galárraga-Espinosa et al. (2020).

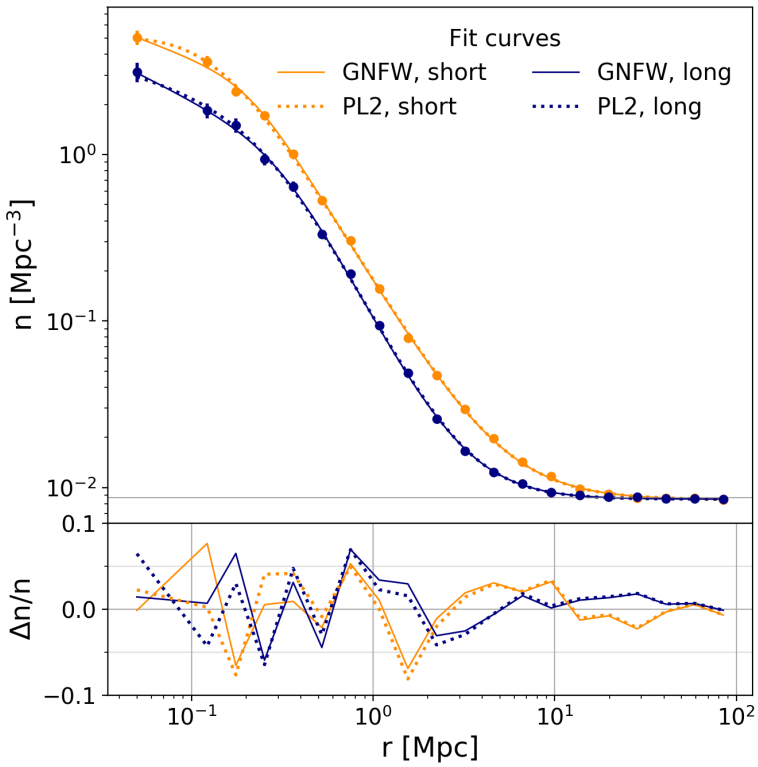

Figure 4.13: *Top*: Fit-curves of short (orange) and long (blue) filaments. Solid and dashed lines correspond respectively to the GNFW (Eq. 4.3) and the double power law (Eq. 4.6) models. The fit curves are plotted using the parameters of Tables 4.2 and 4.3. *Bottom*: Relative difference of the fits with respect to the data, defined as: $\Delta n/n(r) = [n^{data}(r) - n^{model}(r)]/n^{data}(r)$. This figure is extracted from Galárraga-Espinosa et al. (2020).

form of corner plots in Fig. 4.12 (orange is for short, blue for long, and black for all filaments). Overall, the parameters are rather well constrained except for the GNFW, where several degeneracies are observed (as expected for the model with the highest number of parameters). Note that fitting short and long filaments separately yields different and distinct parameters, confirming that these are two very different populations.

More quantitatively, the best-fit parameters (namely the median values of the posterior distributions) are presented in Tables 4.2 and 4.3 for the short and long filaments respectively. The parameters fitting the entire population are shown in Table 4.4. For all the models, short filaments have always lower $r_{\rm f}$ values than long filaments, meaning that the transition between the two radial regimes occurs at smaller scales for the short population. Moreover, long filaments have in general steeper slopes, especially at large radii, indicating a faster drop of the galaxy density with radial distance. This is in qualitative agreement with the findings of the previous subsections. As an example, I quantified the differences between the two populations for the case of the double power law model. Applying Eq. 4.2 to the n_0, $r_{\rm f}$, α and β best-fit values yielded, respectively, on a 5.7, 3.3, 2.7 and 7.2 σ difference between short and long filaments.

These results can be put in context with the radial DM density profiles of filaments of Colberg et al. (2005), González, Padilla (2010), Aragón-Calvo et al. (2010b), and Rost et al. (2021), where it is shown that the DM density follows a power law of slope -2 at the outskirts of the filament. In this work, the density of galaxies around short and long filaments is found to follow outer slopes of roughly -1.82 and -2.14, suggesting that, at the outskirts of the filament, galaxies follow the DM skeleton. This will be proven in the next Section (Sect. 4.2) with the study of DM density profiles of short and long filaments.

Finally, the upper panel of Fig. 4.13 displays the data points and the models obtained using the best-fit parameters of the double power law and the GNFW model plotted in dotted and solid lines, respectively. These two models illustrate a case where parameters are well constrained (double power law) and another with significant degeneracies (GNFW). In the lower panel of this figure, the relative difference between the data and the model, defined as $\Delta n/n(r) = [n^{\rm data}(r) - n^{\rm model}(r)]/n^{\rm data}(r)$, is presented. Note that both models fit well the data, in agreement with the χ^2_ν values of Fig. 4.11. The largest relative difference reaches 8% and is observed in the inner part of the filament. Beyond 2 Mpc from the spine of the filaments, the relative difference is less than 4% for both the GNFW and the double power law models, which additionally agree together quite well at these radii.

4.2 DM, gas, and stars

The study of the galaxy distribution around filaments presented in the previous Section has shown that the galaxy number density is the highest near the core of filaments, and that the density decreases with increasing radial distance. Two filament populations were identified: the short ($L_{\rm f} < 9$ Mpc), which are denser and puffier ($r_2 \sim 5$ Mpc), and the long ones ($L_{\rm f} \geq 20$ Mpc), less dense, thinner ($r_2 \sim 3$ Mpc).

Given that galaxies are biased tracers of the density field, it is natural to investigate what is the profile of filaments in terms of the total distribution of matter. Thus, this Section presents a study of the densities of DM, gas, and stars around the cosmic filaments of the TNG300-1 simulation. In a similar fashion as for galaxy number densities (Sect. 4.1), the distribution of matter is probed by computing radial profiles centred on the filament spines. The resulting DM,

gas and stellar density profiles are shown in Sect. 4.2.1. Moreover, the relative distribution of these matter components around filaments is also investigated, and a special focus is given to the fraction of baryons. This study is presented in Sect. 4.2.2.

4.2.1 Radial densities

Method

The full snapshot of the TNG300-1 box at $z = 0$ contains $14,454,722,210$ DM particles, the same number of gas cells, and $711,967,677$ star particles. Running the analysis on this extremely large amount of information is computationally very expensive and time consuming, so in order to compute the density profiles in reasonable computing time, the DM, star particles, and the gas cells were sampled by randomly selecting one out of 1000 (the resulting densities were then rescaled by this factor). This sub-sampling factor turned out to be a good compromise between computational speed and precision. For example, radial density distributions of stars in filaments computed from a dataset with a sub-sampling factor of 50 differ by no more than 4%. Moreover, performing the analysis on different random extractions gave stable results, so this sub-sampling does not undermine the statistical conclusions presented in the following.

The density profiles of the matter component i (i = DM, gas, or stars) around filaments were computed by averaging the profiles of individual filaments so that, for a number $N_{\rm fil}$ of filaments, the average density of i at a distance r from the filament spines is given by:

$$\rho_i(r) \equiv \frac{1}{N_{\rm fil}} \sum_{f=1}^{N_{\rm fil}} \rho_i^{{\rm fil},f}(r). \tag{4.8}$$

Here $\rho^{{\rm fil},f}(r)$ denote the individual profiles, which are obtained as follows. For a given filament f, the density of the matter component i is computed by summing its mass enclosed in hollow cylinders around all the $N_{\rm seg}$ segments belonging to the filament. Then, this mass is divided by the corresponding volume, as shown by:

$$\rho_i^{{\rm fil},f}(r_k) = \frac{\sum_{s=1}^{N_{\rm seg}} M_i^s(r_k, r_{k-1})}{\pi(r_k^2 - r_{k-1}^2) \sum_{s=1}^{N_{\rm seg}} l^s}, \tag{4.9}$$

where, for the filament segment s, the quantity $M_i^s(r_k, r_{k-1})$ is the mass enclosed within the cylindrical shell of outer radius r_k and of thickness $r_k - r_{k-1}$, centred on the segment axis, and $\sum_{s=1}^{N_{\rm seg}} l^s$ corresponds to the total length of the filament. Therefore, the total density of matter at a distance r_k from the filament spine can be simply computed by summing the individual contributions of DM, gas and stars, such that:

$$\rho_{\rm TOT}(r_k) = \rho_{\rm DM}(r_k) + \rho_{\rm gas}(r_k) + \rho_*(r_k). \tag{4.10}$$

Moreover, since this study focuses on the main stem of filaments and not on their connection with nodes, all the filament segments lying closer than $3 \times R_{200}$ to the centre of the CPmax points, the topological nodes found by `DisPerSE`, are excluded from the following analysis.

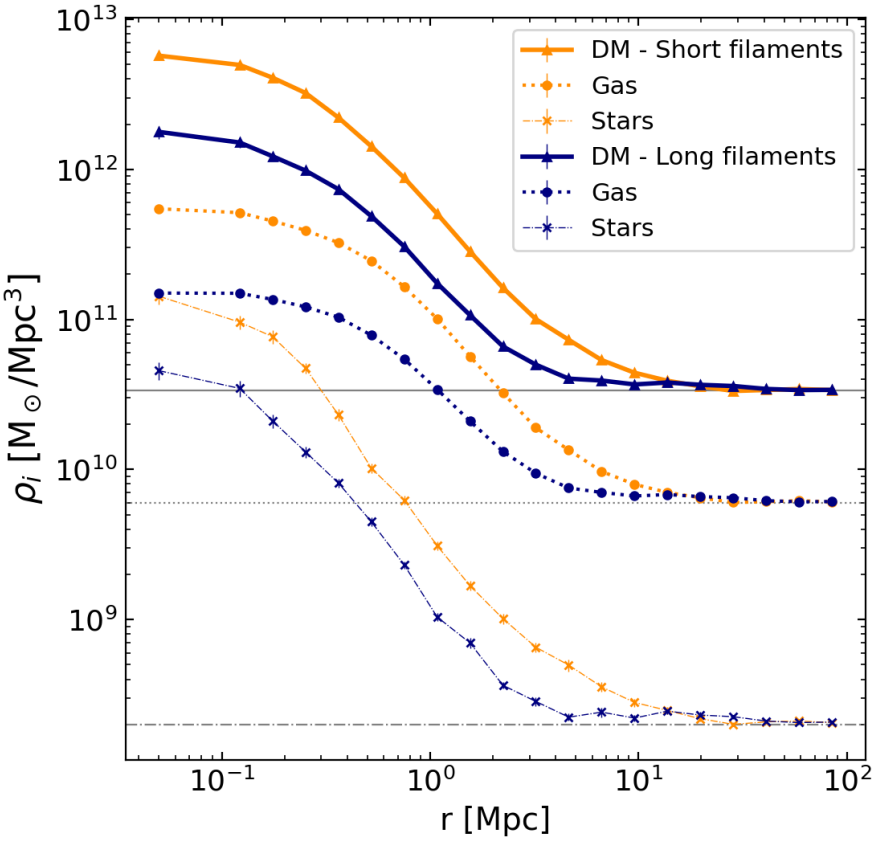

Figure 4.14: Radial densities of DM (solid lines with triangles), gas (dotted lines with circles) and stars (dash-dotted lines with crosses) around filaments. Results for the short and long populations are presented respectively on orange and blue. The horizontal gray lines correspond to the densities of the matter component i in the full simulation box, $\rho_i^{\rm box}$.

Section 4.1 showed that filaments can be classified into two populations: short ($L_f < 9$ Mpc) and long ($L_f \geq 20$ Mpc) filaments. From the total of 5550 filaments of the TNG300-1 catalogue (details in Table 2.1), 2846 are short and 632 are long. In the following, only the filaments whose density profile is complete (i.e. whose density profile does not have empty bins) are kept. Due to the sampling of the DM particles and gas cells described above, this selection results on respectively 969 and 446 short and long filaments. Though strongly reduced, the final number of filaments of each population is still large enough to perform a statistical analysis. Moreover, in order to estimate the statistical variance of the densities around these limited samples of filaments, all the error bars are computed by using the bootstrap method over the final number of filaments in each population.

DM, gas and stellar density profiles

The density profiles of DM, gas and stars around short and long filaments, from their spine up to large radial distances of $\sim$ 100 Mpc are presented in Fig. 4.14. First of all, note that, at large radial scales, all the curves of Fig. 4.14 reach their respective background density (gray horizontal lines) computed as $\rho_i^{\rm box} = M_i^{\rm TOT}/V_{\rm box}^{\rm TOT}$.

Table 4.5: Density values at the cores of short and long filaments. These values correspond to the first bins of the curves of Fig. 4.14 ($r = 0.05$ Mpc). They are all expressed in $M_\odot/Mpc^3$.

	Short filaments	Long filaments
ρ_{DM}	$(5.72 \pm 0.37) \times 10^{12}$	$(1.78 \pm 0.16) \times 10^{12}$
ρ_{gas}	$(5.46 \pm 0.26) \times 10^{11}$	$(1.50 \pm 0.09) \times 10^{11}$
ρ_*	$(1.43 \pm 0.17) \times 10^{11}$	$(4.55 \pm 0.64) \times 10^{10}$

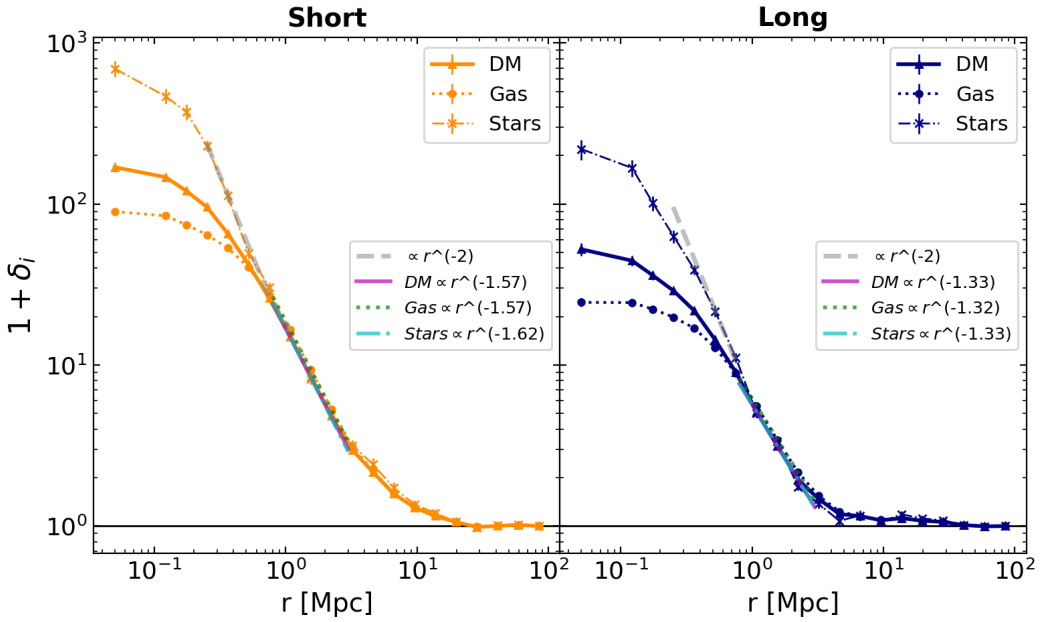

Figure 4.15: Over-density profiles of DM (solid lines with triangles), gas (dotted lines with circles) and stars (dash-dotted lines with crosses) for short and long filaments, respectively in orange and blue. The pink, green, and light blue lines denote respectively the fitting results of the DM, gas and stellar profiles in the $r \in [0.7, 3]$ Mpc range (where the profiles lie on top of each other). For reference, a generic line of slope -2 is presented in gray.

Similarly to the galaxy number density profiles of Sect. 4.1, when approaching the cores of filaments, the densities of these three matter components increase, as expected, and peak at the innermost region of the filaments. Moreover, as in Sect. 4.1, a clear difference is seen between the densities in the different filament populations. For example, at their centre, short filaments are respectively 3.2, 3.6, and 3.1 denser than long filaments in DM, gas and stars. The exact density values in this first bin in short and long filaments are reported in Table 4.5.

Over-densities

Let us now focus on the relative distribution of DM, gas and stars around filaments by looking at their over-density profiles. These are computed by dividing the densities of Fig. 4.14 by their respective background value:

$$1 + \delta_i(r) = \frac{\rho_i(r)}{\rho_i^{box}}. \tag{4.11}$$

The over-density profiles of DM, gas and stars are presented in Fig. 4.15. Qualitatively, the overlap between the three $1+\delta_i$ profiles is striking at large distances from the cores of filaments.

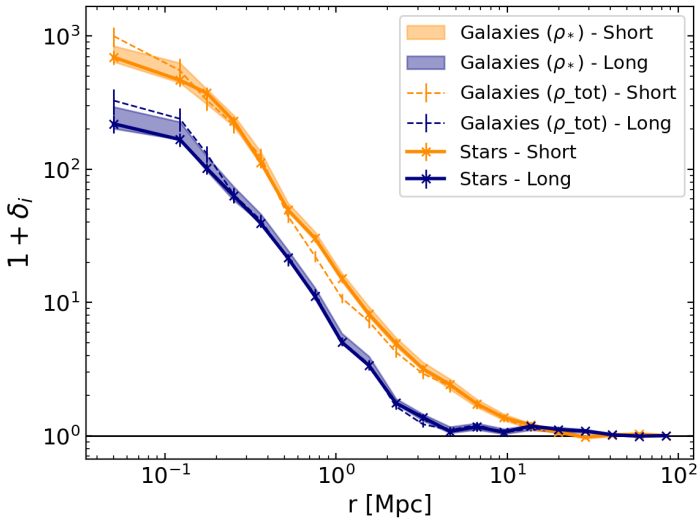

Figure 4.16: Comparison of the over-density profiles of stars (same as in Fig. 4.15), to these of galaxy mass (stellar and total), for short and long filaments (respectively in orange and blue).

This shows that, at these distances, gas and stars closely follow the DM distribution and fall, unperturbed, into the DM gravitational potential wells.

Nevertheless, when approaching the cores of filaments, gas and stars clearly depart from the DM over-density. This departure happens at $r \sim 0.7$ Mpc in both short and long filaments. Section 4.2.2 will show that this radial scale marks a well defined regime in the baryon fraction profiles of filaments. Notice that this scale is smaller than the typical filament thickness at the outskirts of clusters (which are excluded in this work) of Rost et al. (2021), showing that the filamentary structures connected to clusters of galaxies are different from the main stems of cosmic filaments, as expected for structures in those extremely dense environments of cluster outskirts.

A special attention is given to the slopes of the profiles. Figure 4.15 shows that, at intermediate distances from the spines ($r \sim 0.7 - 3$ Mpc) where they all lie on top of each other, the DM, gas, and stellar profiles exhibit very similar slopes. Indeed, the slopes of the profiles of these three matter components in the $r \sim 0.7-3$ Mpc radial regime are encompassed within the thin intervals of $[-1.62, -1.57]$ (short filaments) and of $[-1.33, -1.32]$ (long filaments). Note that the intervals of the short and long populations do not overlap and that the slopes of short filaments are always steeper than those of long. This will be interpreted in Sect. 4.3 by looking at the environment of these different filament populations.

From $r \sim 0.7$ Mpc and down to ~ 0.2 Mpc, the profiles of stars deviate, and they become steeper as their slope approaches a function $\propto r^{-2}$. Figure 4.16 compares the over-density profile of stellar mass to these of galaxy mass (stellar and total), showing that the mass distribution of stars around filaments is essentially the same as that of galaxies (as expected since stars trace the position of galaxies). Therefore, the observed -2 slope is easily explained by looking at the results of the distribution of galaxies around filaments of Sect. 4.1.3 (see e.g. the PL1 and PL2 slopes of Tables 4.2 and 4.3). This is also in agreement with the analyses of Aragón-Calvo et al. (2010b) in N-body and hydro-dynamical simulations, and Bonjean et al. (2020) in observations.

The profiles of DM and gas of Fig. 4.15, however, do not exhibit the same -2 slope in

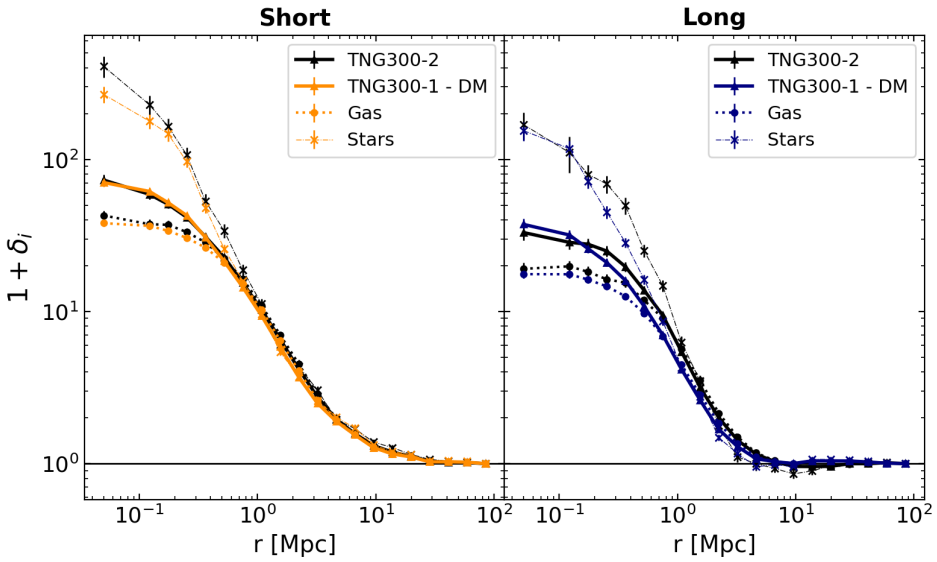

Figure 4.17: Comparison between the matter over-density profiles of the TNG300-1 box (high resolution), and the TNG300-2 one (lower resolution).

the $0.2 < r < 0.7$ Mpc range, but show a gentler slope instead. It is interesting to note that this differs from the trends of DM and gas found in intracluster bridges and in those filaments, sometimes called 'spider-legs', that are found at the very outskirts of massive clusters (e.g. Colberg et al., 2005; Dolag et al., 2006; Rost et al., 2021). These filamentary structures do not belong to the main stem of cosmic filaments, and, as presented above, the regions at the outskirts of clusters are excluded from this analysis (within $3 \times R_{200}$).

All the results presented in this Section are independent from the resolution of the simulation. This was checked by running the same analysis in the TNG300-2 box, that corresponds to the medium resolution run of the TNG300 series. The comparison between the TNG300-1 and TNG300-2 profiles is shown in Fig. 4.17. Note that the mean profiles presented in this figure were computed by taking into account the totality of short and long filaments available in the TNG300-1 and TNG300-2 catalogues, i.e. the filaments having profiles with empty bins were also included. This prevents the comparison to be biased by filament selection effects coming from the initial sampling of DM particles, gas cells, and stars, see the method above. Apart from the (expected) slight enlargement of the filament cores due to the `DisPerSE` uncertainty in finding the position of the filament spines (see Sect. 4.1.1), the radial profiles of the TNG300-2 filaments are essentially the same as those of TNG300-1, i.e. the $1+\delta_i$ the values at the first radial bins of the two simulations are remarkably close, and the gas and stars departure from the DM over-density also happens at $r \sim 0.7$ in the TNG300-2 filaments.

4.2.2 Baryon fractions of cosmic filaments

Baryons (gas + stars) account for $\sim 15.7\%$ of the total budget of matter (Planck Collaboration et al., 2016a). Under the effect of gravity, they fall into the gravitational potential wells created by DM, following the cosmic skeleton. Nevertheless, due to their nature, baryons are subject to a variety of other processes besides gravity (e.g. feedback events and star formation). These processes taking place at smaller scales can sometimes alter the large scale distribution of

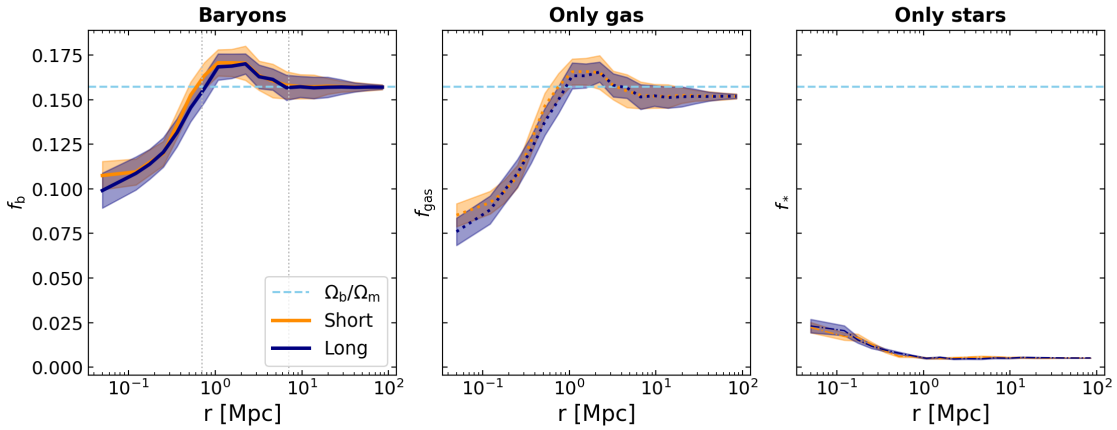

Figure 4.18: Baryon fraction radial profiles of filaments (first panel), and the individual contributions of gas and stars (second and third panels). The dashed horizontal line shows the cosmic value of $f_{\rm cosmic} = \Omega_{\rm b}/\Omega_{\rm m} = 0.157$.

baryons with respect to the underlying DM density field. In order to further investigate the relative distribution between dark and baryonic matter in filaments, this Section presents the study of the radial distribution of the baryon fraction, $f_{\rm b}(r)$, in these structures.

The radial profiles of the baryon fraction in filaments are computed by combining the densities presented in Sect. 4.2.1 in the following way:

$$f_{\rm b}(r) \equiv \frac{\rho_{\rm b}(r)}{\rho_{\rm TOT}(r)} = \frac{\rho_{\rm gas}(r) + \rho_*(r)}{\rho_{\rm DM}(r) + \rho_{\rm gas}(r) + \rho_*(r)}. \tag{4.12}$$

The resulting profiles are presented in the first panel of Fig. 4.18. The individual contributions of gas and stars, namely the gas fraction ($f_{\rm gas}$) and stellar fraction profiles (f_*), are shown in the second and third panels of this figure. Note that the equality $f_{\rm b} = f_{\rm gas} + f_*$ holds at all radii.

As expected, the baryon fraction profiles of filaments converge to the cosmic value, $f_{\rm cosmic} = \Omega_{\rm b}/\Omega_{\rm m} = 0.157$ (Planck Collaboration et al., 2016a) at very large radii. A deviation from $f_{\rm cosmic}$ arises as we approach the cores of filaments. The departure from the cosmic value begins at a specific radial scale of $r \sim 7$ Mpc (outer gray vertical line) hereafter called $r_{\rm ext}$. While at the large radial distances of $r > r_{\rm ext}$ matter is essentially ruled by gravity and simply falls into the filament potential wells, at distances $r \leq r_{\rm ext}$ baryons stop following the cosmic fraction, showing that their distribution is altered by the mere presence of the filament. Moreover, it is interesting to note that the $r_{\rm ext}$ scale coincides well with the sharp increase of gas temperature in the filament temperature profiles of Fig. 5.10a. All this allows us to interpret $r_{\rm ext}$ as the radial extent to which baryonic processes taking place in filaments can affect the large-scale distribution of baryons. This interpretation is checked by computing the total baryon fraction (normalised to the cosmic value) enclosed within a cylinder of radius $r_{\rm ext}$ centred on the filament axis. This quantity is defined as:

$$F(r < r_{\rm ext}) \equiv \frac{f_{\rm b}(r < r_{\rm ext})}{f_{\rm cosmic}} = \frac{\displaystyle\int_0^{r_{\rm ext}} r \left[\rho_{\rm gas}(r) + \rho_*(r)\right] dr}{f_{\rm cosmic} \times \displaystyle\int_0^{r_{\rm ext}} r\, \rho_{\rm TOT}(r)\, dr}, \tag{4.13}$$

and the resulting values for the average short and long filaments are respectively $1.01^{+0.08}_{-0.07}$ and $1.01^{+0.06}_{-0.06}$, i.e. compatible with one.

Remarkably, short and long filaments exhibit the same value of $r_{\rm ext} \sim 7$ Mpc and quite overlapping baryon fraction profiles at these large distances. This means that, at $r > r_{\rm ext}$, the distribution of gas and stars with respect to that of DM is independent from the specific absolute density ranges (Fig. 4.14 and Sect. 4.2.1), also from the large scale environments particular to each filament population (see Sect. 4.3). Potentially, this similarity between filament populations suggests that the baryonic processes responsible for modifying the baryonic density profile from that of the DM are mostly environment independent, i.e. likely depend on the galaxy properties. This is in line with previous studies showing that AGN feedback can modify the distribution of baryons up to several Mpc away from the AGN (see e.g. Chisari et al., 2018).

At radii $r \leq r_{\rm ext}$, i.e. inside the filaments, the baryon fraction profiles show two very different regimes. Let us identify them from the inner to the outer regions. Firstly, a clear baryon depletion is seen at the cores, as shown by the sharp decrease of the baryon fractions. This depletion is quantified by a factor of $Y_{\rm b} \equiv f_{\rm b}/f_{\rm cosmic} \sim 0.68$ and 0.63 respectively in the innermost region of short and long filaments. Note the similar $Y_{\rm b}$ values between the two different filament populations. For comparison, these values are much lower than the usual depletion factor in cores of clusters of galaxies, $Y_{\rm b} \sim 0.85$ (e.g. Kravtsov et al., 2005; Planelles et al., 2013). Secondly, an excess of baryons with respect to the cosmic value is observed. This excess is characterised by a bump in the profiles. The transition between these two regimes happens at a radius of $\sim$ 0.7 Mpc, that is hereafter called $r_{\rm int}$ and that is identified as the intersection point between $f_{\rm b}$ and $\Omega_{\rm b}/\Omega_{\rm m}$ (inner gray line in Fig. 4.18). Note that this distance is also consistent with the radius where the DM and gas over-density profiles of Fig. 4.15 separate. The two different regimes identified above can be understood by focusing only on the gas component. Indeed the fraction of gas $f_{\rm gas}$ in filaments (second panel of Fig. 4.18) shows the same features as the total fraction of baryons, i.e. a depletion at the cores ($r < r_{\rm int}$), and a bump in the $[r_{\rm int}, r_{\rm ext}]$ radial range. This resemblance between the total fraction and that of gas is not surprising, given that gas represents on average $\sim 78\%$ of the baryonic mass in the innermost bin, and $\sim 96\%$ in the $[r_{\rm int}, r_{\rm ext}]$ interval, thus corresponding to the most abundant form of baryonic matter in filaments.

Before analysing the two regimes identified above, let us comment on the stellar fractions of filaments, f_* (the third panel of Fig. 4.18). These show a flat trend in the profiles at large distances from the spines of filaments, and contrary to gas, f_* increases at the filament cores ($r < r_{\rm int}$). This increase of the fraction of stars at the cores reflects well the results of previous studies of galaxies which have found that cores of filaments are more populated by massive galaxies than more remote regions (Malavasi et al., 2017; Laigle et al., 2018; Kraljic et al., 2018, 2019; Bonjean et al., 2020). Note that further studies of the properties of galaxies in filaments will be presented in Chapter 6.

Analysis of the gas depletion at $r < r_{\rm int}$

Gas depletion can be easily understood by analogy with the case of clusters of galaxies (e.g. Kravtsov et al., 2005; Puchwein et al., 2008; Planelles et al., 2013; Le Brun et al., 2014; Barnes et al., 2017; McCarthy et al., 2017; Chiu et al., 2018; Henden et al., 2020, and references therein). In these structures, the decrease of the gas fraction is due to the conversion of gas into stars (that lowers the gas fraction and enhances the stellar one), and the ejection of gas due to feedback events (which displace, disperse, and redistribute the gas, e.g. Cen, Ostriker, 2006). The following paragraphs investigate whether feedback effects from AGNs are potentially powerful enough to deplete the cores of filaments by ejecting their gas away. A funda-

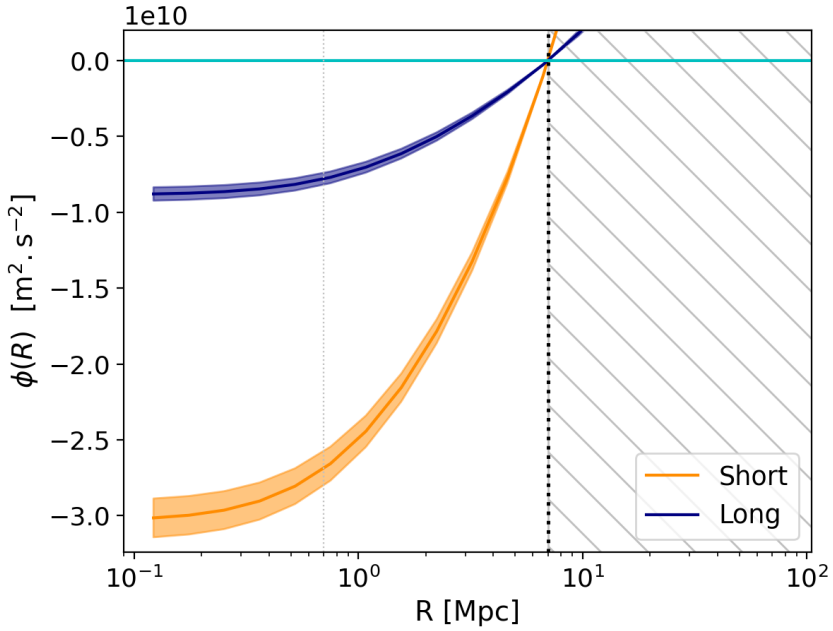

Figure 4.19: Gravitational potential (Eq. 4.17) felt by a test mass inside short (orange) and long filaments (blue). The limit between inside and outside for the computation of the gravitational potential is set to $R_{\rm lim} = r_{\rm ext} = 7$ Mpc. The outside regions are hatched in gray.

mental requirement for filamentary gas ejection is that the injected energy (coming from the feedback of AGNs inside filaments) be higher than the gas gravitational potential energy (i.e. competition between pushing and pulling of gas).

Firstly, the gravitational potential energy of a test particle of mass $m_{\rm part}$ falling towards the filament is:

$$E_p(R) = m_{\rm part}\ \phi(R). \tag{4.14}$$

In this equation, $\phi(r)$ denotes the gravitational potential felt by the particle at a distance R from the spine of the filament. The gravitational potential is computed by applying the Gauss theorem to the total matter over-density, $\Delta\rho_{\rm TOT} = \rho_{\rm TOT} - \rho_{\rm bkg}$, in the closed volume defined by a cylinder whose axis corresponds to the filament spine. In the following, let us assume that the matter density is invariant by rotation around the axis of the filament, and by translation along this axis, so that $\Delta\rho_{\rm TOT}$ depends only on the radial coordinate. Within this hypothesis, the result of the Gauss theorem in polar coordinates reads

$$\overrightarrow{g} = \frac{-2G}{r}\int_0^r {\rm d}r'\ r'\ \Delta\rho_{\rm TOT}(r')\,\overrightarrow{e_r}, \tag{4.15}$$

where $\overrightarrow{g}$ is the gravitational field, and G is the universal gravitational constant. The gravitational field $\overrightarrow{g}$ is just the gradient of the potential ϕ. Therefore the expression above (Eq. 4.15), allows us to compute ϕ by numerically integrating the equation

$$\overrightarrow{g} = -\overrightarrow{\nabla}\phi, \tag{4.16}$$

which yields the following expression:

$$\phi(R) = 2\,{\rm G}\int_0^R {\rm d}r\,\frac{1}{r}\int_0^r {\rm d}r' r' \Delta\rho_{\rm TOT}(r') + \phi_0. \tag{4.17}$$

The integration constant, ϕ_0, is chosen so that the potential at the limit between the interior and the exterior of the filament is zero, such that $\phi(R_{\rm lim}) = 0$. Thus, Eq. 4.17 gives:

$$\phi_0 = -2\,\mathrm{G} \int_0^{R_{\rm lim}} \mathrm{d}r\, \frac{1}{r} \int_0^{r} \mathrm{d}r' r' \Delta\rho_{\rm TOT}(r'). \tag{4.18}$$

Based on the studies of the baryon fractions profiles presented above (see Fig. 4.18), the limit between the interior and the exterior of the filament is set to $R_{\rm lim} = r_{\rm ext} = 7$ Mpc. The resulting $\phi(R)$ profiles for short and long filaments are shown in Fig. 4.19. As expected, the gravitational potential of short filaments is deeper than that of the long filaments. This is due to the higher density values of the former with respect to the later, e.g. three times higher at the cores, see Fig. 4.14. Note that this factor of three between the densities of short and long filament cores is also reflected in the values of the gravitational potential. Physically, the calculations presented above show that, in order to be displaced outside of filaments, baryonic gas particles need to acquire a kinetic energy that is bigger than their potential energy in the depth of the gravitational well

$$|\Delta\phi| \equiv |\phi(0) - \phi(R_{\rm lim})| = |\phi_0|. \tag{4.19}$$

By construction, the values of $|\Delta\phi|$ can by read directly from the first bin of Fig. 4.19.

Secondly, the amount of energy (per unit of gas mass) injected by AGN feedback events into a cylindrical shell of thickness $|r_{k-1} - r_k|$ around the axis of the filament is defined as

$$\varepsilon_{\rm AGN}(R) \equiv \frac{E^{\rm inj}_{\rm AGN}(R)}{M_{\rm gas}(R)}, \tag{4.20}$$

where $R \in [r_{k-1}, r_k]$. Assuming that filaments are cylinders of length $L_{\rm fil}$, homogeneous along their axis, the numerator in this equation is given by:

$$E^{\rm inj}_{\rm AGN}(R) = \int_0^{L_{\rm fil}} \mathrm{d}l \int_0^{2\pi} \mathrm{d}\theta \int_{r_{k-1}}^{r_k} \mathrm{d}r\, r\; e^{\rm kin}_{\rm AGN}(r), \tag{4.21}$$

where $e^{\rm kin}_{\rm AGN}$ is the energy per unit volume, which corresponds to the cumulative amount of kinetic AGN feedback energy (total over the entire lifetime of the corresponding black-holes) injected into the surrounding gas, divided by the volume of the cylinder centred on the filament axis. For reference, the $e^{\rm kin}_{\rm AGN}$ profiles are presented in the first panel of Fig. 4.20. Note that, from the two possible AGN energy injection modes available in the TNG model (i.e. thermal and kinetic), only the kinetic mode (field `BHCumEgyInjectionRM` in the PartType5 catalogue) is studied here. It was indeed shown that it is the only mode able to expel gas away from the centre of galaxies (Weinberger et al., 2018; Terrazas et al., 2020; Quai et al., 2021) thanks to the release of mechanical energy into the gas (via winds in random directions). On the other hand, as shown by Weinberger et al. (2018), the AGN thermal injection mode does not efficiently couple with the gas in the galaxy environment, and thus it does not alter its spatial distribution (see also Terrazas et al., 2020; Quai et al., 2021). Of course, this thermal injection mode contributes to heating the gas in the inter-galactic medium in the filament.

The denominator of Eq. 4.20 is just the integral of the gas density over the cylindrical volume:

$$M_{\rm gas}(R) = \int_0^{L_{\rm fil}} \mathrm{d}l \int_0^{2\pi} \mathrm{d}\theta \int_{r_{k-1}}^{r_k} \mathrm{d}r\, r\, \rho_{\rm gas}(r). \tag{4.22}$$

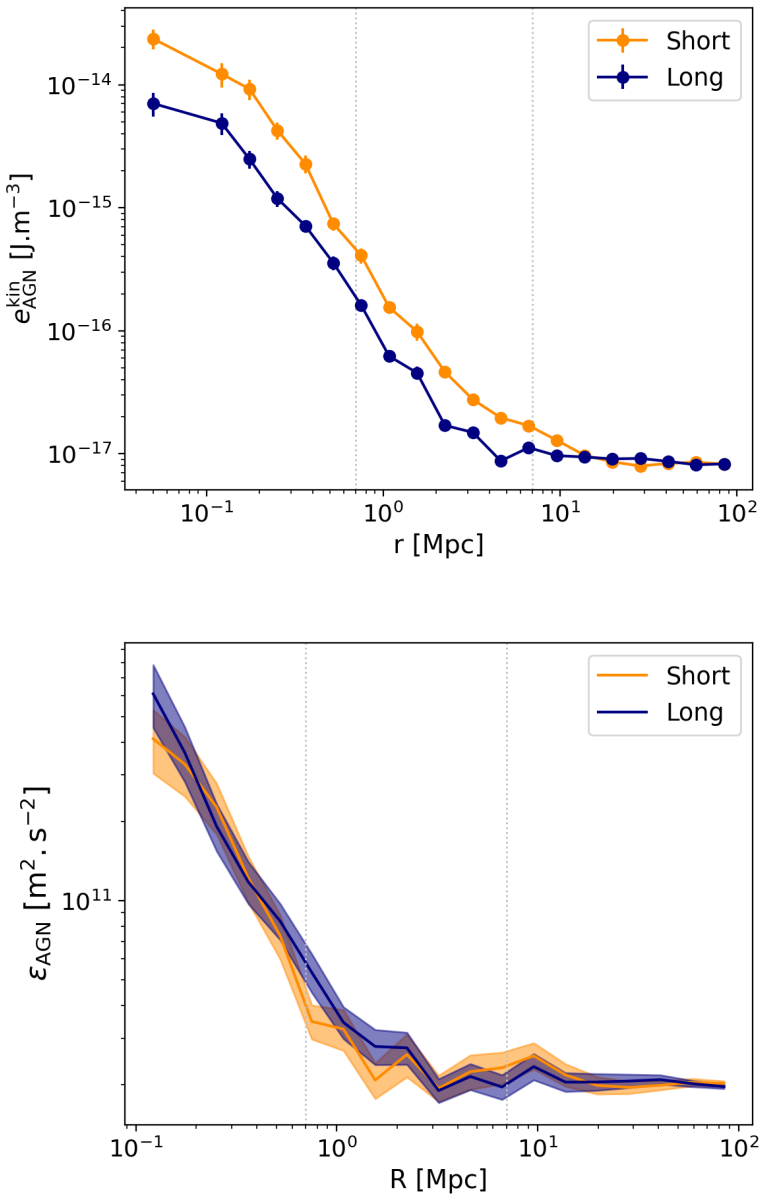

Figure 4.20: Top: Average radial profiles of kinetic energy per unit volume injected by AGNs into the medium. **Bottom:** Radial profiles of the kinetic energy by unit of gas mass injected by AGNs into the medium (see Eq. 4.23). The inner and outer vertical dashed lines correspond respectively to the $r_{\rm int}$ and $r_{\rm ext}$ radii.

Thus, the final expression of $\varepsilon_{\rm AGN}$ is:

$$\varepsilon_{\rm AGN}(R) = \frac{\int_{r_{k-1}}^{r_k} {\rm d}r\, r\, e^{\rm kin}_{\rm AGN}(r)}{\int_{r_{k-1}}^{r_k} {\rm d}r\, r\, \rho_{\rm gas}(r)}, \tag{4.23}$$

The resulting $\varepsilon_{\rm AGN}$ profiles are presented in the second panel of Fig. 4.20. Overall, the two filament populations have very similar profiles. This is due to the fact that the differences between short and long filaments shown by the $e^{\rm kin}_{\rm AGN}$ profiles (first panel) are compensated by the different gas masses of the two populations. This means that the potential efficiency of AGN feedback events relative to the gas distribution is quite the same in short and long filaments. Note, however, the slightly higher $\varepsilon_{\rm AGN}$ value at the inner cores of long filaments.

Let us finally investigate whether these feedback processes are potentially powerful enough to contribute to the gas depletion observed at the cores of filaments (see Fig. 4.18). This is done by comparing the values of $\varepsilon_{\rm AGN}$ to $|\Delta\phi|$, the depth of the gravitational potential well (see Eq. 4.19). The ratio between these two quantities, $\varepsilon_{\rm AGN}/|\Delta\phi|$ is presented in Fig. 4.21. In short filaments, this ratio is greater than one at distances close to $r_{\rm int}$ and reaches the maximum value of $\sim$ 13 at the innermost bin. At distances larger than $\sim r_{\rm int}$, AGN feedback energy is negligible with respect to the gravitational potential of short filaments. On the other side, due to their shallower gravitational potential, long filaments possess a ratio $\varepsilon_{\rm AGN}/|\Delta\phi|$ that is always larger than one, reaching the maximum value of $\sim$ 69. These results show that AGN feedback processes most probably affect more the cores of long filaments than those of short filaments, revealing once again a difference between the two populations. These findings are interpreted in analogy with clusters of galaxies, where the link between gas depletion and density has been thoroughly studied, finding that AGN feedback effects are efficient enough to displace large amounts of gas outside the potential wells of the small-scale structures (groups), but barely affect the more massive (larger-scale) clusters of galaxies (e.g. Planelles et al., 2013; Le Brun et al., 2014; McCarthy et al., 2017; Barnes et al., 2017; Henden et al., 2020, and references therein). Regarding filaments, similar trends with density are observed in this work. It is important to recall that not all the kinetic energy deposited into the medium by AGN feedback processes is necessarily transferred to the gas. Indeed, this depends on several factors such as the AGN jet geometry and orientation, their stability, and the coupling between the energetic jets and winds and the gas, which is not the focus of this study. The main result of this study is that the feedback from AGNs can potentially inject enough energy into the medium to contribute to the gas depletion observed in Fig. 4.18, with an efficiency that also depends on the filament population. Note that these results agree well with those of Gheller et al. (2016) and Gheller, Vazza (2019).

Analysis of the bump at $r \in [r_{\rm int}, r_{\rm ext}]$

Let us now focus on the bump of the profiles, observed at $r \in [r_{\rm int}, r_{\rm ext}]$ in Fig. 4.18. In order to understand this feature, it is crucial to disentangle between the different 'types' of gas that co-exist in the cosmic web, e.g. the diffuse inter-galactic medium, the warm-hot inter-galactic medium (WHIM), the hot gas, etc. Based on its position in the density vs temperature phase-space, gas is separated into different phases as defined by Martizzi et al. (2019), and the respective gas fraction profiles around filaments are computed. Note that these different gas phases will be properly introduced in the following Chapter, and the reader can refer to Sect. 5.1 for further details.

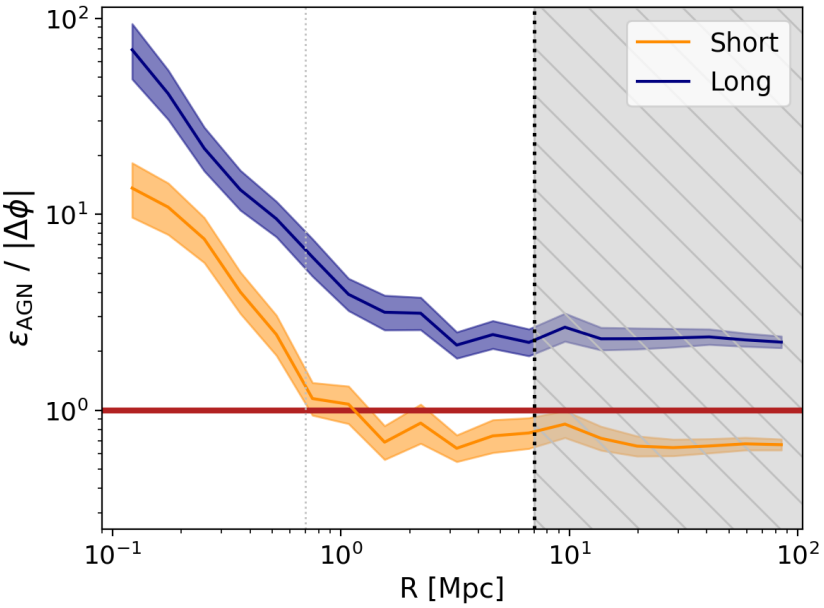

Figure 4.21: Ratio between the AGN feedback energy by unit of gas mass, ε_{AGN} (Eq. 4.23), and the depth of the gravitational potential, $|\Delta\phi|$ (Eq. 4.19). The inner and outer vertical dashed lines correspond respectively to the r_{int} and r_{ext} radii. The regions outside filaments (i.e. $r > r_{ext}$) are hatched in gray and must not be considered in the analysis.

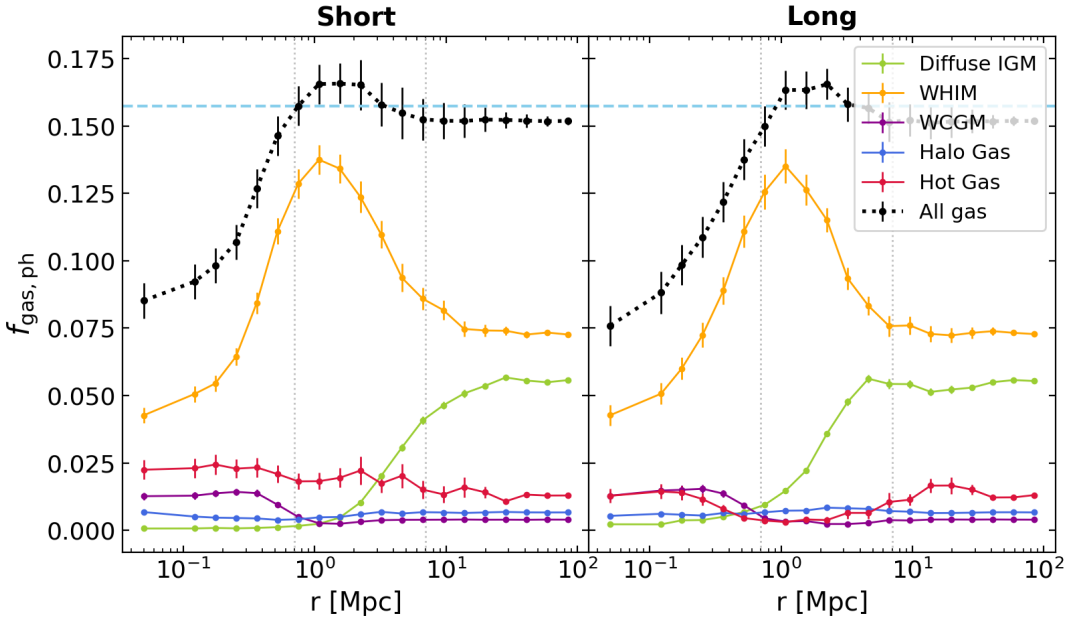

Figure 4.22: Gas fraction profiles separated in five different phases, according to the classification of (Martizzi et al., 2019). The vertical lines show the positions of the r_{int} (left) and r_{ext} (right) radial scales.

Table 4.6: Mean enclosed mass (by unit length) up to $r_{\rm ext} = 7$ Mpc (see Eq. 4.24). These values are in units of $M_\odot$/Mpc.

	Short filaments	Long filaments
DM	$10^{13.25}$	$10^{12.93}$
Gas	$10^{12.51}$	$10^{12.19}$
Stars	$10^{11.12}$	$10^{10.75}$

The resulting gas fractions are shown in Fig. 4.22. It is evident that the observed bump is specific to gas in the WHIM, with temperature $T \sim 10^5 - 10^7$ K (warm), and density $n_{\rm H} < 10^{-4}\,{\rm cm}^{-3}$ (diffuse). Indeed, diffuse gas is accreted towards the cores of filaments by gravitational attraction, and due to its collisional nature, it is shock heated and converted into WHIM gas. Unable to efficiently cool down, WHIM gas assembles at the outskirts ($r \sim 1$ Mpc) of filaments. These results are in agreement with the study of gas properties around filaments, which will be presented in Chapter 5.

Interestingly, the work of Rost et al. (2021), focusing on the filaments at the outskirts of clusters and their connection to these structures, has also detected a bump in the gas fraction profiles of filaments connected to the clusters of The ThreeHundred simulation (Cui et al., 2018a). In that work, this feature was exclusively interpreted as the turbulent fuelling of clusters with filament gas (i.e. filaments acting as highways of gas towards clusters). However, since the outskirts of clusters are not included in my analysis (regions within $3 \times R_{200}$ from cluster centres are excluded), the bump highlighted here is rather found to be an intrinsic property of radial accretion shocks of WHIM gas at the boundaries of filaments. Of course, this intrinsic radial feature can be enhanced by other processes, like the turbulent motions for the filamentary structures at the outskirts of clusters detected by Rost et al. (2021).

4.2.3 Masses by unit length

Finally, let us compute the DM, gas, and stellar mass content of the two populations. Their enclosed mass by unit length is computed by integrating the radial profile of matter (DM, gas, or stars, as presented in Fig. 4.14) up to a given radius R, such that:

$$m_R \equiv \frac{M(R)}{L_{\rm fil}} = \frac{2\pi \int_0^R r'\rho(r')\,dr'}{L_{\rm fil}}. \tag{4.24}$$

This quantity is computed for the 969 and 446 selected short and long filaments (see Sect. 4.2.1), and the resulting mass distributions are shown in Fig. 4.23. The choice of R was determined by the results of the baryon fraction profiles (Fig. 4.18), and it set to the $r_{\rm ext}$ value of 7 Mpc. Note that smaller radii only shift the distributions towards the smaller masses, and do not change the observed trends.

The mass by unit length distribution of short filaments peaks at higher values than that of long ones, regardless of the matter component. The maximum values of the distributions of short filaments are respectively $\log m_{r_{\rm ext}} = 14.17, 13.38$ and $12.18\,M_\odot$/Mpc for DM, gas and stars, which is on average 4.7 times higher than the maximum masses exhibited by the distribution of the long population (i.e. $\log m_{r_{\rm ext}} = 13.48, 12.72$ and, 11.53). The mean mass values, reported in Table 4.6 and marked by the vertical dashed lines in Fig. 4.23, of short and long filaments are also distinct.

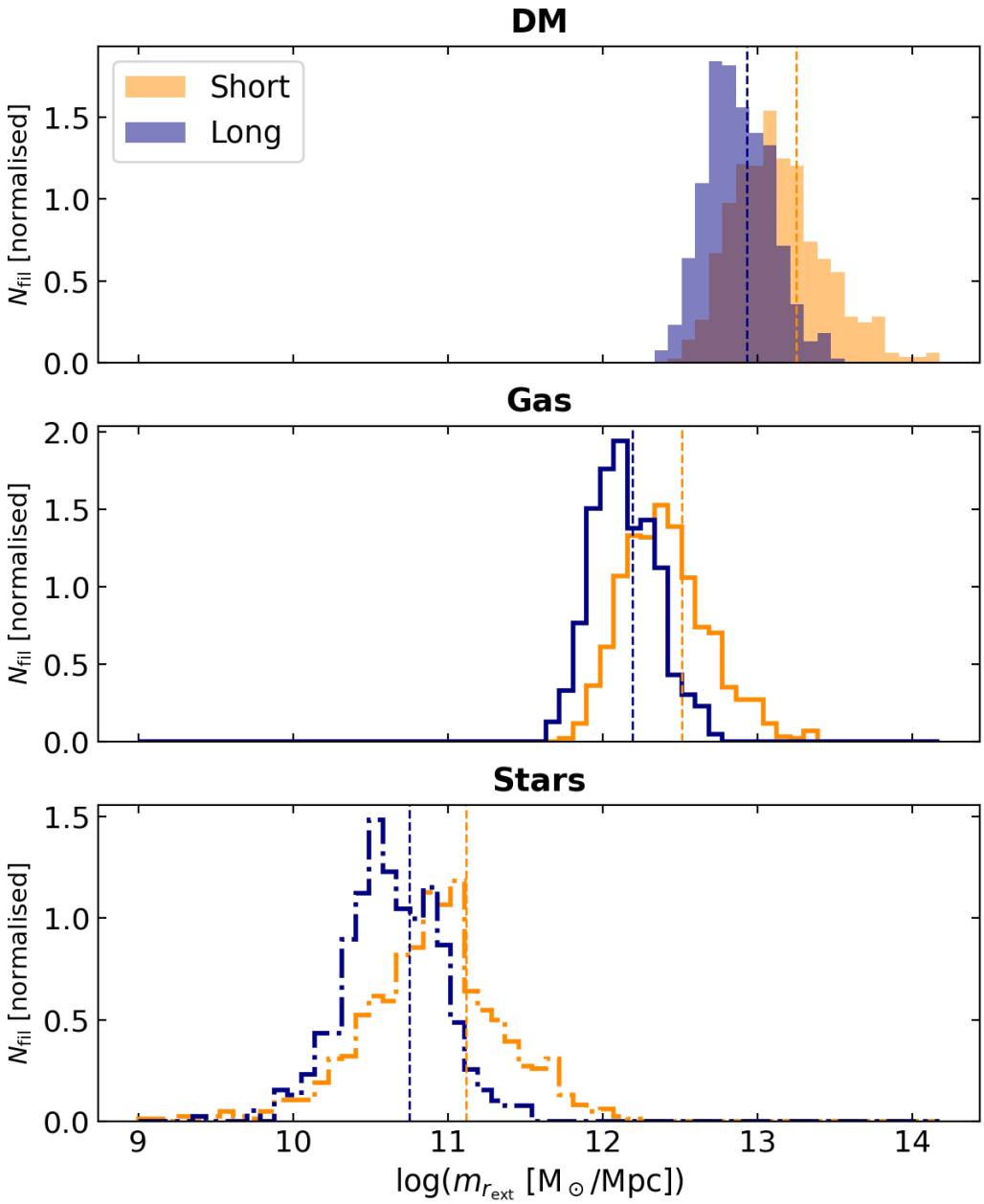

Figure 4.23: Distribution of masses by unit length of short and long filaments. The m_{rext} are computed for the DM, gas, and stellar matter components (top to bottom panels). The vertical dashed lines correspond to the mean values of the mass distributions distributions.

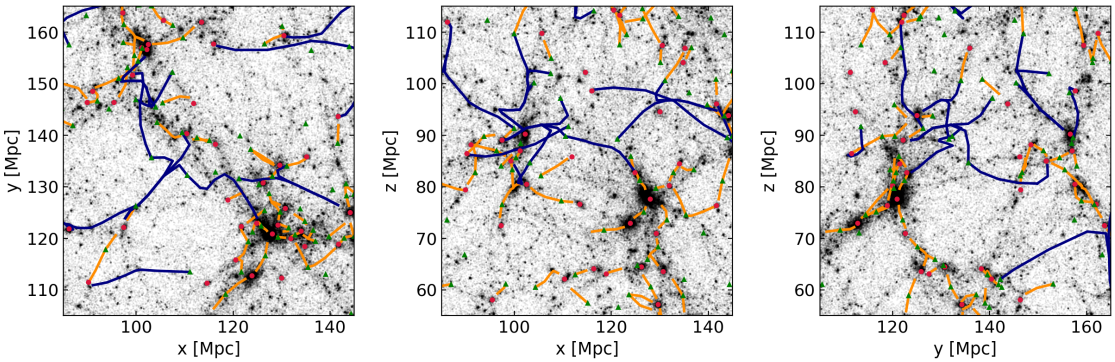

Figure 4.24: Box of 60 Mpc side length, projections onto the *xy*,*xz*, *yz* planes. Orange and blue lines represent the spines of short and long filaments, respectively. The black points show the underlying DM distribution. Red squares and green triangles mark respectively the positions of CPmax and saddles (the `DisPerSE` critical points).

4.3 Different environments for short and long filaments

Sections 4.1 and 4.2 presented a comprehensive analysis of the radial distribution of matter around cosmic filaments at $z = 0$. From these studies, it appeared that matter is not distributed in the same way around filaments of different lengths. This led us to the identification of the two different populations of filaments: the short ($L_f < 9$ Mpc) and long ones ($L_f \geq 20$ Mpc). Short filaments show higher densities than the long population at all radial distances (e.g. a factor of ~ 3 between the DM, gas, and stellar densities of short and long filaments, as seen in Table 4.5). Given these results, it is only natural to investigate whether the differences seen between the two populations are related with the possibly different environments of these large-scale structures.

First, let us plot the positions of short and long filaments in an arbitrarily chosen sub-box of the TNG300-1 simulation. This is shown in Fig. 4.24, where orange and blue lines denote respectively the position of the spines of short and long filaments in the *xy*, *xz* and *yz* DM projections of the sub-box. Here, one can already see that the positions of the two populations in the cosmic web are not random. Clearly, short filaments are found at the vicinity of clusters of galaxies (densest regions, shown by the darker colours), while long filaments, connecting more distant regions, seem to live in visually less dense environments.

Galaxy density excess

The environment of these two different populations is probed in a more quantitative way by looking, once again, at the distribution of galaxies. The galaxy density excess, hereafter noted $\langle 1 + \delta \rangle_{r<R}$, corresponds to the excess of density of a filament with respect to the background density, summed up to a radial distance of R, in Mpc. It is defined as:

$$\langle 1 + \delta \rangle_{r<R} = \frac{1}{R} \int_0^R \frac{n_{\rm fil}(r)}{n_{\rm b}} \, {\rm d}r. \tag{4.25}$$

In this equation, $n_{\rm fil}(r)$ is the filament galaxy density profile, which corresponds to the average profile of its segments, and $n_{\rm b}$ corresponds to the background density of the simulation.

The resulting $\langle 1 + \delta \rangle_{r<2}$ probability distributions of the short and long TNG300-1 filaments are shown in Fig. 4.25. The radial scale of integration, $R = 2$ Mpc, was chosen to correspond

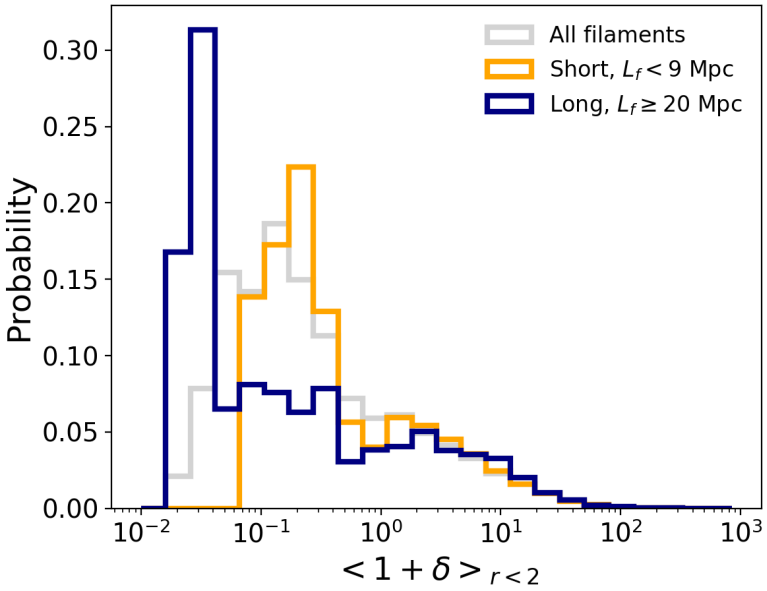

Figure 4.25: Probability distributions of the excess of density $\langle 1+\delta \rangle_{r<2}$ (see Eq. 4.25) of short (orange), long (blue) and the total population of filaments (gray). This quantity corresponds to the excess of density of a filament with respect to the background density, averaged up to a radial distance of $R = 2$ Mpc. This figure is extracted from Galárraga-Espinosa et al. (2020).

to the radius of filaments found in other studies (see for example Aragón-Calvo et al., 2010b; Colberg et al., 2005; González, Padilla, 2010; Bond et al., 2010; Cautun et al., 2014; Santiago-Bautista et al., 2020), although other analyses have found different filament radii (e.g. Bonjean et al., 2020; Tanimura et al., 2020a). The distribution for the total population of filaments is also displayed for comparison. It is important to note that the area under each histogram is normalised to one by dividing the counts by the number of measurements times the bin width.

First, the density excess of filaments spans almost 5 orders of magnitude, from very underdense filaments $\langle 1+\delta \rangle_{r<2} \sim 1.9 \times 10^{-2}$, to filaments with densities of the order of clusters $\langle 1+\delta \rangle_{r<2} \sim 8.5 \times 10^{2}$. These results are in good agreement with those of Cautun et al. (2014) where the densities of filaments, detected in a DM simulation, are also found to span a large range, similar to our findings.

Let us now focus on the specific features of the distributions of the $\mathcal{S}$ and $\mathcal{L}$ populations. These share a common regime at $\langle 1+\delta \rangle_{r<2} \sim [2-300]$, but they are different at lower values. Indeed, the distribution of long filaments exhibits a clear excess towards the lowest values (peak at $\langle 1+\delta \rangle_{r<2} \sim 0.03$) whereas the distribution of short filaments is shifted towards higher values (peak at $\langle 1+\delta \rangle_{r<2} \sim 0.2$) and its minimum is 0.07, which is more than twice the value for long filaments, 0.02. Similarly, towards the highest values, the distribution for the short filaments reaches a maximum density of 848, which is a factor of two larger than the maximum of long ones, 415. The mean values are 41 and 34, respectively for the $\mathcal{S}$ and $\mathcal{L}$ populations, and the medians are 13 and 14. These results indicate that, statistically, short filaments are on average denser than long ones.

Mass of the nodes connected to short and long filaments

In addition to the galaxy density excess, let us study the connection of short and long filaments to the nodes of the cosmic web. Recall that, within the `DisPerSE` network, the position of the

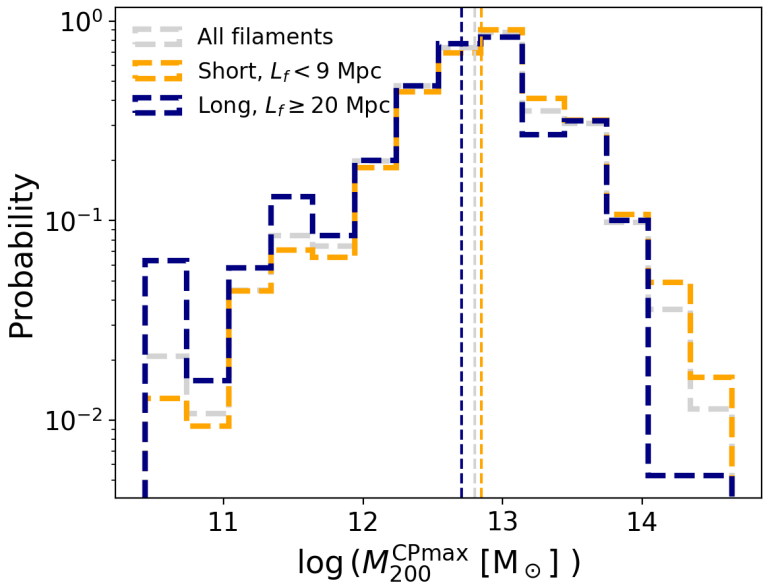

Figure 4.26: Distribution of DM masses M_{200}^{CPmax} of the maximum density critical points (CPmax) in the TNG300-1 simulation. CPmax connected to short (resp. long) filaments are presented in orange (resp. blue). The vertical dashed lines correspond to the mean values of the distributions. This figure is extracted from Galárraga-Espinosa et al. (2020).

nodes are traced by the maximum density critical points (CPmax), which have been masked in the previous analyses in order to focus on the main stem of filaments only.

The masses at the CPmax positions, hereafter called M_{200}^{CPmax}, are defined and computed as the total DM mass enclosed in a sphere of radius R_{200}. The resulting mass distribution is displayed in Fig. 4.26 for short and long filaments, respectively in orange and blue. For comparison, the results for all the filaments of the TNG300-1 catalogue are presented in gray. The M_{200}^{CPmax} mass distributions of short and long filaments overlap in the $\sim 10^{12} - 10^{13.5}$ M$_\odot$ mass range. This is due to the fact that CPmaxs may be connected to more than one filament (3.25 filaments on average in the TNG300-1 skeleton, in agreement with Gouin et al., 2021), regardless of its population. Nevertheless, these distributions show differences at the lowest and highest masses. Short filaments are statistically connected to more massive objects (maximum mass $\sim 10^{14.65}$ M$_\odot$) than long filaments (max $\sim 10^{14.05}$ M$_\odot$). The mean values of the M_{200}^{CPmax} distributions also reflect this trend. These are $10^{12.71}$ and $10^{12.85}$M$_\odot$ for the case of long and short populations, respectively.

Discussion

In the agreement with the the density profiles derived in this Chapter (Figs. 4.10 and 4.14), these studies suggest that short and long filaments trace different environments of the cosmic web. Short filaments are always radially more extended ($r_2 \sim 5$ Mpc from the galaxy distribution), denser, on average more massive, and likely to be connected to more massive structures than long filaments. They may thus be embedded in over-dense environments of the cosmic web, and might correspond to elongated bridges of matter between over-dense structures. On the contrary, long filaments are thinner ($r_2 \sim 3$ Mpc), less dense, less massive, and connected on average to less massive objects. This long and thinner population may represent the cosmic filaments shaping the structure of the cosmic web and lying in under-dense regions. Note that

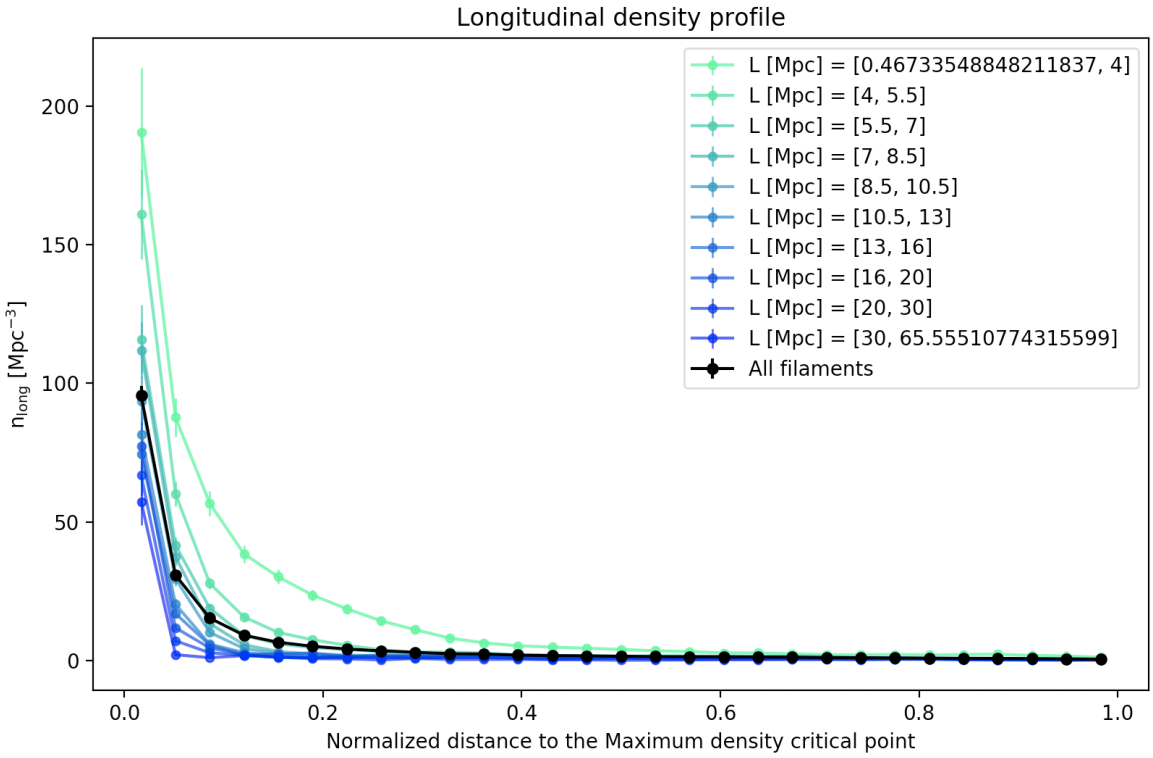

Figure 4.27: Longitudinal galaxy density profiles of cosmic filaments of the TNG300-1 simulation.

the relation between filament length and density is expected given the `DisPerSE` framework (which defines filaments based on the topology of the density field). Indeed, a region showing many local over-densities (e.g near clusters) will naturally present a larger number of critical points, and thus shorter filaments with respect to emptier zones, where the density field is locally smoother. Therefore, filaments of different lengths trace indeed different environments.

Belonging to different environments, the short and long filaments populations may be governed by different dynamical processes. In over-dense regions the dynamics of matter at the largest scales might be dominated by gravitational forces that pull matter from the lowest to the highest density zones. Therefore, short filaments might become shorter with cosmic time, as they might merge with the over-dense structures around them, e.g. clusters and super-clusters. On the other hand, in under-dense regions, the dark energy forces responsible for the cosmic accelerated expansion and stretching of the cosmic web might be dominant over the gravitational forces driving mergers, so long filaments might become even longer and thinner with cosmic time.

4.4 Longitudinal distribution of matter in filaments

The previous sections focused on the radial distribution of matter around cosmic filaments. For a complete characterisation of filaments, it is important to also study the distribution of matter in the longitudinal direction of filaments, i.e. in the direction parallel to their spine. Using N-body simulations, Colberg et al. (2005) computed the average longitudinal over-density profile of filamentary structures between pairs of clusters. By normalising each filament by its length (only filaments of length $> 5\,h^{-1}$ Mpc were selected), they found that the over-density of DM

increases towards the extremes of the filaments, as expected from regions directly connected to clusters. Similar results were found by Santiago-Bautista et al. (2020), who, using observations from the SDSS, analysed the longitudinal density of galaxies in bridges of matter of supercluster environments. These authors estimated a density contrast of $\sim$ 10 between the extremities and the main stem of filaments. Moreover, by performing 2D and 3D stacks of the galaxy distributions around `DisPerSE` filaments in the Horizon-AGN simulation (Dubois et al., 2014), Kraljic et al. (2019) also showed a clear gradient of the number density of galaxies (and of their stellar mass), which was positive in the direction of saddles to nodes. As expected, saddle points were found to be local density minima along filaments, with respect to the local maxima corresponding to the nodes.

The longitudinal distribution of galaxies in filaments was investigated in this thesis using the TNG300-1 simulation, and the preliminary results, presented in Fig. 4.27, are found to be in good agreement with the previously cited works. These longitudinal profiles were computed by counting the number of galaxies in cylinders of radius 1 Mpc centred on the axis of the filament, from the CPmax ($x = 0$ in the horizontal axis) to the saddle, and dividing this number by the corresponding volume. Filaments were divided in thin bins of length, and the resulting profiles were normalised so that the position of the saddle point corresponds to $x = 1$. In agreement with the results discussed in the previous Sections of this thesis, the longitudinal density of shorter filaments (green colours) is higher towards the CPmax than that of longer filaments (blue colours). It is interesting to note that the shortest filaments of our catalogue show a density contrast of $\sim$ 10 at the CPmax, in agreement with the work of Santiago-Bautista et al. (2020) in observations of the SDSS.

Let us conclude this section by mentioning that the way cosmic filaments connect to the clusters at their extremities is a broad and active field of study. For example, the statistical study of the outskirts of clusters by multipole harmonic decomposition performed by e.g. Gouin et al. (2020) detected a significant level of anisotropy in the galaxy distribution at these regions, which might be related to the average number of filaments connected to the clusters ($3-4$). The connectivity of clusters to the filaments of the cosmic web was further investigated in Gouin et al. (2021), finding a larger number of filaments connected to the more massive clusters and groups, and a lower connectivity for less massive structures. Finally, filaments seem to play a key role in the accretion of matter to clusters, since the accretion seems to be preferentially fuelled by matter flowing in the longitudinal direction of filaments, instead of coming from isotropic directions. This was shown by, e.g. the analysis of matter densities and velocity fields in the $[2-7]\times R_{200}$ regions around simulated clusters (Rost et al., 2021, and references therein).

4.5 Conclusions

This Chapter presented a comprehensive analysis of the radial distribution of matter around cosmic filaments. Based on the study of the distribution of galaxies (Sect. 4.1), cores of filaments were found to be $\sim 20\sigma$ denser at their cores than the background density distribution (in agreement with the results using the WISExCOSMOS galaxies, Bonjean et al., 2020). Two different filament populations were identified by analysing how the galaxy density profiles varied as a function of filament length. These populations are the short ($L_{\rm f} < 9$ Mpc) and the long ($L_{\rm f} \geq 20$ Mpc) filaments, and showed significant ($> 2\sigma$) differences of galaxy density with respect to the average profile of all the filaments.

The study of DM, gas, and stellar densities of Sect. 4.2 also showed a gap between the densities of the two populations (a factor of three between short and long filaments), and the analysis of the environment in Sect. 4.3 led to the conclusion that short and long filaments trace in fact different regions of the cosmic web. Short filaments were found to be always denser, puffier ($r_2 \sim 5$ Mpc), statistically more connected to massive objects and tracers of over-dense regions. They may be interpreted as bridges of matter between over-dense structures like clusters. Long filaments, on the contrary, were found to be less dense, thinner ($r_2 \sim 3$ Mpc), statistically connected to less massive objects, and tracers of less-dense environments. They may correspond to the filaments shaping the large scales of the cosmic web. Recent studies have also made a connection between filament properties and the large-scale environment of these structures. For example, the works of Cautun et al. (2014) and Ganeshaiah Veena et al. (2019, 2021) have shown that the thickness of filaments, as defined by the NEXUS+ filament finder (Cautun et al., 2013), is also a tracer of the environment, since thick filaments are embedded in over-dense regions connecting the nodes of the cosmic web, and thinner structures are mostly found in under-dense locations. Qualitatively, this relates well with the relative radial extents shown by the density profiles (of the number of galaxies, DM, gas and stars) around the two populations found in this thesis. Also, in Tuominen et al. (2021), the authors classified filaments based on their luminosity over-density (which was firstly introduced in Nevalainen et al., 2015). As expected, their results showed that high- and low-luminosity filaments trace respectively denser and less-dense environments. A clear parallel can thus be drawn between the relative locations of the filament categories mentioned above, and these of short and long filaments. Of course, an analysis of the velocity field around short and long filaments, and a study at higher redshift might will be useful to unveil the dynamics and the evolution of these two different populations.

Contrary to absolute densities, the relative distribution of baryons (gas + stars) with respect to DM showed a more universal behaviour around filaments, as it was found to be independent from the large-scale environments traced by the short and long populations. The baryon fraction profiles of Sect. 4.2.2 revealed common radial scales ($r_{\rm ext} \sim 0.7$ and $r_{\rm ext} \sim 7$ Mpc), and showed that cores ($r < r_{\rm int}$) of both short and long filaments are baryon depleted (with similar depletion factors of $Y_b \sim 0.68$ and 0.63, respectively). An analysis of the feedback from AGNs in filaments showed that these objects can inject enough energy into the medium to potentially expel the gas outside of the gravitational potential induced by filaments, contributing to the observed gas depletion. On the other hand, an excess of baryons with respect to the cosmic fraction was found at radial distances of $r \in [r_{\rm int}, r_{\rm ext}]$. These baryons were identified as gas in the WHIM phase: unable to cool, WHIM gas assembles at these distances from the filament cores, creating a signature of its radial accretion in the baryon fraction profiles of filaments (i.e. a bump).

These deviations of gas with respect to DM can also be interpreted in terms of gas 'bias' in filaments. Previous works such as Cui et al. (2018b, 2019), have argued that the cosmic skeleton traced by the gas is not biased with respect to the DM one, and that the baryonic processes have almost no impact on large-scale structures. Here this statement is strongly nuanced by showing that gas follows DM in an 'un-biased' way only down to a certain filament radius, $r_{\rm ext}$. Although the bias is small at the intermediate distances of $r \in [r_{\rm int}, r_{\rm ext}]$ (where the bump lies), it is definitely non-negligible at the cores of filaments, i.e. at distances lower than $r_{\rm int}$.

In conclusion, in this Chapter, I have shown that the distribution of matter around cosmic filaments strongly depends on the large-scale environment in which these structures are em-

bedded. Tracers of denser and less-dense environments, the short and long filaments identified in this Chapter present clear differences in terms of their galaxy number density, and of their DM, gas, and stellar radial densities. Further differences between short and long filaments will be revealed in the following Chapters of this thesis, and more specifically with the study of the physical properties of gas (Chapter 5), and galaxies (Chapter 6).

Chapter 5

Properties of gas in cosmic filaments

Contents

After characterising the distribution of matter around cosmic filaments, let us now investigate the physical properties of baryons in these structures. The properties of gas are thus studied in this Chapter, around the cosmic filaments of the TNG300-1 box of the TNGsimulation.

In this study, gas is separated into five different phases, which are states defined by their density and temperature. These gas phases are introduced in Sect. 5.1, along with the results on their spatial distribution around short ($L_f < 9$ Mpc) and long filaments ($L_f \geq 20$ Mpc). For the sake of completeness, the present analysis also considers "medium"-length filaments ($9 \leq L_f < 20$ Mpc). Finally, Sects. 5.2 and 5.3 of this Chapter focus on the temperature and pressure around filaments. This is done by exploring the variations of these two gas thermodynamic parameters as a function of the distance to the filament spine.

5.1 Not all gas is the same

Along with gravity and because of its collisional nature, gas is subject to several complex and interconnected physical processes, which can be essentially summarised by accretion, ejection, heating, and cooling, caused by, for example, stellar and AGN feedback, galactic winds, and radiation. These processes form a complex cycle in which gas is pushed into different physical states, or phases, which co-exist in the cosmic web, and are spatially associated with different

structures at different cosmic scales, as shown e.g. by Ursino et al. (2010); Shull et al. (2012); Cen, Ostriker (2006); Haider et al. (2016); Martizzi et al. (2019); Galárraga-Espinosa et al. (2021); Ramsøy et al. (2021). After presenting first considerations in 5.1.1, the five gas phases examined in this thesis are introduced in Sect. 5.1.2, and analysed in Sect. 5.1.3 by means of their phase space distribution, density, and mass fraction profiles around filaments.

5.1.1 First considerations

Let us first begin by explaining the gas selection performed prior to the study presented in the next sections. Since it represents a contamination in the study of the main stems of filaments, gas in the nodes of the cosmic web is removed from the following analysis. This corresponds to the gas cells located within spheres of radius $3 \times R_{200}$ centred on the position of the CPmax (the topological nodes of the skeleton). The fraction of removed gas cells is $\sim 11\%$ of the total.

Also, the contribution of massive galactic haloes is explicitly identified with the aim of focusing this study on the gas in filaments that is not associated (within $3 \times R_{200}$) with these collapsed structures. Massive galactic haloes are defined as the haloes of mass $M_{\rm tot} > 10^{12}\,{\rm M}_\odot$ that host at least one galaxy of $10^9 \leq {\rm M}_* \leq 10^{12}\,{\rm M}_\odot$ in stellar mass. The fraction of gas cells lying within these structures is 13% of the total.

For illustration, the gas cells within $1 \times R_{200}$ of the CPmax and of the massive haloes are represented respectively by the red and green points in the *xy* slice of Fig. 5.1. After discarding nodes and haloes, the TNG300-1 gas dataset is composed by cells that are not associated (within $3 \times R_{200}$) with these massive structures, and contains 76% of the initial cells. The gas left for the study, i.e. that located inside, around, and between filaments, is hereafter referred to as the inter-filament medium.

5.1.2 Definition of gas phases

Phases can easily be identified with the help of a phase-space diagram, showing the relation between gas temperature and gas density (e.g. Ursino et al., 2010; Shull et al., 2012; Cen, Ostriker, 2006; Haider et al., 2016; Martizzi et al., 2019). The five phases considered in this study are presented in the normalised 2D histogram of Fig. 5.2, and correspond to those of Martizzi et al. (2019): the diffuse intergalactic medium (diffuse IGM), WHIM, warm circumgalactic medium (WCGM), halo gas, and hot gas. These phases are defined according to their hydrogen number density, $n_{\rm H}$, and their temperature. Note that the hydrogen number density is a direct tracer of the total gas mass density $\rho_{\rm cell}$, as $n_{\rm H} = X_{\rm H}\,\rho_{\rm cell}/m_{\rm p}$. The main characteristics of each phase are described in the following:

- The diffuse intergalactic medium (IGM) corresponds to intergalactic gas, which is cold ($T < 10^5$ K), diffuse ($n_{\rm H} < 10^{-4}$ cm^{-3}), and, by definition, located in regions of the cosmic web with small overdensities. Indeed, the selection in $n_{\rm H}$ can be translated into a gas density limit of $\rho_{\rm cell} < 25\,\rho_{\rm crit}$, where $\rho_{\rm crit}$ corresponds to the critical density of the Universe.

- The warm-hot intergalactic medium (WHIM) is defined as warm ($10^5 < {\rm T\,[K]} < 10^7$) and diffuse ($n_{\rm H} < 10^{-4}$ cm^{-3}) gas. This phase corresponds to IGM gas that has been accreted onto cosmic structures like nodes or filaments and heated to such temperatures by shocks.

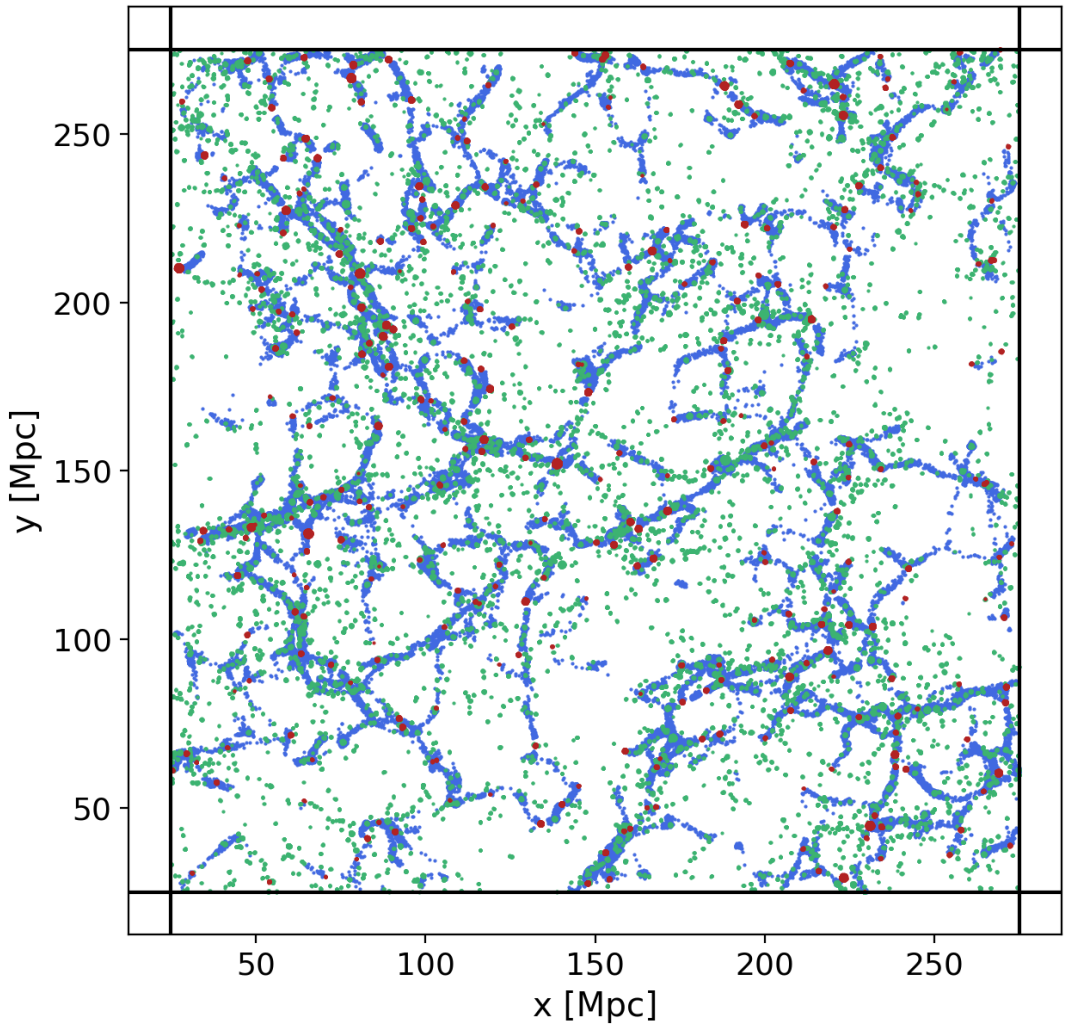

Figure 5.1: Two-dimensional projection of a slice of thickness 50 Mpc in the *xy* plane of the TNG300-1 box. The red points correspond to gas cells within the R_{200} radii of nodes. The blue points represent gas around filaments, at distances closer than 1 Mpc from the spine of the cosmic web. Finally, the green points show gas in the R_{200} region of galactic haloes (i.e. within spheres of radius $1 \times R_{200}$). The galactic haloes residing in filaments are clearly apparent (green over blue regions). The centres of the cells are plotted as points, but the TNG300-1 simulation is described by Voronoi cells having various volumes. This figure is extracted from Galárraga-Espinosa et al. (2021).

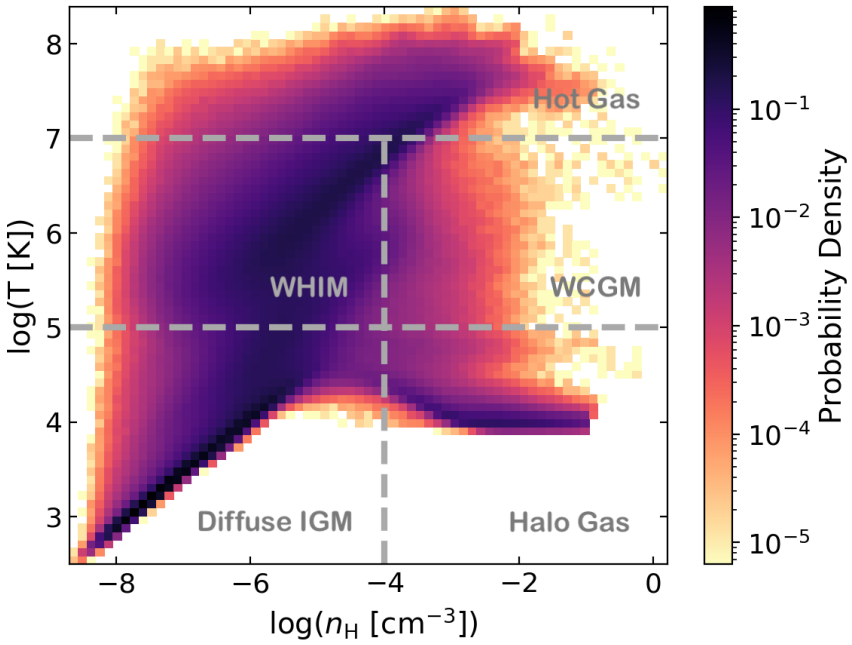

Figure 5.2: Phase-space of the gas cells in the TNG300-1 simulation, shown by the normalised 2D histogram of the cells. The five different gas phases studied in this work are delimited by the thick dashed lines. They are defined as in Martizzi et al. (2019). This figure is extracted from Galárraga-Espinosa et al. (2021).

.

- Halo gas corresponds to the coldest (T $< 10^5$ K) and densest ($n_H > 10^{-4}$ cm^{-3}) gas phase. It is associated with the interstellar medium of galaxies, hence this phase is found inside or near galactic haloes.

- The warm circumgalactic medium (WCGM) features the same temperature range as the WHIM (10^5 < T[K] < 10^7), but is characterised by the same densities as Halo gas ($n_H > 10^{-4}$ cm^{-3}). The WCGM phase is located in the surroundings of galaxies, where it has been heated by shocks and feedback effects. Therefore, the physics shaping this gas is closely tied with these of galaxies.

- Hot gas represents the hottest phase of all (T > 10^7 K), mixing both diffuse and dense phases (no selection in n_H). Hot gas is mainly present in the densest regions of the cosmic web, like the most massive haloes, where shocks have heated gas to these very high temperatures.

Table 5.1 summarises the temperature and densities defining each phase, and further details are available in Sect. 2.3 of Martizzi et al. (2019). Note, however, that this analysis does not consider star-forming gas, which is defined as gas with densities higher than $n_H > 0.13$ cm^{-3}, temperatures lower than $T < 10^7$ K, and star formation rate SFR > 0. This is motivated by the fact that the `ElectronAbundance` field (see Sect. 2.1.1) of star-forming cells is altered by the subgrid model of star formation (Springel, Hernquist, 2003) employed in the simulation. Indeed, this model implicitly assumes a multi-phase interstellar medium, composed of a warm volume-filling gas, and dense cold clumps containing most of the mass of the gas cell (Springel, Hernquist, 2003). The values of `ElectronAbundance` of these cells are thus computed as the

Table 5.1: Definition of the five different gas phases studied in this thesis. Further details can be found in Martizzi et al. (2019).

	Density [cm^{-3}]	Temperature [K]
Diffuse IGM	$n_{\rm H} \leq 10^{-4}$	$T \leq 10^5$
WHIM	$n_{\rm H} \leq 10^{-4}$	$10^5 < T \leq 10^7$
WCGM	$n_{\rm H} > 10^{-4}$	$10^5 < T \leq 10^7$
Halo gas	$n_{\rm H} > 10^{-4}$	$T \leq 10^5$
Hot gas	no cut	$T > 10^7$

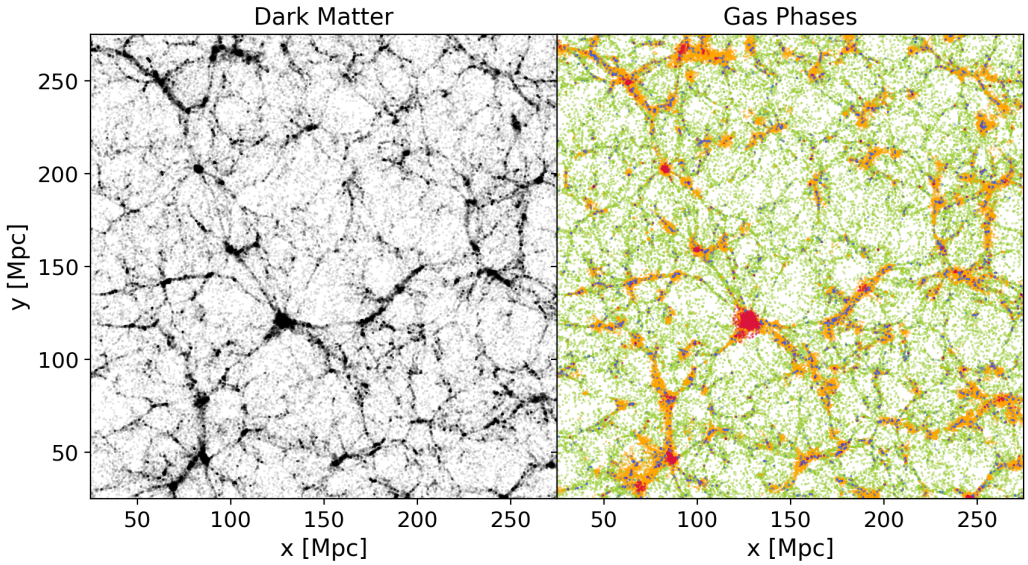

Figure 5.3: *xy* projection of the DM distribution (left), and the gas cells positions (right) in a slice of thickness 5 Mpc of the TNG300-1 simulation. The different colours denote different gas phases: green, yellow, purple, blue and red correspond respectively to diffuse IGM, WHIM, WCGM, halo and hot gas.

average between the hot and cold ISM phases, and so this quantity presents a contribution, or 'contamination', of cold clumps that does not allow the calculation of physical (thermal) quantities. A clear example of this point can be found in Pakmor et al. (2018). It is worth noting that gas cells with SFR > 0 account for only a tiny fraction of the total gas budget ($\sim 0.1\%$).

For visualisation, a slice of the TNG300-1 simulation box showing the spatial distribution of the gas phases studied in this thesis is presented in Fig. 5.3. This figure is a clear illustration that the properties of gas are associated with the different structures of the cosmic web. Particularly, the filamentary structure traced by WHIM gas (yellow points) is already discernible.

Before moving to the next sections, the reader should remember that the frontiers between these phases are somewhat artificial and should not be considered as sharp limits. Gas cells in the neighbourhood of these limits may suddenly move from one phase to another under the influence of even the tiniest perturbation; for example WCGM gas just needs to be heated up to temperatures beyond 10^7 K to be counted as hot gas. Similarly, gas cells at a given place in the phase diagram may have reached their location through a large variety of processes. For instance, gas within the boundaries of the WCGM phase may correspond to WHIM gas that has been accreted and has become denser, to halo gas that has been heated by feedback effects,

or to hot gas that has cooled down. Therefore these density and temperature limits defining the gas phases should simply be considered as guiding references.

5.1.3 Spatial distribution of gas phases around filaments

This section describes how the various gas phases are distributed around the filaments of the TNG300-1 catalogue (see Sect. 3.2). This is assessed through the building of mass density radial profiles, from which I derived the mass fraction of each phase as a function of the distance to the spine of the filament.

Radial profiles of the mass fraction of gas phases (hereafter called φ_i) were computed along the direction perpendicular to the filament spine, r. These mass fractions are defined by

$$\varphi_i(r) = \frac{\rho_{\mathrm{gas},i}(r)}{\rho_{\mathrm{gas,tot}}(r)}, \tag{5.1}$$

where $\rho_{\mathrm{gas},i}(r)$ corresponds to the mass density of the gas phase i (i = WHIM, WCGM, etc.) at a given location around filaments, and $\rho_{\mathrm{gas,tot}}(r)$ is the total mass density of gas (all phases included) at this location.

These densities, ρ_{gas}, are computed as mass averages in volumes of concentric cylindrical shells (denoted by the index k) around the axis of filaments. For all the N_{seg} filament segments, for a given distance r_k from their axes, I summed the masses of the gas cells m_{cell} located inside the cylindrical shells of outer radius r_k and of thickness $r_k - r_{k-1}$ to get the total enclosed gas mass at this location. This result was then divided by the corresponding volume, that is the volume of the hollow cylinder of thickness $r_k - r_{k-1}$ and of height the total segment length. This is given by

$$\rho_{\mathrm{gas}}(r_k) = \frac{\sum_{s=1}^{N_{\mathrm{seg}}} \left(\sum_{j=1}^{N(k)} m_{\mathrm{cell},j} \right)_s}{\pi(r_k^2 - r_{k-1}^2) \sum_{s=1}^{N_{\mathrm{seg}}} l_s}, \tag{5.2}$$

where, $N(k)$ corresponds to the number of cells within the k-th shell around the segment s of length l_s. Note that, similarly to the study of galaxies around filaments, the radial distance r is binned in $k = 20$ equally spaced logarithmic bins, starting from the filament spine up to distances large enough (100 Mpc) to probe the outskirts of filaments and beyond. For illustration, the resulting gas mass density profiles are displayed by Fig. 5.4. The error-bars in this figure are obtained using the bootstrap method (i.e. by computing the standard deviation of 1000 density profiles, obtained by applying Eq. 5.2 to a set of $N_{\mathrm{seg}} = 1000$ randomly extracted (with replacement) filament segments). These errors thus quantify the statistical variance of the density around the limited sample of filaments.

The mass fraction profiles φ_i of each phase are presented in Fig. 5.5a for short ($L_f < 9$ Mpc), medium-length ($9 \leq L_f < 20$ Mpc), and long filaments ($L_f \geq 20$ Mpc) in the left, middle, and right panels, respectively. The error bars in this figure are obtained by propagating these of the density measurements. In this figure, three different regimes can be distinguished for all the filaments:

(i) At distances $r > 10$ Mpc from the filament spine, gas is mainly in a diffuse state (more than 95% of the total budget). This is shown by the fractions of diffuse IGM and WHIM gas,

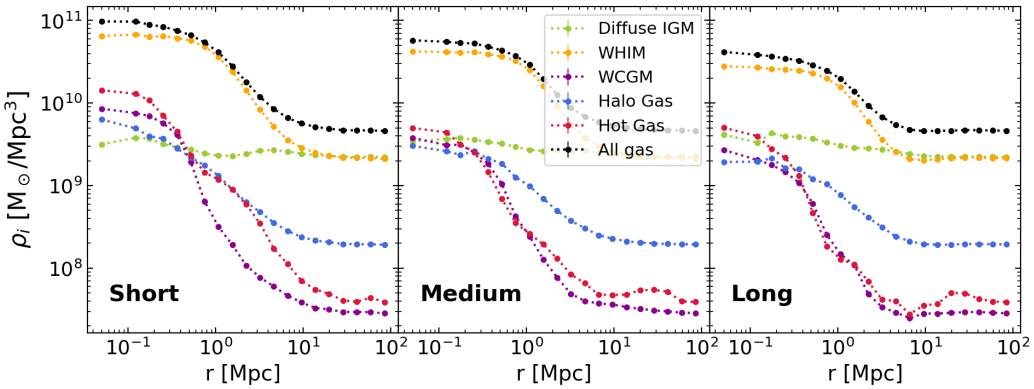

Figure 5.4: Gas mass density profiles $\rho_{\mathrm{gas},i}$ (see Eq. 5.2) of the five different phases (labelled by the index i) around short (left panel), medium-length (centre), and long filaments (right panel). The different gas phases are presented in Sect. 5.1.2.

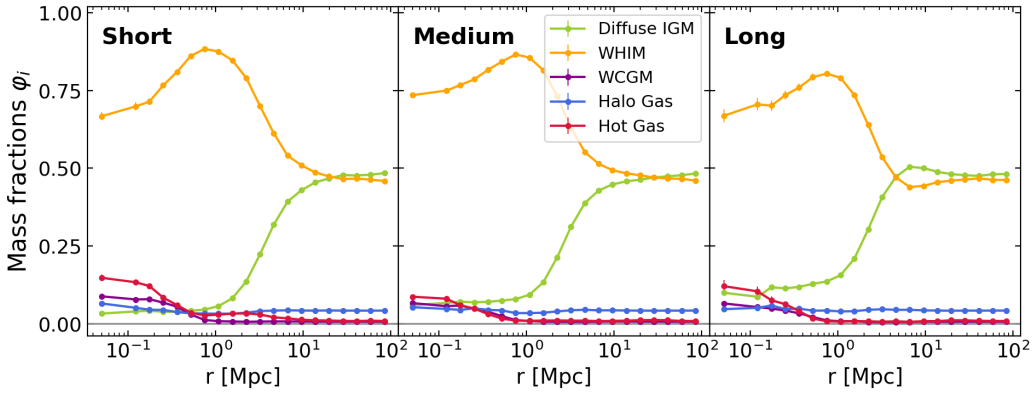

(a) Gas mass fraction profiles

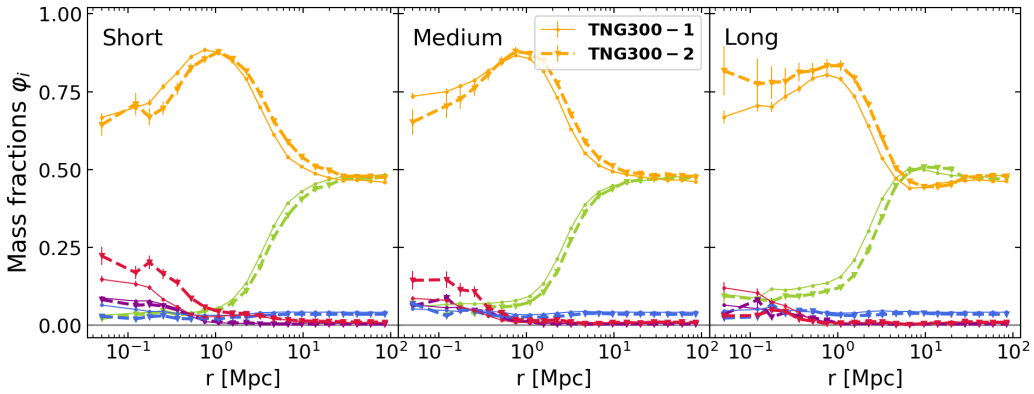

(b) Comparison with lower a resolution simulation, TNG300-2

Figure 5.5: (a): Gas mass fraction profiles φ_i (see Eq. 5.1) of the five different gas phases (labelled by the index i) around short (left panel), medium-length (centre), and long filaments (right panel) in the reference TNG300-1 box. **(b):** Same as (a) but including the results for the lower resolution TNG300-2 simulation (thick dashed lines). These figures are extracted from Galárraga-Espinosa et al. (2021).

which are the highest for all the filaments; as expected, diffuse IGM is the most representative phase ($\sim$ 50%) at such large distances. In the case of short filaments (left panel), from the outside to the inside, a decline of the diffuse IGM fraction is observed, starting at distances of $\sim$ 20 Mpc from the spine. This goes along with a rise of the fraction of WHIM. This feature can be interpreted as the accretion of diffuse gas to filaments, which starts at these large distances in the short population. Accreted gas is gravitationally heated (as will be explicitly shown by the temperature profiles later on in this Chapter), and diffuse IGM gas is thus converted to WHIM, which becomes the dominant phase at $r \sim 20$ Mpc from the spine of the filament (see intersection point). However, in long filaments (right panel), this accretion feature happens at distances much closer to the spine because the diffuse IGM and WHIM fractions intersect only at $r \sim 5$ Mpc. These differences are likely due to the fact that short and long filaments reside in different environments of the cosmic web (Sect. 4.3). Short filaments are in denser regions, where the heating of the gas due to accretion happens at larger radii from the spine than in less dense environments, which are traced by long filaments. Finally, the fractions of WCGM, halo, and hot gas are only tiny (< 6%) at these large distances from the spines.

(ii) At intermediate distances ($1 < r \leq 10$ Mpc) from the filament spine, the accretion of cold and diffuse gas to the core continues. A very significant decrease of the fraction of diffuse IGM is observed, along with an abrupt increase of that of the WHIM phase. The fraction of WHIM reaches its maximum ($\sim$ 88% of the total baryon budget in short and $\sim$ 80% in long filaments) at distances of $r \sim 1$ Mpc from the spine. This radial distance of 1 Mpc is independent of the length of the filament and does not depend on the resolution of the simulation either, as shown by the analysis of the lower resolution simulation, TNG300-2, presented by Fig. 5.5b. This radial distance can be put in regard with the results of the baryon fraction profiles of the previous Chapter (see Fig. 4.18), showing again the presence of a radial extent at which the baryonic processes in filaments (e.g. shocks, feedback effects, mergers) start counteracting the pure gravitational infall of gas. Moreover, in this radial range of $1 < r \leq 10$ Mpc, almost all the diffuse IGM gas has been heated and turned into another phase, thereby becoming negligible (less than 5% and decreasing) in the total baryon budget, which is completely dominated by WHIM. There are no significant changes in the denser phases (WCGM, halo and hot gas), whose fractions remain constant and tiny on the outskirts of filaments.

(iii) The cores of filaments ($r \leq 1$ Mpc) are characterised by a very sharp decrease of the fraction of WHIM and the increase of the WCGM and hot gas, which remained negligible so far. Precisely, Table 5.2 reports the fractions of each gas phase in the first radial bin, that is $r = 0.05$ Mpc. Notice that, despite the observed decrease, WHIM remains the dominant phase in all types of filaments (accounting for $\sim$ 70% of the baryons), which is in qualitative agreement with previous findings at $z = 0$, using different simulations and filament finders (e.g. Nevalainen et al., 2015; Cui et al., 2018b, 2019; Martizzi et al., 2019; Tuominen et al., 2021). Cores of filaments are also composed of hotter and denser gas (WCGM and especially hot gas). This can be explained by the fact that, as WHIM gas approaches or falls into the filament, it is subject to a variety of baryonic processes (shocks, feedback effects, and mergers) whose rates and efficiencies are higher in these inner regions of filaments of higher densities than the outskirts (as shown in Chapter. 4). These baryonic processes alter the density and temperature of WHIM gas, thus pushing this phase into hotter and denser states. Note that the contribution of gas in haloes to the content of filament cores is studied later on in this Section (see Fig. 5.8).

Before continuing with the analysis, let us discuss the impact of the resolution of the simulation on the previously presented results. As argued above in this Section, the profiles of the TNG300-1 and TNG300-2 (lower resolution) simulations shown in Fig. 5.5b are found quite

Table 5.2: Mass fractions φ_i of the different gas phases at the core of short, medium-length and long filaments. The values here are given in %, and correspond to the first radial bin of the φ_i profiles of Fig. 5.5a, that is $r = 0.05$ Mpc

	Short	Medium	Long
Diffuse IGM	(3 ± 1)%	(6 ± 1)%	(10 ± 1)%
WHIM	(67 ± 1)%	(73 ± 1)%	(67 ± 2)%
WCGM	(9 ± 1)%	(7 ± 1)%	(6 ± 1)%
Halo Gas	(6 ± 1)%	(5 ± 1)%	(5 ± 1)%
Hot Gas	(15 ± 1)%	(9 ± 1)%	(12 ± 2)%

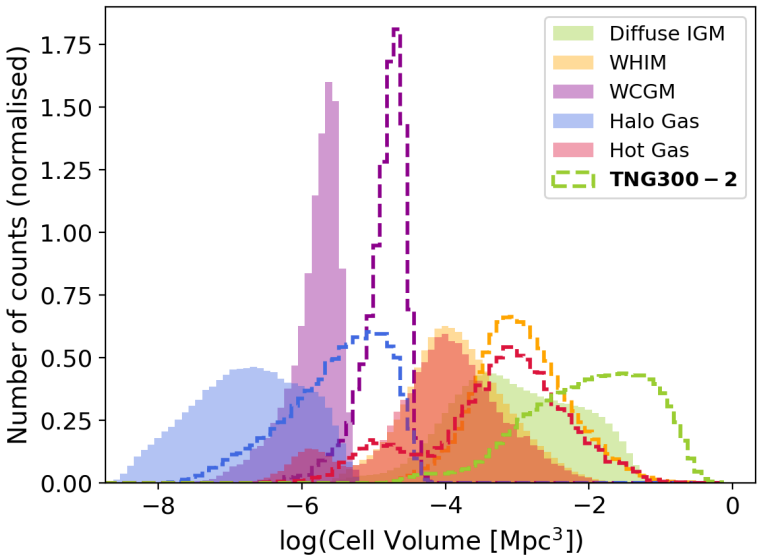

Figure 5.6: Distribution of the volumes of the gas cells in the TNG300-1 box (colour-filled histograms) and in the TNG300-2 simulation (dashed lines). The different colours correspond to the different gas phases considered in this work.

Table 5.3: Fractions of cells in the five different gas phases considered in this work, for the full TNG300-1 and TNG300-2 simulations. These numbers exclude the gas cells lying within spheres of radius $3 \times R_{200}$ centred at the positions of CPmax (i.e. the topological nodes) and of galactic haloes, and thus focus only on the inter-filament gas of the simulation.

	TNG300-1	TNG300-2
Diffuse IGM	48.0%	47.2%
WHIM	46.8%	48.3%
WCGM	0.6%	0.4%
Halo Gas	3.7%	3.0%
Hot Gas	0.9%	1.1%

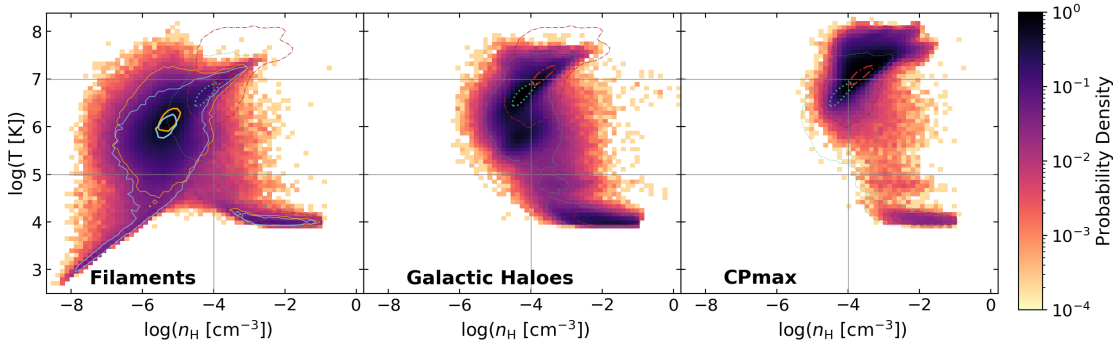

Figure 5.7: Phase portraits of gas, presenting the normalised 2D histograms of the gas cells in the corresponding structures. *First panel*: gas in filaments (within 1 Mpc from the core). *Second panel*: gas within the R_{200} radius of galactic haloes (defined as haloes of mass $M_{\rm tot} > 10^{12}\,{\rm M}_\odot$ hosting at least one galaxy of mass $10^9 \leq {\rm M}_*[{\rm M}_\odot] \leq 10^{12}$). *Third panel*: gas within the R_{200} radius of the DisPerSE maximum density critical points (CPmax), tracers of nodes. The 68% and 99% contours correspond to results of short (orange) and long filaments (blue), to galactic haloes (dotted green lines), and CPmax (dashed-dotted red contours).

similar, except for a very slight difference in the φ_i amplitudes, that is most noticeable at the core of filaments ($r \leq 1$ Mpc). This difference is explained by the coarser Voronoi grid of the TNG300-2 box. Indeed, Fig. 5.6 clearly shows that the distribution of the cell volumes in the TNG300-2 simulation is considerably shifted towards the larger values with respect to the TNG300-1 distributions, and this is the case for all the gas phases. As a consequence, the coarser grid of the TNG300-2 box leads to a slightly different distribution of the gas cells in the phase-space plane, meaning that, unsurprisingly, the classification of the gas cells into the different phases is less precise in this simulation. For quantitative purposes, Table 5.3 shows the total fractions of the five different gas phases in the two simulations (the full simulation boxes, excluding nodes and haloes, are considered here). This table shows that, indeed, the TNG300-2 box possesses slightly different fractions of cells with respect to the reference TNG300-1, with larger fractions in the hotter phases (e.g. hot gas and WHIM), and reduced ones in the cooler phases (e.g. Diffuse IGM, halo gas). Nevertheless, the differences between the TNG300-1 and TNG300-2 simulations have an effect on the results that remains very tiny, concluding that the main findings presented here are resolution-independent.

5.1.4 Phase-diagrams

After characterising the general trends of how the different gas phases are distributed around filaments, let us now present a more refined study focusing on the distribution of gas in filaments at the cell level.

The study of mass fraction profiles has shown that the proportions of the different phases are not the same in filaments of different populations. In order to have a clearer picture of the physical properties of gas in the core of filaments, their gas content, at the cell level, is now analysed by means of phase diagrams. Such study at the cell level is necessary because, as previously mentioned, the frontiers between the five phases used in Fig. 5.5a must not be considered as sharp boundaries. This is particularly the case in cores of filaments (and in haloes and nodes) due to the numerous physical processes affecting the gas in these dense regions.

The phase diagrams of gas were built by considering cylinders of radius 1 Mpc around the spine of filaments. This radius was chosen following the results of Fig. 5.5a, as it corresponded to the distance from which the WHIM fraction starts decreasing, giving room to the other hotter and denser baryonic phases. The phase diagram of cells in filaments is presented in the 2D histogram of Fig. 5.7 (first panel). For the sake of comparison, the phase diagram of gas inside galactic haloes (see definition in the introduction of this Chapter) and around the nodes of the skeleton (i.e. the `DisPerSE` CPmax points) were also analysed. These are presented respectively in the second and third panels of Fig. 5.7, where the gas cells within spheres of radius $1 \times R_{200}$ centred on galactic haloes and on CPmax are displayed. Note that, as mentioned in the introduction of this Chapter, gas in these structures is not counted in the phase diagram of filaments.

The phase diagram of gas in filaments shows that most of the gas cells in these structures have temperatures and densities corresponding to the WHIM phase, which is in agreement with the previous results of Fig. 5.5a and Table 5.2. The contours of short and long filaments (orange and blue lines) are rather circular and share the common region around $n_{\rm H} = 10^{-5.3}$ cm^{-3} and $T = 10^{6.1}$ K. However, their overall distribution is significantly different, showing that these two populations of filaments are not made of exactly the same gas.

Indeed, contours of long filaments are shifted towards the cooler values with respect to short filaments, and they present a contribution of cold and diffuse IGM gas. The latter corresponds to primordial gas that has never been heated by baryonic processes, and whose temperature is regulated by the competition between radiative heating (by the UV background) and the expansion of the Universe (e.g. Valageas et al., 2003). On the other hand, short filaments present larger contributions of hot gas, as expected from these puffy and dense structures.

Let us now comment on the small, but non-negligible, presence of cold and dense gas (halo gas), in the bottom right of the phase portrait of filaments, as it might play a major role in the star formation of galaxies in filaments. Indeed, it is known that cores of filaments are mainly populated by quiescent galaxies, that have ceased forming stars (e.g. Malavasi et al., 2017; Kraljic et al., 2018, 2019; Bonjean et al., 2020). However, recent studies have claimed the detection of a slight increase of star formation in galaxies located in cores of filaments, at distances lower than $r < 1$ Mpc (Liao, Gao, 2019; Singh et al., 2020). According to Liao, Gao (2019), this burst of star formation might be explained by the presence of filaments, that can feed galaxies residing at their cores with cool and dense gas, acting as a reservoir of star formation for galaxies in these regions (see in particular Singh et al., 2020). This gas might correspond to the halo gas revealed in this work, and in the following paragraph it is shown that the presence of this cold and dense gas in the phase diagram of filaments is not a contribution of massive galactic haloes residing in these cosmic structures.

Indeed, Fig. 5.8 presents the phase-space of gas in filaments (within 1 Mpc from their spine), including the contribution from gas in galactic haloes residing in these core regions. Note substantial differences in the filament contours with respect to those of Fig. 5.7. The contours are now in elliptical shapes that follow exactly those of galactic haloes towards the hottest and densest values at the boundaries between the WHIM, WCGM, and hot phases. The comparison of this phase-space to the first panel of Fig. 5.7 explicitly shows the contribution of gas associated with galactic haloes residing in filaments. As previously mentioned, halo gas is also present in Fig. 5.8, with essentially the same significance as in Fig. 5.7, meaning that this phase cannot be interpreted as a contribution from massive galactic haloes in filaments.

The gas content of filaments is now compared with gas in galactic haloes and around CPmax

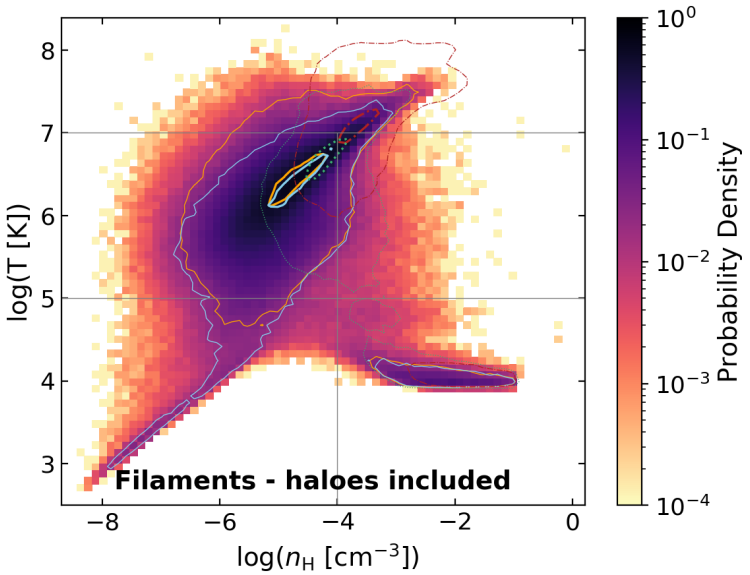

Figure 5.8: Phase-space of gas in filaments, including the contribution of galactic haloes (i.e. haloes of mass $M_{\rm tot} > 10^{12}\,{\rm M}_\odot$ hosting at least one galaxy of mass $10^9 \leq {\rm M}_*[{\rm M}_\odot] \leq 10^{12}$). The 68% and 99% contours correspond to results of short (orange) and long filaments (blue), to galactic haloes (dotted green lines), and gas around the maximum density critical points of the field (CPmax, in dash-dotted red contours).

(second and third panels of Fig. 5.7). Galactic haloes show a large amount of their cells in an elliptical pattern at temperatures from $10^{6.5}$ K to 10^7 K, that forms an elongated contour from WHIM to hot gas. As expected, there is also a significant contribution of cold and dense gas (halo gas) in these structures.

Gas around the CPmax, the tracers of nodes in this work (last panel) also exhibits the elliptical contour mentioned above, but the most striking feature of this phase portrait is the significant excess towards the hottest and densest parts of the plot, in the hot gas domain. This hot gas is expected around these critical points, that coincide with the densest structures of the universe where the shock-heating processes are the most efficient. Note that only a tiny fraction of gas in the WHIM region is detected around the CPmax, and that diffuse IGM gas is absent near these points, as well as in galactic haloes.

These results are found to be independent from the resolution of the simulation. The same analysis was run on the (lower resolution) TNG300-2 simulation, and the results on the phase-space of gas at cores of filaments ($r \leq 1$ Mpc) are presented in Fig. 5.9. In a similar way as for the mass fraction profiles, the impact of the simulation resolution is only tiny. The main difference highlighted by this figure is that the contours corresponding to the gas content of short and long filaments of the TNG300-2 box are slightly shifted in comparison to these of TNG300-1. This small difference is explained by the lower precision of the classification of the gas cells into the different phases, as previously shown in Fig. 5.6 and Table 5.3.

Finally, the phase diagrams presented here are compared with the existing literature, namely with the study of filaments and nodes of Martizzi et al. (2019), who also analysed the TNG300-1 simulation (see their Fig. 4). In that paper, the phase portrait of filaments exhibits a large

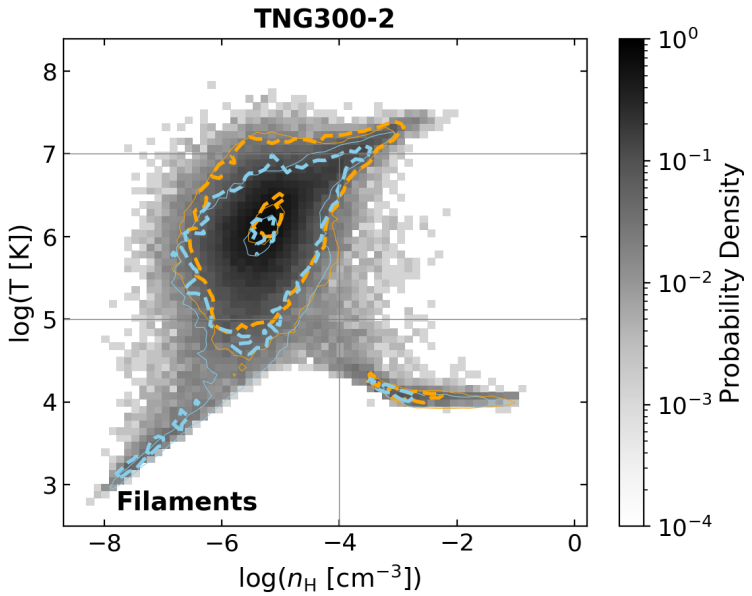

Figure 5.9: Phase-space diagram of cells at cores of filaments ($r \leq 1$ Mpc) in the TNG300-2 simulation. The specific contours of short and long filaments are shown by the thick dashed lines, respectively in orange and blue. The results from TNG300-1 (presented in Fig. 5.7) are over-plotted in thin solid lines. The contribution from gas in haloes are excluded.

number of cells aligned in the elliptical pattern (from WHIM to Hot medium) specific to collapsed structures. This is similar to that of Fig. 5.8 where the elliptical shape in the phase-space of filaments is due to the contribution of gas in haloes. Moreover, the phase portrait of nodes in Martizzi et al. (2019) shows a mixture of contributions from both the galactic haloes, and the gas around the CPmax points identified in this thesis. These differences can be explained by the very different cosmic classification method of Martizzi et al. (2019), where the association of gas to the different structures of the cosmic web (nodes, sheets, filaments and voids) is performed with an algorithm based on the Hessian of the density field. On the contrary, filaments are here detected using the `DisPerSE` algorithm and, since they are defined as the ridges of the Delaunay tessellation (see Sect. 3.1), one is able to locate the position of the filament spines as well as those of the CPmax points. In this thesis, galactic halo signatures have been identified in the phase portraits of filaments and nodes, and the gas content of different populations of filaments has been shown to be different. Such results are thus an interesting complement to those of Martizzi et al. (2019).

5.2 Temperature of gas in filaments

The previous Section presented the analysis of the distribution of the different gas phases around the filaments of the cosmic web. In what follows, the focus will be on a couple of thermodynamic parameters of gas, namely temperature and pressure. How do these quantities vary when approaching the filament spine? Do the different gas phases described in Sect. 5.1.2 vary in the same way? How does the picture change from one type of filament to the other? Gas temperature will be analysed in this Section, while the study of gas pressure is left for the next, Sect. 5.3.

One way to probe the radial evolution of gas temperature as a function of the distance to the

spine of the filament is to build radial temperature profiles. These were computed as volume-weighted averages of the temperature of the different gas cells, as shown by Eq. 5.3:

$$T(r_k) = \frac{\sum_{s=1}^{N_{\rm seg}} \left(\sum_{j=1}^{N(k)} T_{{\rm cell},j} \times V_{{\rm cell},j} \right)_s}{\sum_{s=1}^{N_{\rm seg}} \left(\sum_{j=1}^{N(k)} V_{{\rm cell},j} \right)_s} \ , \tag{5.3}$$

At the distance r_k from the spine of the filament, I summed the products between temperature and volume ($T_{\rm cell} \times V_{\rm cell}$) of the $N(k)$ cells inside the k-th cylindrical shell around the segment s. This procedure was repeated for the same k-th cylindrical shell of all the segments, and all the contributions were summed. This result was then divided by the sum of the volumes of all cells in the corresponding k-th shell of each segment. The aim of this method (volume-weighted profiles) is to retrieve results that are independent of the Arepo grid, i.e. independent of the irregular volumes of the simulation's Voronoi gas cells. More explicitly, the cell refinement criterion of the moving-mesh Arepo code is based on a fixed mass threshold (Weinberger et al., 2020), leading to a broad distribution of cell volumes. Therefore, the more conventional mass-weighted average profiles would have been biased by the different volumes of the gas cells. Finally, the error bars in all the following plots are estimated using the bootstrap method applied on the distribution of filament segments. As explained in Sect. 5.1.3, these error bars quantify the statistical variance of the different quantities around our limited sample of filaments.

5.2.1 Average profiles of all the gas

Figure 5.10a shows the temperature profiles for short ($L_f < 9$ Mpc), medium-length ($9 \leq L_f < 20$ Mpc), and long filaments ($L_f \geq 20$ Mpc) respectively in orange, green and blue. Note that these profiles present the temperature of all the gas, regardless of the phase. The following discussion focuses on the thick solid lines with circles, given that the thin dotted lines with squares correspond to the results when contributions of galactic haloes are included (these will be discussed in a dedicated paragraph at the end of this Section). The horizontal gray lines in this figure represent the mean temperatures of all the gas cells in the box (CPmax excluded), in each case.

The temperature profiles exhibit the main feature of an isothermal core up to $r_{\rm core} = 1.5$ Mpc from the axis of the filament. This trend is present in profiles of all three filament types (short, medium-length and long). It is worth noticing that the radial scale of $r_{\rm core} = 1.5$ Mpc is independent from the resolution of the simulation, as shown in Fig. 5.10b. Most likely, a more fundamental physical reason is behind this characteristic scale (for example, an equilibrium between the gas pressure, volume and density), but any conclusion is still premature at this stage and would require further investigations that are not addressed in this thesis. Note, however, that isothermal filament cores have already been observed in the temperature profiles of single simulated filaments in e.g. Klar, Mücket (2012) and Gheller, Vazza (2019). Here, this property is retrieved in a statistically significant way, despite the very different approach of filament detection (in Gheller, Vazza, 2019, the authors use an algorithm based on fixed density thresholds to detect filaments in the gas density field).

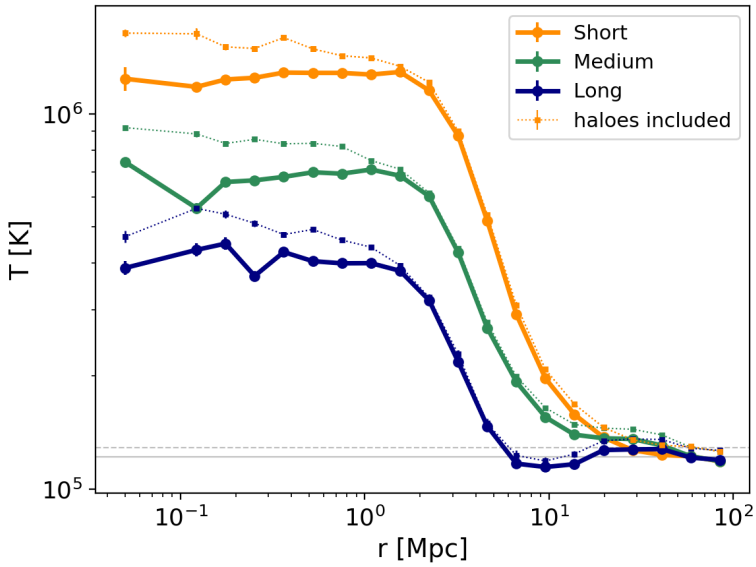

(a) Gas temperature profiles of short ($L_f < 9$ Mpc), medium-length ($9 \leq L_f < 20$ Mpc), and long filaments ($L_f \geq 20$ Mpc) respectively in orange, green and blue colours. Thick solid lines with circles correspond to the temperature profiles of gas cells in the inter-filament medium, while thin dotted lines with squares show the results where contributions of galactic haloes are included. For each case, the horizontal gray lines represent the average temperatures of all the gas cells (CPmax points excluded) in the box. These profiles clearly show the isothermal cores of filaments.

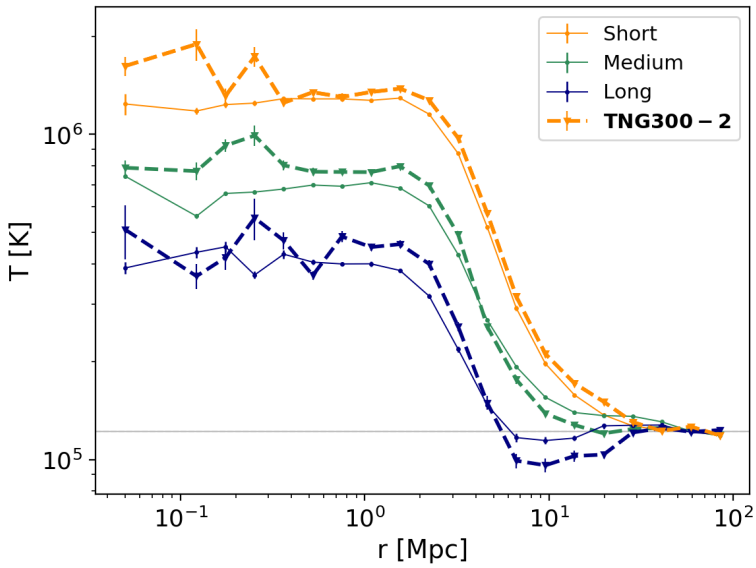

(b) Comparison with lower a resolution simulation. The thick solid lines of *(a)* are overlaid with the results of the TNG300-2 simulation (in thick dashed lines). These figures are extracted from Galárraga-Espinosa et al. (2021).

Figure 5.10: Gas temperature profiles around cosmic filaments.

Table 5.4: Temperature $T_{\rm core}$ [K] at the cores of short ($L_f < 9$ Mpc), medium-length ($9 \leq L_f < 20$ Mpc), and long filaments ($L_f \geq 20$ Mpc). These values are computed as the average temperature of the points at $r < 1.5$ Mpc.

	Inter-filament gas only	Inter-filament gas + haloes
Short	1.3×10^6	1.5×10^6
Medium	6.8×10^5	8.4×10^5
Long	4.1×10^5	4.9×10^5

Interestingly, the value of the plateau, $T_{\rm core}$, strongly depends on the length of the filament (e.g. orange vs blue curves). For quantitative purposes, Table 5.4 reports the different values of $T_{\rm core}$, computed directly from the profiles as the average temperature of the points at $r < 1.5$ Mpc. In the left side of this table, it is clearly seen that cores of short filaments are more than three times hotter than those of long filaments. Indeed, the gravitational heating efficiency is likely stronger in the short population, due to the deeper potential wells of these denser regions. Moreover, this result is independent of the presence or the absence of galactic haloes. Note that the temperature ranges of cores of filaments found in the present analysis are in agreement with the work of Tuominen et al. (2021), that studied filaments detected with the Bisous algorithm (Tempel et al., 2016) in the EAGLE simulation (Schaye et al., 2015).

At distances larger than $r = 1.5$ Mpc from the filament spine, the gas average temperature drops sharply. This drop is monotonic in short filaments, where the minimum of $T \sim 1.1 \times 10^5$ K is reached in the most distant regions from the filament (> 50 Mpc). This value represents the average temperature in regions that are very distant from the spine, so gas from other structures (namely other, distant filaments) is included in this average. By masking the gas cells from other filaments (at $r \leq 2$ Mpc from the spine) and removing their contribution to the temperature at large distances, a lower background average ($T \sim 8.5 \times 10^4$ K) was found. Unlike for short filaments, the temperature profiles of the long filaments do not follow a monotonic trend. They exhibit a global minimum at $r \sim 10$ Mpc, followed by a slight increase of the temperature, to finally reach the same background level as short (and medium-length) filaments. These dissimilarities between populations of short and long filaments at distances larger than $r = 1.5$ Mpc might come from their different environments in the cosmic web. Indeed, since short filaments statistically reside in denser regions (see Sect. 4.3), they are more likely to be immersed in already hot environments that contribute to the relatively high average temperature on the $r > 1.5$ Mpc outskirts. On the contrary, long filaments, tracers of less dense environments, extend into under-dense regions (voids) where the gas is cooler, which explains the dip at $r \sim 10$ Mpc, before the temperature reaches the average value of the entire box. Note that these differences in temperature between short and long filaments reflect well the phase portraits of Fig. 5.7.

5.2.2 Temperature profiles by gas phase

Let us now isolate the different gas phases to see how their temperatures behave around filaments. The five panels of Fig. 5.11 present the temperature profiles of the five different phases. Here, the same colour code as in Fig. 5.10a is adopted, and only the thick solid curves are discussed (corresponding to gas in the inter-filament medium, without the contribution of massive haloes). First of all, note that these profiles span a very broad temperature range, from cold temperatures of $T \sim 10^4$ K exhibited by the diffuse IGM (upper right panel), to the very hot

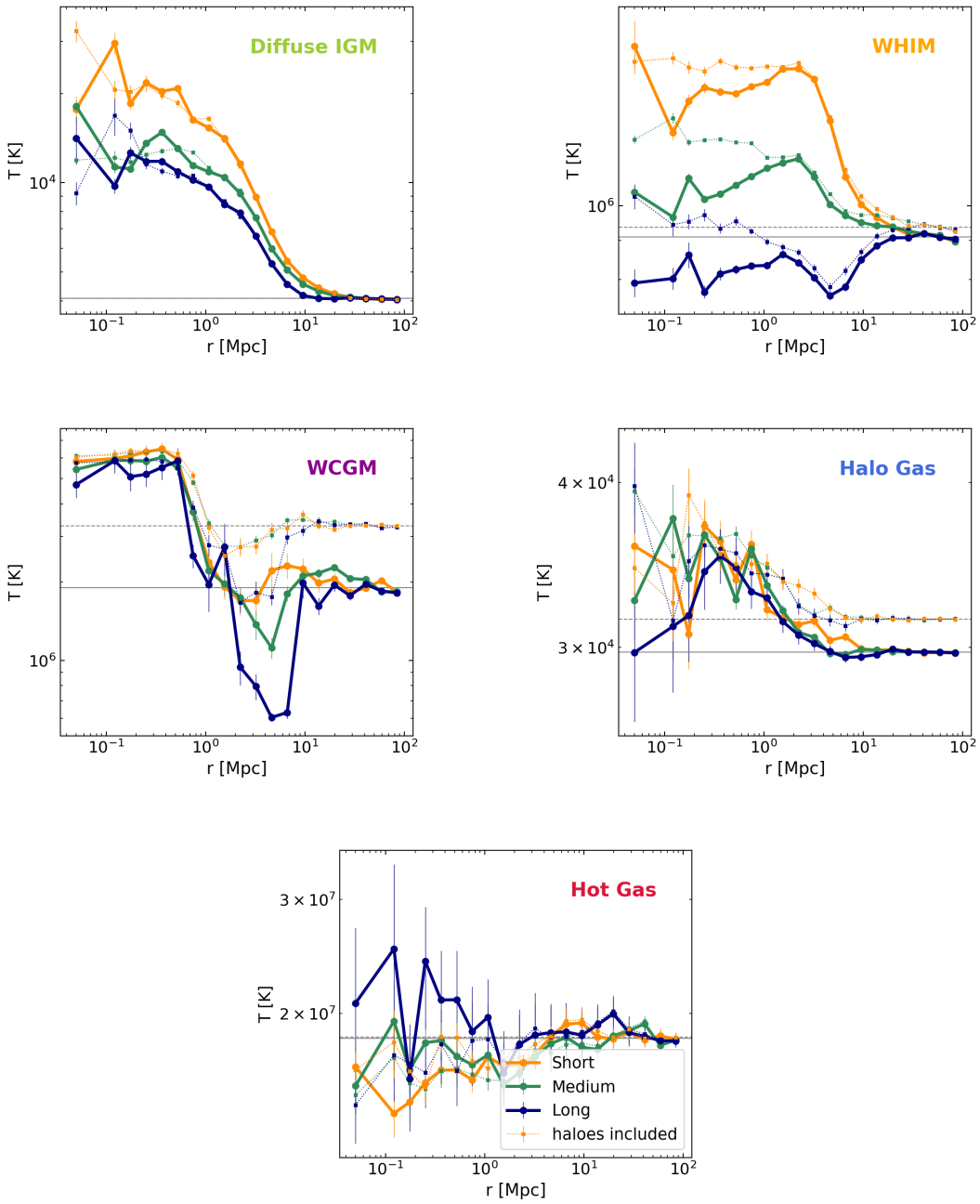

Figure 5.11: Temperature profiles of the different gas phases (see Table 5.1), for short ($L_f < 9$ Mpc, orange curves), medium-length ($9 \leq L_f < 20$ Mpc, green curves), and long filaments ($L_f \geq 20$ Mpc, blue curves). Thick solid lines with circles correspond to the temperature profiles of gas in the inter-filament medium, while thin dotted lines with squares show the results where contributions of galactic haloes are included. For each case, the horizontal gray lines represent the average temperatures of all the gas cells (CPmax points excluded) of each phase in the box.

values, of the order of $T \sim 2 \times 10^7$ K, reached by the hot gas (lower right panel). This broad range simply reflects the definition of the gas phases.

Very different shapes and behaviours, depending on the phase and on the type of filament, are exhibited. All the gas phases around the short population show a rise in temperature from the outskirts to the core, except the hot gas (last panel) that remains flat. The same trend is followed by gas around medium-length filaments, but in this case the temperature rise of the profile of WHIM is only very mild. Finally, the temperature profiles of the phases around long filaments exhibit a broader diversity.

The fact that the temperature profile of the hot gas phase remains essentially flat is easily understood by looking at Fig. 5.7, where the vast majority of the gas cells in filaments occupy only a limited and rather flat region that extends into the Hot gas phase domain. Moreover, these results concerning hot gas are in agreement with recent findings from X-ray ROSAT observations. Indeed, Tanimura et al. (2020b) detected a significant X-ray emission from hot gas at temperatures of $1.0^{+1.1}_{-0.7} \times 10^7$ K ($= 0.9^{+1.0}_{-0.6}$ keV) in filament cores, and this range is compatible with the mean temperature values of hot gas in filaments presented in this thesis.

Contrary to all phases, diffuse IGM gas (upper right panel) exhibits the most significant temperature increase, from the background to the core of filaments. For example, cores of short filaments are up to seven times hotter than their background temperature. The increase of temperature from background to core is smaller in long filaments (for which the temperature is only multiplied by three), and this might once again be related to their location in less dense environments of the cosmic web (see Sect. 4.3). For all filaments, this significant temperature increase in the diffuse IGM profile may be due to the gravitational heating resulting from the accretion of this diffuse gas into the filament (as discussed in Sect. 5.1.3). Note that the maximum temperature is not higher than 10^5 K, given that beyond this threshold gas is counted as part of the WHIM phase.

Concerning the WHIM (middle left panel), notably different temperature profiles for short, medium-length and long filaments are observed. The temperature of WHIM gas around short filaments increases with decreasing distance to the core, while in long filaments, the WHIM temperature shows a decrease in the outskirts ($r \sim 6 - 10$ Mpc). Once again, this can be seen as a consequence of the different cosmic web environments of the short and long filaments. Gas accreted towards short filaments is likely rapidly heated by shocks taking place in the denser environments that characterise these structures. On the contrary, due to its shallower potential wells, gas falling into long filaments is subject to less efficient gravitational interactions as gas falling into the short population.

Interestingly enough, the temperature profiles of the two phases corresponding to gas in and around haloes, respectively halo gas and WCGM, do not appear to be sensitive to the different types of filaments (and therefore to the large scale environment). As approaching the spine, circumgalactic gas gets heated by shocks and feedback processes near galaxies in fairly the same way for short and long filaments, as shown by their very similar profiles (see the WCGM and halo gas panels of Fig. 5.11). The profiles of these phases rather present a notable difference in the mean temperature levels (gray horizontal lines) weather galactic haloes are included (dotted lines) into the temperature estimation or not (solid lines). This feature is expected, given that halo gas and WCGM are tracers of haloes, and that these collapsed structures can be located in background and foreground filaments, thus contributing to the rise of the mean temperature. Further details on the part that galactic haloes contribute to the temperature of filaments are now discussed.

5.2.3 Contribution of galactic haloes in filaments

The results of Sect. 5.2.1 and 5.2.2 presented the properties of gas in the inter-filament medium, that is excluding the contribution of collapsed structures. Here, these findings are compared to the temperature profiles obtained when the galactic haloes (i.e. massive $M_{\rm tot} > 10^{12}$ M$_\odot$ haloes containing at least one galaxy of $10^9 \leq$ M$_* \leq 10^{12}$ M$_\odot$ in stellar mass; see the introduction of this Chapter) are retained. The profiles of filaments including the contribution of gas in haloes are presented by the thin dotted lines with squares in Fig. 5.10a and 5.11.

In general, the inclusion of the gas associated with haloes has the consequence of raising the temperature at the filament cores. These new temperature values are reported in the right side of Table 5.4, which shows that the cores of filaments appear on average ~ 1.2 times hotter when gas in haloes is included in the computation. This rise is expected as the previous Section has shown that galactic haloes (statistically located in cores of filaments) contribute with hotter and denser gas (see the phase-spaces of Fig. 5.7 and 5.8).

The contributions of galactic haloes are also disentangled in the temperature profiles of each of the five different gas phases. The profiles of the WHIM, WCGM, halo, and hot gas are clearly sensitive to the presence of galactic haloes, as solid and dotted curves are significantly different. However, the inverse trends are shown by the diffuse IGM phase. Indeed, the temperature profiles of the diffuse IGM phase are essentially the same whether galactic haloes are included or not. This simply reflects that this phase is absent in galactic haloes (as also shown in Fig. 5.7).

5.2.4 Scaling relations with gas density

As shown by the phase-space diagrams of Sect. 5.1.4, the temperature of gas in the different structures of the cosmic web is related to its density. This Section further studies the scaling relation $T - \rho_{\rm gas}$ of different populations of filaments. With the aim of comparing the results of filaments to those of other cosmic structures, the $T - \rho_{\rm gas}$ relations are also computed for clusters of galaxies, the densest structures of the cosmic web.

These structures were selected from the publicly available friend-of-friend (FoF) halo catalogue of the TNG300-1 simulation box. The most massive haloes of this catalogue were separated into three classes according to the mass: $10^{13} \leq M_{200} < 10^{14}$ (2369 haloes), $10^{14} \leq M_{200} < 10^{14.5}$ (138), and $M_{200} \geq 10^{14.5}$ M$_\odot/h$ (15 haloes), corresponding respectively to groups of galaxies, clusters, and massive clusters. Note that a few details on the FoF algorithm were presented in Sect. 2.1.3.

The mean temperature value (hereafter $\langle T \rangle$) of each filament was computed from its temperature profile, up to the radial distance $r_{\rm ext}$. Recall that this radius was defined in Sect. 4.2.2 as the radial extension of baryons in filaments (Fig. 4.18). The same was done for gas density, $\langle \rho_{\rm gas} \rangle$, using the gas density profiles presented in Sect. 4.2.1. This yielded one $\langle \rho_{\rm gas} \rangle$ and $\langle T \rangle$ value for each filament of the TNG300-1 catalogue. Note that in the case of clusters, the corresponding average quantities were computed up to the R_{200} radial scale.

The $\langle \rho_{\rm gas} \rangle$ and $\langle T \rangle$ distributions of filaments and clusters are presented in Fig. 5.12a. For comparison, this figure also shows the specific distributions of extreme filaments, i.e. the high-density (HD) short, and low-density (LD) long filaments. These filaments correspond respectively to the 25 and 75 percentiles of the short and long populations, and account for a number of 242 (short HD) and 112 (long LD). The distributions of Fig. 5.12a highlight the hierarchical

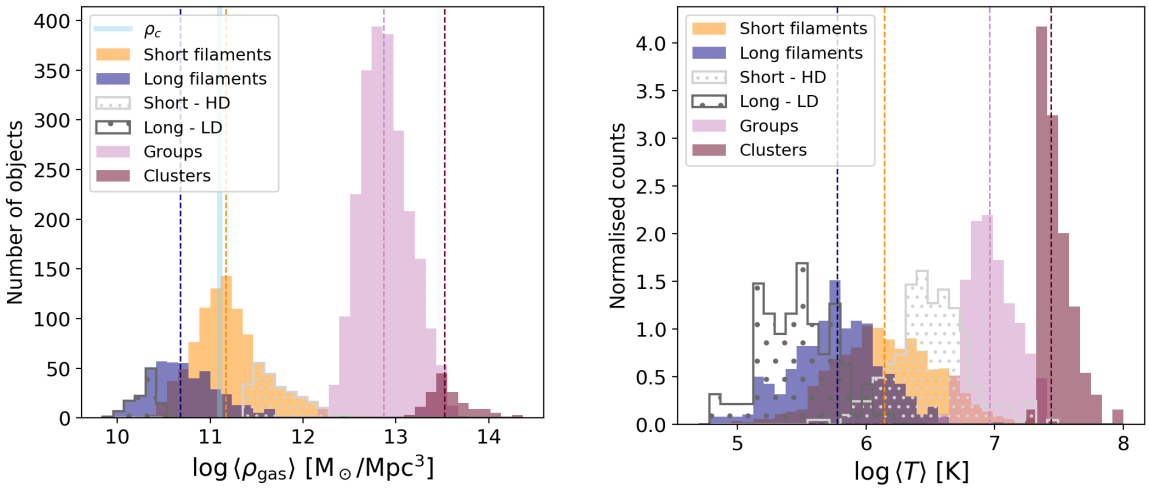

(a) $\langle\rho_{\rm gas}\rangle$ and $\langle T\rangle$ distributions of filaments and clusters. The vertical dashed lines correspond to the median values of each distribution. For reference, the critical density of the Universe, ρ_c, is presented in the gas distribution by the vertical light-blue line.

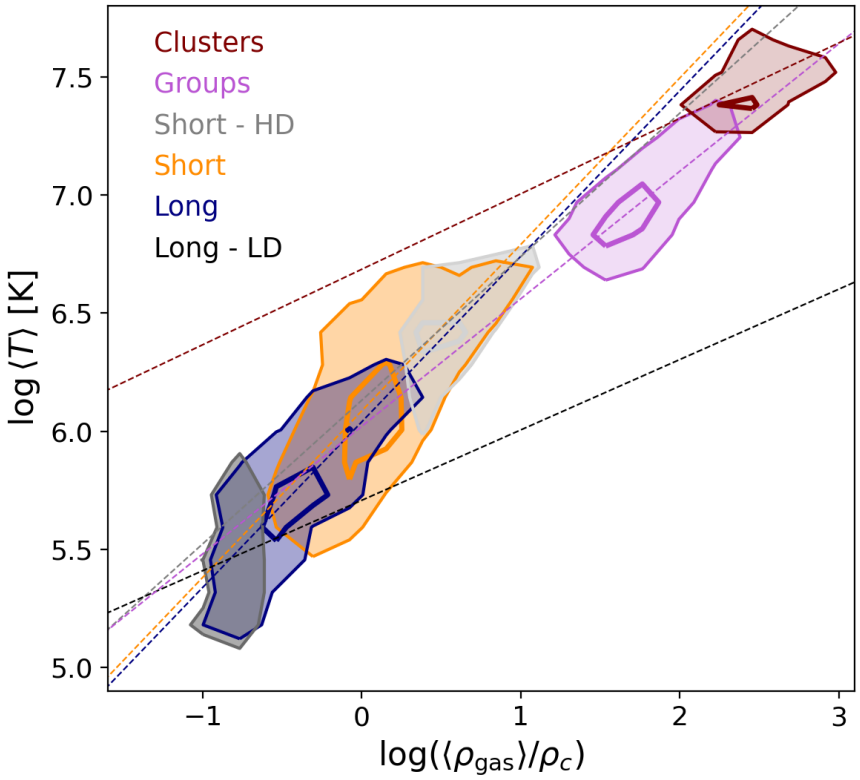

(b) Scaling relations for filaments and galaxy clusters. For each structure, the dashed line corresponds to the linear function of Eq. 5.4 using the parameters resulting from the fit, reported in Table 5.5. Short-HD and Long-LD filaments correspond respectively to the 25 and 75 percentiles of the short and long populations.

Figure 5.12: Scaling relations between gas density and temperature

Table 5.5: Results of the scaling relations between pressure and gas density, $\log\langle T\rangle = \alpha \log\left(\langle\rho_{\rm gas}\rangle/\rho_c\right)+\beta$. The reduced chi-squared values, χ^2_ν, resulting from the fit are presented in the last column.

	α	β	χ^2_ν
Clusters	0.32 ± 0.03	6.69 ± 0.08	0.01
Groups	0.54 ± 0.01	6.02 ± 0.02	0.01
Short filaments - HD	0.61 ± 0.07	6.13 ± 0.05	0.07
Short filaments (all)	0.70 ± 0.03	6.09 ± 0.01	0.10
Long filaments (all)	0.70 ± 0.03	6.04 ± 0.02	0.06
Long filaments - LD	0.30 ± 0.20	5.71 ± 0.17	0.08

structure of the cosmic web, with the densest structures (i.e. clusters) being hotter and with higher pressure values than the least dense ones (i.e. long filaments).

The scaling relations between gas density and temperature for filaments and clusters were obtained by fitting the following function in the $\langle\rho_{\rm gas}\rangle - \langle T\rangle$ plane:

$$\log\langle T\rangle = \alpha \log\left(\langle\rho_{\rm gas}\rangle/\rho_c\right)+\beta. \tag{5.4}$$

The resulting scaling relations are presented in Fig. 5.12b, and the values of the fitting parameters are reported in Table 5.5.

As for the 1D distributions, the 2D contours in the $\langle\rho_{\rm gas}\rangle - \langle T\rangle$ and plane clearly reflect the hierarchy between the considered structures: clusters are found in the upper right corner of the plots (where the density, temperature, and pressure values are the highest), and groups, short, and long filaments are distributed in a decreasing diagonal (in this respective order) down to the lower left corner, where the values are the lowest. Nevertheless, a closer inspection to the resulting fitting parameters shows that the structures do not follow a perfect diagonal in the $\langle\rho_{\rm gas}\rangle - \langle T\rangle$ plane. Indeed, each structure possesses a different value of their slope α. Despite the values being encompassed in a tight range ($\alpha \in [0.30, 0.70]$ see Table 5.5), a clear steepening of the slope is seen in structures with decreasing density. Note the large uncertainties in the α value of the low density long filaments (Long - LD). These are due to the rather broad temperature and pressure ranges exhibited by this sub-set of 112 filaments (see Fig. 5.12a), leading to 2D asymmetrical distributions that are harder to constrain. The differences highlighted above indicate that it is possible to differentiate between the types of cosmic structures by their relation in the $\langle\rho_{\rm gas}\rangle - \langle T\rangle$ plane.

5.3 Pressure of gas in filaments

Following the previous study of the temperature of gas, let us now focus on the gas pressure in cosmic filaments. This analysis is motivated by the fact that gas in filaments can be observed via the Sunyaev-Zel'dovich (SZ) effect, as shown by the recent studies of stacked SZ signal around filaments of de Graaff et al. (2019); Tanimura et al. (2020a,c). Nevertheless, it is difficult to constrain the properties of gas in these observations (for example, the degeneracy between density and temperature complicates the interpretation of the SZ signal). Thus studies in simulations are needed in order to better understand and calibrate the results from observations.

Table 5.6: Pressure $P_{\rm core}$ [keV.cm^{-3}] at the cores of short ($L_f < 9$ Mpc), medium-length ($9 \leq L_f < 20$ Mpc), and long filaments ($L_f \geq 20$ Mpc) of the TNG300-1 box. These numbers correspond to the read from the first radial bin of the profile, that is at $r = 0.05$ Mpc.

	Inter-filament gas only	Inter-filament gas + haloes
Short	1.2×10^{-6}	5.1×10^{-6}
Medium	6.4×10^{-7}	2.8×10^{-6}
Long	3.8×10^{-7}	1.3×10^{-6}

The pressure profiles of gas in filaments are presented in Sects. 5.3.1, and 5.3.2, respectively for all the gas (all phases included), and for each individual phase. The derived pressure profiles are then used in Sect. 5.3.3 to estimate the Sunyaev-Zel'dovich signal of cosmic filaments in the TNG300-1 simulation.

5.3.1 Pressure profiles of all the gas

The profiles of gas pressure around filaments were computed using the same method as for temperature, i.e. by performing volume-weighted averages of the cells located in concentric hollow cylinders, as shown by:

$$P(r_k) = \frac{\sum_{s=1}^{N_{\rm seg}} \left(\sum_{j=1}^{N(k)} P_{{\rm cell},j} \times V_{{\rm cell},j} \right)_s}{\sum_{s=1}^{N_{\rm seg}} \left(\sum_{j=1}^{N(k)} V_{{\rm cell},j} \right)_s}. \tag{5.5}$$

The notations in this equation are the same as in Eq. 5.3.

Before showing the results for each gas phase, let us first focus on the general pressure profiles, computed considering all the gas cells. These are shown in Fig. 5.13a for short, medium-length, and long filaments. As expected from the previous results of this thesis, filaments of different lengths have significantly different pressure profiles. At the core ($r \leq 1$ Mpc) and on the outskirts ($1 < r \leq 10$ Mpc), short filaments show values that are more than three times those of long filaments, as reported on the left side of Table 5.6 (where the values correspond to the pressure read from the first radial bin). The same trends as for the temperature profiles of Fig. 5.10a are observed in Fig. 5.13a; these trends are the monotonic decrease of short filament profiles and the presence of a global minimum in the pressure at the outskirts of long filaments. As for temperature, these differences might be related to the different environments traced by the two populations (see Sect. 4.3).

When the contribution of gas in galactic haloes is included in the computation of the pressure profiles (thin dotted lines with squares), the pressure at the filament cores of all the filament types is multiplied by about a factor of three. These new pressure values (including haloes) are reported on the right side of Table 5.6. Note that the pressure gap between the two columns can be explained by the fact that galactic haloes and clusters reach pressures that are several orders of magnitude higher (see below) than findings in the intra-filament medium, thus raising the average values.

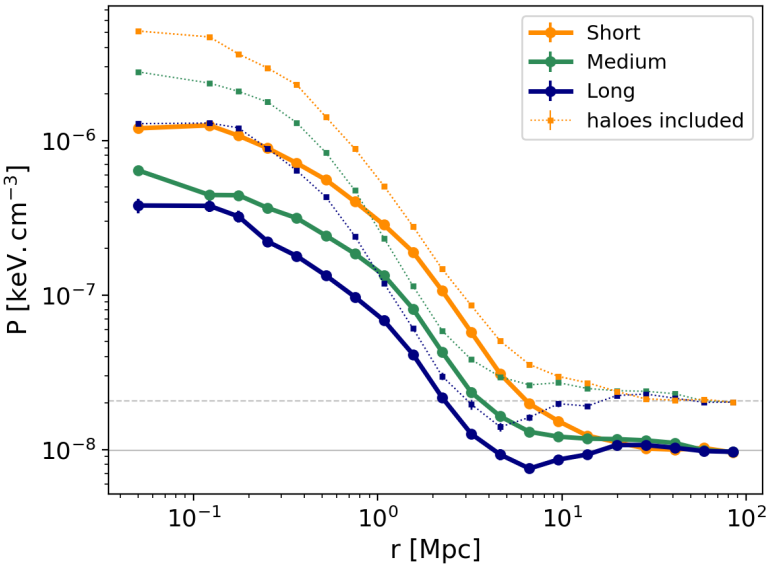

(a) Gas pressure profiles of short (L_f < 9 Mpc), medium-length (9 ≤ L_f < 20 Mpc), and long filaments (L_f ≥ 20 Mpc) respectively in orange, green and blue colours. Thick solid lines with circles correspond to the pressure profiles of gas cells in the inter-filament medium, while thin dotted lines with squares show the results where contributions of galactic haloes are included. For each case, the horizontal gray lines represent the average pressure of all the gas cells (CPmax points excluded) in the box.

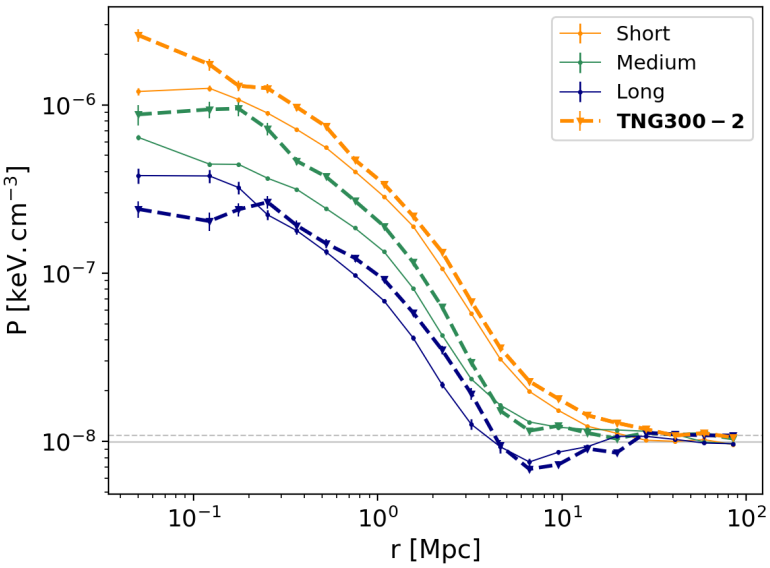

(b) Comparison with lower a resolution simulation. The thick solid lines of *(a)* are overlaid with the results of the TNG300-2 simulation (in thick dashed lines). These figures are extracted from Galárraga-Espinosa et al. (2021).

Figure 5.13: Gas pressure profiles around cosmic filaments.

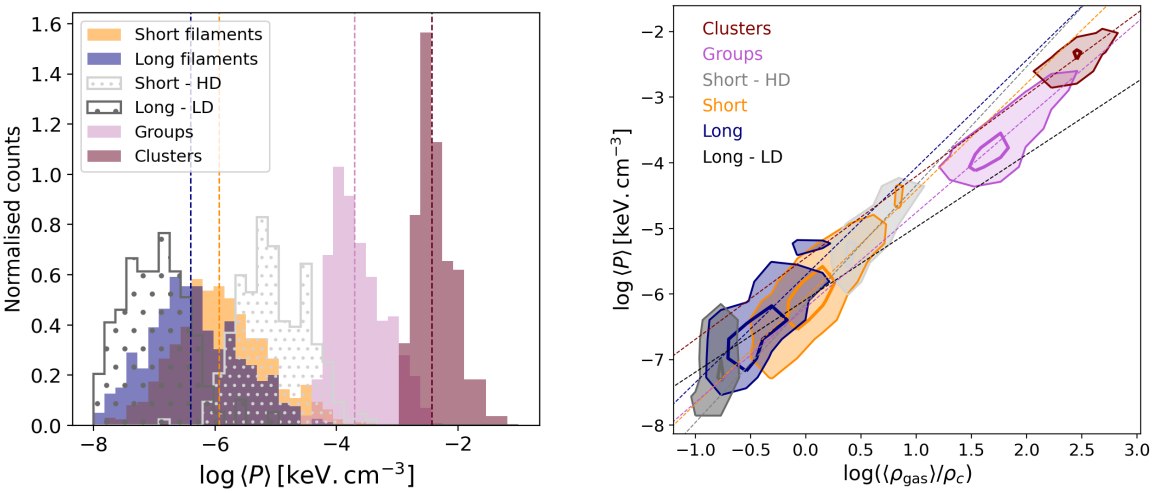

Figure 5.14: *Left:* $\langle P \rangle$ distributions of filaments and clusters. The vertical dashed lines correspond to the median values of each distribution. *Right:* Scaling relations between temperature (left) and pressure (right) with gas density, for filaments and galaxy clusters. For each structure, the dashed line corresponds to the linear function of Eq. 5.4, with the parameters of Table 5.5 and 5.7 for temperature and pressure, respectively.

Table 5.7: Results of the scaling relations between pressure and gas density, $\log \langle P \rangle = \alpha \log \left(\langle \rho_{\rm gas} \rangle / \rho_c \right) + \beta$.

	α	β	χ^2_ν
Clusters	1.24 ± 0.03	-5.45 ± 0.08	0.01
Groups	1.45 ± 0.02	-6.21 ± 0.03	0.05
Short filaments - HD	1.81 ± 0.09	-6.15 ± 0.06	0.11
Short filaments (all)	1.63 ± 0.04	-6.05 ± 0.01	0.19
Long filaments (all)	1.69 ± 0.06	-5.71 ± 0.03	0.22
Long filaments - LD	1.11 ± 0.39	-6.09 ± 0.32	0.31

A comparison of the pressure of filaments to that of groups and clusters is presented in Fig. 5.14. Here, the pressure distributions (left panel) show that filaments and clusters have well defined and distinct pressure ranges. Interestingly, the median values are 1.15×10^{-6} and 3.98×10^{-7} keV.cm^{-3} respectively for short and long filaments, and these are found to be overall 1000 times smaller than the medians of the distributions of groups and clusters (respectively 1.97×10^{-4} and 3.69×10^{-3} keV.cm^{-3}). This difference of three orders of magnitude between the pressure of these two types of cosmic structures is not surprising given that the galaxy clusters are the densest and hottest structures of the cosmic web. Note that these findings are in good agreement with Arnaud et al. (2010), who showed that pressure in the cores of galaxy clusters lies in the range of $P = 1 - 300 \times 10^{-3}$ keV.cm^{-3}.

Following Sect. 5.2.4, the right panel of Fig. 5.14 presents the scaling relations between gas density and pressure. The resulting parameters, determined by the fit of Eq. 5.4 to the 2D distributions in the $\langle \rho_{\rm gas} \rangle - \langle P \rangle$ plane, are presented in Table 5.7. As for temperature, each structure possesses a different value of their slope α in the $\langle \rho_{\rm gas} \rangle - \langle P \rangle$ (here $\alpha \in [1.11, 1.81]$), whose steepening in structures with decreasing density is also apparent.

As for temperature, the pressure of the TNG300-2 filaments is analysed in order to test the effects of resolution on the results. The corresponding profiles, shown in Fig. 5.13b, are overall in good agreement with the results of the higher resolution TNG300-1. Nevertheless, some small discrepancies can be spotted, like the fatter core of the TNG300-2 profiles. These can be explained by the reduced precision in the detection of filaments by the `DisPerSE` algorithm, coming from the smaller number of tracers (i.e. galaxies) in the lower resolution simulation, TNG300-2. These resolution effects, that increase the uncertainty in the position of filaments, were thoroughly studied in the study of galaxy density profiles of Sect. 4.1.

5.3.2 Pressure profiles by gas phase

Figure 5.15 presents the pressure profiles of each gas phase. Similar to the results on gas temperature, pressure exhibits a very broad range of values, that are particular to each of the different gas phases. Notably, the WCGM and hot phases reach maximum values of $P \sim 10^{-4}$ keV.cm^{-3}, which are comparable to pressures on the outskirts of clusters of galaxies (Arnaud et al., 2010). Interestingly, the pressure profiles of the latter phases, along with those of halo gas, do not show a strong dependence on the type of filament (i.e. the coloured curves are essentially the same), showing that the pressures of WCGM, halo, and hot gas are quite insensitive to the large-scale environment in the cosmic web (i.e. denser v.s. less-dense regions). This is expected for phases that are associated with collapsed structures such as haloes. The opposite trend is observed in the pressure profiles of diffuse IGM and WHIM phases (first and second panels of Fig. 5.15). They present significant differences for short, medium-length, and long filaments, showing that the properties of these phases are mainly ruled by the different environments in the cosmic web (traced by short and long filaments). This dependencies were already pointed out by the diffuse IGM and WHIM temperature profiles of Fig. 5.11.

The same qualitative results as for temperature are obtained when the contribution from massive galactic haloes is included in the pressure analysis (thin dotted lines with squares). Indeed, the pressure of all the gas phases is enhanced except for that of the diffuse IGM, which is basically the same as when haloes are excluded from the computation. Again, this just reflects the fact that diffuse IGM gas is absent in haloes. Note the different background levels between the solid and dotted profiles of the WHIM, WCGM, halo and hot gas. This shows that haloes

contribute to the rise of the pressure values not only at the cores of filaments, but also at large distances from their spine, where other structures (e.g. other filaments) are likely to be found.

Let us now specifically focus on the WHIM phase, as some interesting features are exhibited by its pressure profiles. First, note that WHIM pressures increase by almost two orders of magnitude from the outskirts to the cores of filaments. Almost all the profiles show a low-pressure zone at $r \sim 3$ Mpc (with respect to the mean value, see the dip), and this is most marked in the results of long filaments, which are tracers of cosmic regions with low and moderate densities. This dip was already visible in Figs. 5.10a and 5.13a and is probably due to the under-dense environment around the longer filaments, where the gas is cooler and less dense. This decrease of pressure happens at the same distance ($r \sim 3$ Mpc) from the cores of all the filaments regardless of their length, exhibiting a characteristic radius of WHIM pressure around filaments. This common feature shows that WHIM gas might be ruled by the same physical processes (gravity and baryonic effects) in all types of filaments, although with different efficiencies since the pressure values are different. Moreover, WHIM gas pressure does not follow the distribution of galaxies. Indeed, using the same simulations, in Sect. 4.1 it was shown that galaxies are statistically closer to cores of long filaments than to short (with characteristic radii of $r_2 \sim 3$ and 5 Mpc, respectively). These different scales are not exhibited by the pressure of WHIM gas, which instead highlights the existence of different populations by the very marked hierarchy in the values of the pressure profiles.

5.3.3 Estimation of SZ signal

Gas pressure can be measured via the thermal Sunyaev-Zel'dovich (SZ) effect (Zeldovich, Sunyaev, 1969; Sunyaev, Zeldovich, 1970, 1972). From the mean pressure profiles presented in this thesis (Fig. 5.13a), Compton y-profiles of gas around filaments were computed. Two extreme cases of filament orientation with respect to the line of sight (l.o.s.) are presented in this thesis: the filament is perpendicular to the l.o.s., which gives a lower limit of SZ signal; and the filament is parallel to the l.o.s. (upper limit of SZ signal). In the following, the assumption that filaments are far enough from the observer is made, thus all l.o.s. are be parallel.

For the perpendicular orientation, the Compton-y value at the distance R from the spine of the filament (R is the projected distance on the sky) was computed using the following equation:

$$y(R) = \frac{\sigma_T}{m_e\, c^2} \int_0^{+\infty} 2\; P\left(\sqrt{R^2 + l^2}\right) dl, \tag{5.6}$$

where σ_T, m_e, and c are the Thomson scattering cross-section, electron mass, and speed of light in vacuum, P is the mean pressure profile of Fig. 5.13a, and l denotes the distance from the filament to the observer along the l.o.s..

In the second case, the filament is parallel to the l.o.s. and the Compton-y parameter depends on filament length L_f, as shown by

$$y(R) = \frac{\sigma_T}{m_e\, c^2} P(R)\, L_f. \tag{5.7}$$

Given in this computation mean profiles of each filament population are used, the corresponding filament length values that are the average lengths $\overline{L_f} = 5.7, 13.3$, and 27.1 Mpc for short, medium-length, and long filaments, respectively.

The resulting Compton-y profiles are shown in Fig. 5.16 for short (left panel), medium-length (middle), and long filaments (right panel). The curves corresponding to the lower and

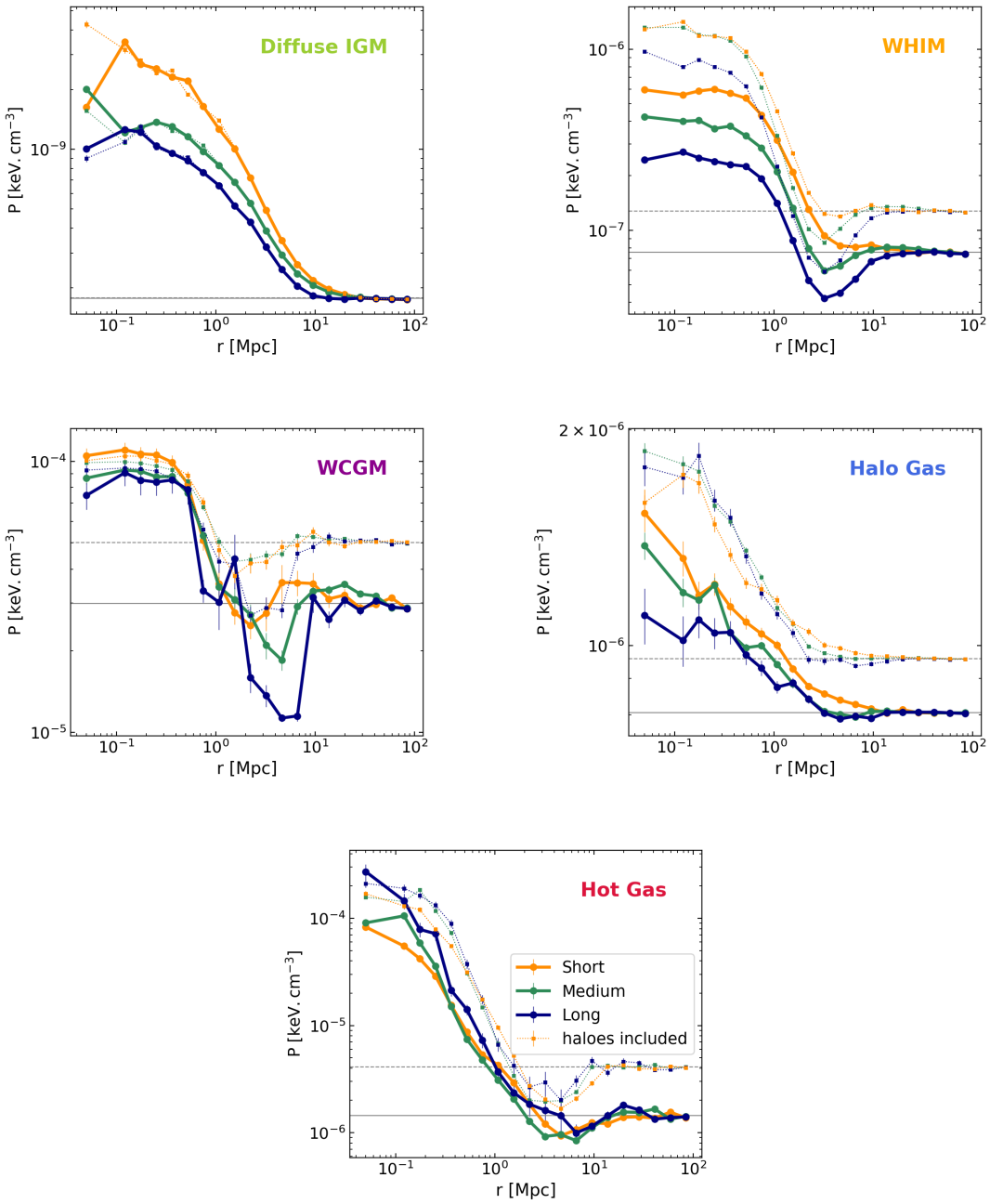

Figure 5.15: Pressure profiles of the different gas phases (see Table 5.1), for short (L_f < 9 Mpc, orange curves), medium-length (9 ≤ L_f < 20 Mpc, green curves), and long filaments (L_f ≥ 20 Mpc, blue curves). Thick solid lines with circles correspond to the pressure profiles of gas in the inter-filament medium, while thin dotted lines with squares show the results where contributions of galactic haloes are included. For each case, the horizontal gray lines represent the average pressure computed from all the gas cells (CPmax points excluded) of each phase in the box.

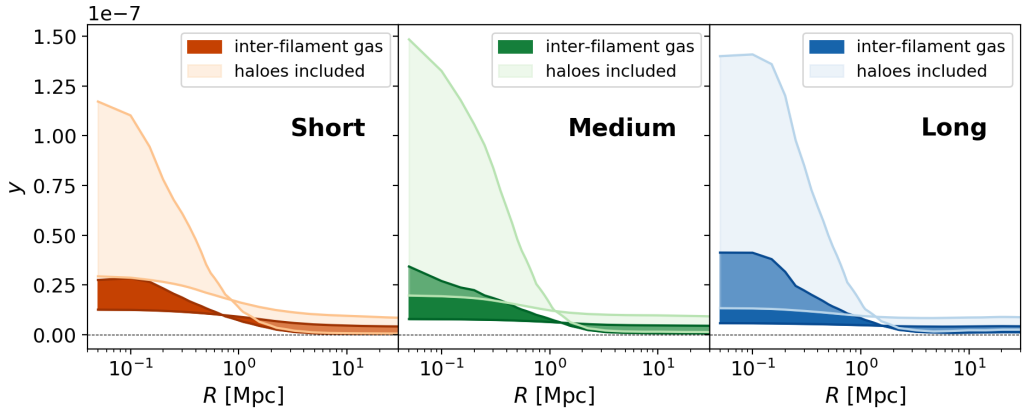

Figure 5.16: Compton-y profiles of short ($L_f < 9$ Mpc), medium-length ($9 \leq L_f < 20$ Mpc), and long filaments ($L_f \geq 20$ Mpc) in the left, middle, and right panels, respectively. The dark colours show the SZ signal from inter-filament gas, that is gas that excludes the contribution of galactic haloes (massive $M_{\rm tot} > 10^{12}\,{\rm M}_\odot$ haloes hosting at least one galaxy of stellar mass $10^9 \leq {\rm M}_* \leq 10^{12}\,{\rm M}_\odot$). The light colours correspond to the SZ signal in filaments, where the contributions of galactic haloes are included. The lower and upper limits are computed with Eq. 5.6 and 5.7, respectively, using the mean filament lengths of each population: $\overline{L_f} = 5.7$ (short), 13.3 (medium), and 27.1 Mpc (long filaments).

upper signal limits are computed with Eq. 5.6 and 5.7, respectively, and so the expected SZ signal from the various orientations should be bracketed between these curves in the colour-filled regions. The dark colours show the results from inter-filament gas excluding galactic haloes, while light colours correspond to the results including the contributions of these structures.

At cores of filaments, we see that the values of the SZ signal for the perpendicular orientation are the largest in short filaments. This is due to the high pressures and the wider shape of the pressure profile of this population with respect to the other medium-length and long filaments. Concerning the parallel orientation, in the case in which the contribution from galactic haloes is removed (dark colours), the maximum SZ signal of the inter-filament medium is associated with long filaments, with $y = 4.1 \times 10^{-8}$ at their core (see dark blue upper limit), as expected from a signal that is proportional to filament length (Eq. 5.7). Interestingly, note that the upper values in cores of short and medium-length filaments, $y \sim 2 - 3 \times 10^{-8}$, are close to that of the long-filament population; this is a result of the larger pressure values of these populations (see Fig. 5.13a), which compensate the smaller filament lengths.

It is worth noticing that the inclusion of gas in galactic haloes (light colours) increases significantly, by a factor three, the SZ signal, which is expected since these structures are hotter and denser and might be strong SZ sources by themselves. Indeed, when galactic haloes are taken into account, the resulting SZ signal at filament cores is around $y \sim 1.2 \times 10^{-7}$ for the short population, $y \sim 1.5 \times 10^{-7}$ for medium-length, and $y \sim 1.4 \times 10^{-7}$ in long filaments. Maximum values are proportional to both pressure and filament length, so the similar y values in medium-length and long filaments are due to the higher pressures in the former, and to the longer lengths of the latter.

The SZ signal between pairs of clusters has been measured in *Planck* data, but the comparison of these results to these findings from simulations faces intrinsic limitations (e.g. instrumental noise, density of sources, foregrounds, etc.). It is however remarkable that the ranges of expected y values from filaments including haloes are of the same order of magnitude as SZ

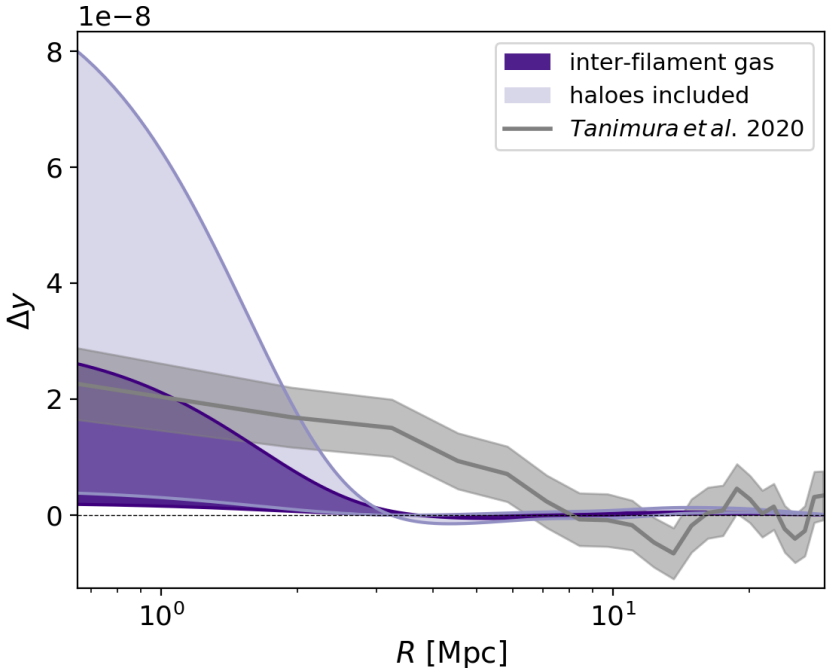

Figure 5.17: Mean Δy profile of long filaments ($L_f \geq 20$ Mpc), convolved with the *Planck* beam at $z = 0.4$. The dark purple shows the results of gas in the inter-filament medium (i.e. excluding the contribution of galactic haloes), while light purple presents our findings when galactic haloes are included. The lower and upper boundaries (solid purple lines) are computed using Eq. 5.6 and 5.7, respectively. We compare our results from simulations with observations from Tanimura et al. (2020a), which are shown in grey (line and 1σ errors).

measurements around luminous red galaxies of mass $M_* > 10^{11.3}$ $M_\odot$ (Tanimura et al., 2019). Also, these results can be compared to the measured SZ signal from the bridge between the clusters A399-A401 of Bonjean et al. (2018). The signal in this filament was found to be remarkably high, with a value of the Compton-y parameter of $\sim 10^{-5}$. This is about two orders of magnitude higher than the predicted ranges in filaments (including the contribution of haloes), which is not surprising from this exceptional bridge.

Finally, a more complete comparison was performed with the recent measurements at 4.4σ significance of SZ signal from hot ionised gas around large-scale filaments presented in Tanimura et al. (2020a). In that paper, the authors built an average Compton-y profile by stacking the *Planck* 2015 (Planck Collaboration et al., 2016b) y map, after removing the contribution of known groups and clusters, around filaments detected in the Sloan Digital Sky Survey (SDSS) by Malavasi et al. (2020a). To reproduce the observational constraints of Tanimura et al. (2020a), the mean y profile obtained for the long filament population was used. This is the closest possible to the sample of long ($30 - 100$ Mpc) filaments used in Tanimura et al. (2020a). Notice that within the `DisPerSE` framework, filament lengths strongly depend on the density of tracers. The filament catalogue in Malavasi et al. (2020a), from SDSS, and in this thesis are derived with 4×10^{-4} and 10^{-2} galaxy/Mpc^3 respectively. As a consequence, the filament length distribution of the SDSS catalogue misses a lot of short filaments and thus peaks at $20 - 30$ Mpc. The mean y profile of long filaments was rescaled to the average redshift of $z = 0.4$ of the observed filament sample. This was performed by multiplying the pressures by the factor $(1 + z)^3$, so that the underlying electron densities measured today are closer to their values at $z = 0.4$. Notice that the implicit assumption that that the expansion of the Universe is negligible in the gas temperature is made here, since at first order temperature is ruled by the baryonic interactions of the local (over-dense) environments. Of course, a more precise comparison should be done by performing the analysis on a simulation at the same redshift as (Tanimura et al., 2020a), but this is beyond the scope of this analysis. Moreover, the y profile was convolved by a Gaussian beam of 10 arcmin at redshift $z = 0.4$, corresponding to resolution of the SZ *Planck* map analysed in Tanimura et al. (2020a). Finally, following their approach, the excess of SZ signal Δy with respect to the background was obtained by dividing the y profile derived from simulations by its background value, defined as the mean value at distances $r > 25$ Mpc from the spine.

The resulting Δy profiles are shown in Fig. 5.17 in light and dark purple, while the measurement from Tanimura et al. (2020a) is shown in grey (lines and shaded regions of 1σ errors). For the inter-filament gas, that the maximum SZ signal derived from the TNGsimulation is expected to be $\Delta y = 2.6 \times 10^{-8}$, which is compatible within the 1σ with the Tanimura et al. (2020a) profile. Given that these values correspond to upper bounds and that the observed filaments have a distribution of orientations, a small contribution from the galactic haloes is expected in the measured signal, as suggested by the predicted signal of filaments including haloes (light purple curve) peaking at $\Delta y = 8.0 \times 10^{-8}$. Moreover, the differences in the radial extent of the profiles could be explained by the reduced number of tracers in the SDSS catalogue (as mentioned above). The low galaxy density increases the uncertainties on the position of the filament spines, thus broadening the cores of the `DisPerSE` filaments (as shown in Sect. 4.1). However at this stage, it is not possible distinguish this effect from possible thicker filament cores that would be expected at higher redshifts.

5.4 Conclusions

This Chapter presented an analysis of the gas distribution and properties around the filamentary structures of the cosmic web. Throughout this analysis, gas was separated into five different phases according to their density and temperature in the phase-space diagram. The following conclusions were derived from the study of the TNG300-1 simulation at redshift $z = 0$, and by performing the same analysis in the TNG300-2 box, these are find to be independent from the resolution of the simulation.

Cores of filaments ($r \leq 1$ Mpc) essentially contain WHIM gas, in agreement with Nevalainen et al. (2015); Cui et al. (2018b, 2019); Martizzi et al. (2019); Tuominen et al. (2021). Nevertheless, the hotter and denser phases of hot gas and WCGM are also significantly present in these innermost regions. Interestingly, cores of short and long filaments were found to host different proportions of gas phases. Short filaments contain hotter gas than the long filaments, and the latter possess a contribution of cold and diffuse IGM gas at their cores that is absent in the former. Following Sect. 4.3, these differences are explained by the different large-scale environments, which are denser and less-dense for short and long filaments, respectively. The average temperature and pressure at cores of filaments ($r \leq 1$ Mpc) is estimated to be $T = 4-13\times10^5$ K, and $P = 4 - 12 \times 10^{-7}$ keV.cm^{-3}, and depends on the filament population, since short filaments have temperature and pressure values that are three times those of long filaments. Moreover, all filaments present isothermal cores up to distances of $r_{\rm core} = 1.5$ Mpc, which agrees with previous studies (Klar, Mücket, 2012; Gheller, Vazza, 2019). Finally, pressures in filament cores were found to be ~ 1000 times lower than those in cores of clusters (in agreement with Arnaud et al., 2010), and well defined pressure ranges are observed between filaments and clusters.

At larger distances from the cores, $r \sim 1$ Mpc from the spine of filaments, WHIM gas is found to completely dominate ($> 80\%$) the entire gas budget, and the other phases are negligible. This reflects very well the results of the baryon fraction profiles analysed in Sect. 4.2.2.

In order to build a clearer picture of the different temperatures and pressures of cosmic structures, scaling-relations were computed for gas in filaments, and the results were compared to the findings in groups and clusters of galaxies. The scaling relations of temperature and pressure showed to be different between the filaments and clusters, indicating that it is possible to differentiate between the types of cosmic structures by their relation in the $\langle\rho_{\rm gas}\rangle - \langle T\rangle$ and $\langle\rho_{\rm gas}\rangle - \langle P\rangle$ planes.

Regarding the different gas phases, this study showed that diffuse phases (diffuse IGM and WHIM) are extremely sensitive to the large-scale cosmic environment, traced by short and long filaments. These phases are the most present at the outskirts of filaments ($r > 1$ Mpc) and in more remote regions, and as already hinted in Sect. 4.2.2, they might be shaped by the gravitational pull towards filament cores: due to its collisional nature, the diffuse IGM that is accreted towards the cores of filaments by gravitational attraction is shock heated and converted into WHIM gas. On the contrary, the hotter and denser phases (WCGM, halo and hot gas) were found to be almost insensitive to the environment of short and long filaments. Given that these phases are associated with haloes, their properties might be rather shaped by processes at smaller-scales (e.g. accretion onto haloes and halo mergers) and by galactic physics (e.g. feedback effects).

Finally, this Chapter presented an estimation of the SZ signal associated with gas in fila-

ments. This signal is found in the range $y = 0.5 - 4.1 \times 10^{-8}$, depending on the type of filament. When gas from galactic haloes is included, the expected SZ signal increases significantly. In this case, the Compton-y parameter is in the range $y = 0.1 - 1.5 \times 10^{-7}$. The expected SZ signal of gas was found to be compatible with the results of recent observations of gas in filaments (Bonjean et al., 2018; Tanimura et al., 2019, 2020a).

The physics of gas in the cosmic web is complex, and since baryonic matter is the only component that can be directly observed, it is essential to characterise its distribution and properties. In this sense, this work allowed us to build a clearer picture of the physical state of gas at any distance from the spine of filaments, and to identify more precisely the scales at which the different processes that shape gas in the cosmic web enter the game. Of course, further studies of the dynamics of gas and its evolution across redshifts are necessary to have a comprehensive understanding of the properties of gas in filaments, including dedicated mapping of the balance of power between the processes at play as function of time and environment in the cosmic web.

Chapter 6

Shaping the properties of galaxies

Contents

The previous Chapters of this thesis presented a characterisation of the properties of matter around cosmic filaments. The focus was put on the distribution of galaxies, on the relative distribution of DM, gas, and stars, and on the physical state of gas around these cosmic structures. This Chapter, the final of this Thesis, focuses on some properties of galaxies at $z = 0$, and on how the different environments in the cosmic web, and more precisely the different filament populations drive these properties. A general overview of how galaxies are shaped by the cosmic web is given in Sect 6.1, some prospective studies concerning the different filament populations are presented in Sect. 6.2, and Sect. 6.3 concludes this Chapter with a final discussion.

6.1 Galaxies in their cosmic web environment

Galaxies, the building blocks of the observed cosmic web, grow, evolve and flow from the less dense to the denser cosmic structures. During their lifetime, they thus experience strong changes of cosmic environments, and these changes affect their properties, such as their masses, star-formation activities, and spins (their angular momenta).

While it is now well established that galaxies located in cluster environments are more massive, less star forming, redder, and with more elliptical morphologies than those in less dense regions (see e.g. the reviews of Dressler 1980; Boselli, Gavazzi 2006, 2014), the study of the properties of galaxies around cosmic filaments has become feasible only in the past few years, thanks to the advent of large galaxy surveys (e.g. GAMA, SDSS, VIPERS, COSMOS2015, SAMI) and to the development of filament detection techniques, e.g. `DisPerSE`, T-ReX, NEXUS, and BISOUS (Sousbie et al., 2011; Sousbie, 2011; Bonnaire et al., 2020; Cautun et al., 2013; Tempel et al., 2016). Analysis in observations such as Alpaslan et al. (2016), Chen et al. (2017), Malavasi et al. (2017), Laigle et al. (2018), Kraljic et al. (2018), Bonjean et al. (2020), Rost et al. (2020), Welker et al. (2020) and Winkel et al. (2021) have shown that, similarly to clusters, the regions closer to the spine of filaments are populated by more massive and less star-forming galaxies than regions further away from the spine.

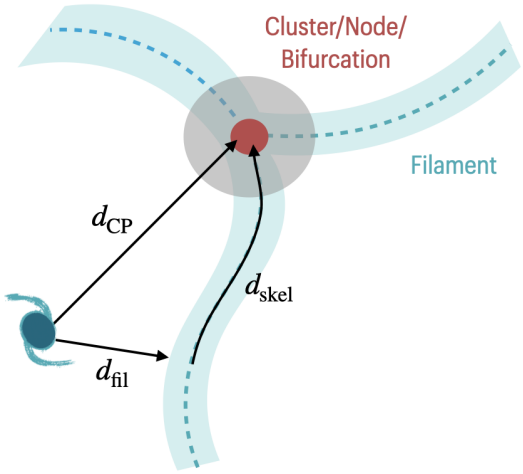

Figure 6.1: Distances between between galaxies and cosmic structures, as considered in Malavasi et al. (2021).

In parallel to observations, the properties of galaxies around filaments have also been studied in numerical simulations (e.g. Laigle et al., 2018; Kraljic et al., 2018, 2019; Ganeshaiah Veena et al., 2018, 2019, 2021). Offering larger statistical samples and the possibility to have access to all galaxy properties, the results in these virtual laboratories have not only been helpful to consolidate the trends observed in actual data, but also to further explore signals that are only difficultly detected in observations. For example, galaxies are formed with their spin parallel to the filaments of the cosmic web (Codis et al., 2015; Laigle et al., 2015), and as shown by e.g. Aragón-Calvo et al. (2007b); Hahn et al. (2007, 2010); Trowland et al. (2013); Ganeshaiah Veena et al. (2018); Krolewski et al. (2019); Kraljic et al. (2020); Welker et al. (2020); Kraljic et al. (2021), as galaxies grow and build-up their mass, their spin orientation flips to become perpendicular to the axis of filaments, until probably adopting a random orientation when galaxies reach the nodes, where they stay. Thus, along with mass and star-formation activity, spin gradients might also be present in the cosmic web and probably depend on the position of the galaxy with respect to to the cosmic structures.

With the aim of better understanding how the galaxy properties are shaped by their relative location with respect to the filaments and the nodes of the cosmic web and, conversely, in order to determine if these different cosmic structures can be traced (and differentiated) by the gradients of galaxy properties, Malavasi et al. (2021) studied the variations of galaxy properties (mainly mass, star-formation activity, and spin) along the three different distances presented in Fig. 6.1. These are: *(i)* the radial distance to the spine of the filament ($d_{\rm fil}$, corresponding to the coordinate r employed in this Thesis), *(ii)* the distance to the closest over-dense critical point ($d_{\rm CP}$), and *(iii)* the distance to the closest over-dense critical point but following the filament ($d_{\rm skel}$). I collaborated to this study, which used the galaxies and the skeleton of the TNG300-1 box detected and analysed in this Thesis (and respectively introduced in Sect. 3.1.1 and 3.2).

In agreement with the studies in observations and simulations cited above, the stellar mass M_* of galaxies was found to increase when approaching the cosmic structures, whereas the star-formation rate (SFR) decreased instead. This simply reflects the fact that the inner regions of structures host more massive galaxies, and are probably the places where the star-formation is the most efficiently quenched (maybe because of the reduced amount of cold gas fuelling

the galaxies in these regions). Quantities related to the spin of galaxies showed only small to no variation, with flat trends with respect to the distances to nodes and filaments. The comparison of the M_* and SFR gradients between the three considered distances ($d_{\rm fil}$, $d_{\rm CP}$, and $d_{\rm skel}$) yielded similar M_* variations between nodes and filaments. This differs from the SFR results, which showed that the SFR variation is not the same whether the galaxy is closer to nodes or to filaments, thus meaning that this quantity can be a good tracer of the different cosmic structures.

One important goal of this study was to disentangle the effects of the local environment (i.e. the local over-density in the close surroundings of the galaxy) from these generated by the global one (i.e. the position of the galaxy relative to filaments or nodes). The local environment of a galaxy was identified by the value of the Delaunay density, $\rho_{\rm DTFE}$, at the position of the galaxy. Note that these values are computed by the Delaunay Tessellation Field Estimator (Schaap, van de Weygaert, 2000; van de Weygaert, Schaap, 2009) during the extraction of the `DisPerSE` skeleton (see Sect. 3.1.2). Unsurprisingly, smaller values of $\rho_{\rm DTFE}$ are associated with smaller values of mass and SFR, exhibiting a relation between galaxy properties and their local density (note that no relation for spin was found). Since galaxies belonging to different large-scale structures can in fact experience the same kind of local environment (because of the partly overlapping density distributions between e.g. filaments and clusters), one can ask the following question: Are the observed gradients only a result of local density? Or does the large-scale environment also play a role?

This question was addressed by performing a reshuffling of the mass, SFR and spin values within bins of local densities, which allowed to conserve the relation between galaxy properties and local environment while completely breaking the dependency with the distances to the cosmic structures. The results from this reshuffling proved that one can not rule out that the observed mass and SFR gradients are driven by local density effects, and that the spin of galaxies is in fact a property more sensitive to the large-scale environment of the different structures of the cosmic web. Thus, although the signal of spin gradients with respect to the distances to cosmic structures is much fainter than those of mass and SFR, this quantity could probably be a better tracer of the cosmic, independent from the local density of galaxies.

All the trends discussed above can be put in regard with the results presented in this Thesis. For example, the study of Malavasi et al. (2021) analysed the properties of galaxies along the distances to different cosmic structures, but without distinguishing between the short and long filament populations identified in this Thesis. The following Section will thus explore the variations of galaxy star-formation activity and mass as a function of the filament populations.

6.2 Galaxies in different populations of filaments

Based on the studies presented in Chapters 4 and 5, it is now well established that the different populations of filaments, identified in Sect. 4.1.2, are tracers of different environments of the cosmic web. Corresponding to bridges of matter between over-dense structures, short filaments are denser, puffier, and hotter than the long population, which is embedded in less dense environments. As discussed in the previous section, galaxies are strongly shaped by their environment, so it is natural to investigate whether the different environments traced by the filament populations play also a role in the galaxy properties, i.e. if galaxies in short filaments are different from these in long.

This study is performed by focusing on the most usually explored galaxy properties, the specific star-formation rate (sSFR) and mass. Note that, since there is a relation between the star-formation activity and the mass of a galaxy (massive galaxies are 'older' and thus less star-forming), the sSFR, defined as the ratio between the SFR and stellar mass M_*, was preferred in this study over the (standard) SFR.

Method

The radial evolution of some galaxy properties around the spines of short and long filaments is probed by building mean profiles. For each filament, the mean value (hereafter $X \equiv \langle X \rangle$) of the galaxy quantity x (e.g. $x = M_*$, SFR, etc.) at a distance r_k from the axis of the filament is computed by summing the values of x in cylindrical shells centred on each of the $N_{\rm seg}$ segments of the filament, and by dividing the result by the number of galaxies enclosed in the total volume, such that, for the k-th shell of outer radius r_k and thickness $r_k - r_{k-1}$:

$$X(r_k) \equiv \langle X \rangle (r_k) = \frac{\sum_{s=1}^{N_{\rm seg}} \left(\sum_{g=1}^{N^s_{{\rm gal}\in k}} x^s_g \right)}{\sum_{s=1}^{N_{\rm seg}} N^s_{{\rm gal}\in k}}. \tag{6.1}$$

In this equation , the indices s and g denote respectively the filament segments and the galaxies, and $N^s_{{\rm gal}\in k}$ corresponds to the number of galaxies enclosed in the k-th cylindrical shell centred on the segment s. Note that the galaxies residing in the surroundings of the nodes of the skeleton, i.e. within spheres of radius $3 \times R_{200}$ centred on the CPmax, are excluded in this analysis. This set up is complementary to the work of *Malavasi et al. (2021)* that focused on the relative trends between filaments and nodes, while here the focus lies solely on the main filament stems.

Let us recall that the TNG300-1 galaxies have been previously selected to have a stellar mass in the range $10^9 \leq {\rm M}_*[{\rm M}_\odot] \leq 10^{12}$ (see Sect. 3.1.1). For this study no other selection was made (e.g. more refined mass bins, a separation between active and passive galaxies, or between centrals and satellites, etc.). Indeed, since the present analysis aims at determining global trends of how cosmic filaments shape the main galaxy properties, the specific refinements (of low/high mass, active/passive, centrals/satellites, etc.) can be overlooked at first order. Of course, for detailed conclusions on how the different filament populations affect a specific galaxy type, one would need a more precise study, but this is beyond the scope of this Thesis.

The following sections present the $X(r)$ profiles of galaxies around the short and long populations of the TNG300-1 filaments at $z = 0$. In order to draw a quantitative comparison between the trends in long filaments with respect to these in short, the deviation $D_{\rm S-L}$ is computed by:

$$D_{\rm S-L}(r) = \frac{{\rm X_S}(r) - {\rm X_L}(r)}{\sqrt{\sigma^2_{\rm X_S}(r) + \sigma^2_{\rm X_L}(r)}}, \tag{6.2}$$

where $\sigma_{\rm X_S}$ and $\sigma_{\rm X_L}$ correspond respectively to the bootstrap errors of the short and long filament profiles, $\rm X_S$ and $\rm X_L$.

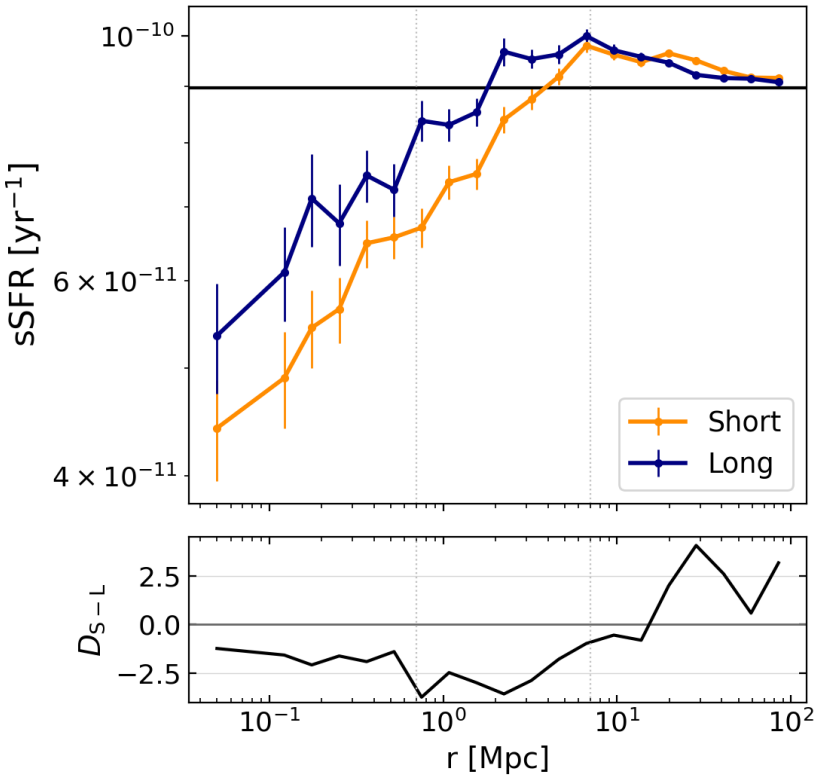

Figure 6.2: *Top:* Radial profile of the mean sSFR around short and long filaments of the TNG300-1 simulation (Eq. 6.1). The thin horizontal line marks the mean sSFR value in the full simulation box (CPmax excluded). *Bottom:* Deviation of long filaments with respect to short ones. This quantity is defined in Eq. 6.2.

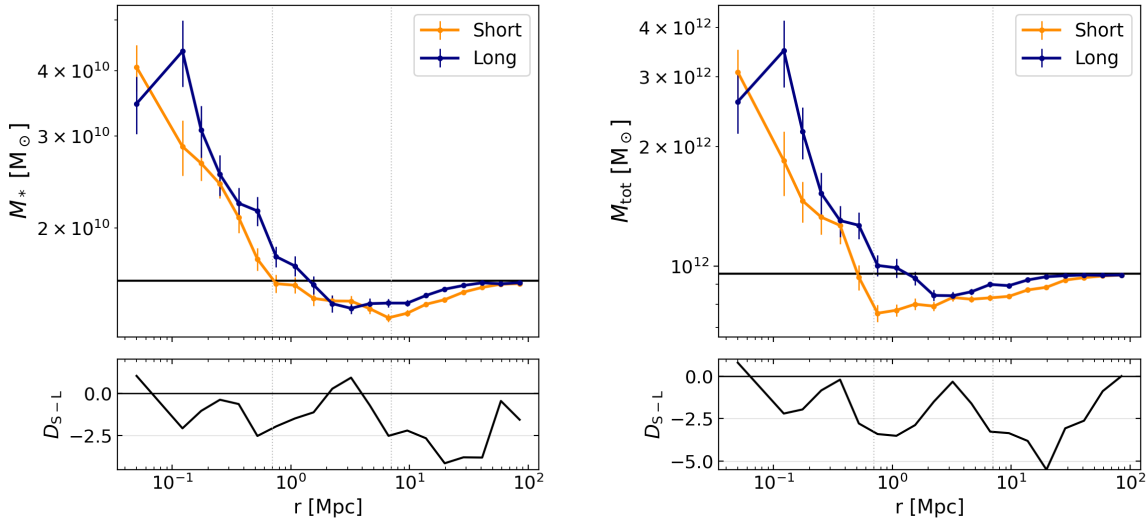

Figure 6.3: *Top:* Radial profile of the mean stellar mass (left), and total mass (right) around short and long filaments of the TNG300-1 simulation (Eq. 6.1). The thin horizontal lines correspond to the mean values in the full simulation box (CPmax excluded). *Bottom:* Deviation of long filaments with respect to long, as defined in Eq. 6.2.

6.2.1 Galaxy sSFR

The mean sSFR profile of galaxies around filaments is presented in Fig. 6.2. In agreement with the studies cited above, (e.g. Malavasi et al. 2017; Laigle et al. 2018; Sarron et al. 2019; Bonjean et al. 2020; Winkel et al. 2021 in observations, and e.g. Kraljic et al. 2018, 2019, and Malavasi et al. 2021 in numerical simulations), the profiles of Fig. 6.2 show a decrease of sSFR with decreasing distance to the filaments. For example, at the filament cores (first bin), they reach sSFR values that are twice as low as the background level. It is interesting to notice that the sSFR starts dropping at the characteristic radius $r_{\rm ext} \sim 7$ Mpc (outer vertical line). Recall that this radius was interpreted as the radial extent of gas in short and long filaments (as it marked the beginning of the deviation of the baryon fractions with respect to the cosmic value, Fig. 4.18).

A clear difference between filament populations is detected, as the average sSFR values in short filaments are smaller, at all radii, than those in the long population. From the deviation $D_{\rm S-L}$ profiles (lower panel), one can see that the deviation of the mean profile of long filaments with respect to that of short is on average $D_{\rm S-L} = 2.16\,\sigma$ in the $r < r_{\rm ext}$ region. These findings show that the denser and hotter environments of short filaments most probably accentuate the decrease of star-formation activity (e.g. by disconnecting the galaxy from the cold gas supply, thermal evaporation, or maybe ram pressure stripping) of galaxies with respect to those lying in the less dense and colder environments of long filaments.

6.2.2 Galaxy stellar and total mass

Let us now focus on the stellar and total mass of galaxies. The radial evolution of the mean stellar mass M_* of galaxies as a function of the distance to the filament spine is shown in Fig. 6.3 (left panel). Apart from the trends already discussed in Sect. 6.1, that more massive galaxies are found near the cores of filaments than in more remote regions, differences are found between

the two filament populations. Indeed, the stellar mass increase is more important towards the cores of long filaments, meaning that more massive galaxies inhabit these long structures than the short ones. While the significance of this trend is only $D_{S-L} = 0.94\,\sigma$ in the $r < r_{ext}$ regime, a stronger signal is found when analysing the total galaxy mass M_{tot} (i.e. the mass including DM, gas, stars, and black holes). Indeed, the mean profiles of total galaxy mass around filaments are presented in the right panel of Fig. 6.3, and in this case the M_{tot} excess of galaxies in long filaments with respect to these in short rises to the average of $D_{S-L} = 1.82\,\sigma$ in the $r < r_{ext}$ region.

Note that at this stage it is not possible to draw any conclusive interpretation of the differences between short and long filaments detected in Fig. 6.3. Mass is the result of the assembly of matter through cosmic time, and galaxies build-up their mass while flowing from one cosmic structure to the other. Since this study focuses on a snapshot of the Universe at $z = 0$, one can only raise hypotheses that could explain the observed trends, but a study at higher redshifts would definitely be needed to test them. Bearing that in mind, the following idea might provide an interpretation of the trends of Fig. 6.3, but absolutely needs to be tested for any conclusive assertion.

An important aspect one can consider is the flow of galaxies from cosmic filaments to nodes. The different masses of galaxies in short and long filaments at $z = 0$ might then be due to possibly different matter accretion flows towards the over-dense structures at the filament ends. For example, a bridge of matter connecting two merging clusters might be drained as galaxies fall towards one of these denser structures. Indeed, throughout their evolution, filaments and clusters merge (e.g. Cadiou et al., 2020), so the lower masses of galaxies in short filaments might be related to a more advanced merging processes. In this scenario, the low star-formation activity of galaxies in this population might not be due to their mass (mass quenching, see e.g. Peng et al., 2010) but rather to the high density and gas temperature, which might be increased by these processes.

6.3 Discussion

This last Chapter briefly discussed the properties of galaxies at $z = 0$, the building blocks of the cosmic structures, in relation with their environment in the cosmic web. First, a general overview of how the galaxy properties are related to cosmic filaments and nodes was presented in Sect. 6.1. Then, the specific effect of the short and long filaments (identified in this Thesis) on the mass and sSFR of galaxies was explored in Sect. 6.2.

In agreement with the literature (Alpaslan et al., 2016; Chen et al., 2017; Malavasi et al., 2017; Laigle et al., 2018; Kraljic et al., 2018, 2019; Bonjean et al., 2020; Rost et al., 2020; Welker et al., 2020), the analysis of Sect. 6.2 showed that the innermost regions of both filament populations host more massive and less star-forming galaxies than regions located further away from the filament spines. Nevertheless, the absolute value of these trends is found to depend on the filament population, as significant differences between short and long filaments are detected. Indeed, galaxies inhabiting the short population are less massive (Fig. 6.3) and possess lower star-formation activity (Fig. 6.2) than those residing in long filaments.

The physical interpretation of these results is not straightforward, given that this study focused on a snapshot of galaxies and filaments at $z = 0$ only. A deeper analysis is therefore required to build a more complete picture of galaxy evolution around the different populations

of cosmic filaments.

First, as discussed above, one would need to perform this study at different redshifts in order to better understand the observed trends of e.g. galaxy mass. For example, the results of Cautun et al. (2014) have shown that galaxies residing in filaments at $z = 2$ might either stay in filaments or migrate into clusters, and be found in these denser structures by $z = 0$. During their migration flows, these galaxies thus experience significant variations of their environment and dynamics, which can definitely affect the properties of these objects, such as their masses and SFR.

Also, it would be interesting to further explore the relation between galaxy SFR and the properties of filament gas. Indeed, the different densities and temperatures of gas in short and long filaments might play an important role in the quenching of the SFR of galaxies. These properties determine the large-scale environment in which galaxies live, evolve, and interact with their environment (see e.g. Peng et al., 2010, 2015; Gabor, Davé, 2015; Winkel et al., 2021, and references threin). Moreover, recent works show that galaxies at higher redshifts are supplied by cold gas via smaller-scale (few kpc thick) cold filaments that are directly connected to these objects (e.g. Ramsøy et al., 2021). The disconnection of the galaxies from these filaments would stop the accretion of cold gas, the main fuel of star formation, thus provoking a quenching of the SFR (Aragon Calvo et al., 2019). All these effects might play a role, more or less important, in the shaping of the properties of galaxies around different populations of filaments.

Despite the several studies in simulations and observations cited in this Chapter, a clear picture of galaxy evolution in the cosmic web, and more particularly in cosmic filaments, has not been reached yet. On one side, this problem is intrinsically related with the fact that galaxy properties are inter-dependent (e.g. spin and SFR quantities depend on stellar mass, as shown for example in Malavasi et al. 2021), resulting on different results or signal strengths as a function of the different selection criteria. This is clearly illustrated by the study of weak signals such as galaxy spin alignments (or non-alignments) performed in the MaNGa and SAMI surveys by Krolewski et al. (2019); Welker et al. (2020); Kraljic et al. (2021).

On the other side, the study of the galaxy properties is also affected by the difficulty in defining the different cosmic web environments. These are often detected using specialised web finders, like the `DisPerSE` algorithm used in this Thesis, or other codes, each with a different approach, such as SpineWeb (Aragón-Calvo et al., 2010a), NEXUS (Cautun et al., 2013), BISOUS (Cautun et al., 2013), T-Rex (Bonnaire et al., 2020), among others. The resulting cosmic skeletons can vary between different web finders, thus impacting the studies of galaxies in the different large-scale environments. For example, several works in the literature have tried to determine the transition mass at which the spin changes from parallel to perpendicular, finding results that can vary by more than an order of magnitude. Nevertheless, Ganeshaiah Veena et al. (2018) has explicitly showed that these differences can be due to the fact that this mass depends on the nature of filaments, finding higher transition mass values for galaxies in thicker filaments than in thin ones. In line with the results of this Thesis, the discussion above shows that a clearer picture of how galaxies are shaped by filaments cannot be reached without taking into account the properties specific to these cosmic structures (e.g. their length and width) that have been shown to be related with the environments traced by these structures.

Chapter 7

Conclusions

Cosmic filaments are thought to contain half of the total mass in the Universe (e.g. Cautun et al., 2014; Ganeshaiah Veena et al., 2019) so their study is crucial to understand the distribution of matter in the large scales. However, due to the low densities that characterise these structures (sometimes orders of magnitude lower than those of clusters of galaxies), the observation of filaments represents a major challenge today. In this context, this Thesis offers the first comprehensive analysis of cosmic filaments and of the matter around them at redshift $z = 0$ performed in the true virtual laboratories of large-scale hydro-dynamical simulations. I studied the properties of the cosmic filaments that I detected in the distribution of galaxies of the TNG300-1, TNG300-2, TNG100-3, Illustris-1 and Magneticum simulations, using the publicly available `DisPerSE` code.

I first characterised how galaxies are distributed around the detected filaments. I showed that filaments of different lengths have notably different radial galaxy density profiles, and this led me to the first quantitative and unambiguous identification of two different populations of filaments, that do not share the same physical properties. Short filaments of length $L_f < 9$ Mpc are puffier and denser structures that inhabit denser environments of the cosmic web. On the contrary, long filaments ($L_f > 20$ Mpc) are thinner structures that trace less-dense regions of the web, and they are connected to less massive objects than their short counterparts. This was confirmed by the study of the mass densities of DM, gas, and stars around these two populations. I found again a clear density difference for all the matter components, with short filaments exhibiting on average three times higher densities than long filaments. The former may be interpreted as bridges of matter between over-dense structures like clusters, while the latter may correspond to the filaments shaping the large scales of the cosmic web.

The study of the properties of gas around populations of filaments further showed differences between these structures. I separated gas into different phases (i.e. diffuse IGM, WHIM, WCGM, halo and hot gas) and I performed the first statistical analysis of their spatial distribution, temperature and pressure profiles around the cosmic structures. I started by quantifying, at different distances from the spine of the filament, the part that each gas phase contributes to the total gas budget available. My results showed that, around filaments, gas is mostly in the warm-hot intergalactic medium (WHIM) phase, especially at ~ 1 Mpc from their spines. This is in agreement with Nevalainen et al. (2015); Cui et al. (2018b, 2019); Martizzi et al. (2019); Tuominen et al. (2021). At cores of filaments, other hotter and denser gas phases are also present and, as expected, their part in the total budget reflects the density of the large scale environment, traced by the short and long populations. I thus showed that all the filaments are

not made of the same proportions of different types of gas.

With the aim of characterising the temperature and pressure, I computed average radial profiles of these quantities, for each gas phase, around the different types of filaments. I found a large diversity of trends and ranges in both the temperature and pressure profiles. For example, at the core of filaments ($r \leq 1$ Mpc), I estimated that the average temperature and pressure is $T = 4 - 13 \times 10^5$ K, and $P = 4 - 12 \times 10^{-7}$ keV.cm^{-3}, with values that are roughly three times higher in the short population than in the long one. Moreover, in agreement with previous studies (Klar, Mücket, 2012; Gheller, Vazza, 2019), I found that filaments possess isothermal cores. This feature was apparent for all the filaments regardless of their parent population, up to distances of $\sim$ 1.5 Mpc from their spines. Finally, pressures in filament cores were found to be $\sim$ 1000 times lower than those in cores of clusters, showing different and well defined pressure ranges are observed between these two types of cosmic structures.

In order to relate the results from simulations with actual observed data, from the derived pressure profiles I computed the expected Sunyaev-Zel'dovich (SZ) signal from gas in cosmic filaments. My results were found to be in good agreement with recent observations of filaments (Tanimura et al., 2020a,b), showing not only the consistency between the simulated and observed baryonic properties, but also the capacity to push the analysis forward in the calibration and preparation of future observations of hot and diffuse baryons. In line with the latter, I computed scaling-relations between gas density, temperature and pressure in filaments, and I compared the results to those in groups and clusters of galaxies. I found that the relations in the $\langle \rho_{\rm gas} \rangle - \langle T \rangle$ and $\langle \rho_{\rm gas} \rangle - \langle P \rangle$ planes can be a way to differentiate between different types of cosmic structures (i.e. groups, clusters, short and long filaments). Finally, with the aim of providing a model for the radial distribution of matter useful for observations, I performed MCMC fits of the radial galaxy density profiles, finding that single and double power laws, β-profiles, and generalised Navarro, Frenk and White (GNFW) models are suitable descriptions of the galaxy density around short and long filaments.

Contrary to the absolute densities and properties of matter, the relative distribution of baryons with respect to the underlying DM radial densities does not depend, as I have shown, on the filament population, and seems to be universal instead. By computing baryon fraction radial profiles I found that, regardless the population, baryons exactly follow the DM distribution only down to $r \sim 7$ Mpc to the filament spines. At smaller distances ($r \sim 0.7 - 7$ Mpc) I found an excess of baryons with respect to the cosmic value $\Omega_{\rm b}/\Omega_{\rm m}$ (created by the radial accretion of WHIM gas towards the filaments), and observed a clear depletion of baryons at the filament cores ($r < 0.7$ Mpc). With the aim of better understanding this depletion, I analysed the efficiency of AGN feedback events in filaments, revealing that these astrophysical processes can potentially be powerful enough to eject gas outside of the gravitational potential wells induced by these structures.

Finally, I performed an inspection of how the different populations of filaments shape their population of galaxies. This preliminary study already showed that the properties of galaxies, namely their mass and sSFR, are not the same in short and long filaments. In the future, I plan to push forward this analysis in order to explicitly study the link between galaxy properties, gas properties (i.e. density and temperature), and the denser and less-dense environments traced by the different populations. Such study needs to be performed at different redshifts, in order to follow the evolution of galaxies and their properties in relation with those of their hosting filament. This study will definitely contribute to the understanding of the galaxy properties

observed today in filaments, and will probably help disentangling between the different mechanisms quenching the star formation in galaxies by observing how these objects actually interact with their environment.

Continuing with the perspectives, this Thesis naturally leads to the investigation of the emergence of the two filament populations, a question that I would like to explore. I thus plan on analysing the formation and evolution of the two filament populations in numerical simulations, from initial conditions to the evolved structures observed today. The observed differences in the distributions and state of baryons around short and long filaments at $z = 0$ might probably be the result of a different evolution in time, driven by e.g. different processes and interactions with their respective cosmic environments. For example, short filaments might be dominated by the gravitational force driving the collapse, so the observed short filaments at $z = 0$ might be merging structures, or bridges of matter resulting from these processes, in a more or less advanced merging state. Concerning long filaments, given that they trace less-dense regions, their evolution might rather be ruled by the Hubble flow, thus following the stripping of the cosmic web caused by the cosmic expansion. In addition to following the evolution of the different populations from initial conditions, I would like to analyse them within the theoretical framework of Feldbrugge et al. (2018) that predicts, based on the caustics of dark matter, the emergence of two populations of filaments.

The results presented in this Thesis have allowed a comprehensive understanding of the distribution and properties of matter around these cosmic structures. They also provide invaluable tools for the future in the context of preparing for the forthcoming surveys, like Euclid and Vera Rubin on the galaxy side and, on the side of diffuse baryons, Athena, Simons Observatory, and the ongoing eROSITA surveys.

Bibliography

Akamatsu H., Fujita Y., Akahori T., Ishisaki Y., Hayashida K., Hoshino A., Mernier F., Yoshikawa K., Sato K., Kaastra J. S. Properties of the cosmological filament between two clusters: A possible detection of a large-scale accretion shock by Suzaku // Astron. Astrophys.. Sep 2017. 606. A1. 18

Alpaslan Mehmet, Grootes Meiert, Marcum Pamela M., Popescu Cristina, Tuffs Richard, Bland-Hawthorn Joss, Brough Sarah, Brown Michael J. I., Davies Luke J. M., Driver Simon P., Holwerda Benne W., Kelvin Lee S., Lara-López Maritza A., López-Sánchez Ángel R., Loveday Jon, Moffett Amanda, Taylor Edward N., Owers Matt, Robotham Aaron S. G. Galaxy And Mass Assembly (GAMA): stellar mass growth of spiral galaxies in the cosmic web // Mon. Not. R. Astron. Soc.. IV 2016. 457, 3. 2287–2300. 18, 127, 133

Aragón-Calvo M. A., Jones B. J. T., van de Weygaert R., van der Hulst J. M. The multiscale morphology filter: identifying and extracting spatial patterns in the galaxy distribution // Astron. Astrophys.. X 2007a. 474, 1. 315–338. 28

Aragon Calvo Miguel A., Neyrinck Mark C., Silk Joseph. Galaxy Quenching from Cosmic Web Detachment // The Open Journal of Astrophysics. VII 2019. 2, 1. 7. 134

Aragón-Calvo Miguel A., Platen Erwin, van de Weygaert Rien, Szalay Alexander S. The Spine of the Cosmic Web // Astrophys. J.. XI 2010a. 723, 1. 364–382. 28, 134

Aragón-Calvo Miguel A., van de Weygaert Rien, Jones Bernard J. T. Multiscale phenomenology of the cosmic web // Mon. Not. R. Astron. Soc.. Nov 2010b. 408, 4. 2163–2187. 48, 69, 73, 77, 89

Aragón-Calvo Miguel A., van de Weygaert Rien, Jones Bernard J. T., van der Hulst J. M. Spin Alignment of Dark Matter Halos in Filaments and Walls // Astrophys. J. Lett. I 2007b. 655, 1. L5–L8. 128

Arnaud M. The β-model of the intracluster medium. Commentary on: Cavaliere A. and Fusco-Femiano R., 1976, AAstron. Astrophys.A, 49, 137 // Astron. Astrophys.. VI 2009. 500. 103–104. 67

Arnaud M., Pratt G. W., Piffaretti R., Böhringer H., Croston J. H., Pointecouteau E. The universal galaxy cluster pressure profile from a representative sample of nearby systems (REXCESS) and the Y_{SZ} - M_{500} relation // Astron. Astrophys.. Jul 2010. 517. A92. 17, 67, 119, 125

Barnes David J., Kay Scott T., Bahé Yannick M., Dalla Vecchia Claudio, McCarthy Ian G., Schaye Joop, Bower Richard G., Jenkins Adrian, Thomas Peter A., Schaller Matthieu, Crain Robert A., Theuns Tom, White Simon D. M. The Cluster-EAGLE project: global properties

of simulated clusters with resolved galaxies // Mon. Not. R. Astron. Soc.. X 2017. 471, 1. 1088–1106. 80, 84

Bartalucci I., Arnaud M., Pratt G. W., Vikhlinin A., Pointecouteau E., Forman W. R., Jones C., Mazzotta P., Andrade-Santos F. Recovering galaxy cluster gas density profiles with XMM-Newton and Chandra // Astron. Astrophys.. Dec 2017. 608. A88. 17

Baxter Eric, Chang Chihway, Jain Bhuvnesh, Adhikari Susmita, Dalal Neal, Kravtsov Andrey, More Surhud, Rozo Eduardo, Rykoff Eli, Sheth Ravi K. The Halo Boundary of Galaxy Clusters in the SDSS // Astrophys. J.. May 2017a. 841, 1. 18. 17

Baxter Eric, Chang Chihway, Jain Bhuvnesh, Adhikari Susmita, Dalal Neal, Kravtsov Andrey, More Surhud, Rozo Eduardo, Rykoff Eli, Sheth Ravi K. The Halo Boundary of Galaxy Clusters in the SDSS // Astrophys. J.. V 2017b. 841, 1. 18. 57

Biffi Veronica, Dolag Klaus, Reiprich Thomas H., Veronica Angie, Ramos-Ceja Miriam E., Bulbul Esra, Ota Naomi, Ghirardini Vittorio. The eROSITA view of the Abell 3391/95 field: a case study from the Magneticum cosmological simulation // arXiv e-prints. VI 2021. arXiv:2106.14542. 18

Bilicki Maciej, Peacock John A., Jarrett Thomas H., Cluver Michelle E., Maddox Natasha, Brown Michael J. I., Taylor Edward N., Hambly Nigel C., Solarz Aleksandra, Holwerda Benne W., Baldry Ivan, Loveday Jon, Moffett Amanda, Hopkins Andrew M., Driver Simon P., Alpaslan Mehmet, Bland-Hawthorn Joss. WISE × SuperCOSMOS Photometric Redshift Catalog: 20 Million Galaxies over 3/pi Steradians // Astrophys. J. Suppl. Ser.. VII 2016. 225, 1. 5. 15

Bond J. Richard, Kofman Lev, Pogosyan Dmitry. How filaments of galaxies are woven into the cosmic web // Nature. Apr 1996. 380, 6575. 603–606. 15, 21

Bond Nicholas A., Strauss Michael A., Cen Renyue. Crawling the cosmic network: identifying and quantifying filamentary structure // Mon. Not. R. Astron. Soc.. Nov 2010. 409, 1. 156–168. 48, 89

Bonjean V., Aghanim N., Douspis M., Malavasi N., Tanimura H. Filament profiles from WISExSCOS galaxies as probes of the impact of environmental effects // Astron. Astrophys.. VI 2020. 638. A75. 18, 37, 59, 77, 80, 89, 92, 105, 127, 132, 133

Bonjean V., Aghanim N., Salomé P., Douspis M., Beelen A. Gas and galaxies in filaments between clusters of galaxies. The study of A399-A401 // Astron. Astrophys.. Jan 2018. 609. A49. 18, 124, 126

Bonnaire Tony, Aghanim Nabila, Decelle Aurélien, Douspis Marian. T-ReX: a graph-based filament detection method // Astron. Astrophys.. V 2020. 637. A18. 28, 49, 127, 134

Boselli Alessandro, Gavazzi Giuseppe. Environmental Effects on Late-Type Galaxies in Nearby Clusters // PASP. IV 2006. 118, 842. 517–559. 127

Boselli Alessandro, Gavazzi Giuseppe. On the origin of the faint-end of the red sequence in high-density environments // A&A Rev.. XI 2014. 22. 74. 127

Boylan-Kolchin Michael, Springel Volker, White Simon D. M., Jenkins Adrian, Lemson Gerard. Resolving cosmic structure formation with the Millennium-II Simulation // Mon. Not. R. Astron. Soc.. IX 2009. 398, 3. 1150–1164. 18, 21

Brinchmann J., Charlot S., White S. D. M., Tremonti C., Kauffmann G., Heckman T., Brinkmann J. The physical properties of star-forming galaxies in the low-redshift Universe // Mon. Not. R. Astron. Soc.. Jul 2004. 351, 4. 1151–1179. 38

Bryan Greg L., Norman Michael L., O'Shea Brian W., Abel Tom, Wise John H., Turk Matthew J., Reynolds Daniel R., Collins David C., Wang Peng, Skillman Samuel W., Smith Britton, Harkness Robert P., Bordner James, Kim Ji-hoon, Kuhlen Michael, Xu Hao, Goldbaum Nathan, Hummels Cameron, Kritsuk Alexei G., Tasker Elizabeth, Skory Stephen, Simpson Christine M., Hahn Oliver, Oishi Jeffrey S., So Geoffrey C., Zhao Fen, Cen Renyue, Li Yuan, Enzo Collaboration . ENZO: An Adaptive Mesh Refinement Code for Astrophysics // Astrophys. J. Suppl. Ser.. IV 2014. 211, 2. 19. 22

Bryant J. J., Owers M. S., Robotham A. S. G., Croom S. M., Driver S. P., Drinkwater M. J., Lorente N. P. F., Cortese L., Scott N., Colless M., Schaefer A., Taylor E. N., Konstantopoulos I. S., Allen J. T., Baldry I., Barnes L., Bauer A. E., Bland-Hawthorn J., Bloom J. V., Brooks A. M., Brough S., Cecil G., Couch W., Croton D., Davies R., Ellis S., Fogarty L. M. R., Foster C., Glazebrook K., Goodwin M., Green A., Gunawardhana M. L., Hampton E., Ho I. T., Hopkins A. M., Kewley L., Lawrence J. S., Leon-Saval S. G., Leslie S., McElroy R., Lewis G., Liske J., López-Sánchez Á. R., Mahajan S., Medling A. M., Metcalfe N., Meyer M., Mould J., Obreschkow D., O'Toole S., Pracy M., Richards S. N., Shanks T., Sharp R., Sweet S. M., Thomas A. D., Tonini C., Walcher C. J. The SAMI Galaxy Survey: instrument specification and target selection // Mon. Not. R. Astron. Soc.. Mar 2015. 447, 3. 2857–2879. 15, 55

Buncher Brandon, Carrasco Kind Matias. Probabilistic cosmic web classification using fast-generated training data // arXiv e-prints. XII 2019. arXiv:1912.04412. 28

Cadiou C., Pichon C., Codis S., Musso M., Pogosyan D., Dubois Y., Cardoso J. F., Prunet S. When do cosmic peaks, filaments, or walls merge? A theory of critical events in a multiscale landscape // Mon. Not. R. Astron. Soc.. VIII 2020. 496, 4. 4787–4821. 133

Cautun Marius, van de Weygaert Rien, Jones Bernard J. T. NEXUS: tracing the cosmic web connection // Mon. Not. R. Astron. Soc.. Feb 2013. 429, 2. 1286–1308. 17, 18, 28, 49, 93, 127, 134

Cautun Marius, van de Weygaert Rien, Jones Bernard J. T., Frenk Carlos S. Evolution of the cosmic web // Mon. Not. R. Astron. Soc.. Jul 2014. 441, 4. 2923–2973. 17, 18, 48, 89, 93, 134, 135

Cavaliere A., Fusco-Femiano R. X-rays from hot plasma in clusters of galaxies // Astron. Astrophys.. V 1976. 49. 137–144. 67

Cen Renyue, Ostriker Jeremiah P. Where Are the Baryons? II. Feedback Effects // Astrophys. J.. X 2006. 650, 2. 560–572. 80, 96

Chang C., Baxter E., Jain B., Sánchez C., Adhikari S., Varga T. N., Fang Y., Rozo E., Rykoff E. S., Kravtsov A., Gruen D., Hartley W., Huff E. M., Jarvis M., Kim A. G., Prat J., MacCrann N., McClintock T., Palmese A., Rapetti D., Rollins R. P., Samuroff S., Sheldon E., Troxel

M. A., Wechsler R. H., Zhang Y., Zuntz J., Abbott T. M. C., Abdalla F. B., Allam S., Annis J., Bechtol K., Benoit-Lévy A., Bernstein G. M., Brooks D., Buckley-Geer E., Carnero Rosell A., Carrasco Kind M., Carretero J., D'Andrea C. B., da Costa L. N., Davis C., Desai S., Diehl H. T., Dietrich J. P., Drlica-Wagner A., Eifler T. F., Flaugher B., Fosalba P., Frieman J., García-Bellido J., Gaztanaga E., Gerdes D. W., Gruendl R. A., Gschwend J., Gutierrez G., Honscheid K., James D. J., Jeltema T., Krause E., Kuehn K., Lahav O., Lima M., March M., Marshall J. L., Martini P., Melchior P., Menanteau F., Miquel R., Mohr J. J., Nord B., Ogando R. L. C., Plazas A. A., Sanchez E., Scarpine V., Schindler R., Schubnell M., Sevilla-Noarbe I., Smith M., Smith R. C., Soares-Santos M., Sobreira F., Suchyta E., Swanson M. E. C., Tarle G., Weller J., DES Collaboration . The Splashback Feature around DES Galaxy Clusters: Galaxy Density and Weak Lensing Profiles // Astrophys. J.. IX 2018. 864, 1. 83. 57

Chen Yen-Chi, Ho Shirley, Mandelbaum Rachel, Bahcall Neta A., Brownstein Joel R., Freeman Peter E., Genovese Christopher R., Schneider Donald P., Wasserman Larry. Detecting effects of filaments on galaxy properties in the Sloan Digital Sky Survey III // Mon. Not. R. Astron. Soc.. IV 2017. 466, 2. 1880–1893. 18, 127, 133

Chisari N. E., Richardson M. L. A., Devriendt J., Dubois Y., Schneider A., Le Brun A. M. C., Beckmann R. S., Peirani S., Slyz A., Pichon C. The impact of baryons on the matter power spectrum from the Horizon-AGN cosmological hydrodynamical simulation // Mon. Not. R. Astron. Soc.. XI 2018. 480, 3. 3962–3977. 80

Chiu I., Mohr J. J., McDonald M., Bocquet S., Desai S., Klein M., Israel H., Ashby M. L. N., Stanford A., Benson B. A., Brodwin M., Abbott T. M. C., Abdalla F. B., Allam S., Annis J., Bayliss M., Benoit-Lévy A., Bertin E., Bleem L., Brooks D., Buckley-Geer E., Bulbul E., Capasso R., Carlstrom J. E., Rosell A. Carnero, Carretero J., Castander F. J., Cunha C. E., D'Andrea C. B., da Costa L. N., Davis C., Diehl H. T., Dietrich J. P., Doel P., Drlica-Wagner A., Eifler T. F., Evrard A. E., Flaugher B., García-Bellido J., Garmire G., Gaztanaga E., Gerdes D. W., Gonzalez A., Gruen D., Gruendl R. A., Gschwend J., Gupta N., Gutierrez G., Hlavacek-L J., Honscheid K., James D. J., Jeltema T., Kraft R., Krause E., Kuehn K., Kuhlmann S., Kuropatkin N., Lahav O., Lima M., Maia M. A. G., Marshall J. L., Melchior P., Menanteau F., Miquel R., Murray S., Nord B., Ogando R. L. C., Plazas A. A., Rapetti D., Reichardt C. L., Romer A. K., Roodman A., Sanchez E., Saro A., Scarpine V., Schindler R., Schubnell M., Sharon K., Smith R. C., Smith M., Soares-Santos M., Sobreira F., Stalder B., Stern C., Strazzullo V., Suchyta E., Swanson M. E. C., Tarle G., Vikram V., Walker A. R., Weller J., Zhang Y. Baryon content in a sample of 91 galaxy clusters selected by the South Pole Telescope at 0.2 <z < 1.25 // Mon. Not. R. Astron. Soc.. VIII 2018. 478, 3. 3072–3099. 80

Choi Ena, Bond Nicholas A., Strauss Michael A., Coil Alison L., Davis Marc, Willmer Christopher N. A. Tracing the filamentary structure of the galaxy distribution at z ∼0.8 // Mon. Not. R. Astron. Soc.. Jul 2010. 406, 1. 320–328. 48

Codis Sandrine, Pichon Christophe, Pogosyan Dmitry. Spin alignments within the cosmic web: a theory of constrained tidal torques near filaments // Mon. Not. R. Astron. Soc.. X 2015. 452, 4. 3369–3393. 128

Colberg Jörg M., Krughoff K. Simon, Connolly Andrew J. Intercluster filaments in a ΛCDM Universe // Mon. Not. R. Astron. Soc.. May 2005. 359, 1. 272–282. 69, 73, 78, 89, 91

The 2dF Galaxy Redshift Survey: Final Data Release. // . Jun 2003. 15, 55

Cui Weiguang, Knebe Alexander, Libeskind Noam I., Planelles Susana, Yang Xiaohu, Cui Wei, Davé Romeel, Kang Xi, Mostoghiu Robert, Staveley-Smith Lister, Wang Huiyuan, Wang Peng, Yepes Gustavo. The large-scale environment from cosmological simulations II: The redshift evolution and distributions of baryons // Mon. Not. R. Astron. Soc.. V 2019. 485, 2. 2367–2379. 93, 102, 125, 135

Cui Weiguang, Knebe Alexander, Yepes Gustavo, Pearce Frazer, Power Chris, Dave Romeel, Arth Alexander, Borgani Stefano, Dolag Klaus, Elahi Pascal, Mostoghiu Robert, Murante Giuseppe, Rasia Elena, Stoppacher Doris, Vega-Ferrero Jesus, Wang Yang, Yang Xiaohu, Benson Andrew, Cora Sofía A., Croton Darren J., Sinha Manodeep, Stevens Adam R. H., Vega-Martínez Cristian A., Arthur Jake, Baldi Anna S., Cañas Rodrigo, Cialone Giammarco, Cunnama Daniel, De Petris Marco, Durando Giacomo, Ettori Stefano, Gottlöber Stefan, Nuza Sebastián E., Old Lyndsay J., Pilipenko Sergey, Sorce Jenny G., Welker Charlotte. The Three Hundred project: a large catalogue of theoretically modelled galaxy clusters for cosmological and astrophysical applications // Mon. Not. R. Astron. Soc.. XI 2018a. 480, 3. 2898–2915. 86

Cui Weiguang, Knebe Alexander, Yepes Gustavo, Yang Xiaohu, Borgani Stefano, Kang Xi, Power Chris, Staveley-Smith Lister. The large-scale environment from cosmological simulations - I. The baryonic cosmic web // Mon. Not. R. Astron. Soc.. I 2018b. 473, 1. 68–79. 93, 102, 125, 135

Davé Romeel, Anglés-Alcázar Daniel, Narayanan Desika, Li Qi, Rafieferantsoa Mika H., Appleby Sarah. SIMBA: Cosmological simulations with black hole growth and feedback // Mon. Not. R. Astron. Soc.. VI 2019. 486, 2. 2827–2849. 21

Davis M., Efstathiou G., Frenk C. S., White S. D. M. The evolution of large-scale structure in a universe dominated by cold dark matter // Astrophys. J.. V 1985a. 292. 371–394. 22

Davis M., Efstathiou G., Frenk C. S., White S. D. M. The evolution of large-scale structure in a universe dominated by cold dark matter // Astrophys. J.. V 1985b. 292. 371–394. 27

Di Matteo Tiziana, Springel Volker, Hernquist Lars. Energy input from quasars regulates the growth and activity of black holes and their host galaxies // Nature. II 2005. 433, 7026. 604–607. 27

Diemer Benedikt, Mansfield Philip, Kravtsov Andrey V., More Surhud. The Splashback Radius of Halos from Particle Dynamics. II. Dependence on Mass, Accretion Rate, Redshift, and Cosmology // Astrophys. J.. VII 2017. 843, 2. 140. 57

Dolag K., Borgani S., Murante G., Springel V. Substructures in hydrodynamical cluster simulations // Mon. Not. R. Astron. Soc.. Oct 2009. 399, 2. 497–514. 27, 28

Dolag K., Meneghetti M., Moscardini L., Rasia E., Bonaldi A. Simulating the physical properties of dark matter and gas inside the cosmic web // Mon. Not. R. Astron. Soc.. VIII 2006. 370, 2. 656–672. 78

Dolag K., Stasyszyn F. An MHD GADGET for cosmological simulations // Mon. Not. R. Astron. Soc.. X 2009. 398, 4. 1678–1697. 27

Dolag Klaus. The Magneticum Simulations, from Galaxies to Galaxy Clusters // IAU General Assembly. 29. Aug 2015. 2250156. 21, 26

Dressler A. Galaxy morphology in rich clusters: implications for the formation and evolution of galaxies. // Astrophys. J.. III 1980. 236. 351–365. 127

Driver S. P., Hill D. T., Kelvin L. S., Robotham A. S. G., Liske J., Norberg P., Baldry I. K., Bamford S. P., Hopkins A. M., Loveday J., Peacock J. A., Andrae E., Bland -Hawthorn J., Brough S., Brown M. J. I., Cameron E., Ching J. H. Y., Colless M., Conselice C. J., Croom S. M., Cross N. J. G., de Propris R., Dye S., Drinkwater M. J., Ellis S., Graham Alister W., Grootes M. W., Gunawardhana M., Jones D. H., van Kampen E., Maraston C., Nichol R. C., Parkinson H. R., Phillipps S., Pimbblet K., Popescu C. C., Prescott M., Roseboom I. G., Sadler E. M., Sansom A. E., Sharp R. G., Smith D. J. B., Taylor E., Thomas D., Tuffs R. J., Wijesinghe D., Dunne L., Frenk C. S., Jarvis M. J., Madore B. F., Meyer M. J., Seibert M., Staveley-Smith L., Sutherland W. J., Warren S. J. Galaxy and Mass Assembly (GAMA): survey diagnostics and core data release // Mon. Not. R. Astron. Soc.. May 2011. 413, 2. 971–995. 15, 55

Driver Simon P., Norberg Peder, Baldry Ivan K., Bamford Steven P., Hopkins Andrew M., Liske Jochen, Loveday Jon, Peacock John A., Hill D. T., Kelvin L. S., Robotham A. S. G., Cross N. J. G., Parkinson H. R., Prescott M., Conselice C. J., Dunne L., Brough S., Jones H., Sharp R. G., van Kampen E., Oliver S., Roseboom I. G., Bland-Hawthorn J., Croom S. M., Ellis S., Cameron E., Cole S., Frenk C. S., Couch W. J., Graham A. W., Proctor R., De Propris R., Doyle I. F., Edmondson E. M., Nichol R. C., Thomas D., Eales S. A., Jarvis M. J., Kuijken K., Lahav O., Madore B. F., Seibert M., Meyer M. J., Staveley-Smith L., Phillipps S., Popescu C. C., Sansom A. E., Sutherland W. J., Tuffs R. J., Warren S. J. GAMA: towards a physical understanding of galaxy formation // Astronomy and Geophysics. X 2009. 50, 5. 5.12–5.19. 15

Dubois Y., Pichon C., Welker C., Le Borgne D., Devriendt J., Laigle C., Codis S., Pogosyan D., Arnouts S., Benabed K., Bertin E., Blaizot J., Bouchet F., Cardoso J. F., Colombi S., de Lapparent V., Desjacques V., Gavazzi R., Kassin S., Kimm T., McCracken H., Milliard B., Peirani S., Prunet S., Rouberol S., Silk J., Slyz A., Sousbie T., Teyssier R., Tresse L., Treyer M., Vibert D., Volonteri M. Dancing in the dark: galactic properties trace spin swings along the cosmic web // Mon. Not. R. Astron. Soc.. Oct 2014. 444, 2. 1453–1468. 21, 92

Dubois Yohan, Beckmann Ricarda, Bournaud Frédéric, Choi Hoseung, Devriendt Julien, Jackson Ryan, Kaviraj Sugata, Kimm Taysun, Kraljic Katarina, Laigle Clotilde, Martin Garreth, Park Min-Jung, Peirani Sébastien, Pichon Christophe, Volonteri Marta, Yi Sukyoung K. Introducing the NewHorizon simulation: Galaxy properties with resolved internal dynamics across cosmic time // arXiv e-prints. IX 2020. arXiv:2009.10578. 22

Dubois Yohan, Devriendt Julien, Slyz Adrianne, Teyssier Romain. Self-regulated growth of supermassive black holes by a dual jet-heating active galactic nucleus feedback mechanism: methods, tests and implications for cosmological simulations // Mon. Not. R. Astron. Soc.. III 2012. 420, 3. 2662–2683. 22

Eckert Dominique, Jauzac Mathilde, Shan Huanyuan, Kneib Jean-Paul, Erben Thomas, Israel Holger, Jullo Eric, Klein Matthias, Massey Richard, Richard Johan, Tchernin Céline. Warm-hot baryons comprise 5-10 per cent of filaments in the cosmic web // Nature. XII 2015. 528, 7580. 105–107. 18

Einasto J. On the Construction of a Composite Model for the Galaxy and on the Determination of the System of Galactic Parameters // Trudy Astrofizicheskogo Instituta Alma-Ata. Jan 1965. 5. 87–100. 67

Ettori Stefano, Donnarumma Annamaria, Pointecouteau Etienne, Reiprich Thomas H., Giodini Stefania, Lovisari Lorenzo, Schmidt Robert W. Mass Profiles of Galaxy Clusters from X-ray Analysis // Space Sci. Rev.. Aug 2013. 177, 1-4. 119–154. 67

Fabjan D., Borgani S., Tornatore L., Saro A., Murante G., Dolag K. Simulating the effect of active galactic nuclei feedback on the metal enrichment of galaxy clusters // Mon. Not. R. Astron. Soc.. I 2010. 401, 3. 1670–1690. 27, 59

Feldbrugge Job, van de Weygaert Rien, Hidding Johan, Feldbrugge Joost. Caustic Skeleton & Cosmic Web // J. Cosmol. Astropart. Phys.. V 2018. 2018, 5. 027. 137

Forman Robin. Morse theory for cell complexes // Advances in mathematics. 1998. 134, 1. 90–145. 31, 35

Forman Robin. A user's guide to discrete Morse theory // Sém. Lothar. Combin. 2002. 48. 35pp. 31, 35

Gabor J. M., Davé R. Hot gas in massive haloes drives both mass quenching and environment quenching // Mon. Not. R. Astron. Soc.. II 2015. 447, 1. 374–391. 134

Galárraga-Espinosa Daniela, Aghanim Nabila, Langer Mathieu, Gouin Céline, Malavasi Nicola. Populations of filaments from the distribution of galaxies in numerical simulations // Astron. Astrophys.. IX 2020. 641. A173. 47, 56, 58, 60, 61, 64, 68, 70, 71, 72, 89, 90

Galárraga-Espinosa Daniela, Aghanim Nabila, Langer Mathieu, Tanimura Hideki. Properties of gas phases around cosmic filaments at z = 0 in the IllustrisTNG simulation // Astron. Astrophys.. V 2021. 649. A117. 96, 97, 98, 101, 109, 117

Ganeshaiah Veena Punyakoti, Cautun Marius, Tempel Elmo, van de Weygaert Rien, Frenk Carlos S. The Cosmic Ballet II: spin alignment of galaxies and haloes with large-scale filaments in the EAGLE simulation // Mon. Not. R. Astron. Soc.. Aug 2019. 487, 2. 1607–1625. 17, 93, 128, 135

Ganeshaiah Veena Punyakoti, Cautun Marius, van de Weygaert Rien, Tempel Elmo, Frenk Carlos S. Cosmic Ballet III: Halo spin evolution in the cosmic web // Mon. Not. R. Astron. Soc.. V 2021. 503, 2. 2280–2299. 93, 128

Ganeshaiah Veena Punyakoti, Cautun Marius, van de Weygaert Rien, Tempel Elmo, Jones Bernard J. T., Rieder Steven, Frenk Carlos S. The Cosmic Ballet: spin and shape alignments of haloes in the cosmic web // Mon. Not. R. Astron. Soc.. XI 2018. 481, 1. 414–438. 128, 134

Genel Shy, Vogelsberger Mark, Springel Volker, Sijacki Debora, Nelson Dylan, Snyder Greg, Rodriguez-Gomez Vicente, Torrey Paul, Hernquist Lars. Introducing the Illustris project: the evolution of galaxy populations across cosmic time // Mon. Not. R. Astron. Soc.. XI 2014. 445, 1. 175–200. 25, 59, 65

Gheller C., Vazza F. A survey of the thermal and non-thermal properties of cosmic filaments // Mon. Not. R. Astron. Soc.. VI 2019. 486, 1. 981–1002. 84, 108, 125, 136

Gheller C., Vazza F., Brüggen M., Alpaslan M., Holwerda B. W., Hopkins A. M., Liske J. Evolution of cosmic filaments and of their galaxy population from MHD cosmological simulations // Mon. Not. R. Astron. Soc.. Oct 2016. 462, 1. 448–463. 84

Ghirardini V., Ettori S., Eckert D., Molendi S. Polytropic state of the intracluster medium in the X-COP cluster sample // Astron. Astrophys.. Jul 2019. 627. A19. 17

González Roberto E., Padilla Nelson D. Automated detection of filaments in the large-scale structure of the Universe // Mon. Not. R. Astron. Soc.. Sep 2010. 407, 3. 1449–1463. 73, 89

Gouin C., Aghanim N., Bonjean V., Douspis M. Probing the azimuthal environment of galaxies around clusters. From cluster core to cosmic filaments // Astron. Astrophys.. III 2020. 635. A195. 48, 92

Gouin C., Bonnaire T., Aghanim N. The shape and connectivity of groups and clusters: Impact of dynamical state and accretion history // arXiv e-prints. I 2021. arXiv:2101.04686. 48, 90, 92

Govoni F., Orrù E., Bonafede A., Iacobelli M., Paladino R., Vazza F., Murgia M., Vacca V., Giovannini G., Feretti L., Loi F., Bernardi G., Ferrari C., Pizzo R. F., Gheller C., Manti S., Brüggen M., Brunetti G., Cassano R., de Gasperin F., Enßlin T. A., Hoeft M., Horellou C., Junklewitz H., Röttgering H. J. A., Scaife A. M. M., Shimwell T. W., van Weeren R. J., Wise M. A radio ridge connecting two galaxy clusters in a filament of the cosmic web // Science. Jun 2019. 364, 6444. 981–984. 18

Guzzo L., Scodeggio M., Garilli B., Granett B. R., Fritz A., Abbas U., Adami C., Arnouts S., Bel J., Bolzonella M., Bottini D., Branchini E., Cappi A., Coupon J., Cucciati O., Davidzon I., De Lucia G., de la Torre S., Franzetti P., Fumana M., Hudelot P., Ilbert O., Iovino A., Krywult J., Le Brun V., Le Fèvre O., Maccagni D., Małek K., Marulli F., McCracken H. J., Paioro L., Peacock J. A., Polletta M., Pollo A., Schlagenhaufer H., Tasca L. A. M., Tojeiro R., Vergani D., Zamorani G., Zanichelli A., Burden A., Di Porto C., Marchetti A., Marinoni C., Mellier Y., Moscardini L., Nichol R. C., Percival W. J., Phleps S., Wolk M. The VIMOS Public Extragalactic Redshift Survey (VIPERS). An unprecedented view of galaxies and large-scale structure at 0.5 < z < 1.2 // Astron. Astrophys.. Jun 2014. 566. A108. 15, 55

Haardt Francesco, Madau Piero. Radiative Transfer in a Clumpy Universe. II. The Ultraviolet Extragalactic Background // Astrophys. J.. IV 1996. 461. 20. 22

Hahn Oliver, Carollo C. Marcella, Porciani Cristiano, Dekel Avishai. The evolution of dark matter halo properties in clusters, filaments, sheets and voids // Mon. Not. R. Astron. Soc.. X 2007. 381, 1. 41–51. 128

Hahn Oliver, Teyssier Romain, Carollo C. Marcella. The large-scale orientations of disc galaxies // Mon. Not. R. Astron. Soc.. VI 2010. 405, 1. 274–290. 128

Haider M., Steinhauser D., Vogelsberger M., Genel S., Springel V., Torrey P., Hernquist L. Large-scale mass distribution in the Illustris simulation // Mon. Not. R. Astron. Soc.. IV 2016. 457, 3. 3024–3035. 59, 65, 96

Henden Nicholas A., Puchwein Ewald, Sijacki Debora. The baryon content of groups and clusters of galaxies in the FABLE simulations // Mon. Not. R. Astron. Soc.. X 2020. 498, 2. 2114–2137. 80, 84

Hernquist Lars. An Analytical Model for Spherical Galaxies and Bulges // Astrophys. J.. Jun 1990. 356. 359. 67

Hirschmann Michaela, Dolag Klaus, Saro Alexandro, Bachmann Lisa, Borgani Stefano, Burkert Andreas. Cosmological simulations of black hole growth: AGN luminosities and downsizing // Mon. Not. R. Astron. Soc.. Aug 2014. 442, 3. 2304–2324. 21, 26, 27

Huchra J. P., Geller M. J. Groups of Galaxies. I. Nearby groups // Astrophys. J.. VI 1982. 257. 423–437. 27

Jõeveer Mikhel, Einasto Jaan, Tago Erik. Spatial distribution of galaxies and of clusters of galaxies in the southern galactic hemisphere // Mon. Not. R. Astron. Soc.. XI 1978. 185. 357–370. 15, 55

Jones D. Heath, Read Mike A., Saunders Will, Colless Matthew, Jarrett Tom, Parker Quentin A., Fairall Anthony P., Mauch Thomas, Sadler Elaine M., Watson Fred G., Burton Donna, Campbell Lachlan A., Cass Paul, Croom Scott M., Dawe John, Fiegert Kristin, Frankcombe Leela, Hartley Malcolm, Huchra John, James Dionne, Kirby Emma, Lahav Ofer, Lucey John, Mamon Gary A., Moore Lesa, Peterson Bruce A., Prior Sayuri, Proust Dominique, Russell Ken, Safouris Vicky, Wakamatsu Ken-Ichi, Westra Eduard, Williams Mary. The 6dF Galaxy Survey: final redshift release (DR3) and southern large-scale structures // Mon. Not. R. Astron. Soc.. Oct 2009. 399, 2. 683–698. 15, 55

Kennicutt Jr. Robert C. Star Formation in Galaxies Along the Hubble Sequence // . I 1998. 36. 189–232. 22

Klar J. S., Mücket J. P. Filaments and sheets of the warm-hot intergalactic medium // Mon. Not. R. Astron. Soc.. VI 2012. 423, 1. 304–319. 108, 125, 136

Klypin Anatoly A., Trujillo-Gomez Sebastian, Primack Joel. Dark Matter Halos in the Standard Cosmological Model: Results from the Bolshoi Simulation // Astrophys. J.. X 2011. 740, 2. 102. 21

Komatsu E., Smith K. M., Dunkley J., Bennett C. L., Gold B., Hinshaw G., Jarosik N., Larson D., Nolta M. R., Page L., Spergel D. N., Halpern M., Hill R. S., Kogut A., Limon M., Meyer S. S., Odegard N., Tucker G. S., Weiland J. L., Wollack E., Wright E. L. Seven-year Wilkinson Microwave Anisotropy Probe (WMAP) Observations: Cosmological Interpretation // Astrophys. J. Suppl. Ser.. Feb 2011. 192, 2. 18. 27

Kraljic K., Arnouts S., Pichon C., Laigle C., de la Torre S., Vibert D., Cadiou C., Dubois Y., Treyer M., Schimd C., Codis S., de Lapparent V., Devriendt J., Hwang H. S., Le Borgne D., Malavasi N., Milliard B., Musso M., Pogosyan D., Alpaslan M., Bland-Hawthorn J., Wright A. H. Galaxy evolution in the metric of the cosmic web // Mon. Not. R. Astron. Soc.. Feb 2018. 474, 1. 547–571. 80, 105, 127, 128, 132, 133

Kraljic K., Pichon C., Dubois Y., Codis S., Cadiou C., Devriendt J., Musso M., Welker C., Arnouts S., Hwang H. S., Laigle C., Peirani S., Slyz A., Treyer M., Vibert D. Galaxies flowing in the oriented saddle frame of the cosmic web // Mon. Not. R. Astron. Soc.. Mar 2019. 483, 3. 3227–3254. 45, 80, 92, 105, 128, 132, 133

Kraljic Katarina, Davé Romeel, Pichon Christophe. And yet it flips: connecting galactic spin and the cosmic web // Mon. Not. R. Astron. Soc.. III 2020. 493, 1. 362–381. 128

Kraljic Katarina, Duckworth Christopher, Tojeiro Rita, Alam Shadab, Bizyaev Dmitry, Weijmans Anne-Marie, Boardman Nicholas Fraser, Lane Richard R. SDSS-IV MaNGA: 3D spin alignment of spiral and S0 galaxies // Mon. Not. R. Astron. Soc.. VII 2021. 504, 3. 4626–4633. 128, 134

Kravtsov Andrey V., Nagai Daisuke, Vikhlinin Alexey A. Effects of Cooling and Star Formation on the Baryon Fractions in Clusters // Astrophys. J.. VI 2005. 625, 2. 588–598. 80

Krolewski Alex, Ho Shirley, Chen Yen-Chi, Chan P. F., Tenneti Ananth, Bizyaev Dmitry, Kraljic Katarina. Alignment between Filaments and Galaxy Spins from the MaNGA Integral-field Survey // Astrophys. J.. V 2019. 876, 1. 52. 128, 134

Laigle C., McCracken H. J., Ilbert O., Hsieh B. C., Davidzon I., Capak P., Hasinger G., Silverman J. D., Pichon C., Coupon J., Aussel H., Le Borgne D., Caputi K., Cassata P., Chang Y. Y., Civano F., Dunlop J., Fynbo J., Kartaltepe J. S., Koekemoer A., Le Fèvre O., Le Floc'h E., Leauthaud A., Lilly S., Lin L., Marchesi S., Milvang-Jensen B., Salvato M., Sanders D. B., Scoville N., Smolcic V., Stockmann M., Taniguchi Y., Tasca L., Toft S., Vaccari Mattia, Zabl J. The COSMOS2015 Catalog: Exploring the 1 < z < 6 Universe with Half a Million Galaxies // Astrophys. J. Suppl. Ser.. Jun 2016. 224, 2. 24. 15

Laigle C., Pichon C., Arnouts S., McCracken H. J., Dubois Y., Devriendt J., Slyz A., Le Borgne D., Benoit-Lévy A., Hwang Ho Seong, Ilbert O., Kraljic K., Malavasi N., Park Changbom, Vibert D. COSMOS2015 photometric redshifts probe the impact of filaments on galaxy properties // Mon. Not. R. Astron. Soc.. Mar 2018. 474, 4. 5437–5458. 37, 80, 127, 128, 132, 133

Laigle C., Pichon C., Codis S., Dubois Y., Le Borgne D., Pogosyan D., Devriendt J., Peirani S., Prunet S., Rouberol S., Slyz A., Sousbie T. Swirling around filaments: are large-scale structure vortices spinning up dark haloes? // Mon. Not. R. Astron. Soc.. I 2015. 446, 3. 2744–2759. 128

Le Brun Amandine M. C., McCarthy Ian G., Schaye Joop, Ponman Trevor J. Towards a realistic population of simulated galaxy groups and clusters // Mon. Not. R. Astron. Soc.. VI 2014. 441, 2. 1270–1290. 80, 84

Le Fèvre O., Vettolani G., Garilli B., Tresse L., Bottini D., Le Brun V., Maccagni D., Picat J. P., Scaramella R., Scodeggio M., Zanichelli A., Adami C., Arnaboldi M., Arnouts S., Bardelli S., Bolzonella M., Cappi A., Charlot S., Ciliegi P., Contini T., Foucaud S., Franzetti P., Gavignaud I., Guzzo L., Ilbert O., Iovino A., McCracken H. J., Marano B., Marinoni C., Mathez G., Mazure A., Meneux B., Merighi R., Paltani S., Pellò R., Pollo A., Pozzetti L., Radovich M., Zamorani G., Zucca E., Bondi M., Bongiorno A., Busarello G., Lamareille F., Mellier Y., Merluzzi P., Ripepi V., Rizzo D. The VIMOS VLT deep survey. First epoch VVDS-deep survey: 11 564 spectra with 17.5 ≤ IAB ≤ 24, and the redshift distribution over 0 ≤ z ≤ 5 // Astron. Astrophys.. Sep 2005. 439, 3. 845–862. 15, 55

Leitherer Claus, Schaerer Daniel, Goldader Jeffrey D., Delgado Rosa M. González, Robert Carmelle, Kune Denis Foo, de Mello Duília F., Devost Daniel, Heckman Timothy M. Starburst99: Synthesis Models for Galaxies with Active Star Formation // Astrophys. J. Suppl. Ser.. VII 1999. 123, 1. 3–40. 22

Liao Shihong, Gao Liang. Impact of filaments on galaxy formation in their residing dark matter haloes // Mon. Not. R. Astron. Soc.. V 2019. 485, 1. 464–473. 105

Libeskind Noam I., van de Weygaert Rien, Cautun Marius, Falck Bridget, Tempel Elmo, Abel Tom, Alpaslan Mehmet, Aragón-Calvo Miguel A., Forero-Romero Jaime E., Gonzalez Roberto, Gottlöber Stefan, Hahn Oliver, Hellwing Wojciech A., Hoffman Yehuda, Jones Bernard J. T., Kitaura Francisco, Knebe Alexander, Manti Serena, Neyrinck Mark, Nuza Sebastián E., Padilla Nelson, Platen Erwin, Ramachandra Nesar, Robotham Aaron, Saar Enn, Shand arin Sergei, Steinmetz Matthias, Stoica Radu S., Sousbie Thierry, Yepes Gustavo. Tracing the cosmic web // Mon. Not. R. Astron. Soc.. I 2018. 473, 1. 1195–1217. 28, 49

Ludlow Aaron D., Angulo Raúl E. Einasto profiles and the dark matter power spectrum // Mon. Not. R. Astron. Soc.. Feb 2017. 465, 1. L84–L88. 67

Malavasi N., Arnouts S., Vibert D., de la Torre S., Moutard T., Pichon C., Davidzon I., Kraljic K., Bolzonella M., Guzzo L., Garilli B., Scodeggio M., Granett B. R., Abbas U., Adami C., Bottini D., Cappi A., Cucciati O., Franzetti P., Fritz A., Iovino A., Krywult J., Le Brun V., Le Fèvre O., Maccagni D., Małek K., Marulli F., Polletta M., Pollo A., Tasca L., Tojeiro R., Vergani D., Zanichelli A., Bel J., Branchini E., Coupon J., De Lucia G., Dubois Y., Hawken A., Ilbert O., Laigle C., Moscardini L., Sousbie T., Treyer M., Zamorani G. The VIMOS Public Extragalactic Redshift Survey (VIPERS): galaxy segregation inside filaments at z 0.7 // Mon. Not. R. Astron. Soc.. Mar 2017. 465, 4. 3817–3822. 18, 37, 80, 105, 127, 132, 133

Malavasi Nicola, Aghanim Nabila, Douspis Marian, Tanimura Hideki, Bonjean Victor. Characterising filaments in the SDSS volume from the galaxy distribution // Astron. Astrophys.. X 2020a. 642. A19. 18, 32, 43, 48, 56, 124

Malavasi Nicola, Aghanim Nabila, Tanimura Hideki, Bonjean Victor, Douspis Marian. Like a spider in its web: a study of the large-scale structure around the Coma cluster // Astron. Astrophys.. II 2020b. 634. A30. 18, 43

Malavasi Nicola, Langer Mathieu, Aghanim Nabila, Galárraga-Espinosa Daniela, Gouin Céline. On the relative effect of nodes and filaments of the cosmic web on the quenching of galaxies and the orientation of their spin // arXiv e-prints. IX 2021. arXiv:2109.14623. 128, 129, 132, 134

Martizzi Davide, Vogelsberger Mark, Artale Maria Celeste, Haider Markus, Torrey Paul, Marinacci Federico, Nelson Dylan, Pillepich Annalisa, Weinberger Rainer, Hernquist Lars, Naiman Jill, Springel Volker. Baryons in the Cosmic Web of IllustrisTNG - I: gas in knots, filaments, sheets, and voids // Mon. Not. R. Astron. Soc.. Jul 2019. 486, 3. 3766–3787. 84, 85, 96, 98, 99, 102, 106, 107, 125, 135

McCarthy Ian G., Schaye Joop, Bird Simeon, Le Brun Amandine M. C. The BAHAMAS project: calibrated hydrodynamical simulations for large-scale structure cosmology // Mon. Not. R. Astron. Soc.. III 2017. 465, 3. 2936–2965. 80, 84

More Surhud, Diemer Benedikt, Kravtsov Andrey V. The Splashback Radius as a Physical Halo Boundary and the Growth of Halo Mass // Astrophys. J.. Sep 2015. 810, 1. 36. 57

More Surhud, Miyatake Hironao, Takada Masahiro, Diemer Benedikt, Kravtsov Andrey V., Dalal Neal K., More Anupreeta, Murata Ryoma, Mandelbaum Rachel, Rozo Eduardo, Rykoff Eli S., Oguri Masamune, Spergel David N. Detection of the Splashback Radius and Halo Assembly Bias of Massive Galaxy Clusters // Astrophys. J.. VII 2016. 825, 1. 39. 57

Nagai Daisuke, Kravtsov Andrey V., Vikhlinin Alexey. Effects of Galaxy Formation on Thermodynamics of the Intracluster Medium // Astrophys. J.. Oct 2007. 668, 1. 1–14. 17, 67

Naiman Jill P., Pillepich Annalisa, Springel Volker, Ramirez-Ruiz Enrico, Torrey Paul, Vogelsberger Mark, Pakmor Rüdiger, Nelson Dylan, Marinacci Federico, Hernquist Lars, Weinberger Rainer, Genel Shy. First results from the IllustrisTNG simulations: a tale of two elements - chemical evolution of magnesium and europium // Mon. Not. R. Astron. Soc.. VI 2018. 477, 1. 1206–1224. 27

Navarro Julio F., Frenk Carlos S., White Simon D. M. A Universal Density Profile from Hierarchical Clustering // Astrophys. J.. XII 1997. 490, 2. 493–508. 67

Nelson D., Pillepich A., Genel S., Vogelsberger M., Springel V., Torrey P., Rodriguez-Gomez V., Sijacki D., Snyder G. F., Griffen B., Marinacci F., Blecha L., Sales L., Xu D., Hernquist L. The illustris simulation: Public data release // Astronomy and Computing. XI 2015. 13. 12–37. 16, 21, 25

Nelson Dylan, Pillepich Annalisa, Springel Volker, Pakmor Rüdiger, Weinberger Rainer, Genel Shy, Torrey Paul, Vogelsberger Mark, Marinacci Federico, Hernquist Lars. First results from the TNG50 simulation: galactic outflows driven by supernovae and black hole feedback // Mon. Not. R. Astron. Soc.. XII 2019a. 490, 3. 3234–3261. 22, 24

Nelson Dylan, Springel Volker, Pillepich Annalisa, Rodriguez-Gomez Vicente, Torrey Paul, Genel Shy, Vogelsberger Mark, Pakmor Ruediger, Marinacci Federico, Weinberger Rainer, Kelley Luke, Lovell Mark, Diemer Benedikt, Hernquist Lars. The IllustrisTNG simulations: public data release // Computational Astrophysics and Cosmology. May 2019b. 6, 1. 2. 21, 22, 25, 38

Nevalainen J., Tempel E., Liivamägi L. J., Branchini E., Roncarelli M., Giocoli C., Heinämäki P., Saar E., Tamm A., Finoguenov A., Nurmi P., Bonamente M. Missing baryons traced by the galaxy luminosity density in large-scale WHIM filaments // Astron. Astrophys.. XI 2015. 583. A142. 93, 102, 125, 135

Pakmor Rüdiger, Guillet Thomas, Pfrommer Christoph, Gómez Facundo A., Grand Robert J. J., Marinacci Federico, Simpson Christine M., Springel Volker. Faraday rotation maps of disc galaxies // Mon. Not. R. Astron. Soc.. XII 2018. 481, 4. 4410–4418. 99

Pakmor Rüdiger, Springel Volker. Simulations of magnetic fields in isolated disc galaxies // Mon. Not. R. Astron. Soc.. VI 2013. 432, 1. 176–193. 27

Pakmor Ruediger, Bauer Andreas, Springel Volker. Magnetohydrodynamics on an unstructured moving grid // Mon. Not. R. Astron. Soc.. XII 2011. 418, 2. 1392–1401. 27

Peebles P. J. E. Large-scale background temperature and mass fluctuations due to scale-invariant primeval perturbations // Astrophys. J. Lett. XII 1982. 263. L1–L5. 22

Peng Y., Maiolino R., Cochrane R. Strangulation as the primary mechanism for shutting down star formation in galaxies // Nature. V 2015. 521, 7551. 192–195. 134

Peng Ying-jie, Lilly Simon J., Kovač Katarina, Bolzonella Micol, Pozzetti Lucia, Renzini Alvio, Zamorani Gianni, Ilbert Olivier, Knobel Christian, Iovino Angela, Maier Christian, Cucciati Olga, Tasca Lidia, Carollo C. Marcella, Silverman John, Kampczyk Pawel, de Ravel Loic,

Sanders David, Scoville Nicholas, Contini Thierry, Mainieri Vincenzo, Scodeggio Marco, Kneib Jean-Paul, Le Fèvre Olivier, Bardelli Sandro, Bongiorno Angela, Caputi Karina, Coppa Graziano, de la Torre Sylvain, Franzetti Paolo, Garilli Bianca, Lamareille Fabrice, Le Borgne Jean-Francois, Le Brun Vincent, Mignoli Marco, Perez Montero Enrique, Pello Roser, Ricciardelli Elena, Tanaka Masayuki, Tresse Laurence, Vergani Daniela, Welikala Niraj, Zucca Elena, Oesch Pascal, Abbas Ummi, Barnes Luke, Bordoloi Rongmon, Bottini Dario, Cappi Alberto, Cassata Paolo, Cimatti Andrea, Fumana Marco, Hasinger Gunther, Koekemoer Anton, Leauthaud Alexei, Maccagni Dario, Marinoni Christian, McCracken Henry, Memeo Pierdomenico, Meneux Baptiste, Nair Preethi, Porciani Cristiano, Presotto Valentina, Scaramella Roberto. Mass and Environment as Drivers of Galaxy Evolution in SDSS and zCOSMOS and the Origin of the Schechter Function // Astrophys. J.. IX 2010. 721, 1. 193–221. 133, 134

Pereyra Luis A., Sgró Mario A., Merchán Manuel E., Stasyszyn Federico A., Paz Dante J. Detection and analysis of cluster-cluster filaments // Mon. Not. R. Astron. Soc.. XII 2020. 499, 4. 4876–4886. 28

Pillepich Annalisa, Springel Volker, Nelson Dylan, Genel Shy, Naiman Jill, Pakmor Rüdiger, Hernquist Lars, Torrey Paul, Vogelsberger Mark, Weinberger Rainer, Marinacci Federico. Simulating galaxy formation with the IllustrisTNG model // Mon. Not. R. Astron. Soc.. I 2018. 473, 3. 4077–4106. 22, 25, 26, 27

Pintos-Castro I., Yee H. K. C., Muzzin A., Old L., Wilson G. The Evolution of the Quenching of Star Formation in Cluster Galaxies since z 1 // Astrophys. J.. May 2019. 876, 1. 40. 17

Planck Collaboration , Ade P. A. R., Aghanim N., Arnaud M., Ashdown M., Aumont J., Baccigalupi C., Banday A. J., Barreiro R. B., Bartlett J. G., Bartolo N., Battaner E., Battye R., Benabed K., Benoît A., Benoit-Lévy A., Bernard J. P., Bersanelli M., Bielewicz P., Bock J. J., Bonaldi A., Bonavera L., Bond J. R., Borrill J., Bouchet F. R., Boulanger F., Bucher M., Burigana C., Butler R. C., Calabrese E., Cardoso J. F., Catalano A., Challinor A., Chamballu A., Chary R. R., Chiang H. C., Chluba J., Christensen P. R., Church S., Clements D. L., Colombi S., Colombo L. P. L., Combet C., Coulais A., Crill B. P., Curto A., Cuttaia F., Danese L., Davies R. D., Davis R. J., de Bernardis P., de Rosa A., de Zotti G., Delabrouille J., Désert F. X., Di Valentino E., Dickinson C., Diego J. M., Dolag K., Dole H., Donzelli S., Doré O., Douspis M., Ducout A., Dunkley J., Dupac X., Efstathiou G., Elsner F., Enßlin T. A., Eriksen H. K., Farhang M., Fergusson J., Finelli F., Forni O., Frailis M., Fraisse A. A., Franceschi E., Frejsel A., Galeotta S., Galli S., Ganga K., Gauthier C., Gerbino M., Ghosh T., Giard M., Giraud-Héraud Y., Giusarma E., Gjerløw E., González-Nuevo J., Górski K. M., Gratton S., Gregorio A., Gruppuso A., Gudmundsson J. E., Hamann J., Hansen F. K., Hanson D., Harrison D. L., Helou G., Henrot-Versillé S., Hernández-Monteagudo C., Herranz D., Hildebrand t S. R., Hivon E., Hobson M., Holmes W. A., Hornstrup A., Hovest W., Huang Z., Huffenberger K. M., Hurier G., Jaffe A. H., Jaffe T. R., Jones W. C., Juvela M., Keihänen E., Keskitalo R., Kisner T. S., Kneissl R., Knoche J., Knox L., Kunz M., Kurki-Suonio H., Lagache G., Lähteenmäki A., Lamarre J. M., Lasenby A., Lattanzi M., Lawrence C. R., Leahy J. P., Leonardi R., Lesgourgues J., Levrier F., Lewis A., Liguori M., Lilje P. B., Linden-Vørnle M., López-Caniego M., Lubin P. M., Macías-Pérez J. F., Maggio G., Maino D., Mandolesi N., Mangilli A., Marchini A., Maris M., Martin P. G., Martinelli M., Martínez-González E., Masi S., Matarrese S., McGehee P., Meinhold P. R., Melchiorri A., Melin J. B., Mendes L., Mennella A., Migliaccio M., Millea M., Mitra S., Miville-Deschênes M. A., Moneti A., Montier L., Morgante G., Mortlock D., Moss A., Munshi D., Murphy J. A., Naselsky P., Nati F.,

Natoli P., Netterfield C. B., Nørgaard-Nielsen H. U., Noviello F., Novikov D., Novikov I., Oxborrow C. A., Paci F., Pagano L., Pajot F., Paladini R., Paoletti D., Partridge B., Pasian F., Patanchon G., Pearson T. J., Perdereau O., Perotto L., Perrotta F., Pettorino V., Piacentini F., Piat M., Pierpaoli E., Pietrobon D., Plaszczynski S., Pointecouteau E., Polenta G., Popa L., Pratt G. W., Prézeau G., Prunet S., Puget J. L., Rachen J. P., Reach W. T., Rebolo R., Reinecke M., Remazeilles M., Renault C., Renzi A., Ristorcelli I., Rocha G., Rosset C., Rossetti M., Roudier G., Rouillé d'Orfeuil B., Rowan-Robinson M., Rubiño-Martín J. A., Rusholme B., Said N., Salvatelli V., Salvati L., Sandri M., Santos D., Savelainen M., Savini G., Scott D., Seiffert M. D., Serra P., Shellard E. P. S., Spencer L. D., Spinelli M., Stolyarov V., Stompor R., Sudiwala R., Sunyaev R., Sutton D., Suur-Uski A. S., Sygnet J. F., Tauber J. A., Terenzi L., Toffolatti L., Tomasi M., Tristram M., Trombetti T., Tucci M., Tuovinen J., Türler M., Umana G., Valenziano L., Valiviita J., Van Tent F., Vielva P., Villa F., Wade L. A., Wandelt B. D., Wehus I. K., White M., White S. D. M., Wilkinson A., Yvon D., Zacchei A., Zonca A. Planck 2015 results. XIII. Cosmological parameters // Astron. Astrophys.. Sep 2016a. 594. A13. 22, 78, 79

Planck Collaboration , Aghanim N., Arnaud M., Ashdown M., Aumont J., Baccigalupi C., Band ay A. J., Barreiro R. B., Bartlett J. G., Bartolo N., Battaner E., Battye R., Benabed K., Benoît A., Benoit-Lévy A., Bernard J. P., Bersanelli M., Bielewicz P., Bock J. J., Bonaldi A., Bonavera L., Bond J. R., Borrill J., Bouchet F. R., Burigana C., Butler R. C., Calabrese E., Cardoso J. F., Catalano A., Challinor A., Chiang H. C., Christensen P. R., Churazov E., Clements D. L., Colombo L. P. L., Combet C., Comis B., Coulais A., Crill B. P., Curto A., Cuttaia F., Danese L., Davies R. D., Davis R. J., de Bernardis P., de Rosa A., de Zotti G., Delabrouille J., Désert F. X., Dickinson C., Diego J. M., Dolag K., Dole H., Donzelli S., Doré O., Douspis M., Ducout A., Dupac X., Efstathiou G., Elsner F., Enßlin T. A., Eriksen H. K., Fergusson J., Finelli F., Forni O., Frailis M., Fraisse A. A., Franceschi E., Frejsel A., Galeotta S., Galli S., Ganga K., Génova-Santos R. T., Giard M., González-Nuevo J., Górski K. M., Gregorio A., Gruppuso A., Gudmundsson J. E., Hansen F. K., Harrison D. L., Henrot-Versillé S., Hernández-Monteagudo C., Herranz D., Hildebrand t S. R., Hivon E., Holmes W. A., Hornstrup A., Huffenberger K. M., Hurier G., Jaffe A. H., Jones W. C., Juvela M., Keihänen E., Keskitalo R., Kneissl R., Knoche J., Kunz M., Kurki-Suonio H., Lacasa F., Lagache G., Lähteenmäki A., Lamarre J. M., Lasenby A., Lattanzi M., Leonardi R., Lesgourgues J., Levrier F., Liguori M., Lilje P. B., Linden-Vørnle M., López-Caniego M., Macías-Pérez J. F., Maffei B., Maggio G., Maino D., Mandolesi N., Mangilli A., Maris M., Martin P. G., Martínez-González E., Masi S., Matarrese S., Melchiorri A., Melin J. B., Migliaccio M., Miville-Deschênes M. A., Moneti A., Montier L., Morgante G., Mortlock D., Munshi D., Murphy J. A., Naselsky P., Nati F., Natoli P., Noviello F., Novikov D., Novikov I., Paci F., Pagano L., Pajot F., Paoletti D., Pasian F., Patanchon G., Perdereau O., Perotto L., Pettorino V., Piacentini F., Piat M., Pierpaoli E., Pietrobon D., Plaszczynski S., Pointecouteau E., Polenta G., Ponthieu N., Pratt G. W., Prunet S., Puget J. L., Rachen J. P., Reinecke M., Remazeilles M., Renault C., Renzi A., Ristorcelli I., Rocha G., Rossetti M., Roudier G., Rubiño-Martín J. A., Rusholme B., Sandri M., Santos D., Sauvé A., Savelainen M., Savini G., Scott D., Spencer L. D., Stolyarov V., Stompor R., Sunyaev R., Sutton D., Suur-Uski A. S., Sygnet J. F., Tauber J. A., Terenzi L., Toffolatti L., Tomasi M., Tramonte D., Tristram M., Tucci M., Tuovinen J., Valenziano L., Valiviita J., Van Tent B., Vielva P., Villa F., Wade L. A., Wandelt B. D., Wehus I. K., Yvon D., Zacchei A., Zonca A. Planck 2015 results. XXII. A map of the thermal Sunyaev-Zeldovich effect // Astron. Astrophys.. IX 2016b. 594. A22. 124

Planelles S., Borgani S., Dolag K., Ettori S., Fabjan D., Murante G., Tornatore L. Baryon

census in hydrodynamical simulations of galaxy clusters // Mon. Not. R. Astron. Soc.. V 2013. 431, 2. 1487–1502. 80, 84

Potter Douglas, Stadel Joachim, Teyssier Romain. PKDGRAV3: beyond trillion particle cosmological simulations for the next era of galaxy surveys // Computational Astrophysics and Cosmology. V 2017. 4, 1. 2. 21

Prada Francisco, Klypin Anatoly A., Cuesta Antonio J., Betancort-Rijo Juan E., Primack Joel. Halo concentrations in the standard Λ cold dark matter cosmology // Mon. Not. R. Astron. Soc.. VII 2012. 423, 4. 3018–3030. 21

Press W. H., Davis M. How to identify and weigh virialized clusters of galaxies in a complete redshift catalog // Astrophys. J.. VIII 1982. 259. 449–473. 27

Puchwein E., Sijacki D., Springel V. Simulations of AGN Feedback in Galaxy Clusters and Groups: Impact on Gas Fractions and the L_X-T Scaling Relation // Astrophys. J. Lett. XI 2008. 687, 2. L53. 80

Quai Salvatore, Hani Maan H., Ellison Sara L., Patton David R., Woo Joanna. Interacting galaxies in the IllustrisTNG simulations - III: (the rarity of) quenching in post-merger galaxies // Mon. Not. R. Astron. Soc.. IV 2021. 82

Ragagnin A., Dolag K., Biffi V., Cadolle Bel M., Hammer N. J., Krukau A., Petkova M., Steinborn D. A web portal for hydrodynamical, cosmological simulations // Astronomy and Computing. VII 2017. 20. 52–67. 21, 26

Ramsøy Marius, Slyz Adrianne, Devriendt Julien, Laigle Clotilde, Dubois Yohan. Rivers of gas - I. Unveiling the properties of high redshift filaments // Mon. Not. R. Astron. Soc.. III 2021. 502, 1. 351–368. 96, 134

Rost Agustin, Kuchner Ulrike, Welker Charlotte, Pearce Frazer, Stasyszyn Federico, Gray Meghan, Cui Weiguang, Dave Romeel, Knebe Alexander, Yepes Gustavo, Rasia Elena. The ThreeHundred: the structure and properties of cosmic filaments in the outskirts of galaxy clusters // Mon. Not. R. Astron. Soc.. III 2021. 502, 1. 714–727. 73, 77, 78, 86, 92

Rost Agustín, Stasyszyn Federico, Pereyra Luis, Martínez Héctor J. A comparison of cosmological filaments catalogues // Mon. Not. R. Astron. Soc.. Feb 2020. 307. 18, 127, 133

Santiago-Bautista Iris, Caretta César A., Bravo-Alfaro Héctor, Pointecouteau Etienne, Andernach Heinz. Identification of filamentary structures in the environment of superclusters of galaxies in the Local Universe // Astron. Astrophys.. V 2020. 637. A31. 89, 92

Sarron F., Adami C., Durret F., Laigle C. Pre-processing of galaxies in cosmic filaments around AMASCFI clusters in the CFHTLS // Astron. Astrophys.. XII 2019. 632. A49. 132

Schaap W. E., van de Weygaert R. Continuous fields and discrete samples: reconstruction through Delaunay tessellations // Astron. Astrophys.. Nov 2000. 363. L29–L32. 31, 35, 129

Schaye Joop, Crain Robert A., Bower Richard G., Furlong Michelle, Schaller Matthieu, Theuns Tom, Dalla Vecchia Claudio, Frenk Carlos S., McCarthy I. G., Helly John C., Jenkins Adrian, Rosas-Guevara Y. M., White Simon D. M., Baes Maarten, Booth C. M., Camps Peter, Navarro Julio F., Qu Yan, Rahmati Alireza, Sawala Till, Thomas Peter A., Trayford James. The

EAGLE project: simulating the evolution and assembly of galaxies and their environments // Mon. Not. R. Astron. Soc.. Jan 2015. 446, 1. 521–554. 17, 21, 38, 110

Scoville N., Aussel H., Brusa M., Capak P., Carollo C. M., Elvis M., Giavalisco M., Guzzo L., Hasinger G., Impey C., Kneib J. P., LeFevre O., Lilly S. J., Mobasher B., Renzini A., Rich R. M., Sanders D. B., Schinnerer E., Schminovich D., Shopbell P., Taniguchi Y., Tyson N. D. The Cosmic Evolution Survey (COSMOS): Overview // Astrophys. J. Suppl. Ser.. Sep 2007. 172, 1. 1–8. 15, 55

Shin T., Adhikari S., Baxter E. J., Chang C., Jain B., Battaglia N., Bleem L., Bocquet S., DeRose J., Gruen D., Hilton M., Kravtsov A., McClintock T., Rozo E., Rykoff E. S., Varga T. N., Wechsler R. H., Wu H., Zhang Z., Aiola S., Allam S., Bechtol K., Benson B. A., Bertin E., Bond J. R., Brodwin M., Brooks D., Buckley-Geer E., Burke D. L., Carlstrom J. E., Carnero Rosell A., Carrasco Kind M., Carretero J., Castander F. J., Choi S. K., Cunha C. E., Crawford T. M., da Costa L. N., De Vicente J., Desai S., Devlin M. J., Dietrich J. P., Doel P., Dunkley J., Eifler T. F., Evrard A. E., Flaugher B., Fosalba P., Gallardo P. A., García-Bellido J., Gaztanaga E., Gerdes D. W., Gralla M., Gruendl R. A., Gschwend J., Gupta N., Gutierrez G., Hartley W. G., Hill J. C., Ho S. P., Hollowood D. L., Honscheid K., Hoyle B., Huffenberger K., Hughes J. P., James D. J., Jeltema T., Kim A. G., Krause E., Kuehn K., Lahav O., Lima M., Madhavacheril M. S., Maia M. A. G., Marshall J. L., Maurin L., McMahon J., Menanteau F., Miller C. J., Miquel R., Mohr J. J., Naess S., Nati F., Newburgh L., Niemack M. D., Ogando R. L. C., Page L. A., Partridge B., Patil S., Plazas A. A., Rapetti D., Reichardt C. L., Romer A. K., Sanchez E., Scarpine V., Schindler R., Serrano S., Smith M., Smith R. C., Soares-Santos M., Sobreira F., Staggs S. T., Stark A., Stein G., Suchyta E., Swanson M. E. C., Tarle G., Thomas D., van Engelen A., Wollack E. J., Xu Z. Measurement of the splashback feature around SZ-selected Galaxy clusters with DES, SPT, and ACT // Mon. Not. R. Astron. Soc.. VIII 2019. 487, 2. 2900–2918. 57

Shull J. Michael, Smith Britton D., Danforth Charles W. The Baryon Census in a Multiphase Intergalactic Medium: 30% of the Baryons May Still be Missing // Astrophys. J.. XI 2012. 759, 1. 23. 96

Sijacki Debora, Vogelsberger Mark, Genel Shy, Springel Volker, Torrey Paul, Snyder Gregory F., Nelson Dylan, Hernquist Lars. The Illustris simulation: the evolving population of black holes across cosmic time // Mon. Not. R. Astron. Soc.. IX 2015. 452, 1. 575–596. 25

Singh Ankit, Mahajan Smriti, Bagla Jasjeet Singh. Study of galaxies on large-scale filaments in simulations // Mon. Not. R. Astron. Soc.. VII 2020. 497, 2. 2265–2275. 105

Sousbie T. The persistent cosmic web and its filamentary structure - I. Theory and implementation // Mon. Not. R. Astron. Soc.. Jun 2011. 414, 1. 350–383. 28, 29, 30, 31, 32, 33, 44, 127

Sousbie T., Pichon C., Kawahara H. The persistent cosmic web and its filamentary structure - II. Illustrations // Mon. Not. R. Astron. Soc.. VI 2011. 414. 384–403. 28, 32, 34, 127

Springel Volker. The cosmological simulation code GADGET-2 // Mon. Not. R. Astron. Soc.. Dec 2005. 364, 4. 1105–1134. 18, 21, 27

Springel Volker. E pur si muove: Galilean-invariant cosmological hydrodynamical simulations on a moving mesh // Mon. Not. R. Astron. Soc.. Jan 2010. 401, 2. 791–851. 22, 25

Springel Volker, Di Matteo Tiziana, Hernquist Lars. Modelling feedback from stars and black holes in galaxy mergers // Mon. Not. R. Astron. Soc.. VIII 2005. 361, 3. 776–794. 27, 59

Springel Volker, Hernquist Lars. Cosmological smoothed particle hydrodynamics simulations: a hybrid multiphase model for star formation // Mon. Not. R. Astron. Soc.. II 2003. 339, 2. 289–311. 27, 98

Springel Volker, White Simon D. M., Tormen Giuseppe, Kauffmann Guinevere. Populating a cluster of galaxies - I. Results at [formmu2]z=0 // Mon. Not. R. Astron. Soc.. Dec 2001. 328, 3. 726–750. 27, 28

Stoica R. S., Martínez V. J., Saar E. A three-dimensional object point process for detection of cosmic filaments. // Journal of the Royal Statistical Society: Series C (Applied Statistics) 56 (4. VIII 2007. 56. 1. 28

Sunyaev R. A., Zeldovich Ya. B. Small-Scale Fluctuations of Relic Radiation // Ap&SS. IV 1970. 7, 1. 3–19. 120

Sunyaev R. A., Zeldovich Ya. B. The Observations of Relic Radiation as a Test of the Nature of X-Ray Radiation from the Clusters of Galaxies // Comments on Astrophysics and Space Physics. XI 1972. 4. 173. 120

Tanimura H., Aghanim N., Bonjean V., Malavasi N., Douspis M. Density and temperature of cosmic-web filaments on scales of tens of megaparsecs // Astron. Astrophys.. V 2020a. 637. A41. 89, 115, 123, 124, 126, 136

Tanimura H., Aghanim N., Kolodzig A., Douspis M., Malavasi N. First detection of stacked X-ray emission from cosmic web filaments // Astron. Astrophys.. XI 2020b. 643. L2. 112, 136

Tanimura Hideki, Hinshaw Gary, McCarthy Ian G., Van Waerbeke Ludovic, Aghanim Nabila, Ma Yin-Zhe, Mead Alexander, Hojjati Alireza, Tröster Tilman. A search for warm/hot gas filaments between pairs of SDSS Luminous Red Galaxies // Mon. Not. R. Astron. Soc.. Feb 2019. 483, 1. 223–234. 18, 124, 126

Tanimura Hideki, Hinshaw Gary, McCarthy Ian G., Van Waerbeke Ludovic, Aghanim Nabila, Ma Yin-Zhe, Mead Alexander, Tröster Tilman, Hojjati Alireza, Moraes Bruno. Probing hot gas around luminous red galaxies through the Sunyaev-Zel'dovich effect // Mon. Not. R. Astron. Soc.. Jan 2020c. 491, 2. 2318–2329. 115

Taylor Edward N., Hopkins Andrew M., Baldry Ivan K., Brown Michael J. I., Driver Simon P., Kelvin Lee S., Hill David T., Robotham Aaron S. G., Bland -Hawthorn Joss, Jones D. H., Sharp R. G., Thomas Daniel, Liske Jochen, Loveday Jon, Norberg Peder, Peacock J. A., Bamford Steven P., Brough Sarah, Colless Matthew, Cameron Ewan, Conselice Christopher J., Croom Scott M., Frenk C. S., Gunawardhana Madusha, Kuijken Konrad, Nichol R. C., Parkinson H. R., Phillipps S., Pimbblet K. A., Popescu C. C., Prescott Matthew, Sutherland W. J., Tuffs R. J., van Kampen Eelco, Wijesinghe D. Galaxy And Mass Assembly (GAMA): stellar mass estimates // Mon. Not. R. Astron. Soc.. Dec 2011. 418, 3. 1587–1620. 38

Tempel E., Stoica R. S., Kipper R., Saar E. Bisous model-Detecting filamentary patterns in point processes // Astronomy and Computing. Jul 2016. 16. 17–25. 28, 110, 127

Tempel E., Stoica R. S., Martínez V. J., Liivamägi L. J., Castellan G., Saar E. Detecting filamentary pattern in the cosmic web: a catalogue of filaments for the SDSS // Mon. Not. R. Astron. Soc.. Mar 2014. 438, 4. 3465–3482. 49

Terrazas Bryan A., Bell Eric F., Pillepich Annalisa, Nelson Dylan, Somerville Rachel S., Genel Shy, Weinberger Rainer, Habouzit Mélanie, Li Yuan, Hernquist Lars, Vogelsberger Mark. The relationship between black hole mass and galaxy properties: examining the black hole feedback model in IllustrisTNG // Mon. Not. R. Astron. Soc.. IV 2020. 493, 2. 1888–1906. 82

Teyssier R. Cosmological hydrodynamics with adaptive mesh refinement. A new high resolution code called RAMSES // Astron. Astrophys.. IV 2002. 385. 337–364. 22

Tornatore L., Borgani S., Dolag K., Matteucci F. Chemical enrichment of galaxy clusters from hydrodynamical simulations // Mon. Not. R. Astron. Soc.. XII 2007. 382, 3. 1050–1072. 27

Tornatore L., Borgani S., Springel V., Matteucci F., Menci N., Murante G. Cooling and heating the intracluster medium in hydrodynamical simulations // Mon. Not. R. Astron. Soc.. VII 2003. 342, 4. 1025–1040. 27

Trowland Holly E., Lewis Geraint F., Bland-Hawthorn Joss. The Cosmic History of the Spin of Dark Matter Halos within the Large-scale Structure // Astrophys. J.. I 2013. 762, 2. 72. 128

Tuominen T., Nevalainen J., Tempel E., Kuutma T., Wijers N., Schaye J., Heinämäki P., Bonamente M., Ganeshaiah Veena P. An EAGLE view of the missing baryons // Astron. Astrophys.. II 2021. 646. A156. 38, 93, 102, 110, 125, 135

Ursino E., Galeazzi M., Roncarelli M. Effect of Metallicity on X-ray Emission from the Warm-hot Intergalactic Medium // Astrophys. J.. IX 2010. 721, 1. 46–58. 96

Valageas Patrick, Schaeffer Richard, Silk Joseph. The phase diagram of the intergalactic medium and the entropy floor of groups and clusters: are clusters born warm? // Mon. Not. R. Astron. Soc.. IX 2003. 344, 1. 53–59. 105

Vernstrom T., Heald G., Vazza F., Galvin T. J., West J. L., Locatelli N., Fornengo N., Pinetti E. Discovery of magnetic fields along stacked cosmic filaments as revealed by radio and X-ray emission // Mon. Not. R. Astron. Soc.. VIII 2021. 505, 3. 4178–4196. 18

Vogelsberger Mark, Genel Shy, Sijacki Debora, Torrey Paul, Springel Volker, Hernquist Lars. A model for cosmological simulations of galaxy formation physics // Mon. Not. R. Astron. Soc.. XII 2013. 436, 4. 3031–3067. 27

Vogelsberger Mark, Genel Shy, Springel Volker, Torrey Paul, Sijacki Debora, Xu Dandan, Snyder Greg, Nelson Dylan, Hernquist Lars. Introducing the Illustris Project: simulating the coevolution of dark and visible matter in the Universe // Mon. Not. R. Astron. Soc.. X 2014. 444, 2. 1518–1547. 21, 25

Vogelsberger Mark, Marinacci Federico, Torrey Paul, Puchwein Ewald. Cosmological simulations of galaxy formation // Nature Reviews Physics. I 2020. 2, 1. 42–66. 23, 24

Weinberger Rainer, Springel Volker, Hernquist Lars, Pillepich Annalisa, Marinacci Federico, Pakmor Rüdiger, Nelson Dylan, Genel Shy, Vogelsberger Mark, Naiman Jill, Torrey Paul. Simulating galaxy formation with black hole driven thermal and kinetic feedback // Mon. Not. R. Astron. Soc.. III 2017. 465, 3. 3291–3308. 27, 59

Weinberger Rainer, Springel Volker, Pakmor Rüdiger. The AREPO Public Code Release // Astrophys. J. Suppl. Ser.. VI 2020. 248, 2. 32. 25, 108

Weinberger Rainer, Springel Volker, Pakmor Rüdiger, Nelson Dylan, Genel Shy, Pillepich Annalisa, Vogelsberger Mark, Marinacci Federico, Naiman Jill, Torrey Paul, Hernquist Lars. Supermassive black holes and their feedback effects in the IllustrisTNG simulation // Mon. Not. R. Astron. Soc.. IX 2018. 479, 3. 4056–4072. 82

Welker C., Bland-Hawthorn J., Van de Sande J., Lagos C., Elahi P., Obreschkow D., Bryant J., Pichon C., Cortese L., Richards S. N., Croom S. M., Goodwin M., Lawrence J. S., Sweet S., Lopez-Sanchez A., Medling A., Owers M. S., Dubois Y., Devriendt J. The SAMI Galaxy Survey: first detection of a transition in spin orientation with respect to cosmic filaments in the stellar kinematics of galaxies // Mon. Not. R. Astron. Soc.. I 2020. 491, 2. 2864–2884. 37, 127, 128, 133, 134

Wiersma Robert P. C., Schaye Joop, Smith Britton D. The effect of photoionization on the cooling rates of enriched, astrophysical plasmas // Mon. Not. R. Astron. Soc.. II 2009a. 393, 1. 99–107. 27

Wiersma Robert P. C., Schaye Joop, Theuns Tom, Dalla Vecchia Claudio, Tornatore Luca. Chemical enrichment in cosmological, smoothed particle hydrodynamics simulations // Mon. Not. R. Astron. Soc.. X 2009b. 399, 2. 574–600. 27

Winkel Nico, Pasquali Anna, Kraljic Katarina, Smith Rory, Gallazzi Anna R., Jackson Thomas M. The Imprint of Cosmic Web Quenching on Central Galaxies // arXiv e-prints. V 2021. arXiv:2105.13368. 127, 132, 134

York Donald G., Adelman J., Anderson Jr. John E., Anderson Scott F., Annis James, Bahcall Neta A., Bakken J. A., Barkhouser Robert, Bastian Steven, Berman Eileen, Boroski William N., Bracker Steve, Briegel Charlie, Briggs John W., Brinkmann J., Brunner Robert, Burles Scott, Carey Larry, Carr Michael A., Castander Francisco J., Chen Bing, Colestock Patrick L., Connolly A. J., Crocker J. H., Csabai István, Czarapata Paul C., Davis John Eric, Doi Mamoru, Dombeck Tom, Eisenstein Daniel, Ellman Nancy, Elms Brian R., Evans Michael L., Fan Xiaohui, Federwitz Glenn R., Fiscelli Larry, Friedman Scott, Frieman Joshua A., Fukugita Masataka, Gillespie Bruce, Gunn James E., Gurbani Vijay K., de Haas Ernst, Haldeman Merle, Harris Frederick H., Hayes J., Heckman Timothy M., Hennessy G. S., Hindsley Robert B., Holm Scott, Holmgren Donald J., Huang Chi-hao, Hull Charles, Husby Don, Ichikawa Shin-Ichi, Ichikawa Takashi, Ivezić Željko, Kent Stephen, Kim Rita S. J., Kinney E., Klaene Mark, Kleinman A. N., Kleinman S., Knapp G. R., Korienek John, Kron Richard G., Kunszt Peter Z., Lamb D. Q., Lee B., Leger R. French, Limmongkol Siriluk, Lindenmeyer Carl, Long Daniel C., Loomis Craig, Loveday Jon, Lucinio Rich, Lupton Robert H., MacKinnon Bryan, Mannery Edward J., Mantsch P. M., Margon Bruce, McGehee Peregrine, McKay Timothy A., Meiksin Avery, Merelli Aronne, Monet David G., Munn Jeffrey A., Narayanan Vijay K., Nash Thomas, Neilsen Eric, Neswold Rich, Newberg Heidi Jo, Nichol R. C., Nicinski Tom, Nonino Mario, Okada Norio, Okamura Sadanori,

Ostriker Jeremiah P., Owen Russell, Pauls A. George, Peoples John, Peterson R. L., Petravick Donald, Pier Jeffrey R., Pope Adrian, Pordes Ruth, Prosapio Angela, Rechenmacher Ron, Quinn Thomas R., Richards Gordon T., Richmond Michael W., Rivetta Claudio H., Rockosi Constance M., Ruthmansdorfer Kurt, Sand ford Dale, Schlegel David J., Schneider Donald P., Sekiguchi Maki, Sergey Gary, Shimasaku Kazuhiro, Siegmund Walter A., Smee Stephen, Smith J. Allyn, Snedden S., Stone R., Stoughton Chris, Strauss Michael A., Stubbs Christopher, SubbaRao Mark, Szalay Alexander S., Szapudi Istvan, Szokoly Gyula P., Thakar Anirudda R., Tremonti Christy, Tucker Douglas L., Uomoto Alan, Vanden Berk Dan, Vogeley Michael S., Waddell Patrick, Wang Shu-i., Watanabe Masaru, Weinberg David H., Yanny Brian, Yasuda Naoki, SDSS Collaboration . The Sloan Digital Sky Survey: Technical Summary // AJ. Sep 2000. 120, 3. 1579–1587. 15, 55

Zel'dovich Ya. B. Fragmentation of a homogeneous medium under the action of gravitation // Astrophysics. Apr 1970. 6, 2. 164–174. 15

Zeldovich Ya. B., Sunyaev R. A. The Interaction of Matter and Radiation in a Hot-Model Universe // Ap&SS. VII 1969. 4, 3. 301–316. 120

de Graaff Anna, Cai Yan-Chuan, Heymans Catherine, Peacock John A. Probing the missing baryons with the Sunyaev-Zel'dovich effect from filaments // Astron. Astrophys.. Apr 2019. 624. A48. 18, 115

de Lapparent V., Geller M. J., Huchra J. P. A Slice of the Universe // Astrophys. J. Lett. Mar 1986. 302. L1. 15, 55

van de Weygaert R., Schaap W. The Cosmic Web: Geometric Analysis // Data Analysis in Cosmology, Lecture Notes in Physics, vol. 665. Edited by V. J. Martínez, E. Saar, E. Martínez-González, and M.-J. Pons-Bordería. Berlin: Springer, 2009., p.291-413. 665. 2009. 291–413. 31, 32, 35, 129

université PARIS-SACLAY

ÉCOLE DOCTORALE
Astronomie
et Astrophysique
d'Île-de-France (AAIF)

Titre : Caractérisation des filaments cosmiques et de leur environnement dans des simulations hydrodynamiques cosmologiques

Mots clés : Astrophysique; cosmologie; Structure à grande échelle (astronomie); Toile cosmique; Filaments; Matière sombre (astronomie); Baryons; Simulation par ordinateur

Résumé : La matière dans l'Univers s'assemble sous l'action de la gravité pour former un gigantesque réseau composé de noeuds, de filaments, de murs et de vides, appelé la toile cosmique. Cette structure est principalement définie par la dynamique de la matière noire, qui forme le squelette sur lequel la matière baryonique (ou ordinaire) est accrétée. Alors que les structures cosmiques les plus denses, tracées par les amas de galaxies les plus massifs, ont été minutieusement étudiées, en raison de leurs densités plus faibles et de leurs morphologies complexes, les filaments cosmiques et les propriétés de la matière qui les entoure sont encore mal connus. Or, étant donné que ces structures sont censées contenir près de la moitié de la matière de l'Univers, l'étude de la matière aux plus grandes échelles est inévitablement liée à celle des filaments.

Cette thèse propose la première étude complète des filaments cosmiques au décalage spectral $z = 0$. Les filaments analysés sont détectés dans la distribution des galaxies de simulations hydrodynamiques cosmologiques. Ces structures cosmiques sont tout d'abord caractérisées par leurs profils radiaux de densité de galaxies, révélant que la distribution des galaxies autour des filaments varie avec la longueur de ceux-ci. Deux populations différentes sont ainsi identifiées: les filaments courts ($L_f < 9$ Mpc) et les longs ($L_f \geq 20$ Mpc). Je montre que ces deux populations tracent des environnements différents de la toile cosmique. Les filaments courts sont plus denses, plus épais, et plus chauds que les longs. Ils correspondent aux ponts de matière entre des structures sur-denses, alors que les filaments longs sont à la base du squelette cosmique, souvent enchâssés dans des régions sous-denses.

Les propriétés du gaz autour des filaments cosmiques sont ensuite caractérisées en distinguant différentes phases en fonction de la température et de la densité de gaz. Je montre que les filaments cosmiques sont essentiellement constitués de gaz associé au milieu intergalactique chaud (WHIM), et que leurs parties centrales hébergent également d'importantes contributions de phases gazeuses plus chaudes et plus denses, dont les fractions dépendent du type de filament. En construisant des profils radiaux de température et de pression, je trouve que les filaments cosmiques possèdent des coeurs isothermes et des valeurs de pression environ mille fois inférieures à celles des amas. De plus, la population de filaments courts est caractérisée par des valeurs de densité, de température, et de pression du gaz qui sont trois fois supérieures à celles des filaments longs. Étant donné que certaines propriétés des galaxies sont intimement liées aux propriétés de leur environnement à grande échelle, j'étudie également l'influence des différents environnements tracés par les populations de filaments sur la masse et l'activité de formation d'étoiles des galaxies, en trouvant différentes tendances pour les filaments courts et longs.

Contrairement aux propriétés physiques du gaz et des galaxies, la distribution relative de la matière noire, du gaz et des étoiles autour des filaments s'avère universelle, indépendante de la population de filaments. En obtenant des profils de fraction de baryons, je montre que la distribution de la matière baryonique s'écarte de celle de la matière noire à des distances inférieures à ~ 7 Mpc aux axes des filaments, indiquant un rayon caractéristique du profil des baryons dans ces structures. Enfin, les coeurs des filaments sont fortement appauvris en baryons, tandis que leurs périphéries présentent un excès par rapport à la fraction cosmique, correspondant au gaz dans le WHIM.

Title: Characterising cosmic filaments and their surroundings in large-scale hydro-dynamical simulations

Keywords: Astrophysics; cosmology; Large-scale structure (astronomy); Cosmic web; Filaments; Dark matter (astronomy); Baryons; Numerical simulations

Abstract: Matter in the Universe is assembled under the action of gravity to form a gigantic network of nodes, filaments, walls, and voids, called the cosmic web. This structure is mainly set by the dynamics of dark matter (DM), which forms the skeleton onto which baryonic (or ordinary) matter is accreted. While the denser cosmic structures, traced by the most massive clusters of galaxies, have been thoroughly studied, because of their lower densities and complex morphologies, cosmic filaments and the properties of matter around them are still poorly known. However, these structures are believed to contain almost half of the matter in the Universe. The study of matter at the largest scales is therefore inevitably linked to that of filaments.

This thesis offers the first comprehensive study of cosmic filaments at redshift $z = 0$. The analysed filaments are detected in the distribution of galaxies of large-scale hydro-dynamical simulations. These cosmic structures are firstly characterised by their radial profiles of galaxy density, revealing that the distribution of galaxies around filaments varies with filament length. Two different filament populations are thus identified, the short ($L_f < 9$ Mpc) and the long ($L_f \geq 20$ Mpc). I show that these two populations are tracers of different environments of the cosmic web. Short filaments are denser, puffier, and hotter than long filaments. The former correspond to the bridges of matter between over-dense structures, whereas the latter are at the basis of the cosmic skeleton, often embedded in under-dense regions.

The properties of gas around cosmic filaments are then characterised by distinguishing different phases according to temperature and density. I show that cosmic filaments are essentially made of gas in the warm-hot intergalactic medium (WHIM) phase, and that their cores also host large contributions of hotter and denser gas phases whose fractions depend on the filament population. By building radial temperature and pressure profiles, I find that cosmic filaments possess isothermal cores and pressure values that are ~ 1000 times lower than those of clusters. Moreover, the population of short filaments is characterised by values of gas density, temperature, and pressure that are a factor of three larger than these of long filaments. Since many properties of galaxies are intimately linked to the properties of their large scale environment, I also investigate the influence of the different environments traced by the filament populations on the mass and star-formation activity of galaxies, finding different trends in short and long filaments.

Contrary to the properties of gas and galaxies, the relative distribution of DM, gas, and stars around filaments is found to be universal, independent from the filament population. By deriving baryon fraction profiles, I show that baryonic matter deviates from the DM density field at distances closer than ~ 7 Mpc to the filament spines, indicating a characteristic radius of baryons in filaments. Finally, cores of filaments are strongly baryon depleted, and their outskirts present an excess of baryons with respect to the cosmic fraction, made essentially of WHIM gas.

Université Paris-Saclay
Espace Technologique / Immeuble Discovery
Route de l'Orme aux Merisiers RD 128 / 91190 Saint-Aubin, France